Enhanced Real Time Monitoring and Decision Support for Critical Grid Situations Using Synchronised Measurements

Kevin Kawal

A thesis submitted for the degree of
Doctor of Philosophy

Department of Electronic and Electrical Engineering
University of Strathclyde, Glasgow, UK

8th June, 2026

Abstract

Synchronised power system measurements, conventionally provided by phasor measurement units (PMUs), are essential to the real-time detection and monitoring of abnormal conditions. As the penetration of inverter-based resources (IBRs) increases, accurate monitoring of system dynamics, e.g., non-sinusoidal distortions, sub/super synchronous oscillations (SSOs), etc., becomes critical to ensure system security. However, PMUs rely on a fundamental sinusoidal reference, which limits their ability to accurately characterise the emerging IBR dynamics. In recent years, continuously streamed synchronised waveforms (synchro-waveforms) have enabled the access to higher-resolution voltage and current samples. While they can accurately capture such IBR-induced phenomena, the large data volumes and high streaming requirements hinder their practical wide-area deployment. Consequently, effective monitoring of IBR dominated power grids remains a key challenge. This research therefore aims to investigate novel synchronised measurement methods capable of characterising IBR dynamics with manageable data volumes, and their applications towards critical grid monitoring and decision support functions to facilitate the secure integration of IBRs.

In the thesis, the performance of conventional monitoring solutions in the presence of IBR-induced dynamics is first investigated via an analysis of real-world PMU measurements of SSO events in the Great Britain (GB) power system. Precursory signatures in phasor measurements are identified, and a machine learning (ML) based early warning system is developed. It is demonstrated that PMUs can be inadequate in capturing IBR-induced dynamics and more informative analyses using continuously streamed synchro-waveforms remain impractical. The research therefore proposes a novel generalised synchro-waveform measurement unit (G-SWMU) processing algorithm. The G-SWMU represents non-sinusoidal transients using a wavelet scale correlation transient filter (WSCTF) and estimates multi-frequency phasors using a novel iterative extended discrete Fourier transform based empirical wavelet transform (I-EDFT-EWT). Compatibility with existing supporting infrastructure is demonstrated by mapping the G-SWMU outputs to standard messaging formats, along with theoretical estimates of

the reduced bandwidth requirements. The performance of the G-SWMU is validated using real-world event waveforms from a wide range of system conditions, enabling enhanced SSO analysis and accurate anomalous event measurement. The adaptability and scalability of the proposed G-SWMU algorithm is further demonstrated beyond IBR-specific use cases through a novel G-SWMU enabled open-set event classification algorithm. The transient distortions captured by the G-SWMU algorithm provide discriminative features from limited training data, which enables accurate classification of power system events while effectively rejecting previously unseen events.

The contributions of this thesis therefore provide valuable knowledge and practical insights that support the adoption of the G-SWMU as a foundation for a new generation of synchronised measurement technologies, thereby enabling accurate monitoring and effective mitigation of critical events, which support the secure and reliable operations of IBR-dominated power systems.

Acknowledgements

I would like to express my deepest gratitude to my supervisor, Professor Qiteng Hong, for his invaluable support and guidance throughout the course of this research. His dedication, commitment and mentorship have been instrumental to the success of this PhD and will continue to shape my future career. I would also like to sincerely thank Dr Panagiotis Papadopoulos and Dr Steven Blair for their inspirational and insightful discussions over the course of this research. Their engagement, technical expertise and helpful feedback have greatly enriched this research.

I would also like to thank Professor Campbell Booth, Dr Adam Dysko, Dr Di Liu, Dr Subhadeep Paladhi, Dr Jiaxuan Han and Mr Richard Munro for their help throughout various stages of the PhD.

A special acknowledgement is given to Synaptec and CENSIS for their financial contributions as the industrial sponsors of this research.

I would like to extend my gratitude to the Advanced Electrical Systems team at the University of Strathclyde for their collaboration and friendship over the course of this PhD.

Finally, I would like to thank the family and friends who have supported me over the years. In particular, I wish to give a heartfelt thanks to my parents, Ronny and Wendy, and my sister Trudy, for their love, patience, dedication and support. This thesis is dedicated to them.

Contents

List of Figures

List of Tables

Glossary of Abbreviations

AI	Artificial Intelligence
CPD	Change-point Detection
DEF	Dissipating Energy Flow
DES	Distributed Electrical Sensing
DFT	Discrete Fourier Transform
DWT	Discrete Wavelet Transform
EMO	Electromechanical Oscillations
EVT	Extreme Value Theory
EWT	Empirical Wavelet Transform
FBG	Fibre Bragg Grating
fps	Frames Per Second
G-SWMU	Generalised Synchro-waveform Measurement Unit
GESL	Grid Event Signature Library
GoF	Goodness of Fit
GPD	Generalised Pareto Distribution
GPS	Global Positioning System
HT	Hilbert Transform
HVDC	High Voltage Direct Current
I-EDFT	Iterative Extended Discrete Fourier Transform

I-EDFT-EWT	Iterative Extended DFT based Empirical Wavelet Transform
IBR	Inverter Based Resources
IMF	Intrinsic Mode Function
Ip-DFT	Interpolated DFT
kbps	Kilobits Per Second
LGMVP	Live Grid Monitoring and Visualisation Platform
MP	Matrix Pencil
MP-Dict	Matching Pursuit Dictionary Approach
MPA	Matching Pursuit Algorithm
NNZ	Number of Non-Zeros
OSL	Oscillation Source Localisation
OSR	Open Set Recognition
PCC	Point of Common Coupling
PDC	Phasor Data Concentrator
PMU	Phasor Measurement Unit
POI	Point of Interconnection
RES	Renewable Energy Sources
RMS	Root Mean Squared
RTDS	Real-time Digital Simulator
SCADA	Supervisory Control and Data Acquisition
SG	Synchronous Generation
SSO	Sub-synchronous Oscillations
STFT	Short-time Fourier Transform
STTP	Streaming Telemetry Transport Protocol
SWMU	Synchronised Waveform Measurement Unit
SWT	Stationary Wavelet Transform
TF-CNN	Time-Frequency Convolution Neural Network
TVE	Total Vector Error

UTC	Coordinated Universal Time
VISOR	Visualisation of Real Time System Dynamics using Enhanced Monitoring
WAMS	Wide Area Monitoring System
WMU	Waveform Measurement Units (VISOR)
WS-OSNN	Wavelet Scattering Open Set Nearest Neighbours
WSCTF	Wavelet Scale correlation Transient Filter
WST	Wavelet Scattering Transform
WT	Wavelet Transform
WTMM	Wavelet Transform Modulus Maxima
YI	Youden's Index

Chapter 1

Introduction

1.1 Research Context

In response to global net-zero carbon emissions targets, and more recently, externally driven volatility in fossil-fuel markets, many countries are accelerating the large-scale adoption of renewable energy sources (RES) [1–3]. In 2024, RES were responsible for 46% of global electricity generation [4], and a record 50.5% of the total UK generation [5]. The UK government's Clean Power 2030 plan aims for installed capacity of renewables and low carbon sources to meet Great Britain (GB) demand by 2030 [6], with the electricity system achieving net-zero carbon emissions status by 2035 [7]. Subsequently, the role of unabated (no carbon capture and storage), fossil fuel driven synchronous generation (SG) will be relegated to supporting security of supply and is projected to provide less than 5% of annual generation beyond 2030 [6]. In addition to delivering this transition, network operators and owners also have a responsibility to ensure safe, reliable and secure system operation.

Asynchronous, weather-dependent (and hence intermittent) RES, are connected to the synchronous interconnected power system via power electronics based inverters. Similarly, bulk power transfer, via high voltage direct current (HVDC) links, battery energy storage systems (BESS), and emerging large loads (e.g. data centres) are also interfaced to the AC system via inverters. Collectively, these resources are termed inverter based resources (IBRs). The behaviour of IBRs, particularly under abnormal grid conditions, is vastly different from that of traditional SGs. IBR control is often proprietary and has additional objectives due to the physical limits of the IBR.(e.g. fault current limiting [8]).

The different behaviour of IBRs relative to SGs can lead to various issues that were not previously present in SG dominated power systems. IBR fault responses can negatively impact the performance of legacy protection [9] leading to the incorrect disconnection of IBRs [10]. The unexpected interactions among IBR controllers can introduce new oscillatory dynamics (particularly in weak system conditions), presenting significant threats to system stability and security [11]. Furthermore, system inertia is also decreased due to the reduction of directly grid coupled energy stored in rotating masses of SGs which IBRs do not inherently provide. This compromises the ability of the system to resist frequency deviation during sudden demand and generation imbalances, resulting in frequency control challenges [12]. The synchronous connection of IBRs requires adjustments to their control actions to maintain synchronisation with the network at the point of interconnection (POI). In particular, grid following IBRs track the POI voltage angle and adjusts their current output to maintain synchronous connection and meet their control objectives. This makes them sensitive to perturbations at the POI and leads to a decrease in system strength. In this context, the strength of the system refers to the sensitivity of voltage to variations in current injection or stiffness of voltage at the POI [13].

Consequently, power systems with a high penetration of IBRs are more vulnerable to disturbances, as has been observed recently in North America [14], Australia [15] and GB [10, 16]. Figure 1.1 presents a composite of observed (up to 2024) [17] and forecast (to 2050) generation mix in the GB electricity network assuming a holistic transition as described in the 2024 future energy scenarios (FES) [18]. A timeline highlighting selected representative past system events is also displayed. In 2019, the unexpected response of a large offshore windfarm's controller to voltage fluctuations, caused by a nearby fault, contributed to a large loss of infeed, triggering low frequency demand disconnection schemes [10]. In recent years, system oscillations have been observed and they have a relatively greater impact on the north of Scotland, which has a higher penetration of IBRs than the rest of the system [16].

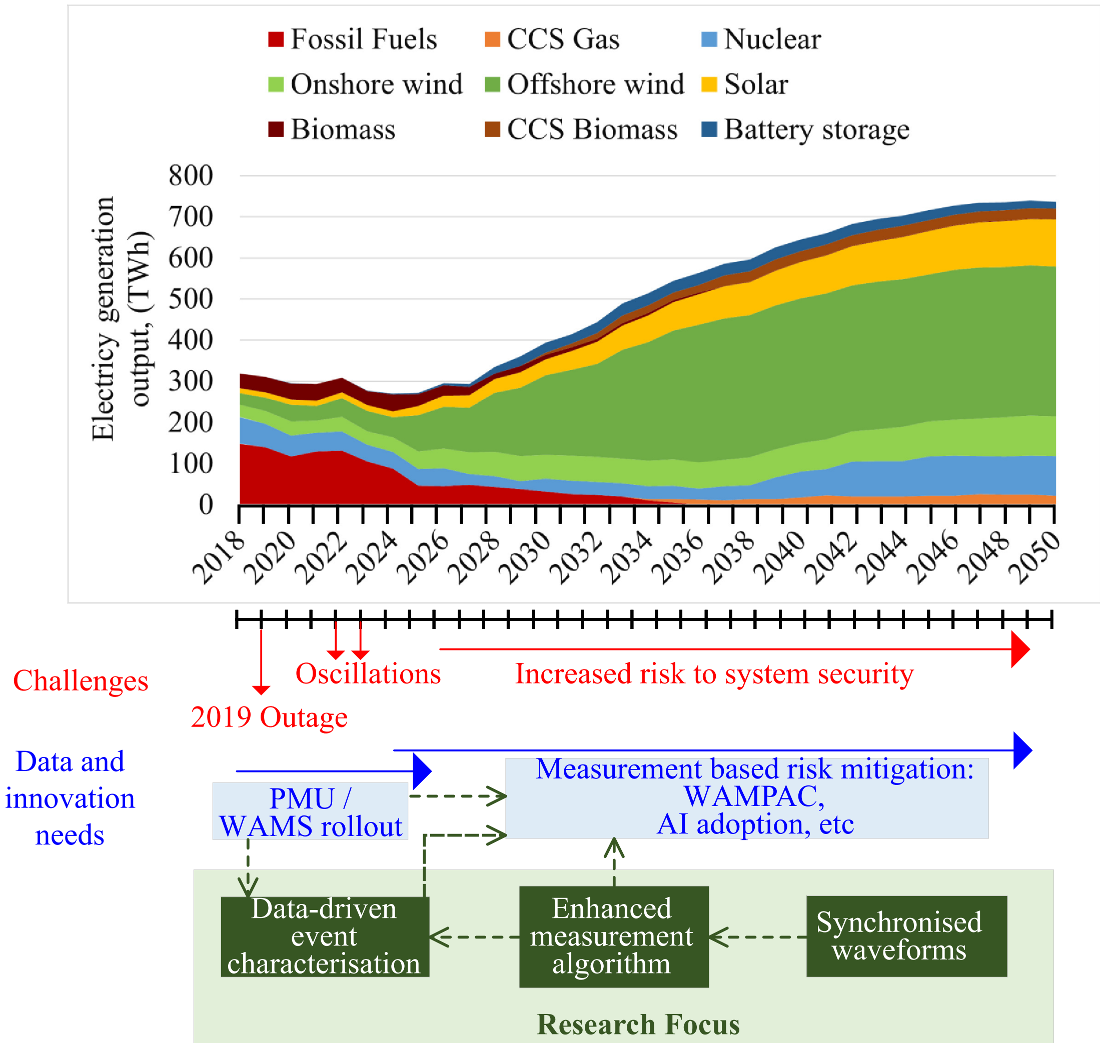

Figure 1.1: Electricity generation by fuel type in the GB network [17] highlighting challenges [10, 16], innovation needs [6] and the research focus.

In the holistic transition FES, illustrated in Figure 1.1, IBRs, especially wind generation, will continue to displace SG, with an estimated 100 GW of offshore wind in 2050. Even under the worst case counterfactual scenario in which net-zero targets are missed, there is still an increase in renewables (e.g. 81GW of offshore wind in 2050) and a small reduction in fossil fuel generation relative to present levels. This highlights that system conditions that contribute to abnormal events at current penetration levels are likely to persist or intensify, increasing both the frequency and severity of disturbances, such as oscillations, that propagate across the network, thus threatening system security.

Real-time detection monitoring and response to emerging system events, typically via time-synchronised measurements from phasor measurement units (PMUs), are paramount in understanding and mitigating such conditions. GB operating codes mandate that PMU installations at key transmission network locations be installed by 2026 to enable real-time system performance monitoring, post event analysis, and benchmarking observed behaviours with offline models [19]. Key network locations include points where interconnectors or generators directly connect to the transmission system and grid supply points [19]. Wide area monitoring systems, (WAMS) which process and visualise multiple PMU measurements for situational awareness, have also been established in the GB network [20].

However, conventional PMUs take measurements relative to a fundamental sinusoidal reference (50Hz in the GB system) with additional filtering around the nominal frequency to meet standard specifications. PMUs therefore may not be sufficient for monitoring certain transient and dynamic phenomena (e.g. non-sinusoidal conditions, oscillations, etc.) that do not align with the standard synchrophasor definition. As the impact of anomalous events (e.g. voltage waveform perturbations in the 2019 GB event) and IBR dynamics (e.g. oscillations) have introduced increasing challenges to system security, it is critical to have effective monitoring solutions that are capable of capturing IBR induced dynamics. To address this, synchronised waveform measurement units (SWMUs) that provide continuous streaming of time-synchronised waveform (synchro-waveform) measurements [21] have emerged, e.g. the SWMUs implemented in the GB WAMS [20] and distributed sensing platforms [22]. It should be noted that the term SWMU is defined by the IEEE task force on big data for synchro-waveform measurements [23] to highlight that the measurements are time-synchronised. The terms SWMUs and waveform measurement units (WMUs) can be used interchangeably in the literature [21, 23]. In this thesis, the term SWMU is adopted.

Synchro-waveform measurements, sampled and streamed at high sampling rates (several kHZ to MHz), preserve underlying dynamics but are burdensome to continuously stream and/or archive due to the large volumes of data [24]. The GB WAMS

SWMUs are limited to downsampled raw measurements streamed at the PMU IEEE 37.118 reporting rate of 200Hz as a compromise between retaining waveform information and meeting communication requirements [20]. This highlights the practical limits on the measurement ability and scalability of state-of-the-art SWMUs. Therefore, improved synchro-waveform processing techniques which can extract relatively sparse features (compared to raw waveforms) that accurately represent dynamics present in the raw measurements sampled at the full sampling frequency (several kHz) are needed. Such methods balance information preservation with minimising data volume requirements. This will position SWMUs as a practical and viable measurement technology better suited for power networks with an increasing share of IBRs.

Additionally, the complexity of large-scale interconnected power systems and the uncertainty associated with IBR behaviours limit the ability of physics-based modelling and engineering design to identify and mitigate threats to secure system operation. Data-driven techniques, including artificial intelligence (AI), provide an opportunity to learn complex patterns and correlations within synchronised measurements. Such an approach can lead to more robust detection and characterisation of IBR dynamics and other system behaviours that would otherwise be difficult to achieve using conventional monitoring and analysis methods which may be sensitive to modelling uncertainties and varying real-world conditions. This means that, in addition to improved synchronised measurement algorithms, supporting applications that derive actionable insights from processed outputs are needed. Accelerating the adoption of AI has therefore been identified as a key enabler of the Clean Power 2030 targets [6]. Additionally, a supporting data sharing infrastructure (DSI), with planned widespread adoption by 2030, can enable scalable, secure and efficient sharing of data between multiple entities in the energy sector [25]. The DSI will therefore act as an enabling repository for the development of data-driven applications and other decision support tools. However, the development of such support tools may be hindered by the lack of suitable measurements caused by the inaccuracy of PMUs and the lack of scalability of continuously streamed synchro-waveforms.

Improved power system monitoring that accurately captures a wide range of emerging dynamics in an efficient manner will therefore be critical in enhancing situational awareness, enabling automatic solutions and aiding in human decision-making processes in order to ensure the secure operation of IBR-dominated systems.

1.2 Research Motivation

Conventionally, synchronised measurements typically consist of continuously streamed PMU measurements that have proven successful in accurately monitoring steady state conditions, and electromechanical dynamics, while facilitating post event investigations [24]. PMU outputs are also communicated via the IEEE C37.118 standard message formats [26] at certain frame rates, which can be used as the basis for informing the design and specifications of established and near-term planned supporting (communication/storage) infrastructure. More recently, raw synchro-waveforms provide access to higher-resolution measurements that retain information relating to IBR dynamics. However, their compatibility with existing infrastructure remains an issue, particularly if the raw synchro-waveforms are continuously streamed. Continuous streaming of synchronised waveforms in real time presents significant challenges in terms of bandwidth requirements, and computational burden [23].

Potential approaches to address these issues include compression of synchro-waveform data combined with centralised processing and/or local edge processing with intermittent communication of derived features representing abnormal events as they occur [27]. Both of these approaches mitigate the need for additional communication and storage infrastructure (particularly at measurement locations), while enabling waveform based monitoring applications. However, large-scale deployment of wide-area SWMUs is expected to favour local synchro-waveform processing and the communication of extracted features, rather than relying on large central repositories associated with the signal compression approach [23]. This will better support localised applications and reduce potentially large storage and processing requirements at centralised locations [23]. The planned DSI [25] can also be utilised to store, communicate and share processed synchro-waveform data, thus ensuring utilisation of high-resolution information while reducing the communication and storage requirements. Furthermore, application specific deployment of SWMUs, e.g. protection applications [28], have been demonstrated. However, they are limited to the targeted application and general-purpose SWMU processing is required in order to enable different concurrent applications (event detection, oscillation monitoring, etc.), thus improving the return on investment in synchro-waveform technologies [23].

To address the limitations of both conventional PMUs and real-time continuous streaming of synchro-waveforms, the research presented in this thesis investigates novel synchronised measurement methods better suited for monitoring abnormal conditions, including emerging IBR dynamics, thus enhancing situation awareness capability. In addition, it aims to enable improved data driven decision support applications to derisk IBR integration. Specifically, the research develops monitoring techniques capable of producing outputs, which can more accurately retain the information present in synchro-waveforms, while remaining compatible with existing supporting (communications and storage) infrastructure. These more informative and scalable processed synchro-waveform outputs are then integrated within data analytic frameworks to develop decision support applications, thus enhancing wider grid monitoring capabilities. Overall, the research seeks to remove the barriers to extracting valuable insights from high-resolution synchro-waveforms, thus supporting the secure and reliable operation of IBR-dominated power systems at both the present and forecasted RES penetration levels. The research objectives of this thesis are listed below:

1. Develop an understanding of IBR-induced phenomena in order to specify requirements of synchronised measurement techniques suited for IBR-dominated systems. This will be based on deriving insights from real-world measurements. PMU and waveform datasets will be analysed to identify event signatures and trends, as well as to inform requirements for improved monitoring capabilities, including synchro-waveform processing requirements.

2. Develop a general-purpose, efficient and scalable synchro-waveform processing algorithm. This involves investigating advanced signal processing techniques cap-

able of capturing appropriate features representative of the information in the synchro-waveform measurements, including IBR dynamics. The algorithm outputs should also be compatible with existing communication formats and infrastructure to support practical, wide scale deployment.

3. Leverage processed synchro-waveform measurements for enhanced decision support. This will be achieved by developing supporting applications that translate the improved, yet compact features, obtained via the improved synchro-waveform processing, into actionable insights via the identification and characterisation of abnormal conditions to inform improved mitigation strategies.

1.3 Principal Contributions

This research provides the following contributions to knowledge:

1. The identification and characterisation of precursory oscillatory signatures preceding oscillation events within the GB network, along with an early warning system to identify such signatures. A framework utilising statistical change-point detection and machine learning to identify oscillation signatures in historic synchronised measurements and classify the state of the system, respectively, has been developed. The early warning system was demonstrated using a real-world PMU dataset and can provide insights into the risk of oscillations via the detection of precursor signs.

2. A novel generalised synchro-waveform measurement unit (G-SWMU) processing algorithm capable of extracting and representing operationally relevant transient, harmonic, and inter-harmonic information contained in raw synchro-waveforms. The G-SWMU outputs have significantly reduced data volume and are in a form compatible with existing supporting infrastructure. The proposed G-SWMU algorithm consists of:

   (a) A novel wavelet scale correlation transient filter (WSCTF) capable of power system transient detection and feature extraction. Transients are compactly represented as correlations in different frequency (wavelet) bands.

(b) A novel iterative extended discrete Fourier transform enabled empirical wavelet transform (I-EDFT-EWT) method for multi-frequency phasor extraction. The module is capable of decomposing multi-modal signals and outputting the fundamental and harmonic / inter-harmonic phasors.

3. A novel G-SWMU-enabled wavelet scattering open-set nearest-neighbour (WS-OSNN) power-system event classifier capable of identifying anomalous events using limited training data. The G-SWMU captures transient signatures in event waveforms, thus providing discriminative features. This enables wavelet-scattering-based nearest-neighbour classification and open-set rejection of unknown events. The classifier is validated using actual event waveforms and demonstrates accurate anomalous event classification in the presence of limited real world data.

1.4 Thesis Overview

A schematic overview of the thesis is presented in Figure 1.2. This thesis is organised as follows:

Chapter 2 provides an overview of real-time power system monitoring. Conventional PMUs and their applications are investigated. Synchro-waveform measurement algorithms and their potential applications are also introduced and reviewed. A comparison between PMU and synchro-waveform measurements is also discussed. Finally, key research gaps to improve power system monitoring in IBR rich power systems are identified.

Chapter 3 presents the analysis of a real-world historic PMU dataset containing several oscillation events in the GB network. Trends in the oscillation properties are presented, and precursor signatures are identified and analysed. An ML based early warning oscillation classifier is trained and evaluated using time-frequency features. The potential limitations of PMU measurements in analysing IBR-driven oscillations are also demonstrated.

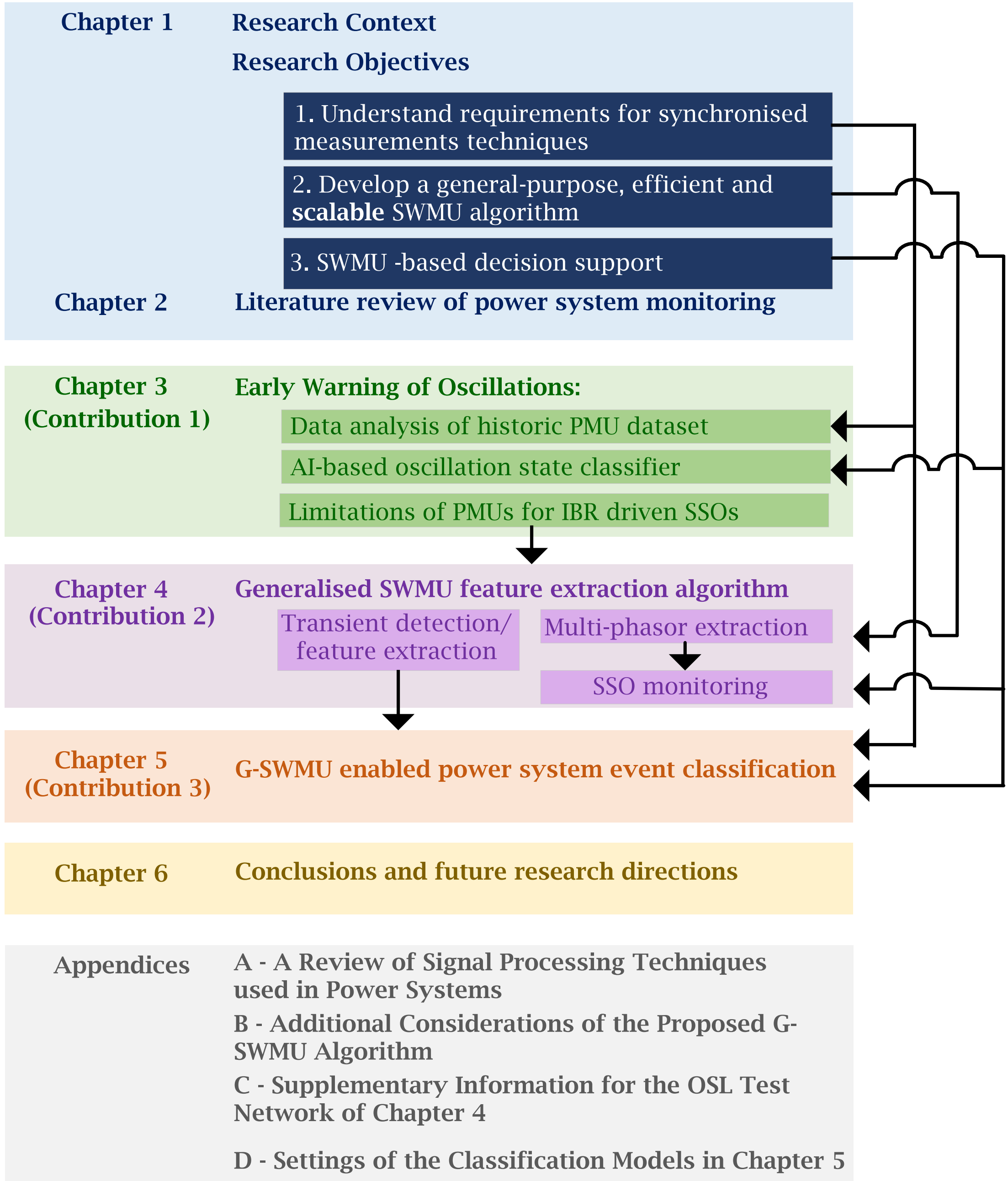

Figure 1.2: Thesis structure

Chapter 4 presents the proposed G-SWMU feature extraction algorithm capable of adapting to and accurately representing different possible dynamics including transient and/or oscillatory conditions, via sparse outputs relative to raw synchro-waveforms. Design considerations are discussed and the G-SWMU's performance is evaluated on a wide range of open-source data and benchmarked against traditional PMUs as well as existing synchro-waveform processing techniques. An SSO monitoring application is also demonstrated via case studies using measurements from actual events.

Chapter 5 utilises the outputs of the proposed G-SWMU algorithm within the wavelet scattering based open set nearest neighbours (WS-OSNN) event classifier. The improved feature extraction of the G-SWMU algorithm and the incorporation of open set recognition, are demonstrated to improve event classification under realistic conditions characterised by limited training data. The model is trained and evaluated using real-world event data, highlighting its practicality. A framework to incorporate the proposed model within a manual incremental learning process to improve training datasets is also demonstrated.

Chapter 6 summarises the contributions of the research presented in this thesis. Recommendations to further develop the proposed measurement algorithm and proposed applications are discussed and future research directions are highlighted.

1.5 Publications

1.5.1 Journal Papers

A journal paper summarising a protection application enabled by synchro-waveform measurements was produced produced in partnership with the industry sponsor Synaptec.

- K. Kawal, S. Blair, Q. Hong, and P. N. Papadopoulos, “Selective Auto-Reclosing of Mixed Circuits Based on Multi-Zone Differential Protection Principle and Distributed Sensing,” *Energies*, vol. 16, no. 6, p. 2558, Mar. 2023, doi: `http://dx.doi.org/10.3390/en16062558` .

1.5.2 Conference Papers

- K. Kawal, Q.Hong, S. Guo, A. Dysko, B. Stephen, A. Egea-Alvarez and C. Booth, “Data-driven early warning of power system oscillations in Great Britain,” *2025*

IEEE Power and Energy Society General Meeting (PESGM), Austin, TX, USA, 2025, pp. 1-5, doi: `https://doi.org/10.1109/PESGM52009.2025.11225355`.

- S. Blair, K. Kawal, P. Papadopoulos and Q. Hong, "Review of Applications and Practicalities of Synchronized Waveform Monitoring," *2024 International Conference on Smart Grid Synchronized Measurements and Analytics (SGSMA)*, Washington, DC, USA, 2024, pp. 1-6, doi:`https://doi.org/10.1109/SGSMA58694.2024.10571536` .

- K. Kawal, Q. Hong, P. N. Papadopoulos, S. M. Blair and C. D. Booth, "A Wavelet Based Synchronized Waveform Measurement Unit Algorithm," *2023 IEEE PES Innovative Smart Grid Technologies Europe (ISGT EUROPE)*, Grenoble, France, 2023, pp. 1-5, doi: `https://doi.org/10.1109/isgteurope56780.2023.10408556`.

- K. Kawal, S. Blair, and P. N. Papadopoulos, 2023, "Selective auto-reclosing of mixed circuits based on multi-zone differential protection principle and distributed sensing," Protection, Automation and Control (PAC) World Conference, Glasgow, UK, 2023.

- K. Kawal, Q. Hong, S. Paladhi, D. Liu, P. N. Papadopoulos, S. Blair and C. Booth, "Vulnerability assessment of line current differential protection in converter–dominated power systems," *16th International Conference on Developments in Power System Protection (DPSP 2022)*, Hybrid Conference, Newcastle, UK, 2022, pp. 362-367, doi: `https://doi.org/10.1049/icp.2022.0967`.

1.5.3 Book Chapters

- Q. Hong, K. Kawal, S. Paladhi, G. Zhang, C. Booth, and V. Terzija, "Wide Area Monitoring, Protection and Control (WAMPAC)" in *Encyclopedia of Electrical and Electronic Power Engineering*, Elsevier, 2023, Pages 278-293, ISBN 9780128232118, doi: `https://doi.org/10.1016/B978-0-12-821204-2.00145-8`.

- S. Paladhi, K. Kawal, Q. Hong, and C. Booth, “System integrity protection

schemes for future power systems," in *Synchrophasor Technology : Real-time operation of power networks*, Institution of Engineering and Technology eBooks, pp. 199–226, Jun. 2023, doi: `https://doi.org/10.1049/pbpo190e_ch8`.

Chapter 2

Literature Review: Real time Monitoring of Power Systems

Accurate measurements of electrical quantities play a critical role in supporting power system planning, real-time operations and post event analyses [29]. Real-time analysis of wide area measurements enables situational awareness of system operating conditions along with their proximities to stability and security margins. Prompt detection and characterisation of abnormal conditions such as faults, frequency deviations, stressed transfer corridors, oscillations etc., allows operators to implement preventive or corrective actions to mitigate further degradation and facilitate recovery to severe disturbances [30, 31]. Real-time, wide area monitoring is therefore essential for preventing local disturbances from propagating across the network thus limiting the severity and duration of outages and hence improving system resilience and reliability.

Real-time monitoring of power systems is typically achieved via a combination of supervised control and data acquisition (SCADA) and phasor measurement units (PMUs). SCADA is widely used and provides relatively low resolution (e.g., 1 sample per second) electrical measurements, device statuses, and alarms. SCADA systems have supported improved situational awareness, incorporating measurements and real-time network topology into state estimation algorithms while also facilitating automated actions such as tap-changing or network reconfiguration [32]. However, SCADA typically does not provide (high precision, system wide) time synchronisation [33]. Relying solely on SCADA systems therefore results in limitations for capturing emerging power system dynamics and is unsuitable for real time monitoring of IBR dominated systems, particularly across a wide area.

Voltage and current waveform measurements represent the most granular electrical measurements, which are typically processed to derive equivalent average quantities across observation windows, e.g. root-mean-square, (RMS) values. Active and reactive power, as well as quantities relevant to periodic sinusoidal AC waveforms (e.g. frequency and rate of change of frequency, RoCoF), can also be further derived. Such measurements may be compared over wide geographical areas, once appropriately time synchronised. Accurate time synchronised wide-area measurements are therefore critical in maintaining steady state operations and where applicable for detecting, analysing and responding to potential high impact, system-wide events.

PMUs, initially developed in 1988, have been widely adopted as the business-as-usual solution for obtaining time-synchronised power system measurements, particularly in transmission networks [34]. Time synchronisation allows locally measured magnitudes and angles of voltages and currents to be compared over wide geographical areas. This supports dependable protection applications such as differential protection [35] and provides insights into the propagation of dynamics across the physical network, including phase angle separation, power flows and oscillations, thus providing real time situational awareness of system stability [36]. The large-scale adoption of PMUs, combined with associated communication and storage infrastructure, enables wide-area monitoring, allowing power system stakeholders to better manage the network.

However, as power systems evolve with increasing penetration of IBRs, new system dynamics have emerged, which can not be accurately represented by phasors, thus resulting in traditional PMU measurement techniques facing limitations. Recent research and development of continuously streamed synchronised waveform measurements offer higher resolution measurements, capturing transient behaviours that may be filtered out by PMUs. However, these techniques also face challenges of large data volume and the associated high requirements on communications infrastructures. This has led to the emergence of synchro-waveform processing methods as alternatives to PMU processing techniques.

This chapter presents a state-of-the-art review of techniques for real-time monitoring of power systems. The fundamentals of traditional PMU measurements, including standard definitions and a review of existing applications, are presented. Synchro-waveform measurements are explained and compared to PMUs to evaluate their relative advantages and disadvantages. Emerging synchro-waveform processing methods are described and categorised in terms of their suitability for monitoring different types of dynamics and events. It should be noted that the underlying theory of signal processing techniques is not the focus of this review and therefore not discussed in detail in this Chapter. There is a wide array of signal processing techniques that can be applied or combined to achieve similar functionality, with the design choice influenced by proprietary designs and intended application. Selected techniques are briefly introduced and compared in Appendix A. Additionally, emerging monitoring needs of IBR rich networks are identified and mapped to their corresponding measurement requirements. Finally, research gaps and opportunities to better capture, process and utilise synchronised measurements are highlighted.

2.1 Synchrophasors and Phasor Measurement Units

2.1.1 Synchrophasor Concept

Steady state AC voltage and current are sinusoidal waveforms, typically at the nominal system frequency (50 or 60 Hz) and possibly containing a small amount of harmonics. These waveforms can be described by phasors consisting of a complex number with a magnitude, X and angle, θ as illustrated in Figure 2.1. Phasors may be equivalently represented in polar ($X\angle\theta$), rectangular ($X\cos(\theta) + jX\sin(\theta)$) or exponential ($Xe^{j\theta}$) forms. The phasor magnitude corresponds to the RMS value of the sinusoidal waveform, while the angle represents the phase displacement of the waveform relative to a pre-defined reference. In order to allow the comparison of measurements taken in different locations across the power network, it is necessary to define a common time [37].

This is achieved by using a cosine wave at the nominal power system frequency that is synchronised with coordinated universal time (UTC). The phase angle of the time synchronised phasor (i.e. synchrophasor) being measured is the difference between the phase of the signal of interest and the phase angle of the reference cosine wave at the UTC timestamp [38] as illustrated in Figure 2.1.

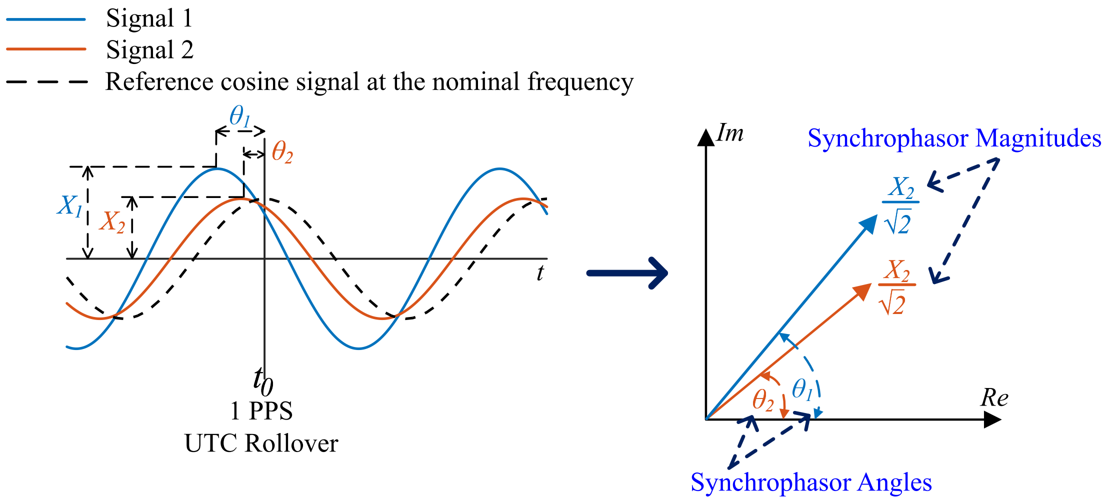

Figure 2.1: Synchrophasor concept

An AC power system signal (e.g. voltage or current) can be modelled as:

$$x(t) = X_m(t)\cos(\theta(t)) + D(t), \tag{2.1}$$

where $X_m(t)$ is the time varying amplitude of the signal and $\theta(t)$ is the time varying angular position of the signal in radians with $t = 0$ aligned with a UTC second rollover. $D(t)$ includes harmonics, noise, DC offset and out of band interferences, which are attenuated during synchrophasor estimation. $\theta(t)$ can further be expressed in terms of the signal frequency f, and an initial phase $\theta(t_0)$ as:

$$\theta(t) = 2\pi f t + \theta(t_0). \tag{2.2}$$

The reference signal is defined as [38]:

$$x_{ref}(t) = \cos(2\pi f_n t), \tag{2.3}$$

where f_n is the nominal system frequency (50 Hz in the GB network). The UTC timestamp, t, can be provided by a one Pulse Per Second (1 PPS) signal at the beginning of a UTC second, typically provided by a Global Positioning System (GPS) source. The time instant coincident with the 1 PPS UTC timestamp becomes the reference time from which the phase displacement is measured.

Under steady-state conditions at nominal frequency, the phasor parameters to be measured are constant over the observation window and are defined as [38]:

$$\tilde{X} = \frac{X_m}{\sqrt{2}} e^{j\Theta}, \tag{2.4}$$

where the synchrophasor angle, Θ, is defined as the phase difference between angular position of the sinusoidal AC signal, $\theta(t)$, and the phase due to the nominal frequency:

$$\Theta = \theta(t) - 2\pi f_n t. \tag{2.5}$$

Substituting 2.2 into 2.5 gives:

$$\Theta = \theta(t_0) - 2\pi(f - f_n)t. \tag{2.6}$$

The measured synchrophasor angle therefore includes a measurement of the phase displacement of the signal at the measurement instant relative to a UTC time. This measurement also includes the phase displacement due to the difference between the nominal frequency and actual system frequency. This difference is usually very small in steady state and within statutory limits of $f_n \pm 0.2$Hz, with an analysis of GB data performed in [39] showing that frequency fluctuations are typically within ± 0.1Hz in steady state. Figure 2.1 illustrates the synchrophasor concept for two waveforms, potentially from different measurement locations, with respect to a UTC cosine reference waveform. The common time reference allows for a valid and accurate phase angle comparison between the measurement locations.

The frequency of a signal $x(t)$ is defined as the angular velocity of the signal as:

$$f(t) = \frac{1}{2\pi}\frac{\mathrm{d}\theta(t)}{\mathrm{d}t}. \tag{2.7}$$

The frequency can be expressed in terms of the measured synchrophasor angle by substituting for $\theta(t)$ in (2.7) using (2.5) :

$$f(t) = f_n + \frac{1}{2\pi}\frac{\mathrm{d}\Theta(t)}{\mathrm{d}t}, \tag{2.8}$$

and the rate of change of frequency (RoCoF), as:

$$RoCoF(t) = \frac{1}{2\pi}\frac{\mathrm{d}^2\Theta(t)}{\mathrm{d}t^2} \ . \tag{2.9}$$

Phasor frequency and RoCoF are estimated as rated of changes of phase and frequency respectively across multiple windows.

Figure 2.1 and Equations (2.3)-(2.9) illustrate that synchrophasors are defined with respect to a steady state, sinusoidal reference at the nominal system frequency. There is an underlying assumption that within the measurement window, the system is in a quasi-steady state and near the nominal frequency.

2.1.2 Phasor Measurement Units (PMUs)

PMUs refer to a device (or a functional element within a device) capable of accepting voltage and/or current waveforms, along with a synchronised time source (e.g. GPS), and producing Synchrophasors, frequency and RoCoF estimates [38]. Figure 2.2 illustrates a high-level schematic overview of a PMU. The input waveform is filtered to prevent aliasing and discretised, digital samples are produced using an analogue to digital converter (ADC). A sampling clock, which is typically phase locked to the 1 PPS from the UTC time source, is used to timestamp the digital samples [40].

A microprocessor hosts the PMU algorithm (i.e. a signal processing algorithm) that computes the synchrophasors across the measurement windows. System frequency and RoCoF are then derived across successive measurement windows. Additionally, active/reactive powers and sequence components may also be derived. Examples of synchrophasor measurement algorithms include DFT [41], demodulation and filtering [38, 41], and adaptive cascading filtering [42]. However, commercial PMUs might be equipped with different manufacturers' proprietary measurement algorithms, which should also meet the requirements specified in the performance standard [38]. Low pass filtering is applied to balance measurement performance with reporting latency. Window size, filtering and algorithm selection reflect trade-offs between measurement accuracy and the ability to quickly track dynamic changes in the measurements.

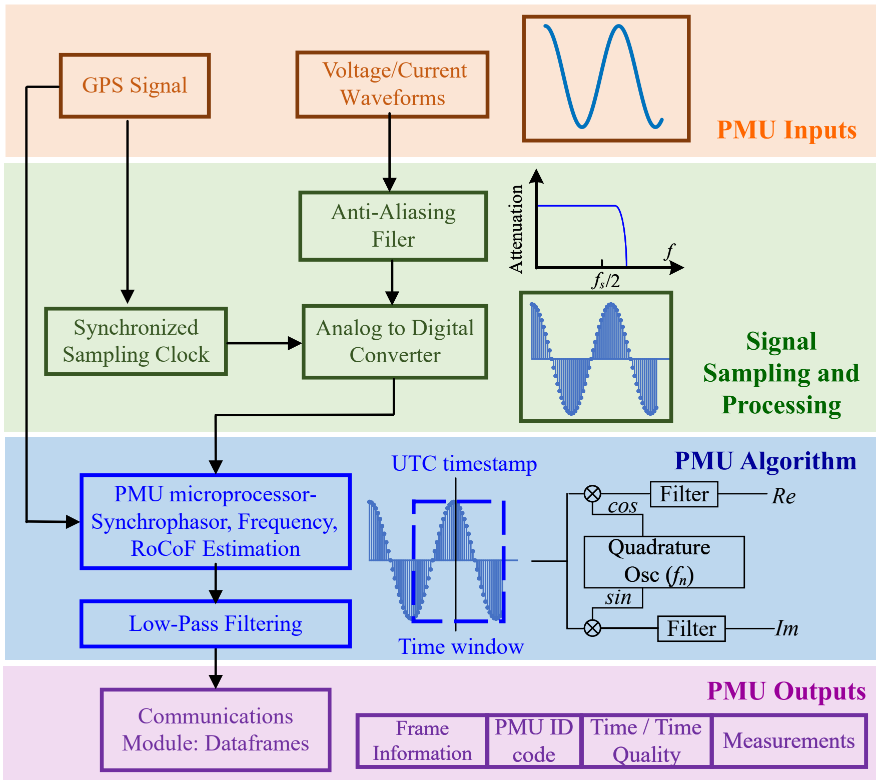

Figure 2.2: Schematic overview of a typical standard compliant PMU (adapted from [37])

A key feature and advantage of PMUs is that they output UTC timestamped measurements in a standard message format. This ensures compatibility across vendor specific implementations. Multiple PMUs interfaced by a communication network allow for the real-time transmission and processing of synchrophasor, frequency and RoCoF data with high precision timestamps. This allows for coordinated analysis and comparison of system-wide measurements to monitor and mitigate evolving power system dynamics [37].

2.1.3 PMU Standards

PMU standards are important to ensure a minimum acceptable performance and interoperability across different potential PMU implementations. As of 2025, there are currently two active PMU standards relating to synchrophasor measurements and synchrophasor data transfer, i.e. IEEE/IEC 60255-118-1-2018 International Standard: Synchrophasors for power systems- Measurements [38] and the C37.118.2-2024 - IEEE Standard for Synchrophasor Data Transfer for Power Systems [26].

IEEE/IEC 60255-118-1-2018 synchrophasor measurement standard

The IEEE/IEC 60255-118-1-2018 standard defines steady state and dynamic performance requirements for PMUs with considerations of variations in measured quantities, harmonic distortion and out-of-band frequency interference. Reporting rates that are integer multiples of the nominal frequency (e.g. 10, 25, 50, 100, 200 for a 50 Hz system) are specified. A key measure of synchrophasor accuracy is the total vector error (TVE), which is defined as a combination of magnitude and phase errors. Frequency and RoCoF measurement errors are also defined.

Acceptable limits on these errors are specified for two distinct performance classes. The protection (P) class has shorter measurement latency requirements, employs less filtering, and applies relatively limited harmonic signal rejection with no out-of-band signal rejection. In contrast, the measurement (M) class has stricter filtering, which significantly attenuates signals that are above the Nyquist frequency for the given reporting rate, resulting in increased harmonic and out-of-band signal rejection. M class PMUs therefore have a larger allowed reporting latency in comparison to P class, but can give more accurate fundamental synchrophasor estimates across a wider variety of operating conditions. A maximum TVE of 1% is allowed for both the P class and M class measurements for different operating conditions, which are specified in detail in [38].

The reporting latency is defined as the time delay from the power system event occurring at the measurement point to the time it is reported in the PMU output. It is a function of the measurement window, filtering, synchrophasor algorithm, reporting rate and measurement class. The requirements for the reporting latency are also specified in the standard. Compliant PMUs have a maximum latency of the greater of $2/F_s$ or $2/f_0$ for P class or the greater of $7/F_s$ or $7/f_0$ for M class, where F_s is the reporting rate and f_0 is the nominal frequency. A lower latency is required for the P class to enable fast protection decisions within critical timescales (e.g., critical clearing times) to ensure system resilience to faults. Measurement compliance testing and evaluation as well as informative annexes including a reference signal processing model are also included. This standard however does not specify hardware, software or measurement methods.

IEEE Std C37.118.2-2024: IEEE Standard for Synchrophasor Data Transfer for Power Systems

The IEEE Std C37.118.2-2024 synchrophasor data transfer standard is a recently (2024) adopted standard that supersedes the previous C37.118.2-2011 standard. This standard specifies a frame based communications protocol. Frame (message) types, contents and data formats are defined for real-time communications between PMUs, phasor data concentrators (PDCs) and other applications to facilitate data exchange among measurement, data collection, and application equipment. Five frame types are defined in this standard:

1. Configuration frames which describe the data being transmitted. This can include data types, calibration factors and other associated meta-data.

2. Periodic data frames which contain synchrophasor data including synchrophasor estimates, frequency, RoCoF, analogue and digital data. Periodic data frames are reported at regular time intervals determined by the data reporting rate specified as integer multiples of the nominal frequency.

3. Discrete event data frames which contain digital statuses coincident with some

change in status or digital data. They can be transmitted at the onset of an event and may or may not match the uniform timestamps associated with the periodic data frames, i.e. the timestamps may be aperiodic. This is an added functionality compared to the previous version of the standard.

4. Command frames which are sent by the data collecting device to start or stop data transmission and to request configuration frames from the transmitting device.

5. Error frames which give a message if a command is not understood or rejected.

Each of these frame types are then included within an overall message structure that incorporates an identifier of the frame type, time information (including second of century timestamp), frame size, stream identification and error checking. The current version (C37.118.2-2024) of the standard includes key improvements over the previous version (IEEE Std C37.118.2-2011), and a comparison of the two versions of the standard is presented in Table 2.1.

Table 2.1: Comparison of C37.118 Standards

C37.118.2-2011 (superseded)	**C37.118.2-2024 (active)**	**Enhanced Capability**
One data frame defined: ∗ Data frame: ✓ Synchrophasors ✓ Analogue/digital words ✓ Periodic reporting	Two data frame categories defined: ∗ Periodic Data frame: ✓ Synchrophasors ✓ Analogue/digital words ✓ Periodic reporting ∗ Discrete data frame ✓Digital words ✓Aperiodic reporting	Real time transient detection
∗ Data Quality Status (PMU) ✓Good measurement ✓PMU error no information ✓PMU in test mode ✓PMU error do not use	∗ Data Attributes (per Phasor) ✓Step detected in measurement window ✓Test data ✓Data error	Phasor confidence score

A key change is the splitting of data frames into two distinct categories, as seen in the 'C37.118.2-2024 (active)' column of Table 2.1. The periodic data frame retains similar functionality and is reported using periodic message report rates. The discrete data frame allows for real-time communication of discrete events, i.e. statuses communicated via digital outputs. Previously discrete event timestamps were not accurate as they were time tagged with the synchrophasor time-stamp and reported at the next available message as per the reporting rate. Discrete event frames have applications in better characterising sequence of events information, for example, breaker statuses etc. Transient detection functionality within the PMU may also utilise these frames. Another change is around data quality. Previously, data quality flags were reflective of the entire PMU and gave no signal level quality information [43]. In contrast, the new standard allows each phasor to be followed by an optional data attribute field that includes a flag which informs users (or applications) that the measurement window encompasses a transient. This can serve as a confidence metric when interpreting PMU outputs.

Improved communication of additional information relating to discrete events and measurement validity can aid in the development of the next generation of PMU algorithms that are resilient to conditions that violate the traditional synchrophasor definition.

2.1.4 PMU Applications

Wide-Area Monitoring Systems

Measurements from standard compliant PMUs are typically transmitted via communication networks and collated by phasor data concentrators (PDCs) to form wide-area monitoring systems (WAMS). A GB network WAMS, referred to as VISOR (Visualisation of Real Time System Dynamics using Enhanced Monitoring), has been installed since 2018 [44]. VISOR gathers, collates, visualises and analyses synchronised measurements in real time from approximately 60 PMUs and 10 waveform measurement units (WMUs) (as of 2018) installed across all three of the GB mainland transmission owners (Scottish Power Transmission, Scottish & Southern Electricity Networks Transmission and National Grid Electricity Transmission) [20]. Each transmission owner has visibility of measurements within their network and the system operator has visibility of all measurements.

Applications of VISOR include state estimation, line parameter estimation, dynamic model validation, and SSO monitoring and localisation. VISOR is capable of monitoring oscillations within the range of 4-46 Hz using WMUs, which continuously stream waveform samples at 200 Hz using the IEEE C37.118.2-2011 protocol [45]. However, source localisation is done using relative phase angle measurement from PMUs and online SSO stability management requires further development [44].

A review of WAM implementations across several countries, conducted in [37], including the US, UK and China, showed that several PMU based WAM applications have been successfully implemented. Visualisation of key wide area measurements such as power flows, bus voltages and angles can increase situational awareness [46]. PMU measurements and system topology information are combined in linear state estimation tools to infer the quantities at different locations without measurements. The outputs of state estimation can be used for system planning and operation, event detection, bad data detection and support other applications that require system observability. Online, measurement based stability assessments via the derivation of metrics (e.g. P-V curves, impedance margins) have also been deployed in utility control rooms [46–48]. Detection, monitoring and visualisation of electromechanical, inter-area oscillation modes and forced oscillations have also been adopted [48,49]. Wide area backup protection schemes utilise the enhanced visibility of the network offered by WAMs, to detect, locate and isolate electrical faults [50]. WAM implementations also provide an opportunity to gather historic system-wide data sets, from which data analytics may uncover system dynamics and patterns to inform improved WAM applications.

Existing WAM implementations are therefore reliant on conventional PMU measurements. As a result, WAM applications may be hindered by the measurement limitations of PMUs, particularly in IBR-dominated networks as will be discussed in Section 2.3. Incorporating higher resolution synchro-waveforms will allow for the accurate measurement and valid comparison of emerging IBR dynamics, thus extending the suitability of existing WAM applications beyond electromechanical phenomena. SWMU based WAM applications are the subject of active research, (e.g. oscillation monitoring) and will be discussed further in Section 2.2. However, the large data volumes associated with raw, continuously streamed synchro-waveforms remain an impediment to the adoption of synchro-waveform based WAMs. This challenge will be subsequently addressed in this thesis via the investigation of improved synchro-waveform processing (Section 4) that is suitable for enabling SWMU based WAMS.

Power System Oscillation Monitoring

Power system oscillations are a form of instability manifesting as periodic deviations in system variables. Oscillations may arise in interconnected power systems, via natural interaction of groups of generators in separate regions (natural modes) or external perturbations known as forced oscillations [51]. These oscillations are conventionally associated with electromechanical synchronous machine dynamics and manifest as low frequency electromechanical oscillations (EMOs) ($<\sim$ 5Hz) in phasor measurements. Sub-synchronous oscillations (SSO) conventionally associated with resonances between multi-mass turbine-generator dynamics (torsional) and series compensated transmission networks can occur in a wider frequency range compared to EMOs [52]. For example, the turbine generator of the well studied Mohave SSO event had torsional modes ranging from 15 Hz to 32Hz [53]. PMU's with sufficient reporting rates (at least twice the nominal frequency) have also been utilised to monitor SSO events [45].

PMUs have also been utilised to monitor and characterise inter-area modes in large power systems, providing visualisation to improve situational awareness and valuable insights into conditions under which such modes become undamped [54, 55]. Wide area PMU measurements have also been used to perform oscillation source localisation. [56] presents a dissipating energy flow calculation, compatible with PMU measurements, to trace system elements' participation in oscillation modes. The method can trace both natural and forced oscillations and has been successfully implemented in an actual power system [49]. However it should be noted that IBR dynamics and interactions are introducing new forms of instabilities, including oscillations. The classification of types of oscillations and the term SSO is being revised and extended to include these emerging IBR driven oscillations as will be discussed in Section 2.3. The adequacy of PMU based monitoring for emerging power system oscillations will be investigated in this research.

Wide-Area Control

PMU measurements can be used to enable a range of coordinated, wide-area control actions that support corrective measures in critical grid operational functions, including enhancing angular and voltage stability, facilitating frequency response and managing thermal constraints [33]. A PMU-based wide area enhanced frequency control scheme is presented in [57]. PMU measurements were utilised to detect frequency disturbances and evaluate the magnitude of power imbalances. Regional impacts across different parts of the network were considered to subsequently allocate the required response for different regions of the system. The proposed scheme demonstrated fast and regional frequency response, which more efficiently contains frequency deviation with the reduced and unevenly distributed system inertia.

2.2 Synchronised Waveform Measurements

2.2.1 Synchronised Waveforms

Advances in sensing technologies, including improved sensor development as discussed in Section 2.2.2 and improved computational resources, have made it possible to obtain high-resolution, time-synchronised voltage and current waveform measurements. Such measurements are referred to as synchro-waveforms, and can be collated from different geographical areas of the power system [21, 23]. In the literature, synchro-waveforms have also been referred to as continuous point on wave (CPOW) measurements [58].

Depending on the measurement technology and intended application, the resolution of synchro-waveform measurements can range from a kilohertz to megahertz. Synchro-waveforms can capture the full frequency range (up to the Nyquist) of components in the waveform. Distortions and non-sinusoidal characteristics are also preserved, directly addressing the limitations of the synchrophasor definition as described in Section 2.1.1. This is illustrated in Figure 2.3, which compares synchro-waveform voltage measurements and synchrophasor magnitude for an equipment failure event. Details of sub-cycle distortions are lost due to the sinusoidal reference and additional filtering associated with synchrophasor measurement. In contrast, these distortions are captured in the synchro-waveform samples. Synchro-waveforms therefore can play a critical role in monitoring IBR dynamics, which may exhibit characteristics that deviate from the sinusoidal reference assumed in the adopted synchrophasor definition.

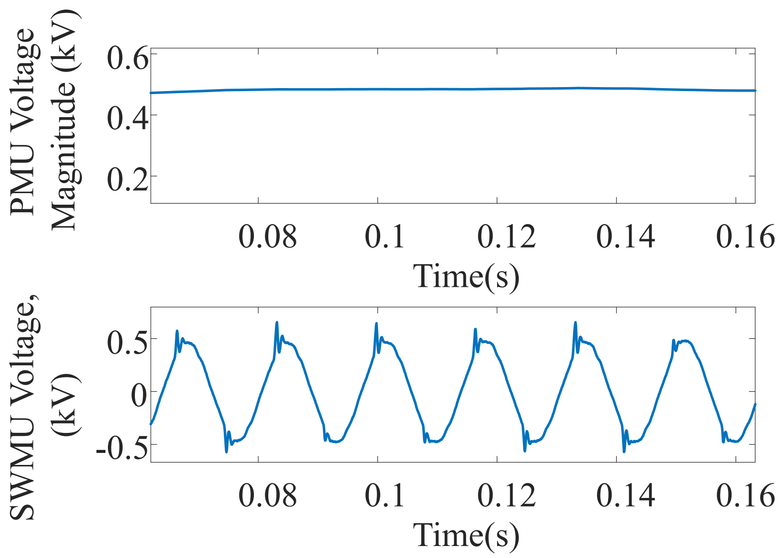

Figure 2.3: PMU vs synchro-waveform measurement

Devices that produce synchro-waveform measurements are referred to as waveform measurement units (WMUs) or synchro-waveform measurement units (SWMUs) [23]. In this thesis, the terms are used interchangeably. Similar to PMUs, these devices use a time source synchronised to UTC. In contrast to PMUs which locally process the voltage and current waveforms to produce synchrophasors, SWMUs typically output time stamped voltage and current samples with little filtering and no processing. SWMU reporting rates therefore range from kilohertz to megahertz. SWMU deployment, while promising, faces challenges related to high communication and computational requirements, as will be discussed later in this chapter.

2.2.2 Synchro-waveform Sensing Technology

Synchro-waveform measurements may be collected and streamed either on an event triggered basis or continuously streamed. Existing DFRs and PQ meters with additional time synchronisation are a form of event triggered synchronised waveform measurement units (SWMUs). Recent advancements in sensing technology have led to various

SMWUs capable of continuous streaming [20, 59–61].

The fibre Bragg grating (FBG) based distributed electrical sensing (DES) solution of [61] is capable of producing continuously streamed voltage and current synchro-waveforms [22]. FBGs are periodic perturbations in the refractive index along a fibre core, with peak reflection at a wavelength referred to as a Bragg wavelength. Straining or compressing the fibre at the location of the grating changes the Bragg wavelength. Combining an FBG with a piezoelectric stack produces a sensor that can be connected to a traditional voltage transformer (VT) or current transformer (CT) (with a burden resistor), which allows voltage and current measurements to be encoded as changes in the Bragg grating wavelengths. These sensors are referred to as passive secondary converters. An interrogator unit with a optical source emits a broadband light via a fibre cable that has an array of passive secondary converters. The converters transduce the voltage and current measurements into Bragg grating wavelengths, which are detected at the interrogator and converted into synchro-waveform samples in real time [62].

The FBG based DES solution is passive, (i.e. the sensors do not require a power supply) and can multiplex (up to ~ 30) sensors along a single length (up to 60 km) of fibre optic cable. This solution therefore significantly reduces the need for additional infrastructure at measurement locations. The interrogator is installed in the substation and can host multiple signal processing, monitoring and protection functions as illustrated in Figure 2.4.

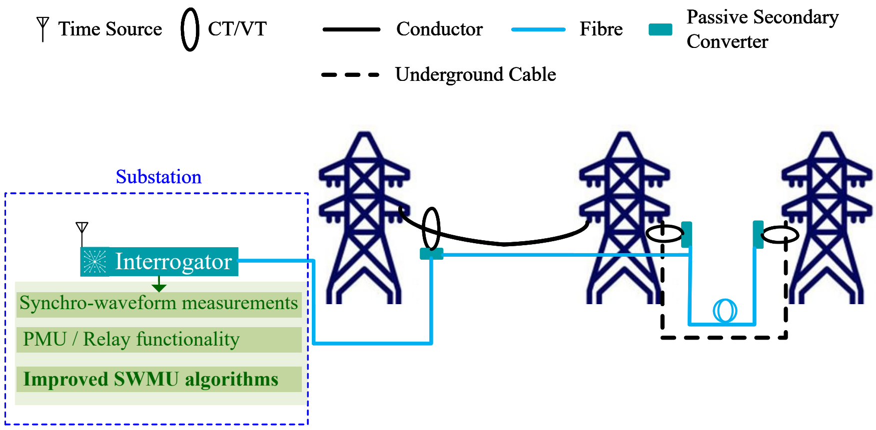

Figure 2.4: Distributed electric sensing platform

The platform can produce standard compliant synchrophasors and has demonstrated traditional protection functions such as distance protection [63], differential protection [64] and mixed (overhead line and underground cable) circuit protection [28]. A key functionality of the passive DES platform is its ability to produce cost-effective synchro-waveforms across multiple sensors and interrogator units. DES can mitigate the waveform data transmission challenges within a relatively local region. However, enabling high resolution, system-wide visibility remains challenging due to data volume (e.g. from multiple interrogators), communication needs and computational burden of processing multiple waveforms concurrently. Improved SWMU processing algorithms to support the real-time analysis, communication and storage of synchro-waveform measurements is necessary to derive valuable insights from such measurements, and is therefore the key focus of this research.

2.2.3 Practical Considerations for Synchro-waveform Measurements

Supporting Infrastructure

The emerging system behaviours of IBR rich networks present a compelling need for incorporating SWMUs to compliment PMU measurements [65]. However, as mentioned previously, synchro-waveform measurements will lead to a large volume of data, which poses a significant challenge to existing communications, storage and computational resources [23]. A survey of several US utilities found that existing communication infrastructure was insufficient for continuous streaming of synchro-waveforms. Instead, a more viable approach would be to collect measurements relevant to specific abnormal events such as faults, harmonics or oscillations as and when they occur via event triggered devices [66].

Table 2.2 presents a comparison between the communication and storage requirements between PMUs and SWMUs. Presently, the main standard for streaming synchronised waveform data is the IEC 61850-9-2 Sampled Value (SV) Ethernet-based protocol [67]. Considerations for aggregating multiple SWMUs into a centralised platform using this protocol are presented in [23]. The IEEE C37.118.2-2024 standard states the importance of supporting synchro-waveform data, but such data is still outside the scope of the standard requirements [23]. However, incorporating synchro-waveform data within the IEEE Std C37.118.2-2024 protocol is an active research area, with notable work presented in [68] and [69]. The frame based structure of the IEEE Std C37.118.2-2024 protocol is not well suited to large datasets and high volume data flows, prompting the development of the Streaming Telemetry Transport Protocol (STTP) [70]. STTP is designed for streaming individual measurements rather than frames and supports sending waveform time-series data and optional lossless data compression [27]. It is therefore expected to supplement or potentially replace the existing IEEE Std C37.118.2-2024 protocol although this still remains active. STTP has been demonstrated in several demonstration projects [71] and is expected to be increasingly adopted as utilities increase measurements in terms of both location and resolution [72].

The significant difference in the real-time streaming bandwidth and annual storage requirements between synchrophasor and synchro-waveform measurements is also highlighted in Table 2.2. A single PMU reporting three-phase synchrophasor data at 30 frames per second (fps) requires a minimum of 15 kilobits per second (kbps) [26]. In comparison, a synchro-waveform stream of three-phase voltage and current reported at 4 kHz requires approximately 5 Mbps of bandwidth [27]. As the amount of measurements streamed in real time from multiple locations and collected at a centralised location increases, a larger bandwidth at the concentrator location is required.

Table 2.2: Comparison of communication and storage requirements for synchrophasors and synchro-waveforms

	Synchrophasor	**Synchro-waveform**
Communication Protocols	IEEE C37.118 STTP (future)	IEC 61850-9-2 STTP (future)
Real-time Streaming	15 kbps for 1 PMU at 30 fps	5 Mbps for 1 SWMU reporting at 4 kHz
Annual Storage	$\sim$ 200GB	$\sim$ 10 TB

A trial conducted at Dominion Energy in the US found that continuous streaming of waveform data for 66 locations at 16 samples per cycle generated 3.9 TB of data per day and that a high-speed 1 Gbps communication network was insufficient for real-time streaming with significant time delays observed [73]. It is reported in [23] that multiple PMUs connected to a PDC can require up to $\sim$ 3Mbps of bandwidth, and multiple SWMUs may require dedicated 10 Gbps Ethernet networks.

Archiving of measurements is important to facilitate post-event analysis. A single PMU requires hundreds ($\sim$ 200) of GB of storage per year when saved in standard compressed file formats [74]. Measurements from a single SWMU with a similar level of compression will need several TB of storage [75]. As the number of measurement locations increases, the storage requirement also increases. It is estimated that large scale deployment (>100 measurement locations) will require $\sim 100's$ TB per year for synchrophasors and $\sim 10's$ PB per year for synchro-waveforms [76].

Present communication and storage infrastructure limits the near-term adoption of continuous synchro-waveform streaming. Presently, application specific synchro-waveform deployments with limited or localised supporting infrastructure, e.g. local high speed communication networks, have been implemented [24]. Examples of this include protection relays and DFRs. To facilitate large scale adoption of real-time, continuously streamed synchro-waveforms will require massive investments to improve existing infrastructure. Alternatively, improved synchro-waveform processing and communication of processed outputs may be more suitable for existing communication networks and archival solutions.

Performance Metrics and Standards

Adopting synchro-waveforms will require a commonly accepted performance baseline and standardisation to ensure compatibility across different SWMU solutions. Presently, performance metrics related to waveform reconstruction errors (e.g. goodness of fit [77]) and compression performance (e.g. compression ratios [69]) may be adopted. Existing standards relating to PQ/DFR measurements and devices may also be applicable [21]. However, at the time this research was conducted, there were no commonly-adopted standards or standards under-development dedicated for real-time continuously streamed synchro-waveforms. This will impede the large-scale adoption of SWMU technologies.

2.2.4 State-of-the-Art Review of Synchro-Waveform Processing Methods

Emerging synchro-waveform processing methods can be broadly categorised into two complimentary categories, i.e. locally processed feature extraction [78–80], and waveform compression techniques [81, 82], as illustrated in Table A.1. Feature extraction involves locally processing synchro-waveform measurements to derive representative quantities or features within the observation window. Lissajous curves and similarity metrics obtained from voltage and current synchro-waveform data are used for event detection and localisation in [78]. In [79], the difference between steady state (pre-event) and event waveforms is used to characterise transient responses of IBRs, thus gaining insights into their dynamic responses. Enhanced phasor based methods have also gained prominence in the literature. [83] uses the wavelet transform to detect and report harmonic phasors. [84] and [85] apply recursive filtering and interpolated DFT (Ip-DFT), respectively, to detect possibly inter-harmonic SSOs.

The preceding methods are application specific and therefore do not extract features that are fully representative of the detail available from synchro-waveform measurements under different operating conditions. A functional basis analysis presented in [80] aims to represent both steady state and transient dynamics in the input waveforms. This approach defines a number of functional bases, including steady state, angle and amplitude steps, frequency ramps and harmonics. A dictionary of functional bases is pre-defined for expected parameter ranges. Optimisation techniques are then employed to find the functional bases and parameters that can optimally represent the signal. A limitation of this approach is the difficulty to pre-determine and accurately describe all possible disturbances via unique functional bases. For example, inter-harmonics are not initially included in the proposed dictionary, resulting in inaccurate measurements and requiring manual updating of the algorithm.

Waveform compression aims to find the most compact representation of information by identifying intrinsic structures within data and removing any redundant information [82]. Compression may be lossless, allowing perfect reconstruction, or lossy, resulting in acceptable reconstruction errors. An open-source, lossless compression scheme that encodes differences between measurements (delta encoding) via a variable length encoding strategy is reported in [86] to reduce the bandwidth requirements of synchro-waveform measurements. The wavelet transform, via a library of different wavelets, can give a sparse representation of distortions. Transient detection and compression of waveforms containing transients using the wavelet transform has been demonstrated in [69,82]. In [81], a multiple model compression scheme for voltage and current samples using a two-stage window is presented. In the first stage, appropriate parametric models, e.g. sinusoidal models, are identified to represent the input. The residuals between the original input and the reconstruction via the parametric models are then calculated. In the second stage, the optimal representation and compression of the residuals (transients) are found using the wavelet transform. The various compression schemes drastically reduce the burden on data communications and improve data archiving. However, the data are usually decoded at centralised locations and relevant features need to be extracted and compared to enable a variety of real-time applications.

A classification of synchro-waveform processing methods based on their communicated outputs, streaming mechanisms (triggered or continuous) and applicability to transient, non-sinusoidal conditions is presented in Table 2.3. The business-as-usual approach utilises continuously streamed fundamental synchrophasors and event-triggered waveform snapshots from DFRs. Waveform compression techniques result in small or no reconstruction errors, so inherently capture both transient and sinusoidal (fundamental and/or oscillatory) properties of the waveform. In contrast, the intended application and design of feature extraction algorithms determines their suitability to represent different characteristics of the input waveforms.

From the previous discussions, it can be seen that event triggered, application specific synchro-waveform processing methods are presently the most commonly adopted approach, which has been used for event detection (characterising transients) or SSO monitoring (characterising sinusoidal components). Recently, generalised approaches that combine a sinusoidal reference under steady state conditions with the ability to detect, characterise and communicate abnormal conditions have been proposed in the literature [80]. The generalised approach therefore continuously streams outputs reflecting steady state conditions and, based on an event trigger, outputs data relevant to the event. The functional basis analysis and multi-model compression methods in Table 2.3 are examples of this generalised approach for the feature extraction and waveform compressions categories, respectively.

Table 2.3: Classification of synchro-waveform processing methods [69, 79–86]

<table>
<tr><th></th><th>Triggered</th><th>Continuous</th></tr>
<tr><td rowspan="5">Locally Processed Feature Extraction</td><td></td><td>Standard PMU</td></tr>
<tr><td>Lissajous Curve [78]</td><td></td></tr>
<tr><td>Differential Waveforms [79]</td><td></td></tr>
<tr><td>Oscillation Phasors [83–85]</td><td></td></tr>
<tr><td colspan="2">Functional Basis [80]</td></tr>
<tr><td rowspan="4">Waveform Compression</td><td>DFRs</td><td></td></tr>
<tr><td>Wavelet-based Compression [69, 82]</td><td></td></tr>
<tr><td colspan="2">Multi-model compression [81]</td></tr>
<tr><td colspan="2">Slipstream [86]</td></tr>
</table>

	Suitable for sinusoidal inputs only
	Suitable for non-sinusoidal distortions (transients)
	Suitable for both sinusoidal and transient conditions

The key challenges for achieving generalised synchro-waveform processing algorithms are:

1. Compression versus feature extraction: It is expected that as deployment of SWMUs increase, advanced event triggering and signal processing algorithms will more commonly reside on the SWMU devices (i.e. local feature extraction similar to PMUs), rather than transferring vast amounts of data to a central repository (compression) [23]. This may be due to the benefits of enhancing PMU functionality and utilising existing supporting infrastructure over investments in large storage requirements at centralised storage locations.

2. Event triggers: Event triggering mechanisms and optimal thresholds that are agnostic of the nature of the event are needed to allow the detection, capturing and processing of appropriate segments of synchro-waveforms [23].

3. Suitable signal processing methods: Signal processing techniques and features suitable for a wide variety of conditions that may be present in synchro-waveforms require investigation. A combination of methods may be necessary.

2.2.5 Synchro-Waveform Applications

Fault Detection and Location

Analysis of synchro-waveforms from multiple locations have been utilised for fault detection and location in [87]. The reported method first identifies harmonics and oscillatory modes present in synchro-waveforms from two ends of a circuit. A circuit model of the monitored section is then constructed, and nodal voltages at the extracted modes are calculated in forward and backward sweeps. The results of the sweeps are then compared with the faulted bus location identified as the bus with minimum difference. This method accounts for transients, incipient faults, different loads, fault types and circuit topologies. Synchro-waveforms from both ends of the circuit of interest and knowledge of the topology are required for this method.

Mixed Circuit Protection

Mixed circuits are comprised of overhead transmission lines and underground cable sections. They may arise due to environmental constraints, physical topology or customer preference. The protection of these circuits is complex due to the changes in electrical properties of overhead lines and underground cables. The remote locations of transition points also makes conventional monitoring and protection potentially costly. Synchro-waveforms available from a passive distributed sensing platform were utilised to enable standard current differential protection algorithms in a cost-effective manner for mixed-circuits [28]. Synchro-waveform measurements at different locations allows for a dependable and cost-effective protection scheme for complex circuits.

Mitigation of Utility Ignited Wildfires

Wildfires have been ignited by electrical faults, particularly during extreme weather events such as heatwaves [88]. Ignitions due to power lines and electrical equipment accounted for approximately eight major wildfires in California [89]. A combination of increasingly severe weather conditions, ageing infrastructure and a lack of preventative maintenance measures can also lead to the increased occurrence of utility ignition events. For example, fire incident data from Southern California Edison shows approximately 119 ignition incidents in 2024 [90] compared to 41 events in 2014 [91].

Root cause analysis of events has identified that synchro-waveforms recorded by power quality meters are able to identify precursor signatures of temporary faults (such as vegetation encroachment) that can lead to arcing and hence contribute to the ignition of wildfires [92]. Arcing usually manifests as high impedance faults, thus presenting challenges to phasor based protection algorithms. The detection and mitigation of utility ignition events can therefore benefit from the high resolution of synchro-waveforms that can capture arcing signatures. Additionally, high-speed, synchro-waveform based protection algorithms are being developed for downed conductor detection and isolation to prevent or minimise arcing. These methods can be based on multi-zone differential protection, high impedance fault detection and waveform signature analysis [27, 93]. Accurate, real-time synchro-waveform monitoring can therefore be critical to addressing utility induced wildfires.

2.3 Emerging Power System Monitoring Needs

2.3.1 New Dynamics Induced by Inverter-based Resources (IBRs)

IBR Transient Performance

IBR controllers modulate their outputs at the point of common coupling (PCC) via power electronic switching. Their dynamics are therefore complex and occur at faster timescales (microseconds to milliseconds) compared to electromechanical generation. During system disturbances, e.g. faults, IBRs limit their fault current magnitude and modulate their voltage and current angles. The dependability and reliability of phasor-based protection elements, designed for based on fault behaviour of SGs, may be adversely impacted, as evidenced by several real-world events [94].

Furthermore, depending on how the IBR control is designed and implemented, IBR may respond to system disturbances in an unexpected and undesired manner. System events and minor disturbances (e.g. capacitor switching, faults) may result in distortions, ramps or step changes in voltage and current waveforms at the PCC of an IBR. In some cases, IBR control's response to such conditions was found to lead to oscillations, distortions in its outputs and even unintended disconnection of IBRs after faults were cleared [23]. This has been attributed to control design and limitations of the internal measurement and filtering processes of IBR controllers in handling distorted waveforms [94]. An example of this occurred in the Blue Cut Fire (USA) when a phase step resulted in an incorrect frequency measurement within an IBR control loop, leading to the disconnection of a 1200MW rated IBR [95].

Figure 2.5 compares a simulated IBR output current waveform of a faulted phase during a phase to earth fault and the corresponding phasor magnitudes. It can be seen that the transient response of the IBR is not captured by the PMU measurement. This may become more important for detection and protection devices as fault limiting may negatively impact legacy protection. Synchro-waveforms are therefore important in characterising IBR dynamic responses that may be filtered out by fundamental synchrophasors. Post event analyses of actual synchro-waveform measurements have highlighted the complexity of IBR dynamics, which includes fluctuations in BESS fault current magnitudes [94], and different responses in several IBRs for the same event [23]. Further characterisation and understanding of IBR dynamics remains an active research area.

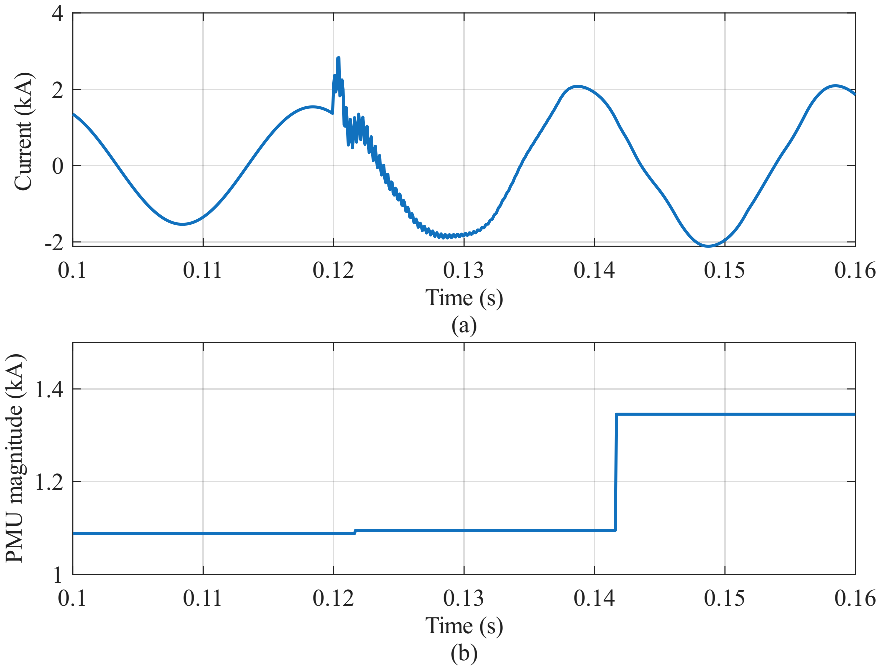

Figure 2.5: Comparison between waveform and PMU measurements of an IBR transient response: (a) waveform, (b) PMU

IBR-driven Sub/Super Synchronous Oscillations

IBR-driven oscillations are influenced by a wide range of complex mechanisms and root causes, some of which are still not fully understood [96]. The IEEE IBR SSO taskforce has collated root cause analyses of oscillation events across several countries [97, 98]. Table 2.4 presents a summary of representative examples of historically observed IBR driven SSO events. IBR control interactions, improper control tuning and resonances between network elements and/or system conditions have all been implicated in actual events.

A key finding from analysing waveform measurements from historical SSO events is the presence of both sub-synchronous and super-synchronous oscillation components centred around the fundamental frequency. These components are sometimes referred to as sideband oscillations or wideband oscillations, and have been attributed to the synchronous reference frame transformations (dq to ABC) of IBR controllers [99, 100]. The oscillations also occur at inter-harmonic frequencies and within a wider frequency range ($0 - 2 \times$ nominal frequency) compared to electromechanical oscillations (EMOs) (< 5Hz) associated with SG.

As discussed in Section 2.1, standard compliant PMUs measure and report fundamental synchrophasors with strict filtering requirements around the nominal frequency. EMOs are relatively slow compared to PMU processing windows and can therefore be tracked as oscillations in the RMS phasor quantities over successive measurement windows. However, PMUs are subject to aliasing and attenuation (due to filtering) when measuring sub/super synchronous inter-harmonic components. Due to the reliance of a fundamental cosine reference, inter-harmonics may result in the measured fundamental phasor being modulated at the sub-synchronous frequency as analysed in [101].

Figure 2.6 compares waveform and PMU measurements, along with their respective frequency analyses, from an actual SSO event in the North China power grid with data available from [102]. This example and the comparison highlighted in Table 2.4 show that critical information relating to the sub/super-synchronous components can be lost due to the PMU processing.

Table 2.4: Examples of past IBR-driven SSO events [97, 103, 104]

Event	**Mechanism**	**SSO Frequency**	
		PMU	Waveform
2021 Dominion Energy USA [103]	Weak grid interaction with solar plant voltage control loop	$\sim$ 22Hz	38 Hz and 82 Hz
2015 Hydro-One Canada [97]	Weak grid interaction with solar plant current control loop	20 Hz	80Hz
2020 Australia West Murray Zone [104]	Weak grid interaction with multiple IBRs	$\sim$ 19Hz	$\sim$ 33Hz and $\sim$ 67Hz

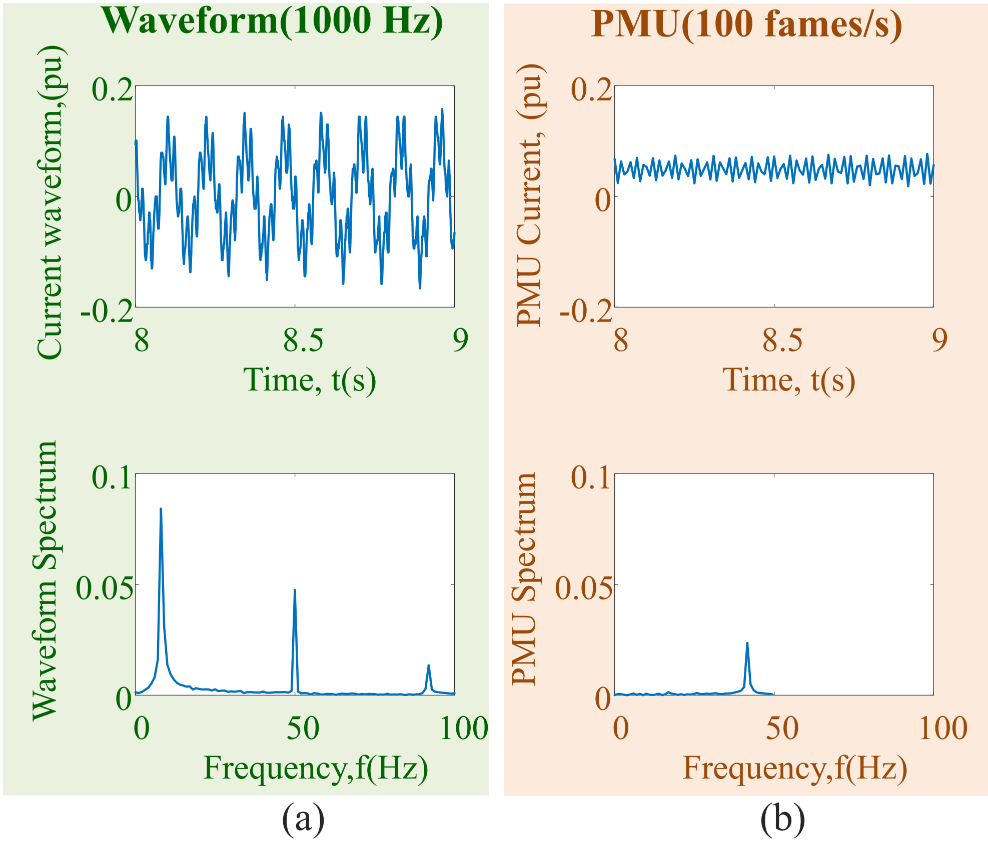

Figure 2.6: Comparison between waveform and PMU measurements for an SSO event available from [102]

2.3.2 Data Analytics

The granular details captured by synchro-waveforms present an opportunity to create rich datasets suitable for pattern recognition applications. Figure 2.3 illustrates an example where distortions in the event waveforms may result in unique event signatures that can be used to train supervised machine learning based event classification algorithms [105, 106]. Unsupervised learning and system identification techniques can also be applied to discover approximate representations of complex power system (including IBR) dynamics [107].

Adopting such algorithms will require the curation and storage of large, historic synchro-waveform datasets. A generalised architecture of the infrastructure to support large synchro-waveform datasets is presented in [23]. Relevant measurements from local (edge) SWMUs, along with associated metadata or event labels, can be stored into accessible data repositories, e.g. the Grid Event Signature Library (GESL) [108]. AI/ML applications can then be hosted in cloud-based servers. Leveraging cross-discipline expertise in information technologies, data analytics and power systems will be important for deriving valuable insights from synchro-waveform data.

However, a key barrier to adopting data informed event detection and characterisation techniques remains access to suitable datasets for the training, testing and validation of data-driven solutions. The higher resolution of synchro-waveforms can better retain diagnostic information, but large data volumes make curating such data difficult. Improved synchro-waveform processing methods that retain information available at higher resolutions while reducing streaming and archival requirements will be essential for converting rich synchro-waveform data into actionable insights.

2.3.3 Monitoring Application Requirements

Table 2.5 compares the suitability of synchrophasors and synchro-waveforms for several power system monitoring applications. PMU measurements have been used to successfully detect, characterise and locate various abnormal conditions [109]. However, high-resolution synchro-waveforms may allow for improved analysis of a wider variety of anomalous events. EMO monitoring using PMUs are fairly mature [49], and synchro-waveform measurements may not yield any significant benefits relative to the required investment for this particular application. PMU measurements may be able to detect IBR dynamics (e.g. via sub-synchronous oscillations or step changes in phasor outputs), but synchro-waveforms (or improved features derived from synchro-waveforms) are becoming increasingly critical to characterise these dynamics.

From the above discussions, it can be seen that synchro-waveforms offer compelling benefits in better facilitating and enhancing many applications, but the associated processing, communication and storage requirements may hinder its adoption. Investments in SWMUs and supporting infrastructure may be warranted in areas of the network with a high penetration of IBRs. Considering the limitation of PMUs along with the large data volume challenges of raw synchro-waveforms, a new approach that balances accurate measurements of IBR dynamics with reduced data volumes is therefore required. This can be achieved by improving the way the raw synchro waveform signal is processed and represented. Measurement algorithm designs should not rely solely on an assumed fundamental reference (as in conventional PMUs) but rather seek to extract the useful information contained in the input synchro-waveforms. Ideally, SWMU processing methods will require limited prior knowledge of the dynamics associated with abnormal events, and will thus be adaptable to a variety of present and future conditions such as faults or emerging IBR dynamics. SWMUs should also, in the near term, operate with similar or minor additional supporting infrastructure associated with conventional PMUs.

Table 2.5: Measurement requirements for different applications

Application	**Synchrophasor**	**Synchro-waveform**
Event detection and classification	✓✓	✓✓✓
Locating Transients	✓	✓✓✓
EMO detection and localisation	✓✓✓	∗
IBR-driven dynamics	✓	✓✓✓
State estimation	✓✓	✓✓✓
Rotor Angle/Voltage/Frequency stability	✓✓✓	∗
Resonance / Converter-driven stability	✓	✓✓✓

∗ Not required
✓ Limited
✓✓ Suitable
✓✓✓ Preferred

2.4 Chapter Summary

This chapter presented a state-of-the-art review of power system monitoring techniques and applications. Synchrophasor measurements, available from PMUs, have been adopted for a wide range of applications including event detection, electromechanical stability assessment and monitoring EMOs. Real-time PMU based monitoring is therefore a key enabler for maintaining power system security, reliability and resiliency. However, standard PMUs assume a sinusoidal reference at the nominal frequency when processing voltage and current waveforms, with band-pass filtering around this frequency. Therefore, conventional PMUs measure and report fundamental synchrophasors even if the input conditions deviate from the assumed reference conditions.

This Chapter further discussed the limitations of the PMU in accurately capturing certain system dynamics, with examples including the measurement of distorted waveforms during power system transients and the presence of inter-harmonic oscillations. The review highlighted that such conditions can be present in the waveforms of utility ignition events (transient arcing signatures), IBR induced oscillations (inter-harmonics) and other emerging phenomena. Such events can have greater impacts in IBR dominated systems operating under increasingly stressed conditions (e.g. loading or weather). Inaccurate monitoring can therefore lead to such events propagating throughout the network potentially resulting in outages, and even damages to infrastructure and life.

Simply increasing the resolution of PMU measurements is not suitable as phasor estimation algorithms and standard requirements attenuate information that is different from the assumed fundamental reference. Voltage and current synchro-waveforms have emerged as an alternative measurement technology that can address the limitations of standard PMUs due to their ability to fully capture power system dynamics. A review of monitoring requirements for existing and emerging applications, conducted in this Chapter, showed that while PMUs will remain a key monitoring tool, richer information retained by synchro-waveforms can improve certain applications. Examples of this include improved diagnostic information for event classification and improved oscillatory monitoring for stability analyses.

However, high processing, communication and storage requirements associated with continually streamed measurements limit SWMU adoption as well as further investigation into synchro-waveform based applications. A review of emerging synchro-waveform processing methods, along with existing communication protocols, found that compression and feature extraction algorithms can produce outputs that are more suited to existing supporting infrastructure. However, the majority of proposed SWMU methods have been application specific and thus incompatible with each other and unsuitable for concurrent applications (unlike standardised PMUs). This impedes the wide-area adoption of SWMUs, thus limiting the diagnostic information that can be extracted by real-time monitoring solutions during emerging phenomena in IBR dominated systems.

The review conducted in this Chapter has uncovered several research gaps that require further attention to improve power system monitoring in the context of IBR rich systems:

1. Improved (near-term) monitoring solutions compatible with both traditional PMU measurements and higher-resolution synchro-waveforms are required to accurately detect and monitor emerging IBR behaviours.

2. Generalised synchro-waveform processing methods that are capable of accurately measuring a variety of anomalous conditions while remaining compatible with existing supporting infrastructure are required to support the near-term, wide-scale adoption of synchro-waveforms.

3. The development and demonstration of data-driven applications, that utilise the improved insights offered by synchro-waveforms (or processed SWMU algorithm outputs), are required to improve situational awareness and inform improved decision-making in IBR rich power systems.

Chapter 3

Early Warning of Power System Oscillations

The integration of IBRs has resulted in the emergence of new oscillatory behaviours. IBR driven oscillations manifest across a wider frequency range, and their underlying mechanisms remain a subject of active investigations and ongoing research [96]. In 2023 and 2024, the GB power system experienced several sub-synchronous oscillation (SSO) events. The national electricity transmission system security and quality of supply standard (SQSS) [110] defines SSO as oscillations at frequencies less than the power frequency (50Hz) arising from interactions between certain elements of the system such as generator shafts, converter controllers, etc. It is noted in an SSO working group report that the term SSO does not include electromechanical oscillations associated with rotor swings which also occur at frequencies below the synchronous frequency [111]. Furthermore, the SQSS defines unacceptable SSOs as oscillations with negative or insufficient damping.

The impact of an SSO can vary depending on the magnitude and how quickly it is damped [110]. The GB SSO events analysed in this Chapter had a relatively larger impact in Scotland [16], which contains a high penetration of IBRs with approximately 17.6 GW of installed RES capacity accounting for 70.3% of annual electricity generation [112]. Post-event investigations typically involved modelling the behaviours of potential IBRs that could potentially contribute to the oscillations under different operating scenarios, based on which the underlying mechanisms were analysed, thus informing mitigations. Mitigating actions include disconnecting and retuning suspected units, tuning IBR controllers, reconfiguring network topology to change unfavourable operating conditions, etc. Among the various historical oscillation events that occurred in the GB system, there were instances where generators not involved in the SSO were unexpectedly disconnected during the events, highlighting the severe consequences of such oscillations [16].

The presently widely adopted approach that uses physics based modelling for understanding SSO events can face significant challenges of IBR model accuracy, transparency and complexity [113]. Measurement based analysis has previously been demonstrated in characterising trends in the behaviour of electromechanical inter-area oscillation modes [55]. This research therefore aims to understand and identify trends, patterns and correlations associated with IBR driven SSO events. It is achieved by comprehensive analysis of synchronised measurements of real-world events that occurred in the GB system, thus reflecting the actual system dynamics. The findings will reveal that by correctly identifying certain measurement signatures, it has the potential to enable real-time, early SSO warning and detection, thus building upon previously reported analyses of [16].

This chapter starts with an analysis of SSO events over an 18-month period captured by a PMU connected to the LV distribution network at the University of Strathclyde, located in Glasgow, Scotland. The analysis uncovered precursory signs in the form of low magnitude (close to noise level) oscillations, manifesting as observable spectral power levels at particular frequencies in the frequency spectrum of the PMU measurements. These precursors can serve as early indicators of oscillatory instability. Statistical change-point analysis is therefore applied to identify segments of historical measurements that contain precursors to inform the design of an SSO state classifier. The proposed oscillation state classification tool can detect precursory signs in incoming PMU measurements, thus providing an early warning of system oscillations. Additionally, it will be shown that relying on traditional measurement technologies, i.e. PMU measurements and triggered waveforms, for capturing emerging SSOs has faced limitations. Based on the analysis, recommendations to improve measurement algorithms and incorporate additional system data for improved monitoring of IBR driven dynamics are also identified, which inform the PhD's work reported in Chapter 4.

3.1 Analysis of Historic Oscillation Events in the GB System

3.1.1 Live Grid Monitoring and Visualisation Platform

The Live Grid Monitoring and Visualisation Platform (LGMVP) is an open platform developed and maintained by the University of Strathclyde for real-time visualisation of the GB grid status [114]. It acquires and archives PMU data from an LV measurement point in Glasgow, Scotland, along with system operational data from Elexon [115] and the National Energy System Operator (NESO) data portal [116]. The PMU is a Schweitzer Engineering Laboratories, SEL-451 protection, automation and bay control device with built in real-time synchrophasor capability and configured for M-class measurement performance with narrow bandwidth filtering around the nominal frequency [117]. The PMU data consists of phase voltage magnitude reported at 50 frames/second and archived using the openHistorian software [118]. The GB system data includes generation mix (including the inter-connectors) [115], system demand [115] and system inertia levels [116]. It should be noted that the system operating conditions may be reported at different time intervals, and may need to be updated or corrected for market actions. Further utilisation of this data will require alignment strategies. In this research, archived PMU phase voltage magnitude data from April 2023 to October 2024 were collated and analysed in detail, only. Pre-processing was also conducted to remove data-quality issues. Missing data were approximated via linear interpolation and PMU outages were removed from the dataset. All times are in coordinated universal time (UTC).

3.1.2 Key Features and Trends of Observed Oscillation Events

Figure 3.1 illustrates an actual oscillation event observed in the GB network in the summer of 2023, as corroborated by the system operator [16, 119]. The oscillation was present in the system for approximately 40 seconds, with an observed amplitude of approximately 1.4% of the nominal voltage and a frequency of 8.3 Hz. It can be seen that the SSO initially has a large negative damping ratio (calculated using Matrix pencil method [120]), and then remains critically (0 damping) damped for the duration of the event, thus satisfying the unacceptable SSO condition of the SQSS.

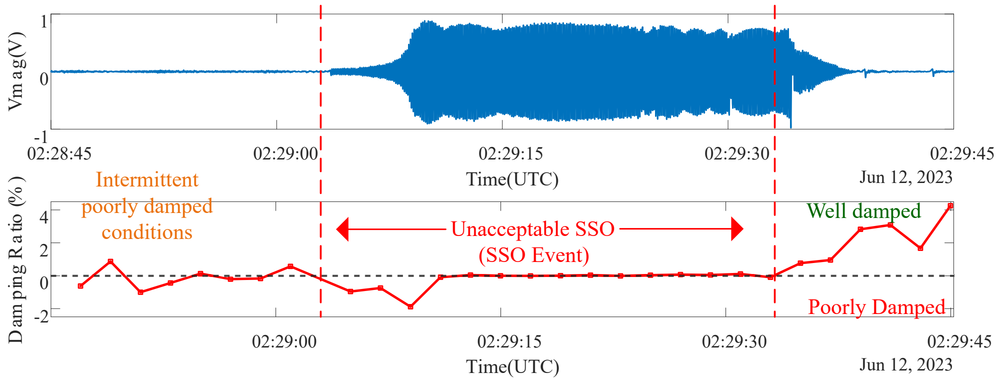

Figure 3.1: SSO event

A total of 42 similar SSO events were observed in the dataset between April 2023 and October 2024. It should be noted that at the time this research was conducted the published report from the system operator [16] mentioned that SSOs were observed in January and May of 2024 but exact dates and further details were not publicly available. In this analysis, SSO events are large amplitude oscillations similar to Figure 3.1 with poorly damped conditions (≤ 0 damping i.e., critically damped or undamped), consistent with the unacceptable SSO conditions in the SQSS [110]. Initially, guidance from publicly available system operator reports [16, 119] was used to obtain event dates of interest. It should be noted that several of these events occur across the same day and may be linked to the same initiating condition.

The key features of the oscillations that were focused on in the study include frequencies, amplitudes and durations of these events. Figure 3.2 shows that the majority of events manifest as the 6-8 Hz oscillation in phasor voltage magnitude. A 9-12 Hz oscillation frequency band has also been observed (although less often), showing the variation in SSO events. The oscillation amplitude measured at the PMU location ranged from 0.5% to 1.5% of the nominal voltage and the durations usually lasted for several seconds (5-10s) but can persist for several minutes.

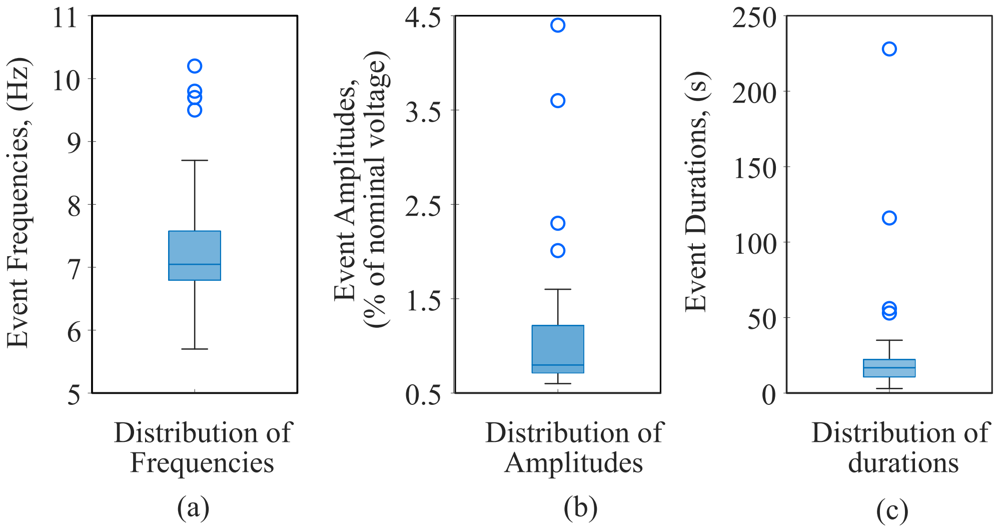

Figure 3.2: Distribution of GB oscillation event properties for the 42 unacceptable SSO instances: (a) frequency, (b) amplitude, (c) duration.

3.2 Precursory Signatures of Oscillation Events

3.2.1 Precursor Oscillation Signatures in the Time-Frequency Domain

To further analyse these events, a time-frequency analysis was conducted using the short-time Fourier Transform (STFT) to obtain the spectrogram of the voltage phasor magnitude. The STFT consists of performing a DFT across multiple sliding windows and aggregating the results. Window effects are mitigated using a combination of window functions and overlapping. This minimises the impacts of discontinuities that lead to spectral ringing (Gibbs phenomenon) [121]. Examining the spectrogram (time-frequency representation) enables the detection of multiple frequency components and their evolution through time, allowing for a more informative analysis [122].

A key finding of this analysis is that there appear to be low-amplitude, close-to-noise-level ($< 0.1\%$ of the nominal voltage) oscillations in the time domain, which can be more clearly observed in the frequency domain as illustrated in Figure 3.3. In this research, these are referred to as precursory signs, which preceded the large amplitude ($\sim 1.04\%$) SSO event illustrated in Figure 3.1. Similarly, these precursors occur in many SSO instances, as will be discussed in detail in Section 3.2.2. These precursor signs may indicate the system is entering a region of marginal stability, thus their detection can serve as a risk indicator, highlighting the potential for the system to transition to an oscillation state. However, the spurious nature and close to noise level amplitudes of the identified precursor mean that simple thresholds (e.g., time-domain magnitude thresholds) may not be suitable for their detection.

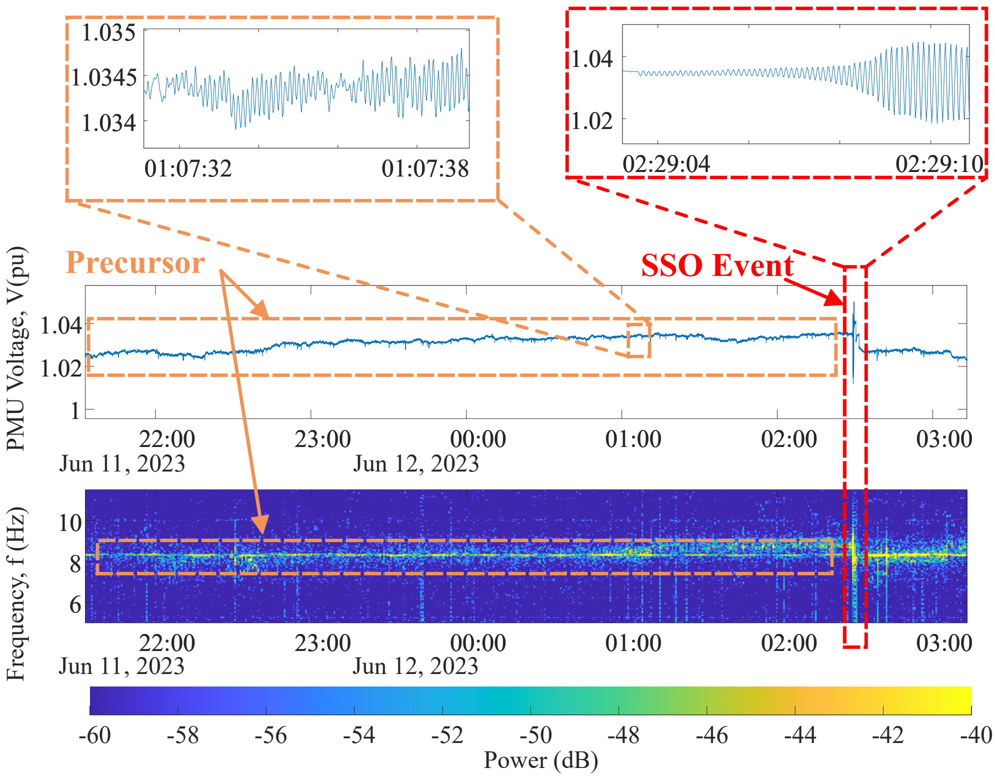

Figure 3.3: Precursor stage and SSO event observed in GB network

3.2.2 Identifying Precursory Signatures in Historic Data via Change-point Analysis

The large amplitude oscillation events can be detected by simple and intuitive methods (such as time domain thresholds, modal analysis), however, precursor oscillations are close to noise levels. As oscillations are periodic, the spectral energy of the voltage magnitude measurements will be concentrated around the frequency of the oscillation. Measurement segments with oscillations will therefore have less variance in the distribution of the spectral energy compared to measurement segments without oscillations. Changes in the statistical properties of the distribution of spectral energy can therefore suitably identify potential precursors, while an empirically determined threshold on the variance of spectral energy of segments can be used as a simple and intuitive method to characterise the segment as oscillatory. To identify the potential precursor signatures from the large amounts of historic data, this research therefore applies change-point detection (CPD) to the time-frequency spectra of the PMU measurements. Change-points are abrupt deviations in structured data that coincide with changes in the properties of the system that generates the data [123]. CPD is the task of locating the time instants coinciding with these change-points [124]. CPD has been previously applied to time domain PMU measurements for event detection [125]. This research extends this concept to the time-frequency spectra of PMU measurements to detect changes in the oscillatory structure of the measurements.

Offline CPD, which processes the entire historic data record at once to locate K change-points, is applied. Consider a random and non-stationary process, Y, producing an ordered sequence of synchronised measurements $\{Y_0, Y_1...Y_T\}$, consisting of T real-valued samples with time instants $\{t_0, t_1...t_T\}$. Some characteristic of Y may change abruptly at K, unknown instants $\{t_{k1}, t_{k2}...t_K\}$. Y therefore consists of $K+1$ segments $\{(t_0 : t_{k1}), (t_{k1} : t_{k2}), ...(t_K : t_T)\}$, each with probability distribution functions, $F_1(\theta_1), F_2(\theta_2), ...F_{K+1}(\theta_{K+1})$, where θ represents the statistical properties that define each distribution. CPD is defined as evaluating [124]:

$$\begin{aligned} H_0 &: F_1(\theta_1) = F_2(\theta_2) = ... = F_{K+1}(\theta_{K+1}) \\ H_1 &: F_1(\theta_1) \neq F_2(\theta_2) \neq ... \neq F_{K+1}(\theta_{K+1}) \end{aligned} \tag{3.1}$$

where H_0 is the null hypothesis that the observation window is homogenous (no change-points) and H_1 is the alternative hypothesis that the data consist of segments characterised by probability distributions with different and abruptly varying statistical properties, e.g. mean and/or variances.

CPD seeks to find the optimal segmentation described by the change-points, $\{t_i, ...t_K\}$ that minimises the following [126]:

$$\sum_{i=1}^{K+1} [C(Y_{t_{i-1}} : Y_{t_i}) + \lambda] \tag{3.2}$$

where C is a cost function for a segment that measures how well an estimated statistical parameter explains the observed data in the segment; λ is a penalty term to prevent over fitting and the indices t_0 and t_{K+1} of the expression (3.2) are set as the first, (t_0), and last (t_T) data-point in the observation window, respectively.

Solving (3.2) involves taking a candidate change-point and estimating statistical parameters for each of the resulting two segments based on the samples within each segment. This can be done using maximum likelihood estimation, which, for a given segment $(Y_{t_{i-1}} : Y_{t_i})$ of measurements, estimates the values of θ that have the highest probability of producing the observed measurement [126]. The ability of the estimated statistical parameters to represent each point within the segments is then found by finding the residual between the observed data point and the estimated value as predicted by the estimated statistical distribution. If the candidate change-point coincides with an abrupt change in statistical parameters, the residuals across both segments will be small. In contrast, if the change-point is within a segment, there will be a larger residual. This process is therefore repeated for different possible candidate change-points until the index that results in a segmentation that minimises the residuals is found. This will be the most prominent change-point, corresponding to the biggest shift in the underlying distribution of the data. This entire process can then be iteratively repeated on the resulting segments to find all possible change-points until a stopping criterion is met. This optimisation problem can be solved using a dynamic programming approach with a maximum number of change-points specified as described in [126] and implemented in [127].

CPD is applied to the spectrogram of the phase voltage magnitude to detect abrupt changes in the distribution of spectral energy. The DC component is first filtered out, after which an STFT is applied using a 1024-sample Hamming window (approximately 20s) with a 512-sample overlap (approximately 10s). Figure 3.4 highlights the outputs of the CPD algorithm for the period 11$^{\text{th}}$ to 12$^{\text{th}}$ June 2023. The CPD algorithm identified four distinct segments defined by the marked changepoints. Figure 3.5 demonstrates the distributions of frequencies that produce the highest spectral energy across each time instant for each segment identified by the CPD algorithm and Table 3.1 highlights statistical properties of the distribution of frequencies in each segment.

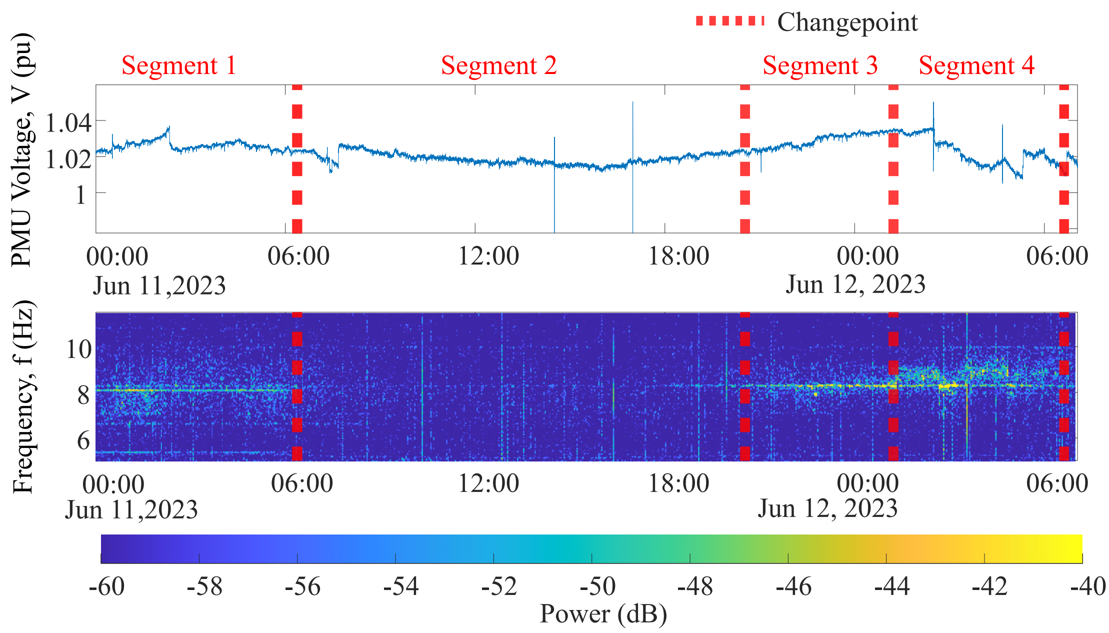

Figure 3.4: CPD of PMU voltage spectrogram

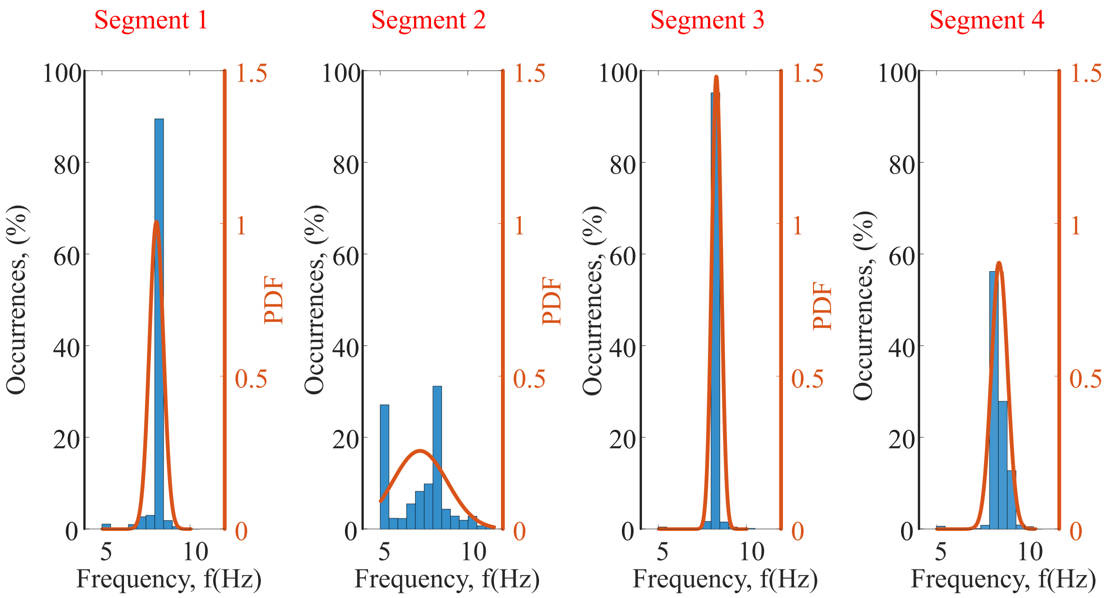

Figure 3.5: Change-point segment analysis

Table 3.1: Segment statistical properties

Property	**Segment 1**	**Segment 2**	**Segment 3**	**Segment 4**
Mean	8.09	7.26	8.31	8.56
Variance	0.15	2.43	0.07	0.21

The analysis demonstrates the mechanism of statistical CPD. It can be seen that the segments of either side of a change-point have different properties, particularly in terms of the variance in the distribution of spectral energy. As shown in Figure 3.5 and Table 3.1, Segment 4, which contains the known oscillation event, has less variance in the distribution of spectral energy around the frequency of the oscillation. In contrast, segment 2 contains a much larger variance due to the presence of randomly distributed noise and the absence of any oscillations.

Figure 3.3 presents a magnified view of segments 3 and 4 identified in Figure 3.4, highlighting the precursory stage and the SSO event. This result provides evidence that the oscillation mode existed in the system prior to the SSO event and the system may be operating in a region of marginal instability. As illustrated in Figures 3.4 and 3.3, the precursor stage could appear and last for a period of hours before the actual

SSO. At the onset of the SSO event, some change in operating condition would have triggered a further degradation in the damping of the oscillation mode, causing the system to transition from the precursor state to an SSO event. Another interesting finding is that there appears to be a similar precursor stage in segment 1 of Figure 3.4. However, this precursor did not appear to lead to an SSO event (as seen at the PMU location). This indicates that an oscillation mode may be present in the system, but no change in operating point to exacerbate the mode occurred, and/or a change in operating point ended up damping out the mode. The identification of these precursory oscillations provides additional insights and information than the analysis presented in [16, 98], which focused only on the large amplitude SSO events. This could serve as valuable indicators for informing SSO risks and potential mitigating actions.

The CPD described above was applied to the 2023-2024 phasor voltage magnitude dataset. For each resulting segment, the frequency corresponding to the highest spectral energy at each time instant evaluated by the STFT was noted. The variance in the distribution of these frequencies across the segment was then estimated. The study also performed an analysis of these results to detect segments that contained actual SSO events and precursors. This is achieved using an empirically determined variance threshold of 0.5, which is set based on the analysis presented in Table 3.1 and examining other examples from the same dataset. Segments with variances below this threshold were determined to be oscillatory. Manual verification was performed, based on which a list of SSO events and precursor states was compiled. Figure 3.6 illustrates a timeline of precursor and SSO events in the summer of 2023. It is observed that, while not all precursors lead to an SSO event, all SSO events in the study period have an associated precursor state. The precursors consistently appeared in the system from minutes to hours before the SSO events, as illustrated in Figure 3.7. The longest duration of a precursor state was found to be approximately 6 hours providing an opportunity for monitoring algorithms to provide early detection of an event. Precursor oscillations therefore persist for operational timescales that allow mitigating actions to be taken, for example, actions to improve system strength including network reconfiguration, or synchronous generation dispatch. Therefore, early detection of these precursor states can improve the situational awareness of system operators and potentially enable mitigations.

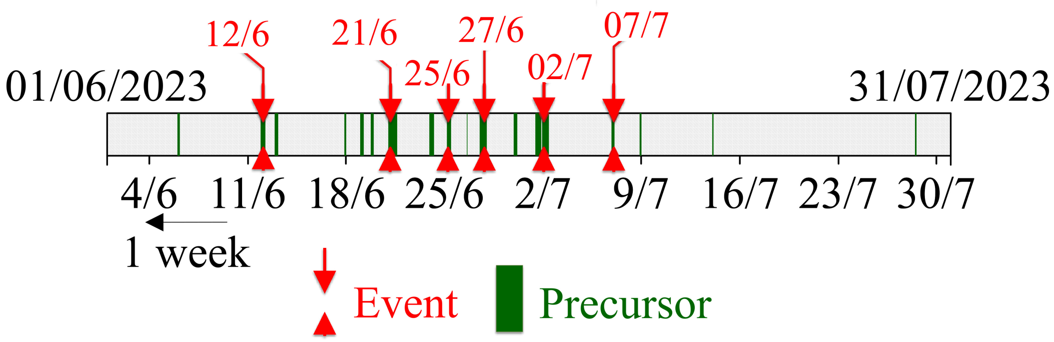

Figure 3.6: Occurrences of precursor stage and SSO event observed in GB network during summer 2023

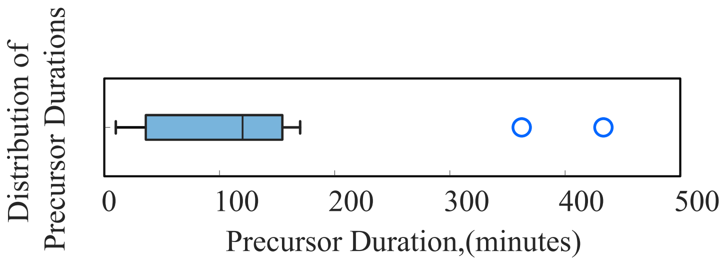

Figure 3.7: Distribution of precursor durations

3.3 Early Warning of System Oscillations

From the analysis conducted in Section 3.2, it can be concluded that the system can be categorised into three distinct system states for the purpose of SSO monitoring, i.e. SSO event, Precursor and Normal, which are illustrated in the examples shown in Figure 3.8. It is observed that spectral power at the oscillation frequency dominates during an SSO event, while it is less distinguishable during precursory signatures. Both of these instances appear to be different from the distribution of spectral power during normal conditions. However, precursors are difficult to differentiate from background noise. Applying thresholds to time-domain measurements and/or modal analysis, as adopted in the GB VISOR WAMs [45], is more suited to detecting relatively larger amplitude SSO events, but may face limitations in detecting precursor signs. These limitations can be addressed by a data-driven approach utilising the time-frequency features illustrated in Figure 3.8 and pattern recognition.

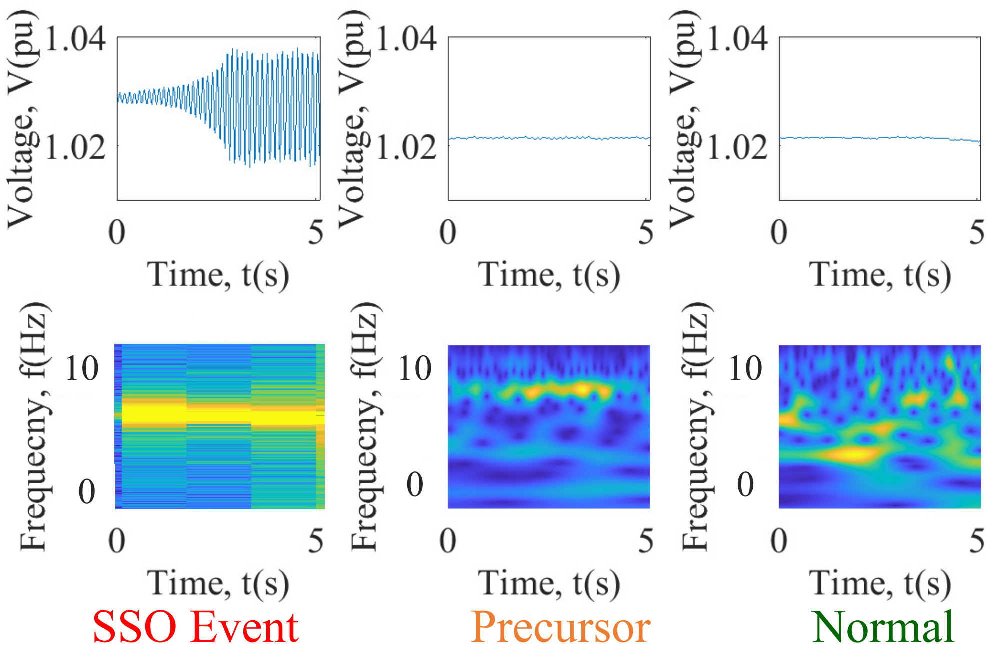

Figure 3.8: System oscillation states

3.3.1 Oscillation State Classification

To facilitate online oscillation detection, an AI-based system state classifier, trained on patterns identified from the results of the change-point analysis, has been developed. The classifier is trained to identify patterns in time-frequency features that correlate to a particular system state. Figure 3.9 provides an overview of the training process and the classifier architecture.

The historic records are analysed and characterised using change-point analysis. Training instances from each state are derived by windowing the relevant segments of measurements. These are then input to a time-frequency convolution neural network (TF-CNN), which incorporates the STFT as the feature extraction layer. The TF-CNN based classifier was selected for this application due to its ability to extract features relating to harmonic and inter-harmonic structures, as well as patterns that characterise how the signal's frequency content and distribution changes across the observation window.

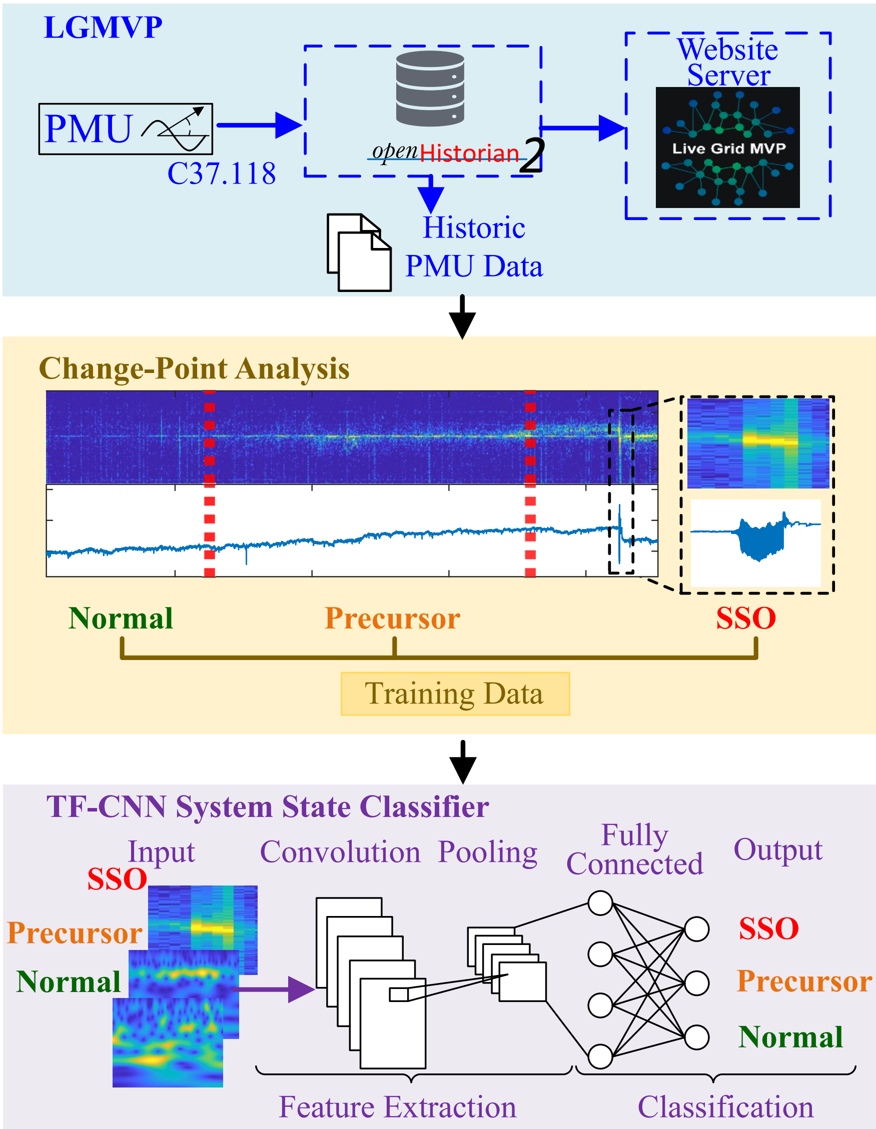

Figure 3.9: Architecture of the system oscillation state classifier.

CNNs are multi-layer neural networks that extract and learn increasingly complex features from structured data [128], e.g. the time-frequency spectrograms extracted from the voltage phasor magnitudes in this work. In the convolution layer, two-dimensional convolutions with local, learnable filters are applied to capture patterns in both time and frequency domains. A non-linear transform is performed to the output of the convolution layer to allow for more complex patterns (non-linear dependencies) to be represented. The pooling layer down-samples and aggregates the extracted features, retaining the most important features and helping to reduce over-fitting. Stacks of the convolution, non-linear operation, and pooling layers form the feature extraction portion of the CNN. The successive layers learn local patterns as well as increasingly complex global dynamics across the observation window. Finally, the fully connected layer combines the learnt features and calculates the probabilities of the input belonging to each class. The class with the highest probability is chosen as the predicted class.

A TF-CNN, with an STFT layer followed by two feature extraction layers, is utilised in the proposed classifier. In the supervised training phase, the filter weights are optimised by minimising a training loss function. This loss function quantifies the discrepancy between the predicted class probabilities and the true labels. Optimisation is performed using gradient-based methods, such as stochastic gradient descent [129]. Accuracy on a validation test set is also calculated and compared to training loss to quantify the generalisation of the trained model and prevent overfitting on the training data. The CNN settings and model configuration parameters, typically referred to as hyperparameters, are initially set and can be tuned empirically during the validation stage [130]. The non-linear operation is performed via the rectified linear unit activation function, which drives negative values to zero [131]. Max pooling is used to aggregate and retain prominent features. The soft-max activation function is then applied to the outputs of the neural network to scale them to class probabilities. The preceding functions and model hyperparameters are utilised in CNN classifiers for a wide range of fields including image recognition [130] and power system fault classification [132] and are therefore considered suitable for this application. Mathematical descriptions and practicalities of the choice CNN model hyperparameters are summarised in [128, 130].

The proposed system state classifier therefore aims to detect not only oscillation events but also potential precursor states, which, as discussed previously, can serve as important insights for providing an early warning of the risk of oscillatory instability.

3.3.2 Performance of the System State Classifier

The curated training dataset consists of 5-second windows of 22 SSO, 245 Precursor and 420 Normal instances derived using the results of the change-point analysis described in Section 3.2. The SSO instances are derived from the 42 SSO events with observable large amplitude in the time domain and poor damping, while the Precursor instances were labelled manually via inspection of both the time-domain measurements and spectrograms of the segments returned by the change-point analysis. The Normal instances include windows from different time periods, in which no oscillation was detected in order to capture different trends and a wide variety of noise patterns.

The data were split into a training set (70%), validation set (10%) and an out of sample test set (20%). All event and precursor windows from a suspected SSO event were assigned exclusively to one of the training, validation, or testing sets. This ensured that oscillatory samples from the same suspected event do not appear in more than one subset. To address the relatively smaller number of available SSO event instances, class weights inversely proportional to the distribution of the three classes were applied in the classification layer so that errors on the minority SSO class contributed more strongly to the training loss. Figure 3.10 illustrates the training and validation accuracies and losses. Accuracy represents the proportion of correctly classified samples, while loss measures the classification error including how confident the network is in its predictions. These metrics are calculated at each training iteration, on the training data used to update the model and a small out of training validation set. The consistent trends between the training and validation set show that the model training is not overfitting but rather finding discriminative information in the training data. Overfitting is typically characterised by a continued improvement in training accuracy and loss while the corresponding validation metrics plateau or deteriorate. This results in a widening gap between the training and validation curves. In this case, the training and validation trends remain closely aligned, suggesting that significant overfitting is not observed.

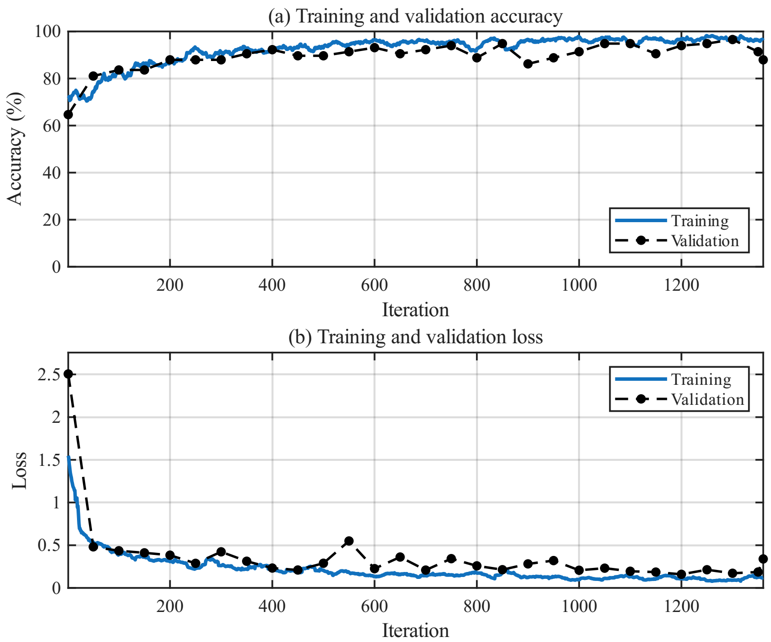

Figure 3.10: Training performance of the TF-CNN classifier.

Figure 3.11 illustrates the performance of the developed system state classifier by presenting the confusion matrix that compares the true class labels with the prediction produced by the TF-CNN classifier on the out-of-sample test set. Two additional metrics, i.e. Precision, P, and Recall, R, are also calculated as:

$$P = \frac{TP}{TP + FP}, \tag{3.3}$$

$$R = \frac{TP}{TP + FN}. \tag{3.4}$$

Precision is the ratio of true positive (TP) predictions to the total number of positive predictions, including false positives (FP). It highlights how often the predictions made by the model are correct. Recall is the ratio of TP to the number of positive instances, which include TP predictions (correctly classified), and false negative (FN) predictions (misclassified). It represents the classifier's ability to accurately identify all instances belonging to a specific class. An ideal classifier will have both high Precision and Recall.

The $F1$ score reflects an average performance of these two scores as:

$$F1 = 2 * \frac{P * R}{P + R}. \tag{3.5}$$

Figure 3.11: Performance of the TF-CNN classifier.

The results indicate that the proposed system state classifier can distinguish between Precursor and Normal classes. The classifier can achieve the task successfully in the majority of the cases, but can misclassify true Precursor signatures as Normal conditions in some instances. This is indicated by the loss in recall associated with the Precursor class and the loss in precision associated with the Normal class. The implication of this is a delayed detection of a precursor signature, possibly until it is more distinguishable from background noise. Additionally, the high recall of the Normal class and the high precision of the Precursor class show that the classifier does not misclassify a true Normal condition as a Precursor event for the out-of-sample test set. This is desirable as it reduces the occurrence of spurious alarms. Early SSO event windows may also be initially detected as precursor windows until the SSO becomes more prominent. The ML model is therefore best suited for precursor detection and can be used in conjunction with traditional modal analysis for poorly damped SSO event detection.

Table 3.2 displays the $F1$ scores per class, highlighting the performance of the proposed classifier. These results demonstrate the potential for data-driven oscillation classification tools to accurately identify SSO events and precursor states in the presence of noise and can therefore form part of an early warning oscillation monitoring tool.

Table 3.2: TF-CNN F-scores

	SSO	**Precursor**	**Normal**
F-score	0.727	0.902	0.791

A supervised learning approach has been applied to develop and train the TF-CNN system state classifier using a single measurement location. This has been shown to be capable of identifying the precursory and oscillatory state of the system. The proposed ML classifier can be used for detection of the normal, precursor and SSO states, but it cannot give a quantitative assessment of the oscillatory state of the system. It also does not incorporate current or power measurements, nor does it account for phase angle or the spatial dynamics captured from multiple measurement points. Therefore, the proposed algorithm does not give further insight into the cause of the SSO, how it propagates across the network or the potential SSO source location. Furthermore, the methods presented did not consider correlations between SSO states and system conditions. Therefore, the findings do not give insights into the mechanisms that cause the system to transition between the Normal, Precursor and SSO event states, which represents future work for the PhD research.

3.3.3 Proposed Framework for Detecting and Quantifying Oscillation Risks

To address these limitations, a framework that integrates a data-driven approach with domain knowledge is developed and illustrated in Figure 3.12. This framework expands the proposed analysis and algorithm by incorporating an improved dataset of multiple measurement locations, and more granular system operating conditions, (e.g. generator outputs and system conditions in Scotland). This data can be further combined with learnings from past event investigations. The aim of the proposed data-driven framework is to supplement the limited oscillatory state detection of the previously proposed ML model with the ability to give insight into the event cause and quantify the risk that the system state may transition from one state to the next based on patterns present in previous events. This quantification can, for example, take the form of risk factors based on system operating condition profiles learned from previous events.

As previously noted, system data including market data, inertia levels etc, will come from different sources and different reporting rates and timestamps. Data alignment and methods that combine PMU measurement data with system level data can be further investigated and applied. The resulting high dimensional feature set will reflect the complex dynamics of SSO mechanisms, including the influence of system conditions.

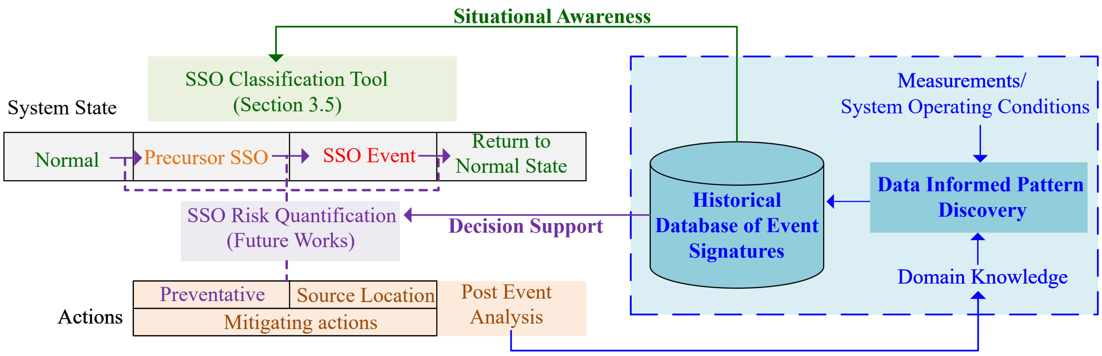

Figure 3.12: Proposed data-driven framework for analysing and mitigating SSOs.

Feature space reduction techniques (e.g., independent component analysis or t-stochastic neighbour embedding [133]) can identify key features and correlations associated with different system states. Explainable AI techniques and causality analysis can also be investigated to link patterns to changes in system states. This process is represented by the data informed pattern discovery block, as shown in Figure 3.12. The output of this can be a database of historical events (as obtained in the analysis of Section3.2) and corresponding features that can explain the present state of the system and quantify the risks of SSO becoming more severe. This can then enable potential preventative actions to move the system back to a normal state when a precursor SSO is detected. The proposed framework therefore aims to enhance the capability of the proposed analysis and TF-CNN classifier from situational awareness (knowledge of system state) towards decision support (quantification of risk).

This proposed early warning framework only requires existing measurement infrastructure (but can incorporate higher resolution measurements if available) and is representative of actual system dynamics. It can also work complementary to traditional physics-based (modelling and stability analysis) approaches. Incorporating physics-based constraints within the data-driven pattern discovery ensures that the discovered patterns are meaningful. The learnt dynamics can then be used to tune models to better reflect the real system, thus improving analytical techniques. However, a key barrier to developing and implementing such a system remains the access to data, hence the development and implementation of the framework will be investigated in future research. This also highlights the need to improve dissemination of event learnings and data across industry and research communities.

3.4 Limitations of Existing Monitoring Solutions for Analysing IBR Driven Oscillations

The analysis conducted in this chapter highlights that PMU measurements can capture SSOs as oscillations in the reported phasor quantities. However, as discussed in Section 2.1, standard compliant PMUs employ narrow bandpass filtering around the nominal frequency. Analysis of waveform recordings from past events in other countries have revealed sub and super-synchronous components centred around the nominal frequency, as shown in [98]. PMU processing results in spectral mixing of these components as well as aliasing in the reported measurements. This means that details of these oscillation components can be lost. The use of PMU data will constrain the features utilised by the proposed state classifier and early warning system, potentially leading to inadequate or even inaccurate results. Existing research has also shown that the distribution of these sub/super-synchronous components are related to the oscillation mechanisms and can influence source location algorithms [98, 134].

Figure 3.13 shows an example of an SSO event [16] in the GB grid with multiple frequency components in the reported phasor magnitude. Typically, waveform snapshots from DFRs would be examined to determine if sub/super-synchronous components are present. Waveform records from a PQube power quality metre connected at the same location as the PMU in this study were examined. The PQ meter only triggered on under-frequency after the large amplitude SSO event appears to have ended. However, the close-to-noise level, precursory signs as discussed in the preceding analysis are seen in the reported phasor measurements before and after the event, thus potentially being captured by the PQ metre.

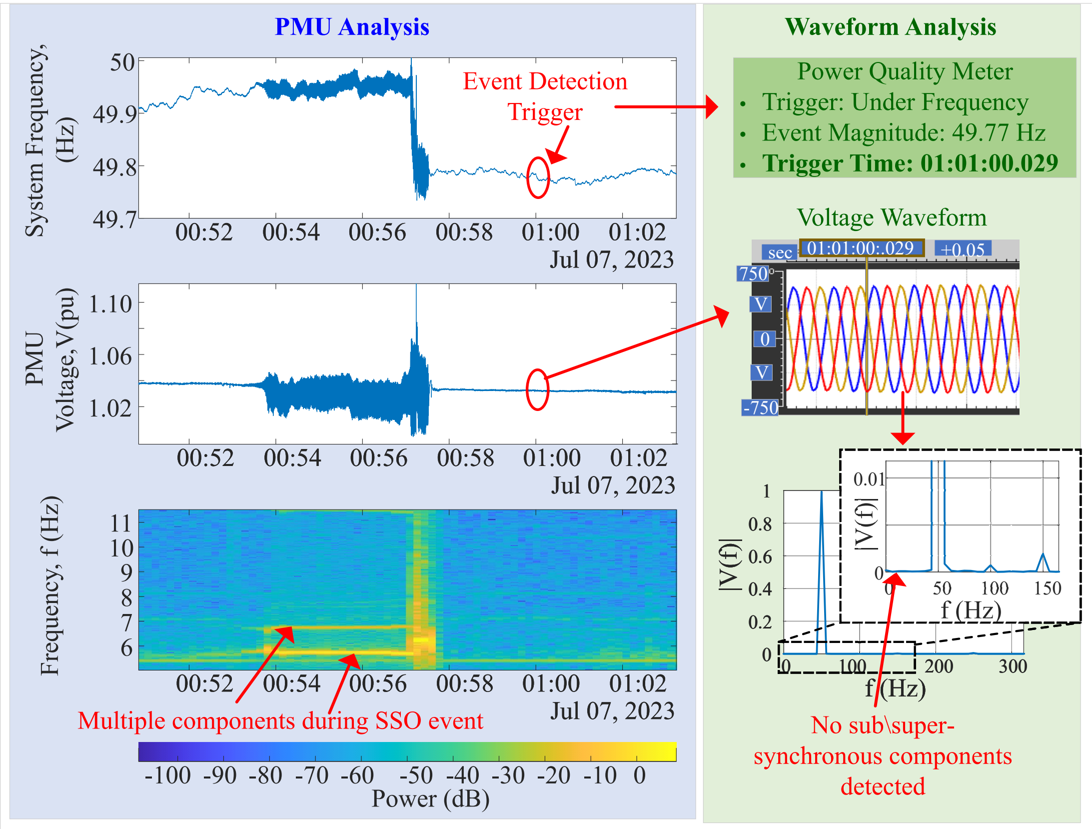

Figure 3.13: Comparison of PMU and waveform analysis for GB SSO event described in [16]

An initial analysis conducted by applying the DFT to the 16 cycles of phase voltage waveform measurements, sampled at 6400 Hz (128 samples/cycle), did not uncover any significant sub/super-synchronous components around the nominal frequency. However, it should be noted that the noise level and the low resolution of the DFT (6400/(128*16) = 3.125 Hz), may impact its ability to separate closely spaced frequencies due to spectral leakage. For example, the oscillation in the phasor voltage magnitude is $\sim$ 5.6 Hz. If present, the suspected sub/super-synchronous oscillations will be at $\sim$ 44.4 Hz and $\sim$ 55.6 Hz, respectively. Since the nominal frequency is not exactly 50 Hz, some of the spectral energy leaks into the adjacent DFT calculation points (50 ± 3.125Hz) and if the sub/super-synchronous components were present they would not be properly separated.

Improved filtering and interpolative methods exist (e.g., [84, 85] as discussed in Section 2.2.4), but the resolution can only be truly improved via longer observation windows. The results are therefore inconclusive and a longer time window, as well as, waveform measurements from the large amplitude SSO events would have allowed for a more conclusive analysis.

This example highlights the need for the following improved monitoring capabilities for IBR rich networks:

1. Improved waveform processing methods that extract details beyond fundamental phasors.
2. Continuous monitoring and characterisation of abnormal conditions.
3. More robust and generalised event detection methods.
4. Improved signal processing methods that can detect multiple frequency components of interest.

3.5 Chapter Summary

Emerging SSO events are attributed to a wide range of mechanisms, including IBR-based dynamics that are less understood compared to electromechanical dynamics induced mainly by SGs. This chapter analysed 18-months of real-world PMU data measured in Scotland. A total of 42 SSO events in the GB network, manifesting mostly as 5-8Hz oscillations in the reported phasor quantities, were found. Offline CPD uncovered the presence of precursors with low-amplitude, close-to-noise level oscillations in the time domain, which can be more clearly observed in the frequency domain. These precursory signatures preceded the more severe SSO events and were present in the system for several minutes to hours.

A TF-CNN based system state classifier was developed and trained using real-world measurements. The proposed classifier can accurately categorise the state of the system as Normal, Precursor or SSO, which can potentially be used by system operators to enable early warning of SSO risks. A framework to extend the state classification to incorporate insights from wide area measurements and system operating conditions to further quantify this risk has also been presented. Finally, an example of an actual SSO event in the GB network showed that typical monitoring via continuous PMU measurements and triggered waveform recording may not be adequate for fully characterising SSO events.

From the analysis, the following key recommendations can be summarised: 1) System operators, network owners, and academia should collaborate to share data and learnings from actual SSO events to improve the overall understanding of these phenomena and develop appropriate solutions and 2) The design criteria for emerging power system monitoring methods should address the limitations of traditional PMUs for detecting and analysing SSOs. This includes the ability to detect multiple oscillatory components in a wider frequency range, as well as improving the frequency resolution in order to detect and accurately measure (potentially) closely spaced inter-harmonic frequencies.

Chapter 4

A Generalised Synchronised Waveform Processing Algorithm for IBR-Dominated Power Networks

Accurate real-time monitoring of power systems under both steady-state conditions and abnormal events, over both local and wide-area distances, is critical in ensuring and maintaining power system security. The ability to detect and characterise abnormal system dynamics are particularly important in IBR-dominated systems in order to take timely mitigating actions. Chapter 3 demonstrated that conventional PMUs may not accurately monitor IBR dynamics, while continuous streaming of synchro-waveforms faces limitations associated with high data volumes. Real-time, utility level deployment of SWMUs will therefore require a new suite of alternative methods to continuously streaming high-resolution synchro-waveform data in an efficient manner, while maintaining adequate accuracy, in order to be scalable for system-wide monitoring. This can be achieved by appropriate processing of the raw waveform data and a review of such synchro-waveform processing methods was conducted in Chapter 2. It has found that the existing methods faces critical limitations as they are either application dependent or lack the ability to adapt to different possible dynamics.

This chapter presents research to address the aforementioned gaps by developing a novel, synchro-waveform signal processing approach, referred to as the generalised synchro waveform measurement unit (G-SWMU) algorithm. The G-SWMU algorithm, retains the valuable information present in the original measurements for a wide variety of conditions, while reducing the requirements of the supporting infrastructure. The proposed G-SWMU algorithm addresses the limitations of previously reported application specific SWMU algorithms by combining suitable signal processing methods to detect and measure different components present in synchro-waveforms. Specifically, the measurand (i.e. the quantity to be measured) of other processing methods are application specific (e.g. focused solely on oscillation or transient), whereas the measurand of the proposed G-SWMU is information based and encompasses a broader range of phenomena, including both oscillatory and transient components. This is advantageous as application specific processing will filter out other potentially relevant components which will limit or even prevent the benefits of increased resolution being fully realised.

This is achieved by first generalising the steady state, fundamental phasor definition to include different dynamics of interest. The G-SWMU algorithm decomposes the input synchro-waveform into non-sinusoidal distortions and oscillatory components, each of which is processed separately. The proposed G-SWMU algorithm therefore produces fundamental phasor measurements under normal system conditions, with the capability to adaptively detect and characterise abnormal conditions for efficient data processing and transmission. The outputs of the algorithm are a sparse representation of broadband transients and multiple phasors at detected frequencies of interest. The proposed G-SWMU algorithm therefore builds on previously reported processing methods by allowing information present at higher sampling rates to be retained in a form that is more easily transmissible with present supporting infrastructure.

Cases studies are presented to illustrate the proposed algorithm's performance for both synthetic and real world waveform measurements. Benchmarking against conventional PMUs and state of the art synchro-waveform processing methods is also conducted to highlight the relative strengths of the proposed algorithm. This chapter also discusses design considerations and practicalities for real-time deployment of the proposed algorithm.

4.1 Problem Definition

The sinusoidal definition of a synchrophasor is adopted for use with alternating current based power grids that conventionally utilise rotating machines to generate power [27]. As demonstrated by equation (2.4) in Section 2.1, this definition assumes the power system is in a quasi-steady state condition, such that the system voltages and currents can be accurately represented by fundamental phasors. It therefore does not take into account possible dynamics and/or transients present in waveforms resulting from abnormal system conditions, e.g. phase/amplitude steps, arcing, faults, harmonic/inter-harmonic oscillations, etc.

Figure 4.1(a)demonstrates the actual current waveform of a faulted phase for a cable fault available from [108]. Step changes in amplitude and phase are observed, as well as sub-cycle distortions. The resulting frequency spectrum, illustrated in Figure 4.1(b), exhibits a broadband spectrum with energy distributed over a wide set of frequencies. A broadband spectrum means that the continuous signal cannot be reconstructed by a finite (and limited) set of sinusoidal components. The narrowband, fundamental synchrophasor definition therefore cannot represent such signals accurately.

In contrast, oscillatory components, including the fundamental and (inter-)harmonics, are narrowband. However, as previously discussed in Section 2.3.1 of Chapter 3, the fundamental reference phasor assumption, filtering and aliasing limit the ability of conventional PMUs to capture all possible oscillatory information. To address the limitations with the standard synchrophasor definition and measurement, this research defines an alternate measurement definition based on the possible information contained in voltage and current synchro-waveforms. An N sample, discrete power system signal, y_n, can be considered as the sum of three components:

$$y_n = \sum\nolimits_k A_k \cos(2\pi f_k t + \phi_{0k}) + Y_n^{TR} + Y_n^{Noise} \tag{4.1}$$

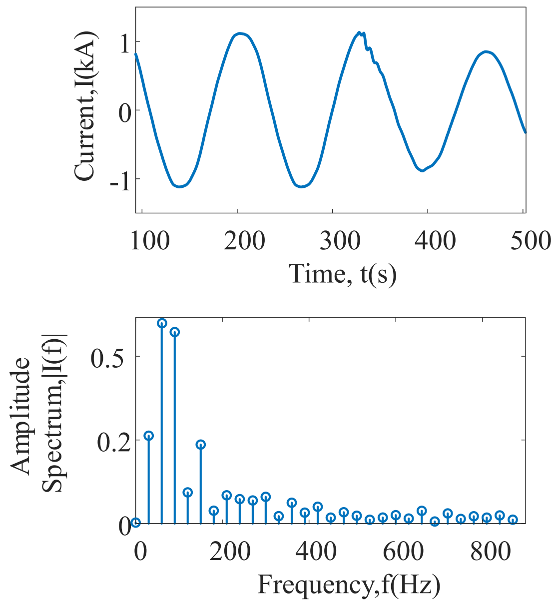

Figure 4.1: Broadband spectrum of a power system transient

The first term consists of k sinusoidal components, including the fundamental component and possible (inter-)harmonics each with A_k amplitudes, f_k frequencies and ϕ_{0k} initial angles. The second term Y_n^{TR} describes broadband transients, and finally the third term Y_n^{Noise} captures noise, e.g. errors introduced during the measurement process. By treating each component separately, a combination of appropriate signal processing tools may be applied to decompose the signal into its constituent parts and retain useful information while suppressing noise.

4.2 A Generalised Synchro-waveform Measurement Unit Processing Algorithm (G-SWMU)

The proposed G-SWMU processing algorithm seeks to detect, separate and process the different possible components in the input signal via a two-stage feature extraction process as illustrated in Figure 4.2. The first stage applies a novel wavelet scale correlation transient filter (WSCTF) that analyses correlations in wavelet coefficients of the input signal to detect and represent transients, i.e. the Y_n^{TR} term of (4.1). Furthermore, filtering, via applying certain thresholds of wavelet coefficients, is performed to decompose the input into its transient component and oscillatory component i.e. the $\sum_k A_k \cos(2\pi f_k t + \phi_{0k})$ term of (4.1). In the second stage, the multi-frequency phasor extraction module utilises a novel iterative extended DFT based empirical wavelet transform (I-EDFT-EWT) to detect and characterise the frequencies of interest present in the smooth signal. After the signal is decomposed into its constituent modes, the Hilbert transform (HT) is applied to extract instantaneous magnitudes, phases, and frequencies of each sinusoidal component. The novel combination of the WSCTF and the I-EDFT-EWT is also complementary, as the WSCTF removes broadband noise which can negatively impact the convergence of the I-EDFT-EWT. The two-stage processing via the WSCTF and the I-EDFT-EWT therefore allows for the measurement of transients as well as an increased resolution based phasor measurement across a range of frequencies. Noise rejection is further incorporated within each stage via thresholds on the proportion of overall signal energy associated with various signal components.

The outputs of the G-SWMU algorithm consist of a time-frequency based wavelet representation of extracted transients and multiple phasors at the frequencies of interest within the input signal. Under normal operating conditions, the proposed SWMU algorithm produces a fundamental phasor, maintaining the functionality of conventional PMUs. During abnormal events, the proposed SWMU algorithm adapts, via the flexibility of the wavelet bases, to different possible system dynamics. This is done with limited or no prior knowledge of the functional form of the system dynamics. The G-SWMU algorithm processes waveforms locally and outputs sparse features relative to raw synchro-waveforms. This reduces the need for additional infrastructure for streaming to, storing and processing large centralised repositories of raw synchro-waveforms. The G-SWMU algorithm therefore provides a tool for identifying and characterising segments of interest within synchro-waveform measurements in an efficient and scalable manner, thus addressing the limitations of conventional PMUs and existing synchro-waveform processing methods. The components of the G-SWMU algorithm are described in the subsequent Sections.

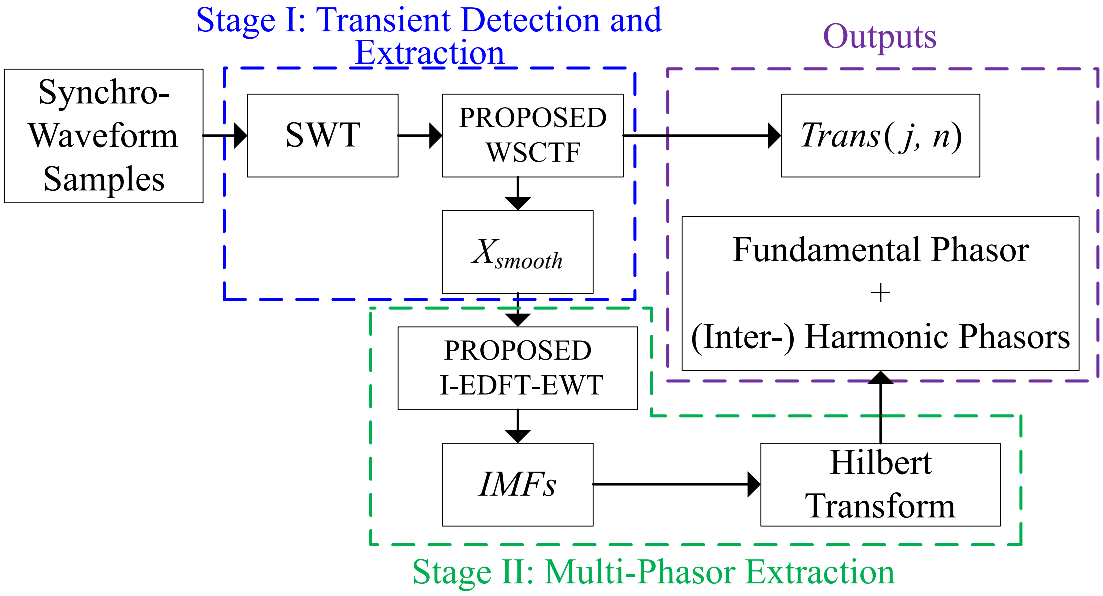

Figure 4.2: The G-SWMU algorithm schematic

4.2.1 Transient Detection and Characterisation via the WSCTF

This research utilises the time-frequency based wavelet transform to represent non-sinusoidal, broadband distortions in power system signals. The theory and properties of the wavelet transform utilised in the proposed WSCTF are first introduced, followed by the design of the WSCTF for synchro-waveform processing.

Wavelet Transform for Power System Transient Analysis

The wavelet transform (WT) is a time-frequency based analysis tool that decomposes a signal into multiple frequency bands while preserving time localised information of the (local) frequency content of the signal, e.g. sub-cycle distortions [135]. This is in contrast to the Fourier transform which extracts frequency information over the entire (global) observation window. The WT analyses a signal using a set of functional bases, called wavelets, derived from scaling and translating a mother wavelet, ψ, as:

$$\psi_{a,b}(t) = |a|^{-1/2}\psi\left(\frac{t-b}{a}\right), \tag{4.2}$$

where a is the scaling parameter and b is the translation parameter. As a changes, the wavelet covers different frequency ranges. Larger values of a (i.e. lager scales) correspond to lower frequencies, while smaller values of a (i.e. lower scales) correspond to higher frequencies. Changing b shifts the position of the wavelet within the observation window, thus facilitating time localisation.

The WT of a signal, $x(t)$ is given by:

$$W_x(a, b) = \int_{-\infty}^{\infty} x(t)\psi^*_{a,b}(t) \tag{4.3}$$

where $*$ denotes complex conjugation. Figure 4.3 illustrates the WT for a power system signal with a non-sinusoidal transient. The scaling parameter actually changes the shape of the wavelet. The narrow time support of the $a = 0.5$ wavelet is better suited to sharp short-time distortions. Equation (4.3) is equivalent to convolution. As the wavelet slides across the observation window, the output of the convolution process is highest where the wavelet shape is most similar to the input. This is reflected by the larger wavelet coefficients that are aligned with the transient portion of the input. For a larger scale parameter, the wavelet time support is larger and this is suitable for smooth, low frequency (slow varying) components. This results in wavelet coefficients that are reflective of the smoothed sinusoidal wave.

Comparing Figures 4.1 and 4.3 highlights the advantage of the WT to localise transients and represent broadband spectrums via discrete frequency bands. WT can therefore be applied in event detection and provides a sparse representation of broadband transients. This means that an input signal with non-sinusoidal distortions can be reasonably reconstructed from wavelet coefficients across a specified and discrete number of wavelet scales (frequency bands).

There are different possible implementations of WT depending on how the scaling and translation are defined. The discrete wavelet transform (DWT) discretises the scale parameter by integer powers of 2 (i.e. 2^J), and proportionally translates the wavelet by $2^J m$ samples where m is a non-negative integer [136]. The DWT is equivalent to band pass filtering of the input signal at 2^J discrete frequency levels.

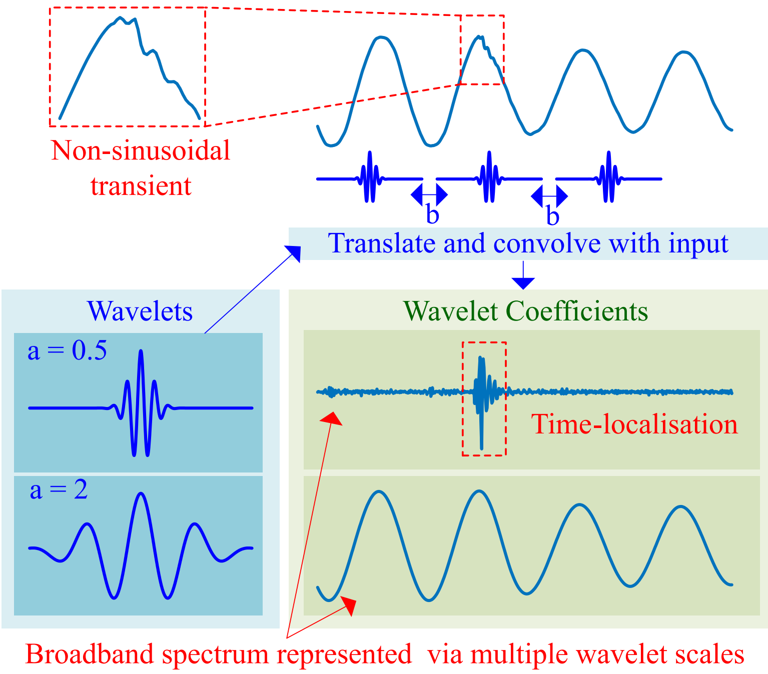

Figure 4.3: Wavelet transform overview

It therefore filters frequency bands starting at the Nyquist frequency and halving the range at each successive decomposition level, J. For example, for a 6.4 kHz signal, the first scale will result in a frequency band of 3.2 kHz to 1.6 kHz, the second scale will result in 1.6 kHz to 0.8kHz and so on. To ensure full coverage of the signal spectrum (i.e. J^{th} scale to 0 Hz) a low pass filter, known as the scaling function, $\phi_(t)$ is applied [135]. WTs have been widely applied in power system event analysis [137] as well as power system protection [138] and will be adopted in this research to process synchro-waveform measurements.

Stationary Wavelet Transform (SWT) for Transient Localisation

The efficient implementation of the DWT results in downsampling between successive wavelet scales. The wavelet coefficients of the DWT are therefore not time-aligned with the input signal. To maintain this time-alignment, the stationary wavelet transform (SWT) sets the translation parameter as m (i.e. the 2^J increments of the translation parameter are removed compared to the DWT) and maintains the scale parameter as

2^J [139]. Applying these parameters to (4.2) gives the discretised SWT wavelet as:

$$\psi^{SWT}(n) = |2^J|^{-1/2}\psi\left(\frac{n-m}{2^J}\right). \tag{4.4}$$

The SWT does not downsample across successive wavelet scales and results in a $(J+1)\times N$ matrix of wavelet coefficients for an N sample signal with J decomposition levels. The SWT coefficients are therefore time-aligned with the input signal, as illustrated in Figure 4.3. The DWT is more suited for compression, while the SWT is more suited for feature extraction and event localisation [140]. However, it should be noted that a large proportion of the SWT coefficients will not be associated with transients or oscillatory components of interest and can be discarded, resulting in a sparse SWT coefficient matrix. The SWT allows for a comparison between time-aligned coefficients across different wavelet scales and retains information about the time of occurrence of transients within the observation window. These properties will be applied to transient event detection and characterisation in the following subsections.

Wavelet Transform Modulus Maxima (WTMM) for Robust Event Detection

Distortions and/or discontinuities in synchro-waveform measurements can be described as singularities or edges in the field of signal processing [141]. Power system transient detection is framed as a singularity detection problem in this research. Wavelet transform modulus maxima (WTMM) refers to a wavelet coefficient that has a larger magnitude compared to other coefficients within a smaller local region to the left and right of the point. For example, for the regions in the red dashed box around the wavelet coefficients of Figure 4.4, a WTMM exists and is the peak in the wavelet coefficients within the box.

It is proven in [141] that non-sinusoidal transients in the input result in WTMMs across the lower wavelet scales (higher frequency bands). This is illustrated in Figure 4.4 which shows a phase jump and the corresponding WTMM across the first three wavelet scales. The energy associated with short duration broadband transients will be distributed across multiple scales and dominate for the time instants coincident with the occurrence of the transient. WTMM across scales that are associated with transients can also be retained and, via the inverse SWT, give an approximate reconstruction of the transient [141].

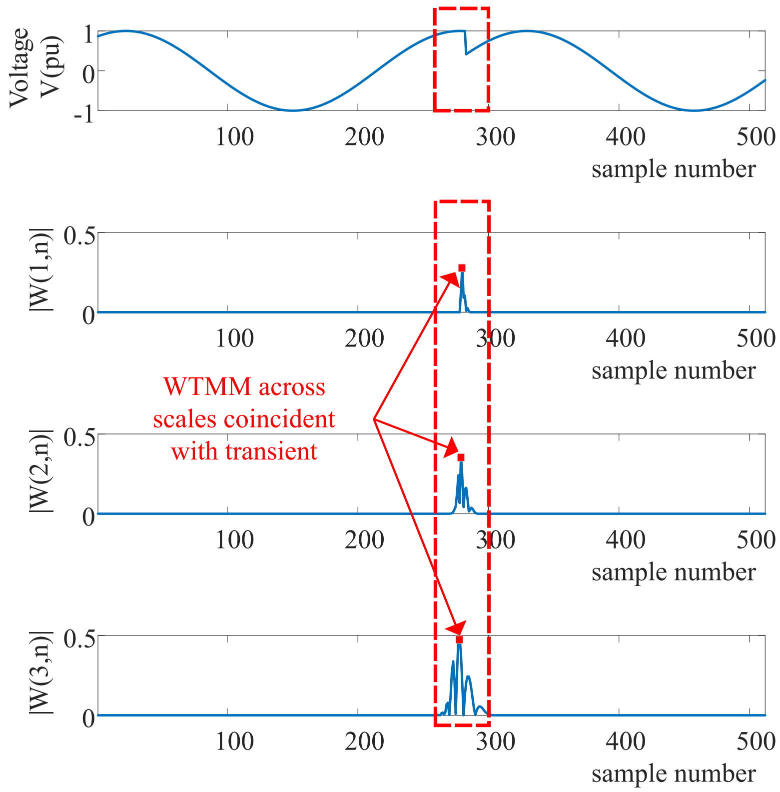

Figure 4.4: WTMM and their correlation across scales for the transient condition

In [142], WTMM is applied to locate step changes within phasor estimation windows in order to improve the accuracy of phasor estimates under abnormal conditions. However, the method does not retain any information about relating to the distortions. In this research, the WTMM provides a mechanism to identify and characterise non-sinusoidal distortions in synchro-waveform measurements.

Wavelet Scale Correlation Transient Filter

The SWT gives a scale-space decomposition of the input signal, resulting in a matrix of wavelet coefficients, $W(j,n)$, where j represents the scale and n represents the time instants or sample indices within the observation window. In this work, a wavelet domain filtration technique proposed in [143] for signal and image de-noising is adapted to detect and characterise power system transients by incorporating the SWT and retaining the WTMMs associated with the transients.

Correlations of the SWT coefficients across several adjacent scales are used to detect WTMM that occur in similar time instants across different wavelet scales. The correlation, $C_l(j,n)$, is simply the element wise product of $W(j,n)$ across l scales:

$$C_l(j,n) = \prod_{i=0}^{l-1} W(j+i,n) \tag{4.5}$$

where $j < J - l + 1$, and J is the total number of scales; $n = 1, ...N$, where N is the total number of samples in the observation window. Figure 4.5 illustrates a test signal with a phase jump and Gaussian noise (signal-to-noise ratio, SNR =25dB).

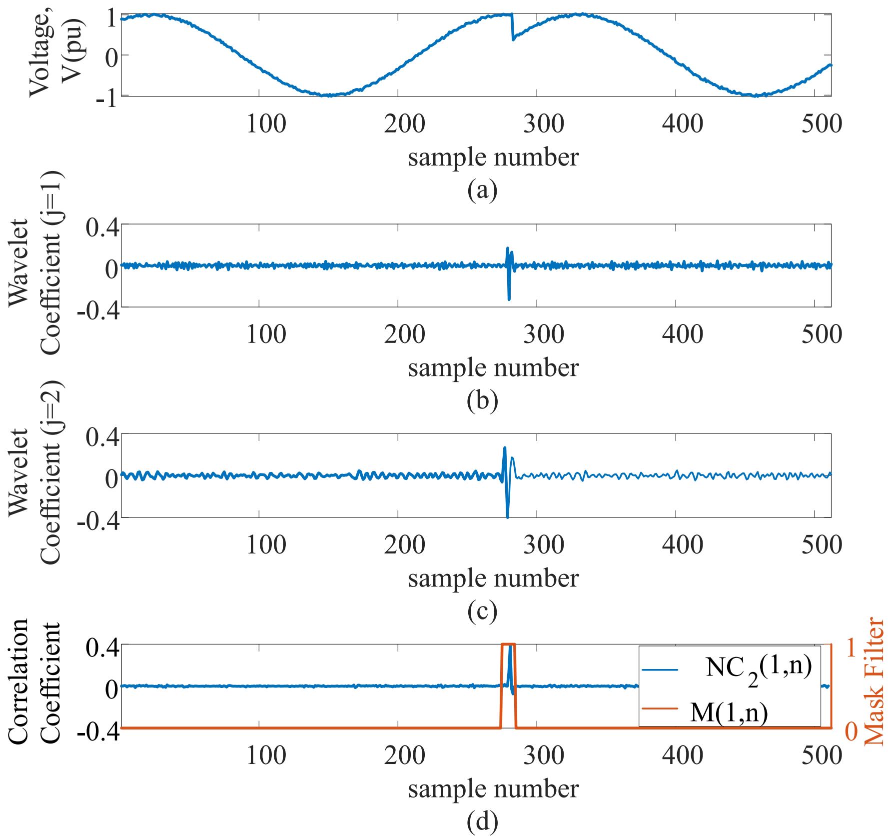

Figure 4.5: Correlation across wavelet scales for a phase jump: (a) input signal, (b) first scale wavelet coefficients, (c) second scale wavelet coefficients, (d) normalised correlation coefficient and mask filter.

The SWT coefficients corresponding to the first two wavelet scales and the correlation are also presented. It is observed that the correlation suppresses the wavelet coefficients associated with noise while enhancing the coefficients in the region of the discontinuity. A wavelet-correlation filter is applied by comparing normalised correlation coefficients with the original wavelet coefficients. The normalised correlation, $NC_l(j,n)$ is given by:

$$PC = \sum_n C_l(j,n)^2 \tag{4.6}$$

$$PW(j) = \sum_n W(j,n)^2 \tag{4.7}$$

$$NC_l(j,n) = C_l(j,n). \times \sqrt{PW(j)/PC(j)} \tag{4.8}$$

where, $PC(j)$ and $PW(j)$ are the power of the correlation coefficients and the wavelet coefficients at the j^{th} level, respectively.

The algorithm of the wavelet scale correlation based transient filter (WSCTF) is illustrated in Figure 4.6. The SWT is applied to the input signal, X, to obtain $W(j,n)$, and $C_l(j,n)$ is then calculated as the product of l successive wavelet levels. The transient feature extraction is then iteratively performed by rescaling correlation coefficients relative to the power of the wavelet coefficients and comparing their magnitudes. If the normalised correlation coefficient is greater than the original wavelet coefficient, then the corresponding element of a transient filter mask matrix, $FM_{tr}(j,n)$ is set to 1, as illustrated in Figure 4.5(d). Elements of $W(j,n)$ are also set to 0, generating $WF(j,n)$, which is input to the next iteration. ($WF(j,n) = W(j,n)$ for the first iteration). This procedure of power normalisation and transient extraction is iterated until the WTMM of $WF(j,n)$ is below a specified threshold, λ_{tr}.

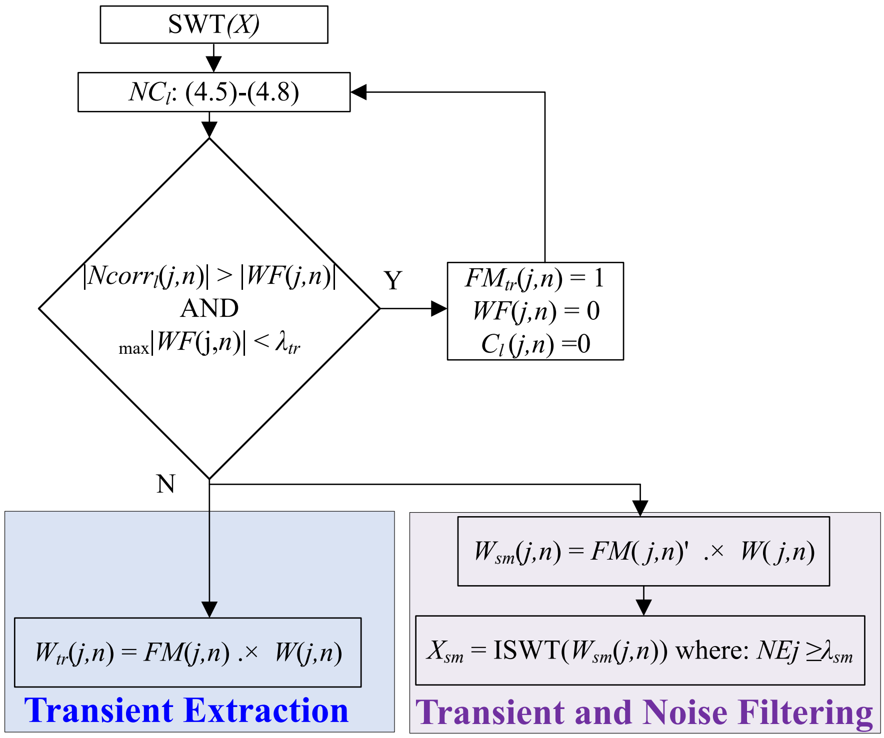

Figure 4.6: Flowchart of the WSCTF

At the end of the iterative procedure, the matrix of wavelet coefficients, Wtr, associated with the transients, i.e. those that are correlated across scales, is obtained via element wise multiplication (denoted by $.\times$) of $FM_{tr}(j,n)$ and the original wavelet coefficient matrix $W(j,n)$. Similarly, the product of $FM(j,n)'$ and $W(j,n)$, where $'$ is the logical complement of the filter matrix, filters out the transient distortions (correlated coefficients), resulting in the matrix $W_{sm}(j,n)$. However, a certain level of noise may still be retained. This noise typically manifests as low amplitude coefficients, which are less correlated across multiple scales (Figure 4.5(b)).

To remove this noise, the relative energy at each scale, $NE(j)$, can be calculated as:

$$NE(j) = \sum_{n} W_{sm}(j,n)^2 / \sum_{j} \sum W_{sm}(j,n)^2 \tag{4.9}$$

X_{sm} is obtained via the inverse SWT of $W_{sm}(j,n)$ at levels where the relative energy is greater than a specified threshold λ_{sm}. The selection of λ_{tr} and λ_{sm} involves a balanced consideration of the sensitivity of the filter and noise rejection, which is discussed in detailed in Section 4.3. The outputs of the WSCTF algorithm are a wavelet feature matrix corresponding to the wavelet decomposition of the distorted waveform, along with the smooth signal containing the oscillatory components.

4.2.2 Multi-Frequency Phasor Extraction via the I-EDFT-EWT

Power system signals typically comprise distinct sinusoidal components with spectral energy centred around specific frequencies. The component of interest is typically at the nominal frequency, while under certain conditions, network elements (e.g., loads, transformers, IBRs) generate harmonic/inter-harmonic components. Accurately measuring the properties of these components requires the ability to separate these components within online processing windows. Adaptive windowing, re-sampling [83], interpolation and reassignment of spectral components [85] and modal analyses [144] have been proposed in the literature. However, limited resolution, spectral leakage, uncertainty of oscillation frequencies and computational complexities limit the practicality of these methods to resolve closely spaced inter-harmonics attributed to emerging IBR driven SSOs (see Appendix A for more details). This can compromise the system operators' ability in early detection of instabilities, which could lead to further cascading failures. The requirements for processing the oscillatory components of synchro-waveforms therefore include the ability to adapt to different oscillation frequencies, as well as, high frequency resolution to separate and accurately measure multiple inter-harmonic components.

Empirical Wavelet Transform (EWT)

The empirical wavelet transform (EWT) [145] defines wavelets based on a segmentation of the frequency spectrum of a signal and is equivalent to bandpass filtering of the signal across each segment. Unlike the SWT, which uses a fixed subdivision of the frequency domain, the EWT adapts the wavelet filters as the spectrum of the signal changes, so it does not require prior knowledge of the properties of oscillatory components [145]. This is an important property as unlike traditional power system harmonics, which are integer multiples of the nominal frequency, emerging IBR driven SSOs can manifest as a wide range of inter-harmonic frequencies. Figure 4.7 illustrates the EWT.

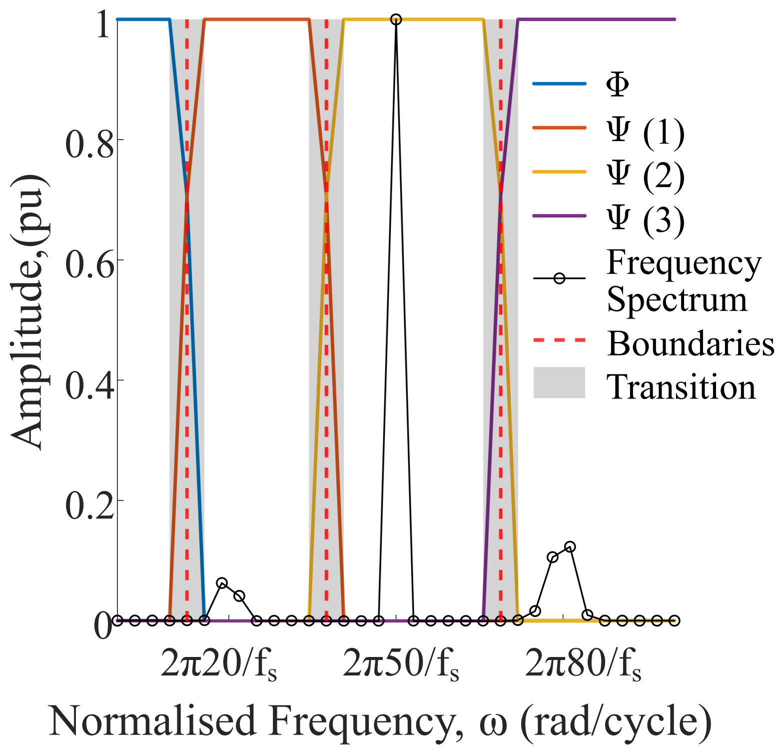

Figure 4.7: EWT Filter

First, the frequency spectrum of the signal is obtained, typically by conventional DFT. Peak detection and segmentation techniques are applied to the spectrum of the signal, e.g. mid-points between successive peaks, in order to determine boundaries on the frequency axis as illustrated in Figure 4.7. A transition width of $2\tau_n$ centred around each boundary, ω_n, is defined. The empirical scaling, $\phi_n(\omega)$, and wavelet filter coefficients, $\psi_n(\omega)$, are defined for each point on the normalised frequency axis, ω as [145]:

$$\phi_n(\omega) = \begin{cases} 1, & \text{if } |\omega| \leq \omega_n - \tau_n, \\ \cos\left[\frac{\pi}{2}\,\beta\left(\frac{|\omega| - \omega_n + \tau_n}{2\tau_n}\right)\right], & \text{if } \omega_n - \tau_n \leq |\omega| \leq \omega_n + \tau_n, \\ 0, & \text{otherwise.} \end{cases} \tag{4.10}$$

$$\psi_n(\omega) = \begin{cases} 1, & \text{if } \omega_{n+1} + \tau_n \le |\omega| \le \omega_{n+1} + \tau_{n+1}, \\ \cos\Big[\frac{\pi}{2}\,\beta\Big(\frac{|\omega| - \omega_{n+1} + \tau_{n+1}}{2\,\tau_{n+1}}\Big)\Big], & \text{if } \omega_{n+1} - \tau_{n+1} \le |\omega| \le \omega_{n+1} + \tau_{n+1}, \\ \sin\Big[\frac{\pi}{2}\,\beta\Big(\frac{|\omega| - \omega_n + \tau_n}{2\,\tau_n}\Big)\Big], & \text{if } \omega_n - \tau_n \le |\omega| \le \omega_n + \tau_n, \\ 0, & \text{otherwise.} \end{cases} \tag{4.11}$$

where the function $\beta(x)$ is defined in [146] as:

$$\beta(x) = x^4(35 - 84x + 70x^2 - 20x^3) \tag{4.12}$$

Within the boundaries, the EWT filter coefficients are set as 1, equivalent to a passband, while outside the transition widths, it is set as 0, equivalent to a stopband. Within the transition widths, the cosine and sine terms in (4.10) and (4.11) represent the falling and rising filter edges, respectively, as illustrated in Figure 4.7. The EWT is performed via the product of the signal spectrum and the defined wavelet filters. This results in the isolation of each spectrum peak. The input signal can then be decomposed via the application of an inverse DFT on each separated spectral component.

The EWT as described above and applied in [83] and [147] for phasor estimation, relies on the conventional DFT, which can have low resolution within the observation window when utilised in an online processing manner. In the presence of potentially closely spaced sideband oscillations, this low resolution can result in spectral leakage into adjacent components, resulting in inaccurate measurements.

Iterative Extended DFT

The conventional DFT, which the EWT utilises, is evaluated at discrete frequencies based on the sampling rate and window size. The resolution of the DFT is f_s/N, where f_s is the sampling frequency and N is the window length in samples. The iterative extended DFT (I-EDFT) [148] estimates the DFT of a signal using additional discrete frequencies within a similar observation window. It first defines kernels ($e^{-j\omega_m t_n}$) along a discrete set of frequencies, ω_m, consisting of M frequencies uniformly spaced by f_s/M increments, with $-\Omega \leq \omega_m \leq \Omega$ and $\Omega \leq$ the Nyquist frequency. Note if M is greater than N then the frequency resolution is increased relative to the DFT. An initial matrix of (non-zero) weights, representing the contribution of each discrete frequency to the signal spectrum, is also defined. The I-EDFT seeks to find the optimal weights that results in a signal spectrum that represents the information contained in the measurements. The weights are iteratively adjusted until a reconstruction of the data using the estimated spectrum results in a minimal error.

The I-EDFT iteratively estimates the DFT of a signal, $x(t)$, using the following expressions [148] (see Appendix B.1 for more details):

$$E = e^{-j\omega_m t_n}, \tag{4.13}$$

$$R = \frac{1}{M} E W_i E^H, \tag{4.14}$$

$$S_i = x(t)(R_i)^{-1}E./\text{diag}\left[E^H(R_i)^{-1}E\right], \tag{4.15}$$

$$W_{i+1} = \text{diag}\left(|S_i|^2\right), \tag{4.16}$$

$$\delta_i = \frac{|\sum W_{i+1} - \sum W_i|}{\sum W_{i+1}}, \tag{4.17}$$

where $t_n = [0, 1, ...N] * 1/f_s$ are the time instants of the samples of the input signal; E is a predefined $M \times N$ kernel matrix with chosen discrete frequencies; R is the autocorrelation matrix; S is the estimated signal spectrum; and W is the initial weight matrix, that is iteratively updated. The subscript i represents the iteration number. The operators $\{\cdot\}^{-1}$ and $\{\cdot\}^H$ represent matrix inversion and Hermitian transpose, respectively. The ./ operator represents element wise division. Equations (4.14)-(4.16) are solved iteratively until the relative change in the power spectrum, δ_i, is less than a specified threshold, λ_{I-EDFT}. The frequency resolution of this method is therefore set by f_s/M, while that of the traditional DFT is set by f_s/N. If M is equal to N, the I-EDFT is equivalent to the DFT. If M is greater than N, then the resolution of the

I-EDFT is increased within the same observation window. After the iterative procedure, the final I-EDFT and the inverse I-EDFT can be calculated as:

$$F_{I\text{-}EDFT}(\omega) = x(t)(R)^{-1}EW, \tag{4.18}$$

$$x(t) = \frac{1}{M}F_{I\text{-}EDFT}(\omega)E^{H}, \tag{4.19}$$

where 4.19 returns the original N samples of the input signal.

The I-EDFT allows a mechanism, via specifying $M > N$, to increase the resolution of the DFT without requiring further measurements outside the observation window potentially reducing detection time, while offering more accurate results than interpolation or spectral reassignment methods and has been applied for high frequency (power quality) inter-harmonic phasor estimation in [149]. To adopt this method for separating sub/super-synchronous oscillations (within the 0 to $2{\times}f_n$) band will require increasing the resolution via increasing M. However, this increases the dimensions of the I-EDFT, thus also increasing the computational burden of the iterative procedure. Additionally, the I-EDFT is essentially a data-driven estimation of the DFT and is sensitive to noise and broadband transients. Under such conditions, it may fail to converge to an appropriate solution of the frequency spectrum required for accurate phasor estimation [150]. An example of this is presented in Appendix B.3.

I-EDFT based EWT Phasor Extraction Algorithm

A novel I-EDFT based EWT phasor extraction algorithm is proposed to improve the frequency resolution of the EWT to sufficiently detect and separate sub/ super-synchronous inter-harmonic components. Integrating the I-EDFT within the EWT framework, is illustrated in Figure 4.8.

The I-EDFT is first applied to the input signal using (4.13)-(4.18) to obtain a higher resolution frequency spectrum at user defined discrete frequencies, ω. The boundaries for the EWT filters are found via a segmentation of the I-EDFT spectrum by detecting midpoints between the spectrum peaks.

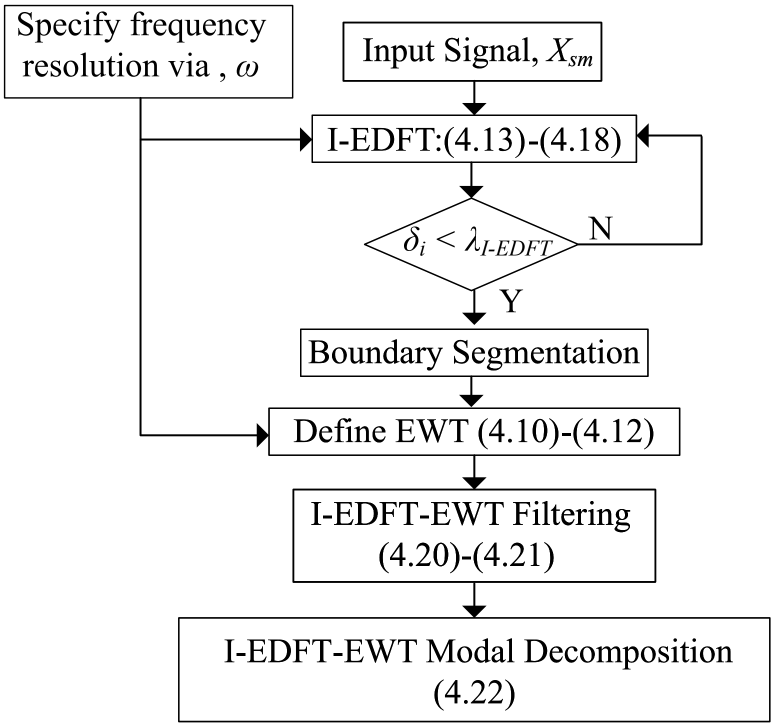

Figure 4.8: I-EDFT-EWT procedure

The EWT filters are then defined using (4.10)-(4.11) at the same discrete frequencies (i.e. at the same frequency resolution) as the I-EDFT spectrum. The I-EDFT-EWT filtering for η spectrum peaks is defined by:

$$\mathcal{W}^{\eta}(\omega) = F_{I\text{-}EDFT}(\omega)\psi_{\eta}^{*}(\omega), \tag{4.20}$$

$$\mathcal{W}^{0}(\omega) = F_{I\text{-}EDFT}(\omega)\phi_{0}^{*}(\omega), \tag{4.21}$$

where $\mathcal{W}^{\eta}(\omega)$ results in η I-EDFT spectrums each with one spectral peak as illustrated in Figure 4.9. $\mathcal{W}^{0}(\omega)$ captures low frequencies from 0Hz to the first spectral speak, usually containing DC offsets or very slow varying trends which are not of interest. The isolated spectral peaks are then converted to individual time-domain signals by applying the inverse I-EDFT as:

$$x^{\eta}(t) = \frac{1}{M}\mathcal{W}^{\eta}(\omega)E^{H}. \tag{4.22}$$

Equation (4.22) results in a modal decomposition of the input signal into its oscillatory components, referred to as intrinsic mode function (IMFs), with each IMF characterised by a single frequency.

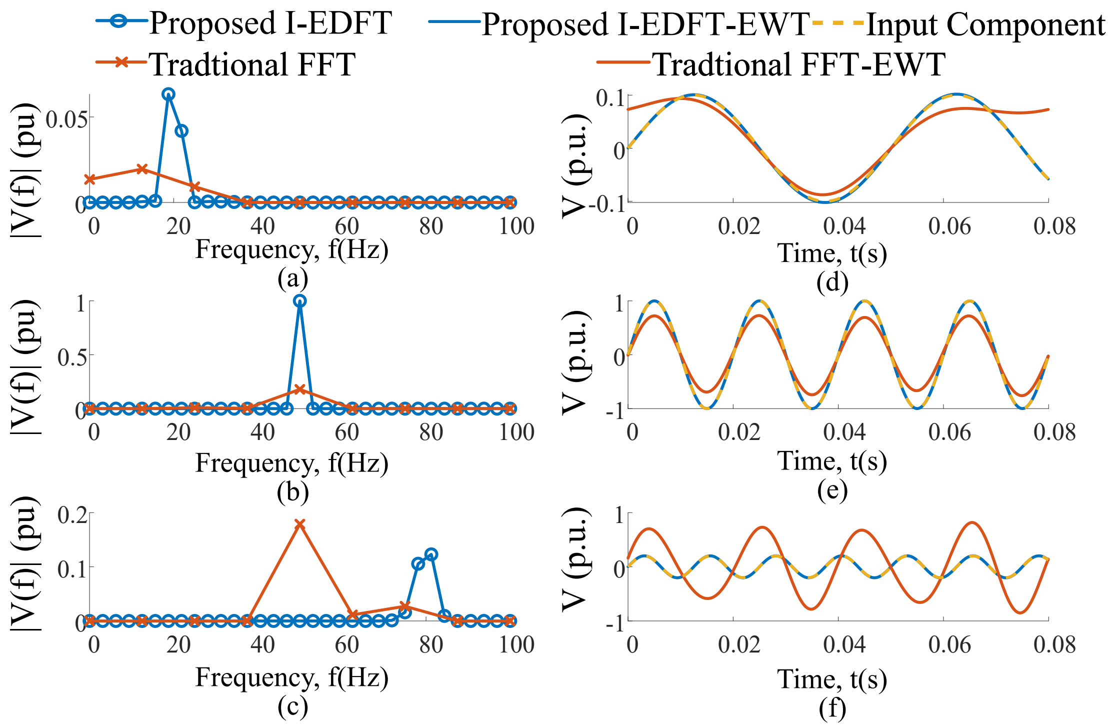

Figure 4.9: Comparison between conventional EWT and proposed I-EDFT-EWT

Figure 4.9 compares the performance of the traditional EWT to the proposed I-EDFT-EWT over a 4 cycle (of 50Hz) window at a sampling rate of 256 samples per cycle (N=1024) for a signal containing 50Hz, 80Hz and 20Hz components. Figure 4.9(a)-(c) illustrate the increased frequency resolution with the value of M set as 4096 (4 times greater than N). Figure 4.9(d)-(f) show that the proposed method improves on the DFT based EWT and has sufficient resolution to accurately extract each IMF and separate the fundamental, sub-synchronous and super-synchronous components.

Established phasor extraction methods can then be applied to each IMF to return the phasor quantities. The Hilbert transform (HT) based phasor extraction method [151, 152], is chosen since it gives dynamic phasor estimates throughout the estimation window allowing to track changes in amplitude, thus giving insights into growing oscillations (via damping or energy). The HT of each IMF is given by:

$$H^{\eta}(t) = \sum_{k=-\infty}^{\infty} h[k]\, x^{\eta}[t-k], \tag{4.23}$$

where

$$h[k] = \begin{cases} \dfrac{2}{\pi\, k}, & k \text{ odd}, \\ 0, & k \text{ even (including 0)}. \end{cases} \tag{4.24}$$

This results in a 90 degree shift of the original time signal. The analytical signals of each IMF are then defined as:

$$\hat{x}^{\eta}(t) = x^{\eta}(t) + jH^{\eta}(t). \tag{4.25}$$

The magnitude and phase of the analytic signal corresponds to the amplitude envelope and instantaneous phase of the real valued input signal (i.e. each IMF). The instantaneous frequency of the signal can then be extracted as the angular velocity of the analytic signal. It should be noted that the HT can only reliably estimate phasor quantities if the input to it only contains a single frequency component [153].

4.3 Design Considerations of the G-SWMU Algorithm

This section discusses the key settings that impact the performance, sensitivity and noise rejection of the G-SWMU algorithm. A complete list of settings is presented in Table B.1 of Appendix B.2.

4.3.1 Settings of WSCTF for Transient Detection

The choice of mother wavelet, decomposition level J, the correlation level l, and the thresholds λ_{tr} and λ_{sm} will influence the performance of the WSCTF. Since the WSCTF requires correlation across higher frequency scales, J should be greater than 2. Increasing J will give a richer scale decomposition with a trade-off of computational cost. If pattern matching is the intended application, a higher J can potentially give more distinct time-frequency representations, whereas for transient detection, a smaller J is suitable. Increasing l makes the filter more sensitive to larger distortions that correlate through many scales, while simultaneously improving noise rejection. In this research, J is set to 6 and l is set to 3 to balance transient detection performance and computational complexity.

Experimental tests with different distortions (simulated angle jump and an actual waveform from a vegetation encroachment event, labelled as signature 249 in [108]) and noise levels are input to the WSCTF. It was found that distortions result in larger, time localised wavelet coefficient amplitudes that coincide across different wavelet scales, while noise (simulated and real noise) result in widely distributed smaller amplitude coefficients, particularly at higher scales as illustrated in Figure 4.10. λ_{tr} is chosen as 3 times the standard deviation of the wavelet coefficients. Figure 4.10 illustrates that for both simulated and real-world noise levels, this empirically selected threshold gives good transient detection performance.

After filtering the coefficients associated with the transient, the majority of the signal energy is distributed in wavelet sub-bands that contain the smooth components, as illustrated in Figure 4.11. The simulated phase jump has a sample frequency of 12,800 Hz, therefore the $j = 6$ wavelet band corresponds to 0-200Hz. Since the 50Hz component falls within this band, the majority of the signal energy falls within this $j = 6$ wavelet scale. Similarly, the event 249 waveform is sampled at 7,680 Hz so the 60Hz fundamental falls with the $j = 6$, 0-120 Hz frequency band. If higher frequencies, i.e. high order harmonics, are present they will be reflected in higher energy at the appropriate wavelet scale. λ_{sm} involves selecting the wavelet scales to use to reconstruct the oscillatory component of the waveform that may contain multiple frequencies of interest for further phasor processing. A λ_{sm} of 1% is chosen to include oscillation components that may be 1% of the nominal component while rejecting noise which has low relative energy.

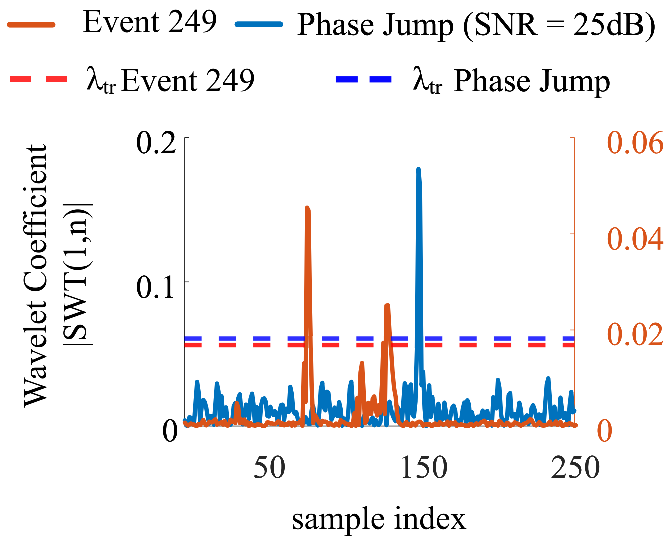

Figure 4.10: WSCTF transient detection threshold

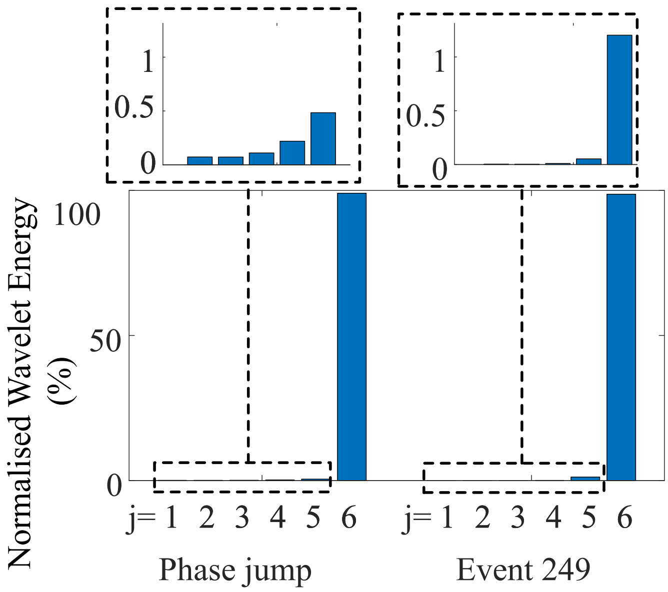

Figure 4.11: Normalised wavelet energies

4.3.2 Choice of Wavelet Family

Different wavelet families may result in similar transients being expressed differently in the wavelet coefficients, however, there is still correlation across scales of the SWT. The WSCTF therefore selects the relevant coefficients, resulting in similar transient detection and reconstruction performance regardless of the mother wavelet. This is illustrated in

Figure 4.12 for different wavelets and different distortions. The Daubechies wavelet with 4 vanishing moments (db4) is chosen in this research as it is widely used in power systems applications due to its suitability to detect short duration transients [137].

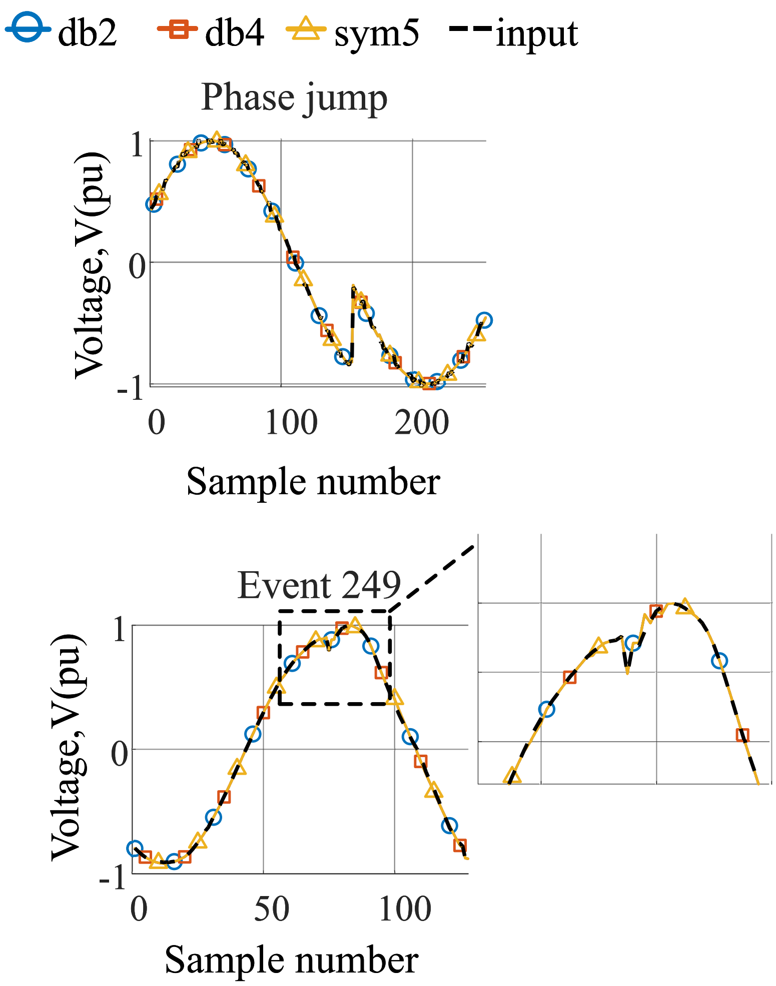

Figure 4.12: Transient reconstruction with different wavelets

4.3.3 I-EDFT-EWT Settings for Multi-frequency Phasor Estimation

The resolution of the I-EDFT is determined by the ratio of the sampling frequency, f_s, to the number of frequency points, M, defined in the kernel function, E, as described in (4.13). The frequency range, $\pm\Omega$, limited by the Nyquist frequency, is divided into fs/M frequency bins. Figure 4.13 shows the performance of the I-EDFT for different configurations using a 2-cycle window of a test signal with 50Hz and 50+/- 13Hz oscillations sampled at 12.8 kHz. Initially, M is set as 4,096 so that the resolution is 3.125Hz (4 times greater than traditional DFT), showing that there is still some spectral leakage, but the components are separated.

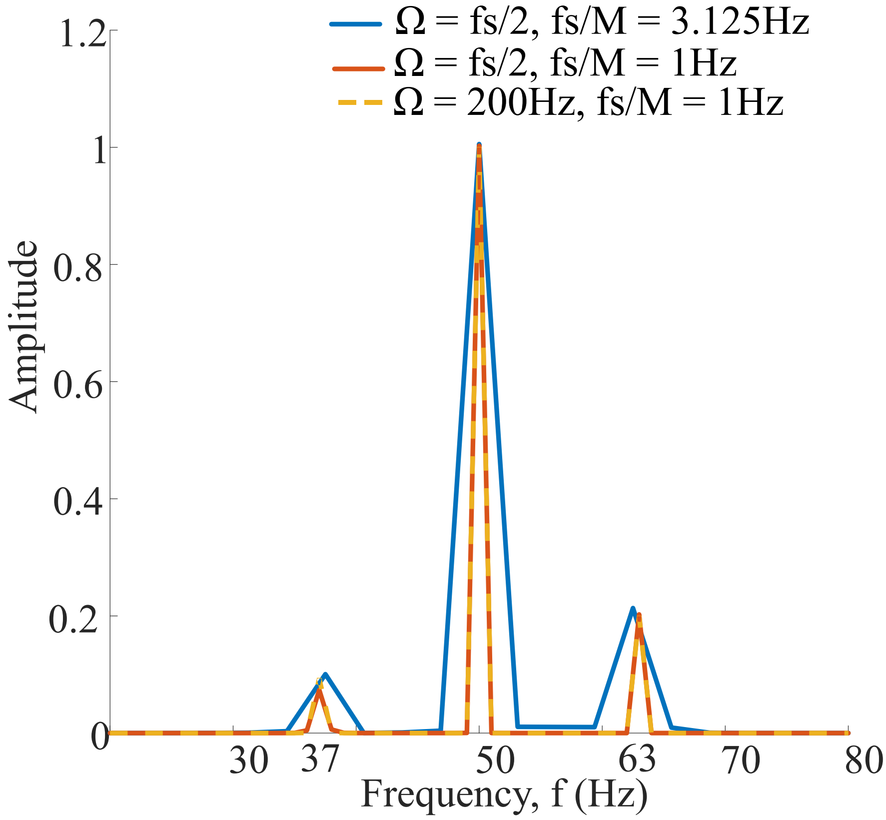

Figure 4.13: I-EDFT-EWT performance for different settings

Increasing M will increase the frequency resolution, with a resolution of 1Hz, allowing the I-EDFT to converge the exact solution. A large M also increases the dimensions of the matrices in (4.13)-(4.18), thus increasing the computational cost. This may be offset by applying the I-EDFT to a targeted frequency range by specifying, Ω (e.g. 200Hz), while maintaining similar frequency resolutions as shown in Figure 4.13. The design of the I-EDFT is flexible as f_s, Ω and M can be chosen to meet certain design specifications based on specific applications, e.g. a targeted frequency range of (0-2f_n) for emerging IBR driven SSOs. Unless otherwise stated, M is set equal to f_s giving a resolution of 1Hz, while Ω is set at the Nyquist frequency to determine any oscillatory components of interest.

The I-EDFT requires an initial spectrum estimate for the first iteration. An initial estimate of $W_1 = [1, 1..., 1]_{1\times M}$ is adopted in [148, 149]. This research improves on this by specifying an initial spectrum estimate with a peak of 1pu at the nominal frequency and using the final estimate from the previous input window as the initial estimate for the present window. This reduces the number of iterations needed to converge to a solution. $\lambda_{I\text{-}EDFT}$ is the change in the estimated I-EDFT across iterations. Small changes in $\lambda_{I\text{-}EDFT}$ correspond to the convergence of a solution. A value of 0.01 as recommended in [150] was found to give accurate results in testing, and so is adopted. I-EDFT spectral peaks below 1% of the maximum are discarded as potential noise. The recommended settings of the EWT including the transition width and boundary segmentation method can impact the ability to separate components but have much less impact than the I-EDFT resolution. These settings are discussed in Appendix B.2.

4.3.4 Impact of Noise

The WSCTF aims to differentiate transients from background noise, as shown in Figure 4.5(d). Applying the WSCTF first retains the sharp edges in the signal that may otherwise be smoothed by low pass filtering noise reduction techniques. The I-EDFT is sensitive to noise and can fail to converge to a solution. This, along with the frequency resolution, can impact the ability of the G-SWMU algorithm to identify and separate potentially closely spaced oscillation components, resulting in unreliable phasors estimates under such conditions. Note that frequency resolution is defined as the distance between adjacent frequencies evaluated by the I-EDFT. A finer resolution therefore corresponds to a smaller frequency interval. For example a resolution of 3.125 Hz is finer than 6.25 Hz, meaning that more frequency points are evaluated. A finer resolution thus increases the ability to separate components that are at least 3.125Hz apart.

Table 4.1 shows the ability of the G-SWMU algorithm to separate sub/super-synchronous oscillations for different combinations of resolution and noise after the signal is filtered by the WSCTF. With a coarse resolution of 6.25 Hz there is not enough separation of the components of interest even with low noise levels. A finer resolution of 3.125Hz provides improved detection capability.

Table 4.1: Impact of resolution and noise on G-SWMU algorithm performance

Resolution	SNR (dB)	All modes detected
$f_s/M = 6.25$ Hz	40	N
$f_s/M = 3.125$ Hz	40	Y
$f_s/M = 3.125$ Hz	25	Y
$f_s/M = 3.125$ Hz	20	Y
$f_s/M = 3.125$ Hz	15	N

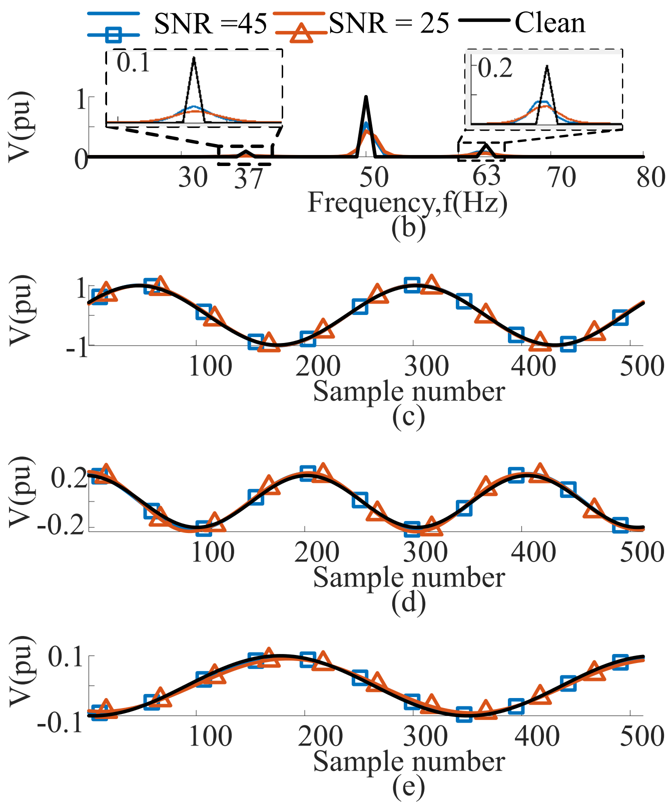

Figure 4.14: Performance of the I-EDFT-EWT with noise

However, noise levels are then increased. It is evident that even with additional filtering, increasing the noise level limits the performance of the multi-frequency phasor estimation module in terms of separating closely spaced oscillation components. An SNR above 20dB is recommended to separate closely spaced sideband oscillations, e.g. at frequencies within nominal +/- 15Hz, while higher noise levels can be tolerated for more widely spaced oscillation frequencies. The proposed multi-frequency phasor estimation algorithm, which incorporates the EWT, does not require the I-EDFT to converge to the exact solution as shown in Figure 4.14, making the G-SWMU algorithm more practical for phasor estimation in IBR dominated power systems compared to relying solely on the I-EDFT or conventional phasor estimates.

4.3.5 Windowing and Group Delay

The G-SWMU algorithm has been implemented in the MATLAB/Simulink environment. The SWT and the WSCTF are applied to a 2-cycle window with 1.5 cycle overlap and symmetric boundary padding to remove window effects. An example of this is shown in Figure 4.15 for a phase jump without noise to highlight the window effects. The output of this step is stored in a 2-cycle buffer and a 2-cycle I-EDFT-EWT is applied to decompose the signal into its constituent IMFs. A 2-cycle Hilbert filter is then used to extract the phasor quantities. The algorithmic group delay, of 4.5 cycles, is the sum of the delay introduced by each step: a 1.5 cycle delay for the transient detection, a 2-cycle delay for the I-EDFT-EWT and a 1 cycle delay (half the filter order) for the phasor extraction.

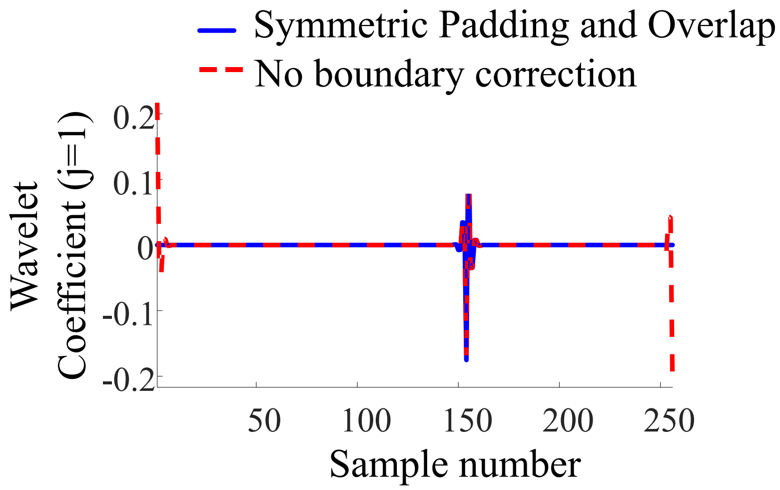

Figure 4.15: Window effects of the WSCTF

4.4 Evaluation of the G-SWMU Algorithm

4.4.1 Performance Metrics

To assess the performance of the G-SWMU algorithm, a goodness of fit (GoF) metric described in [77] was applied to estimate how well the extracted features represent the original waveform. The goodness of fit is calculated as:

$$\text{GoF} = 20\log\left(\frac{|X_n|}{\sqrt{\frac{1}{(N-m_p)}\sum_{n=1}^{N}(u_n - v_n)^2}}\right) \tag{4.26}$$

where, $|X_n|$ is the signal amplitude. This metric is based on information theory and weights the error between the actual signal, u_n, and the reconstructed signal, v_n, within the observation window of N samples, by the number of outputs, m_p, used to represent the information. It therefore gives an indication of how accurately and efficiently the processed outputs represent the input synchro-waveforms. For the proposed G-SWMU algorithm, m_p includes the amplitudes, frequencies and phases of each detected phasor and the number of retained coefficients of the WSCTF transient output.

An approximate reconstruction of the signal can be obtained from the G-SWMU outputs. Transients are reconstructed via the inverse SWT of the retained WSCTF coefficients of the G-SWMU outputs. The oscillatory portion of the input signal is estimated via the sum of each detected sinusoidal component, reconstructed via the G-SWMU phasor estimations. The overall G-SWMU reconstruction is therefore the sum of the transient and oscillatory reconstructions. The phasor reporting rate is either 100 or 120 frames per second for 50 Hz or 60 H signals, respectively. The reconstruction of the original signal assumes that the phasor values are constant at the last reported value for time instants in between reporting instants. Based on real-world testing, a GoF of greater than 20dB is indicative of a useful signal representation [154]. This metric is used to benchmark the performance of the proposed algorithm against standard compliant PMU [42] and emerging sync-wave processing algorithms.

The GoF metric is suitable for assessing the performance of measurement algorithms, regardless of the information in the input signal or assumptions in the proposed model.

This means it is suitable for assessing the ability to measure transients and non-sinusoidal distortions, unlike the phasor based total vector error (TVE) defined in the IEEE/IEC 60255-118-1 standard [38]. To assess the phasor performance of the proposed G-SWMU algorithm and compare it to conventional PMUs, the TVE metric is also applied.

4.4.2 Case Study: Transient Detection and Representation

This section presents case studies to evaluate the performance of the G-SWMU algorithm using both simulated and actual event waveforms. A synthetic test signal consisting of an angle jump (of $\pi/5$ at 0.5s), sampled at 12.8 kHz, was input to the G-SWMU algorithm to evaluate its performance for a broadband transient condition. As shown in Figure 4.16, the algorithm correctly detects the transient, which occurs at 0.5s.

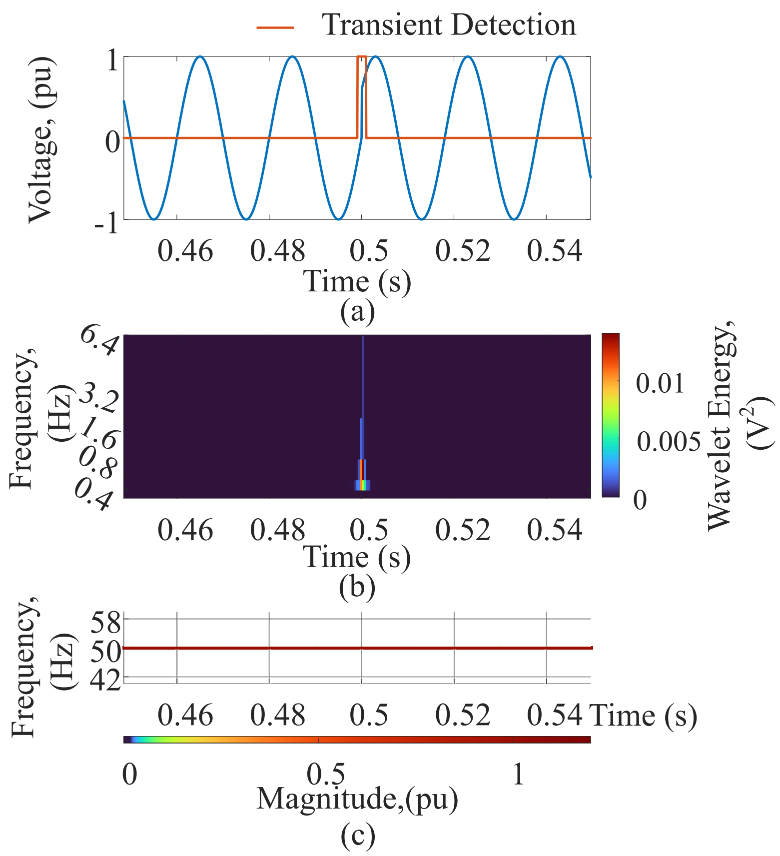

Figure 4.16: G-SWMU performance for a phase jump

Figure 4.17 illustrates the reconstruction and estimated GoF for the phase jump. The G-SWMU output partially reconstructs the phase jump from the retained WSCTF coefficients. It should be noted that a measurement error is introduced due to the G-SWMU phasor module as it gradually tracks the step change in the phase angle. However, the GoF is still within the acceptable band. The transient detection output and the GoF estimate can be used as a warning flag to indicate that the phasor estimate may be unreliable due to the presence of a transient within the processing window, which also has the potential to be used as an enhanced mechanism for possibly triggering DFR capabilities.

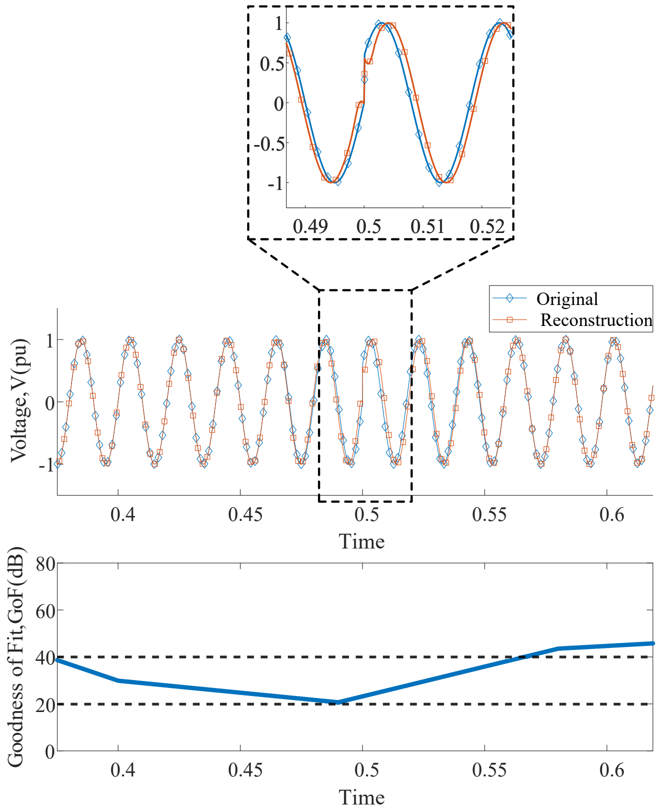

Figure 4.17: Approximate reconstruction and GoF for phase jump

To further assess the adaptability of the G-SWMU algorithm for a variety of possible system conditions, real-world recorded waveforms from different event types available via [108] are input to the algorithm. Figure 4.18 illustrates the G-SWMU outputs for the distorted 60 Hz voltage waveform of a lightning fault (available as event 6 in [108]).

The WSCTF successfully detects the observation window containing the transient distortions. It should be noted that Figure 4.18 illustrates the time corrected outputs that compensate for the group delay of the G-SWMU algorithm. The impact of group delay will be discussed in Section 4.5. The retained wavelet coefficients, visualised as a time-frequency spectrum in Figure 4.19, results in a sparse set of coefficients that can be further encoded and transmitted. The G-SWMU outputs can therefore be transmitted to a centralised location, or across a wide area and either directly utilised by an application or partially reconstructed.

Similarly, waveforms from different historical events are processed in this case study, including events of vegetation encroachment and equipment failure. Table 4.2 illustrate that the G-SWMU algorithm can give a satisfactory performance under a wide range of real-world conditions, as evidenced by the high GoF values. Under severe distortions, the multi-frequency phasor output is not applicable and the main output of G-SWMU algorithm is the wavelet coefficient matrix. This is discussed in Appendix B.3.

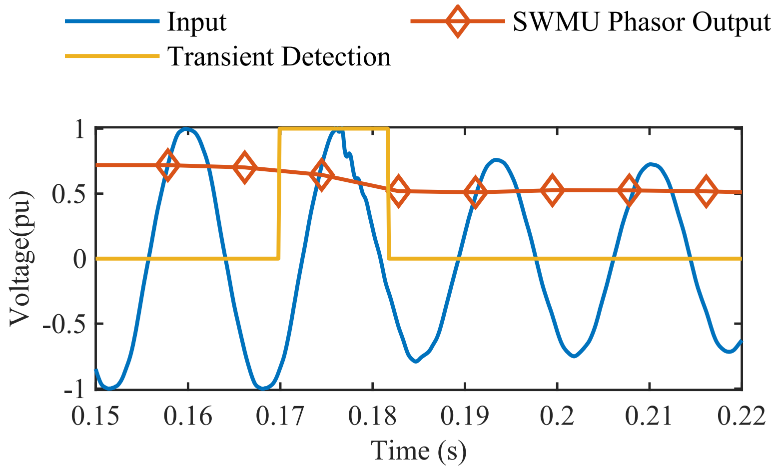

Figure 4.18: G-SWMU phasor and transient detection output for Event 6

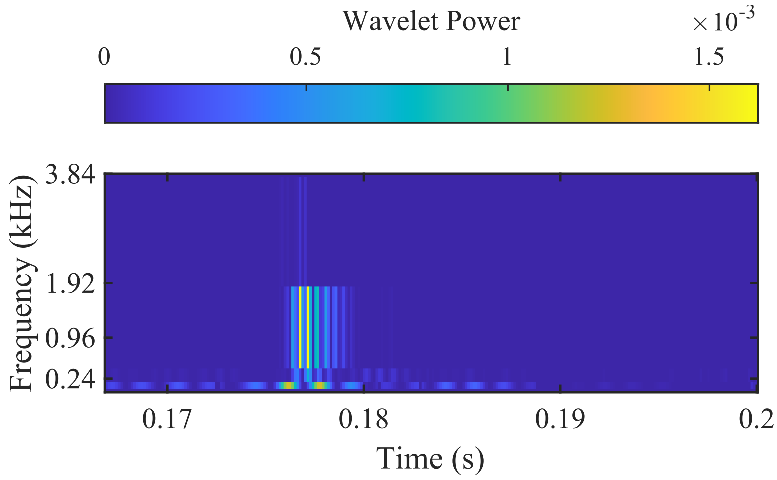

Figure 4.19: G-SWMU transient wavelet spectrum for Event 6

Table 4.2: Performance of the G-SWMU algorithm for different transient events

Input	**Event Description**	**G-SWMU reconstruction GoF (dB)**
Phase Jump	Simulated phase jump	21.7
Event 6	GESL Lightning Fault	31.6
Event 165	GESL Vegetation Encroachment	33.4
Event 187	GESL Equipment Failure	41.3

The WSCTF output extracts features relevant to transient conditions, which can be used to enable decision support applications including event detection and classification. An application utilising wavelet spectrums and pattern recognition to discriminate between different event types will be investigated in Chapter 5.

4.4.3 Case Study: Multi-Frequency Phasor Measurement

A test signal with sideband oscillation components with frequencies, f_r, magnitudes, x_r, and an initial phases, θ_r, is input to the algorithm. The time-frequency plots in Figure 4.20 highlight the adaptability of the G-SWMU algorithm to multiple oscillation components. At the onset of the oscillation at 0.2s, a small discontinuity is also detected, further highlighting the event detection capabilities of the G-SWMU algorithm for different event types. Figure 4.20 demonstrates the ability of the I-EDFT-EWT to detect, separate and accurately measure closely spaced frequencies within typical PMU processing windows and within M-class accuracy standards [38] as shown in Table 4.3. A GoF (>40dB) is obtained by the G-SWMU algorithm for this test case.

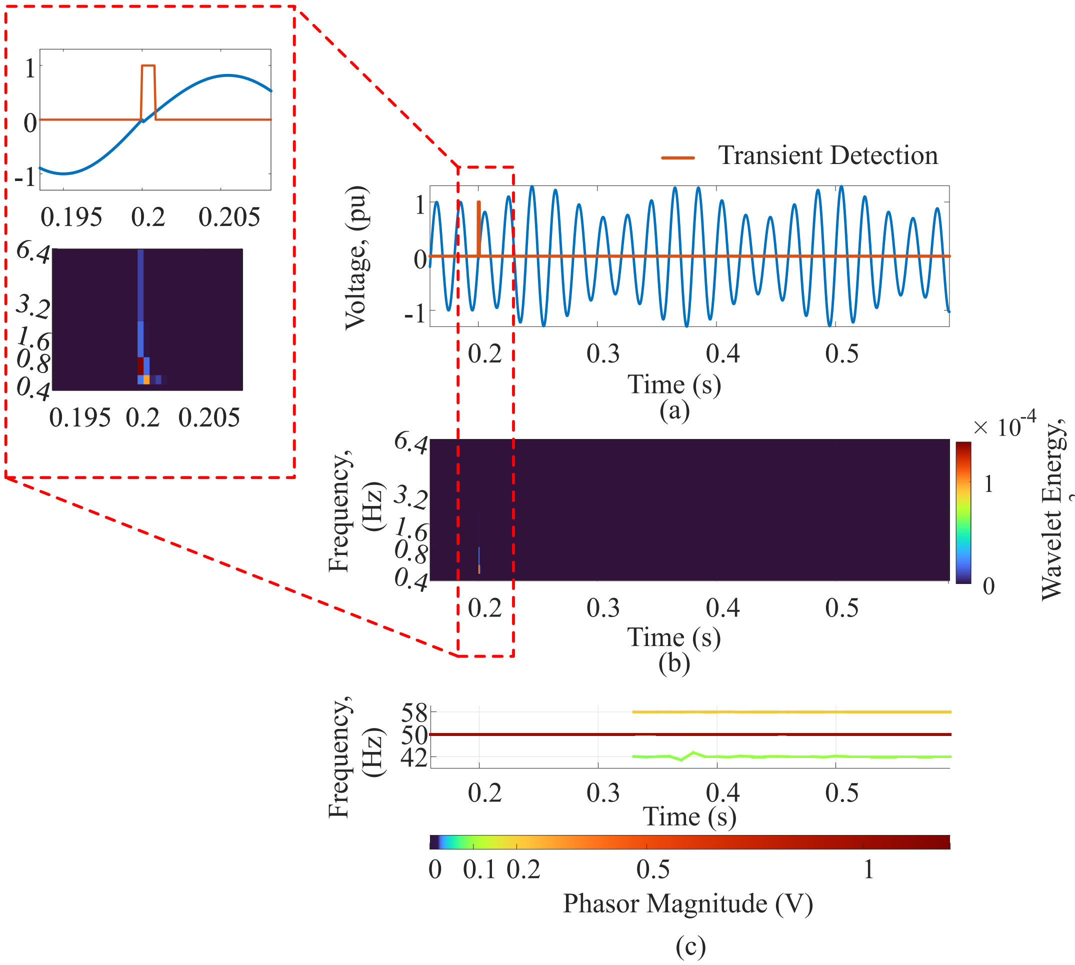

Figure 4.20: SWMU performance for inter-harmonic SSO

Table 4.3: Steady-state multi-phasor performance of the G-SWMU algorithm

Metric {IEE/IEC 60255-118-1 limit}	**Fundamental** ($f_r = 50Hz$,$x_r =$ 1pu, $\theta_r = -\pi/2$)	**Super-Synchronous** ($f_r = 58Hz$, $x_r = 0.2$pu, $\theta_r = 0$)	**Sub-synchronous** ($f_r = 42Hz$, $x_r = 0.1$pu, $\theta_r = 0$)
TVE, (%) {1%}	0.0145	0.0234	0.04
FE, (Hz) {0.005 Hz}	$9{\times}10^{-4}$	$9.285{\times}10^{-4}$	0.0035

4.4.4 Case Study: Comparison to Benchmark Algorithms

The performance of the proposed G-SWMU algorithm is benchmarked against the standard compliant PMU algorithm of [42] for all test cases and where applicable emerging transient and phasor based synchro-waveform processing techniques. A brief overview of the signal processing techniques utilised by these methods are given in Appendix A.

Transient Performance

Based on [80], a simplified functional basis approach (introduced in Section 2.2.4) is replicated using a dictionary of normal conditions, phase jumps and amplitude steps, defined using a range of step sizes and time of occurrences. Matching pursuit based optimisation is then performed to find the optimal dictionary parameters that describe the input signal. This method is referred to as the matching pursuit dictionary (MP-Dict) approach.

Table 4.4 compares the reconstruction performances for a simulated phase jump and the Event 6 waveform as described previously in Section 4.4.2. As highlighted previously, a higher GoF represents an improved measurement and a threshold of 20 dB is considered as a baseline threshold [154]. The proposed G-SWMU achieves GoF values of 21.7 dB for the phase-jump test and 31.6 dB for Event 6, both exceeding the 20 dB level generally regarded as a good fit. The PMU-based P-class and M-class methods fall below this threshold for both cases. Although the MP-Dict method gives the highest

GoF for the phase-jump test, this is expected because the dictionary includes a phase jump component. This result therefore corresponds to a matched-dictionary condition. By contrast, G-SWMU does not rely on an event-specific atom while still maintaining good reconstruction accuracy. The phase jump is also gradually tracked as a step change (with some delay) by the phasor output of G-SWMU and the PMU algorithms. Therefore, a dictionary element specifically representing a phase jump provides limited additional generality.

Although the MP-Dict approaches acceptable performance for Event 6 (21.2 dB), the higher GoF achieved by the G-SWMU (31.6 dB) shows its superior performance when the disturbance characteristics are generally unknown and may not be represented exactly by a predefined dictionary. Approximate reconstructions of the event waveform based on the different algorithms, as illustrated in Figure 4.21, further highlight the superior performance of the G-SWMU. In summary, the proposed SWMU algorithm offers a better representation of the input compared to conventional PMUs and existing synchro-waveform processing methods. Furthermore, the WSCTF within the proposed G-SWMU algorithm does not require a pre-defined dictionary, instead using multi-scale properties of wavelet transforms, thus offering better generalisation to different distortions, making it more suitable and realistic for practical applications.

Table 4.4: Transient Signal Goodness-of-fit Comparison. Values marked with † exceed the 20 dB acceptable-fit threshold.

Test Signal	**G-SWMU**	**PMU**		**MP-Dict.**
		P-class	**M-class**	
Phase Jump	21.7† dB	8.7 dB	8.8 dB	45.4† dB
Event 6	31.6† dB	8.16 dB	18.8 dB	21.1† dB

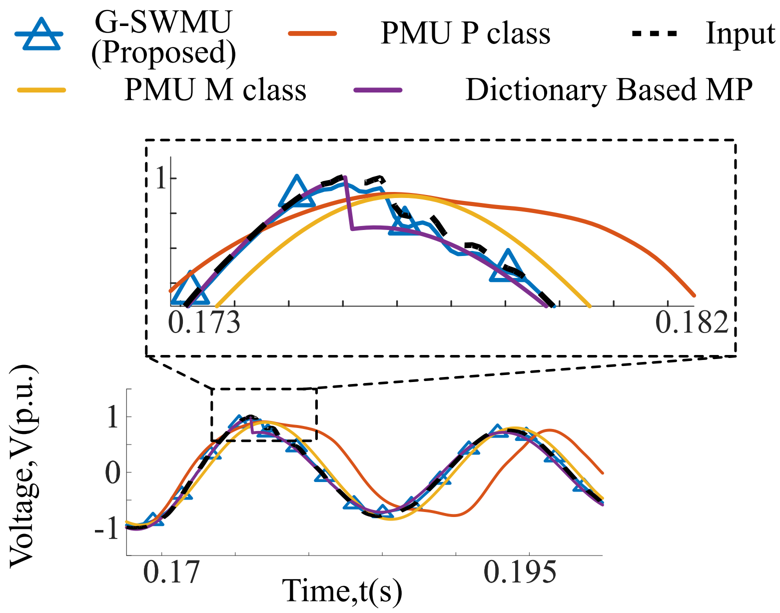

Figure 4.21: Event 6 transient reconstruction

Phasor Estimation Performance

To benchmark the phasor estimation performance, the proposed method is compared to an interpolated DFT (Ip-DFT) phasor extraction method [85], the traditional DFT based EWT used in [83, 147] and the Matrix pencil modal decomposition method [120]. Case 2 of an open source dataset available in [102] is used. This case is derived from a simulation of the Hami (China) power grid and consists of a simulated SSO components sampled at 10 kHz. Tables 4.5-4.8 indicates that the oscillations in standard PMU phasors fail to give a good representation of the underlying dynamics of the waveforms. The DFT-based EWT computed using a similar size window as the proposed algorithm has lower resolution (12.5 kHz). In this instance even though the IMF frequencies (50 Hz, $\sim$ 25 Hz, $\sim$ 75 Hz) are close to points evaluated by the DFT, there is still a level of leakage into surrounding frequency bins leading to mode mixing (similar to Figure 4.9), resulting in oscillations in the phasor output of this method. The Ip-DFT and DFT-based EWT methods can give accurate results but require longer observation windows, i.e. 2 s of PMU data, and 20 cycles respectively. The proposed method achieves accurate results within the first few observation windows, allowing for earlier oscillation mode identification and potentially enabling more prompt mitigations.

Table 4.5: Comparison of SSO Phasor Estimation: Fundamental Component

Method	Frequency, (Hz)	Magnitude(pu)	Initial Phase, (rad)
G-SWMU (4.5 cycle)	49.993	0.0696	-1.360
PMU (M class)	Osc	Osc	Osc
PMU (P class)	Osc	Osc	Osc
DFT-EWT (4 cycle)	Osc	Osc	Osc
DFT-EWT (20 cycle)	49.998	0.0698	-1.376
Ip-DFT (2s PMU data)	50.000	0.07	-1.377
Matrix Pencil (2s Waveform)	49.999	0.07	-1.376

Osc: indicates oscillation in fundamental phasor outputs

Table 4.6: Comparison of SSO Phasor Estimation: Super-synchronous Component

Method	**Frequency, (Hz)**	**Magnitude(pu)**	**Initial Phase, (rad)**
G-SWMU (4.5 cycle)	75.445	0.1540	1.280
PMU (M class)	-	-	-
PMU (P class)	-	-	-
DFT-EWT (4 cycle)	-	-	-
DFT-EWT (20 cycle)	75.425	0.1548	1.445
Ip-DFT (2s PMU data)	75.425	0.1561	1.210
Matrix Pencil (2s Waveform)	75.424	0.1559	1.371

-: indicates component not detected

Table 4.7: Comparison of SSO Phasor Estimation: Sub-synchronous Component

Method	**Frequency, (Hz)**	**Magnitude(pu)**	**Initial Phase, (rad)**
G-SWMU (4.5 cycle)	24.542	0.0875	1.340
PMU (M class)	-	-	-
PMU (P class)	-	-	-
DFT-EWT (4 cycle)	-	-	-
DFT-EWT (20 cycle)	24.915	0.0864	1.068
Ip-DFT (2s PMU data)	24.575	0.0855	1.530
Matrix Pencil (2s Waveform)	24.576	0.0849	1.379

-: indicates component not detected

Table 4.8: Comparison of methods, GoF (dB)

G-SWMU	PMU		DFT-EWT		IpDFT	Matrix Pencil
(4.5 cycle)	M class	P class	(4-cycle)	(20 cycle)	(2 s PMU data)	(2 s waveform)
34.23	14.37	11.68	10.57	24.84	29.24	24.05

4.4.5 Case Study: SSO Monitoring Applications

SSO Event in China's Grid

To demonstrate the performance of the G-SWMU algorithm for real-world events, a current waveform recorded during an actual SSO event in China, sampled a 1 kHz and available from [102] is input to the algorithm. Figure 4.22 shows the oscillation waveform, the identified oscillation components and their respective phasors estimates produced by the G-SWMU algorithm. The inter-harmonic frequencies are detected and are consistent with the (2s window) analysis performed in [85]. However, the proposed algorithm is also able to track the evolution of each component across the observation window. It is noted that the amplitude of the sub-synchronous component increased with time, which indicates the system was poorly damped with respect to this mode.

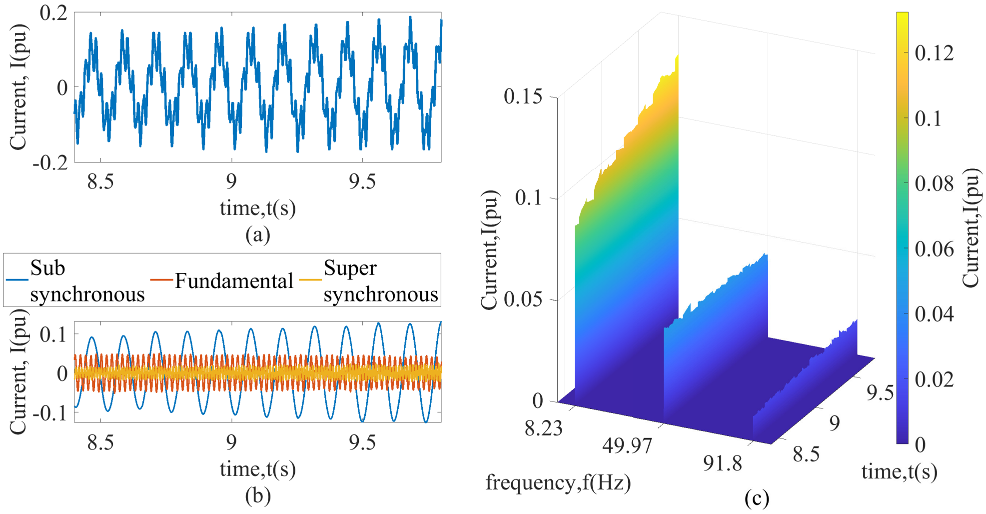

Figure 4.22: G-SWMU output for China SSO event

SSO Event in GB's System

The waveform captured during an SSO event in the GB system and analysed in Section 3.4 is re-analysed using the proposed G-SWMU algorithm to investigate if any sideband, inter-harmonic oscillations were present. As mentioned previously, the SSO frequency, in phasor measurements, was $\sim$ 5-7Hz. Figure 4.23 compares the I-EDFT spectrum (with a resolution of 0.5HZ) to the traditional DFT spectrum for the suspected SSO event, as well as a waveform recorded during a period with no suspected SSO.

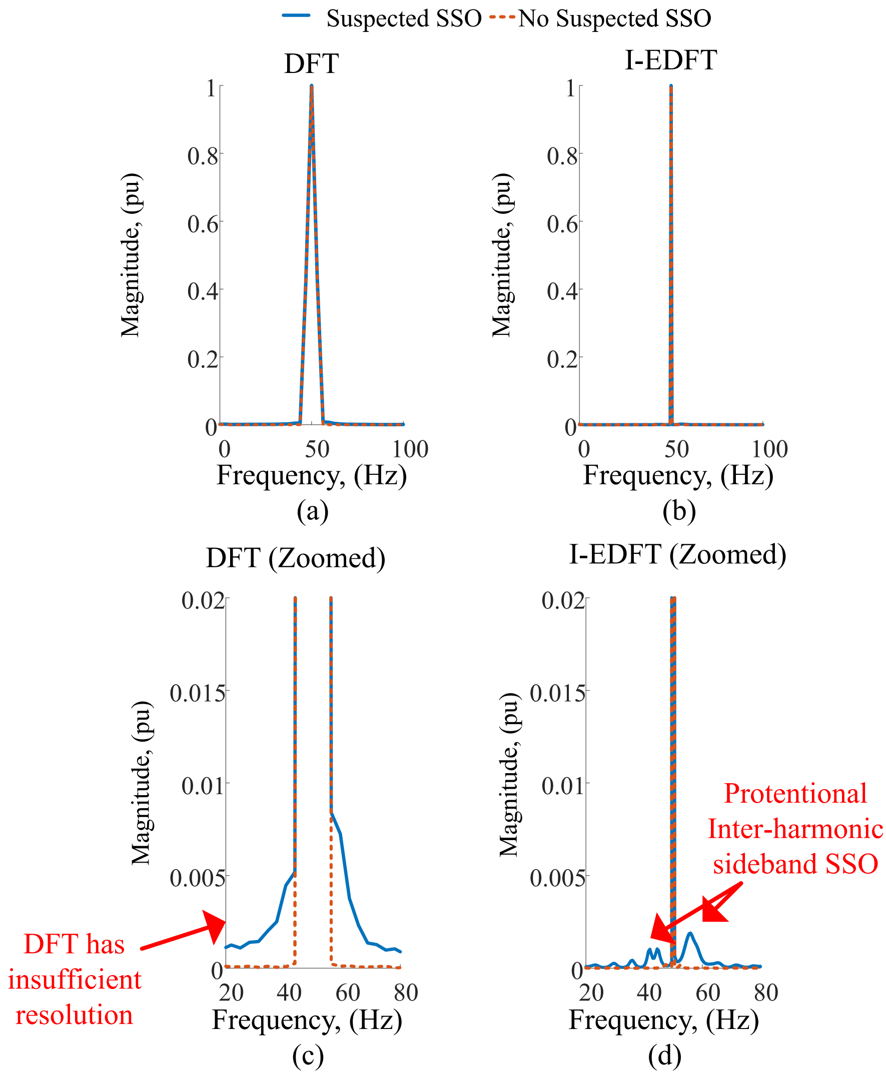

Figure 4.23: Comparison between DFT and I-EDFT for an SSO event in the GB system, with results from a time with no oscillations for reference.

This is done to ensure that any detected peaks are not due to noise or an artifact of the processing methods. It is observed that the increased resolution of the I-EDFT correctly identify potential SSO components. The proposed I-EDFT-EWT is then applied to decompose the input waveform into its oscillatory components, as illustrated in Figure 4.24. The resulting components and their estimated frequencies, produced by the G-SWMU algorithm, are displayed in Figure 4.25. The fundamental frequency was estimated to be ~ 49.23Hz, while the sub/super-synchronous frequencies were estimated to be ~ 42.38Hz and ~ 55.17Hz respectively. The results of this case study provide evidence that inter-harmonic sub/super-synchronous oscillations associated with IBR-driven SSOs are present in the GB system.

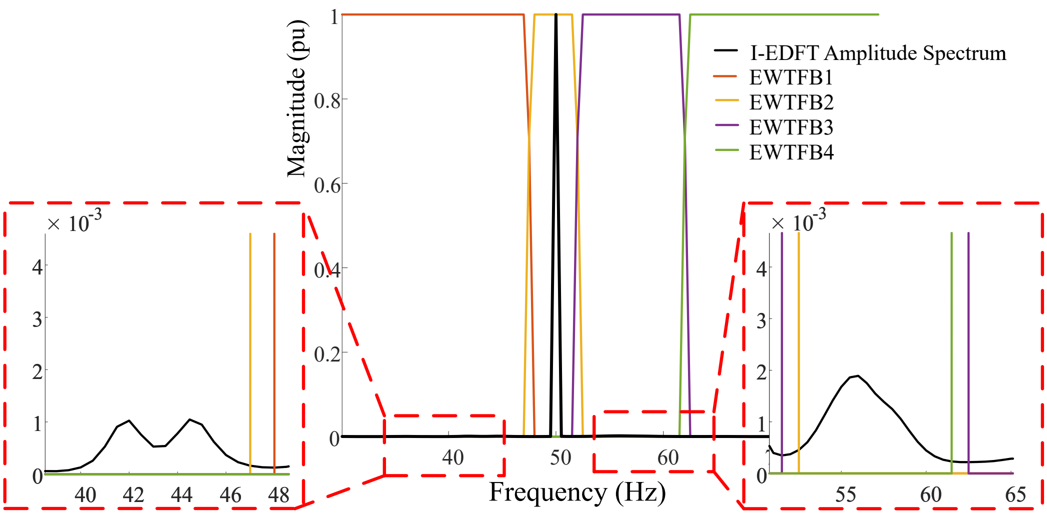

Figure 4.24: I-EDFT-EWT filtering of GB SSO waveform

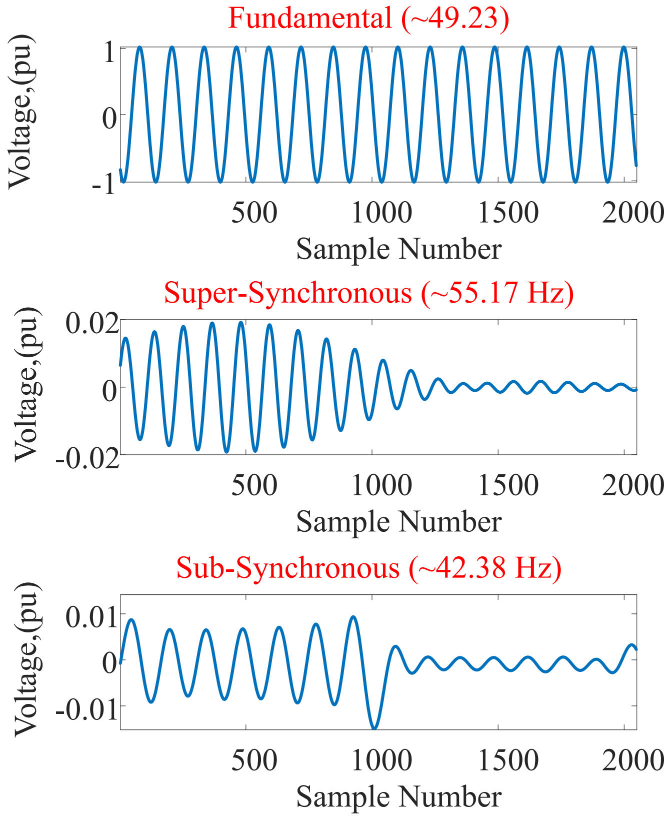

Figure 4.25: Detected inter-harmonic sideband SSO components

Oscillation Source Location Using the G-SWMU Algorithm

A key advantage of the G-SWMU algorithm is that processed outputs can be communicated to a central application, thus enabling wide-area monitoring. A synchro-waveform based oscillation source localisation (OSL) algorithm, utilising the G-SWMU algorithm outputs, is demonstrated in this section. A test network, illustrated in Figure 4.26, was developed based on a portion of the GB network with a high penetration of IBRs (windfarms). The network and scenarios modelled were created in association with industry partners and are representative of real-world scenarios [155].

The IBRs were modelled using a grid following control structure with a synchronous reference frame based PLL, inner current control and AC voltage control. An equivalent voltage source was modelled to represent the rest of the AC network. The PLL bandwidth of Windfarm A was increased, thus making it more sensitive to changes in the gird reference voltage but also, reducing the phase margin, thus making the IBR less stable. A transmission line near the IBR was taken out of service to simulate an IBR driven oscillation stemming from a contingency and a mistuned IBR. More details of the IBR model and the stability analysis can be found in Appendix C.

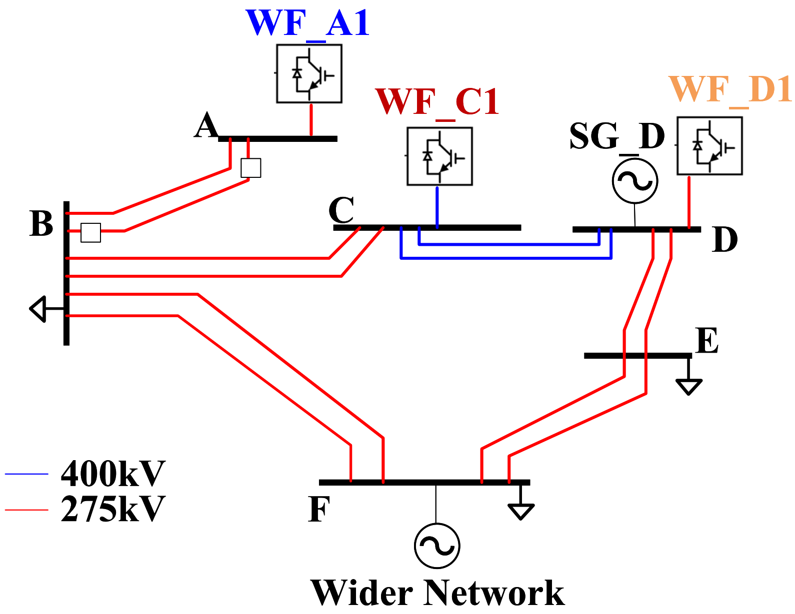

Figure 4.26: Test network for the OSL case study

The test case was simulated in the real time digital simulator (RTDS) and the voltage and current waveforms from the PCC at each windfarm were input to the proposed G-SWMU algorithm and a PMU algorithm. The reference direction for the current measurement is defined as flowing into a system element (windfarms) to be consistent with [156]. The synchro-waveform based OSL application utilises the multi-frequency phasor outputs of the G-SWMU application to calculate the oscillation powers at the detected oscillation frequencies. The oscillation power based criteria with negative power at the oscillation frequency representing a source of oscillation and a positive power representing a sink of the oscillation mode, presented in [156], is utilised in this case study.

The oscillating, fundamental phasor outputs of the PMUs are input to the dissipating energy flow (DEF) method [56]. The DEF method is based on the relationship between the active power of the generator (or system element) and the frequency (i.e.

rate of change of speed), as well was the relation between reactive power and the electromagnetic field energy stored or released, as reflected in the bus voltage. The DEF method calculates a cumulative quantity that is related to the dissipation of the oscillatory energy. The equation of the DEF can be found in Appendix C. It should be noted that with the assumed current convention into the windfarm, a positive DEF means that energy flows from the system into the windfarm, while a negative DEF means that energy flows into the system from the windfarm. The sources of oscillations are the system elements that produce dissipating energy. Therefore, with this current convention, a negative DEF is indicative of the oscillation source, while a positive DEF is indicative of an oscillation sink. This convention is different from that commonly adopted in the literature, but is adopted to maintain consistency when comparing the G-SWMU and PMU-based OSL methods.

Figures 4.27 and 4.28 illustrate the G-SWMU and PMU-based OSL case study results respectively. The G-SWMU-based method highlights sub and super-synchronous components and the oscillation power flows point to Windfarm A as a possible source. In contrast, the PMU method identifies Windfarm D as a possible source and identifies windfarm A as a possible sink. It is possible that the mode-mixing of the PMU measurement and/or the assumption of electromechanical dynamics in the definition of the DEF can account for this inconsistency [157]. To test the outputs of the OSL algorithms, the suspected source produced by each OSL algorithm is disconnected. Figure 4.29 illustrates that disconnecting windfarm A, identified by the G-SWMU-based OSL utilising the proposed algorithm outputs, removes the oscillations from the system as observed via the bus voltage as bus F. In contrast, disconnecting windfarm D does not remove the oscillations. This case study therefore demonstrates the advantages of the G-SWMU over conventional PMUs in enabling security-critical applications in IBR dominated networks.

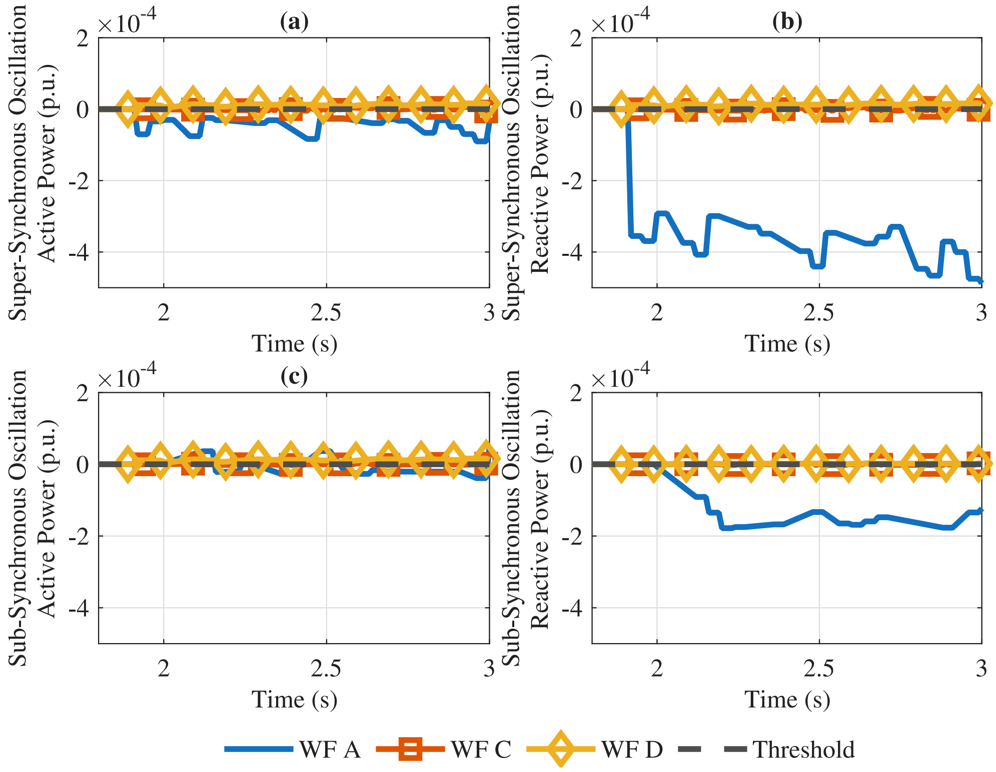

Figure 4.27: SWMU based OSL results

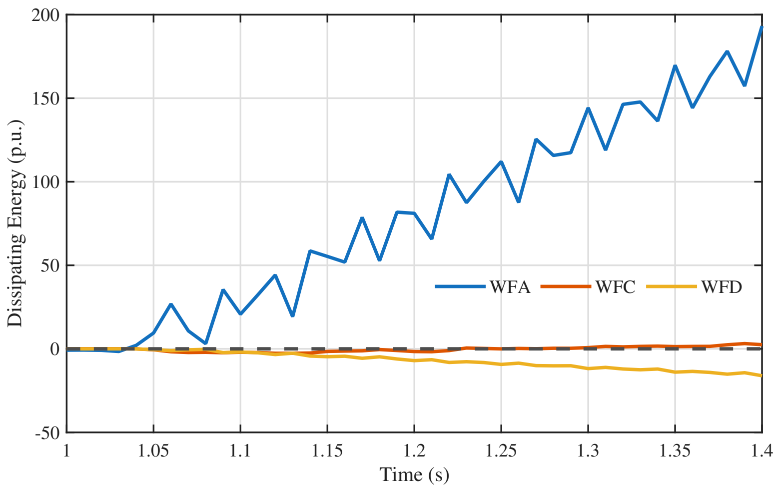

Figure 4.28: PMU based OSL results

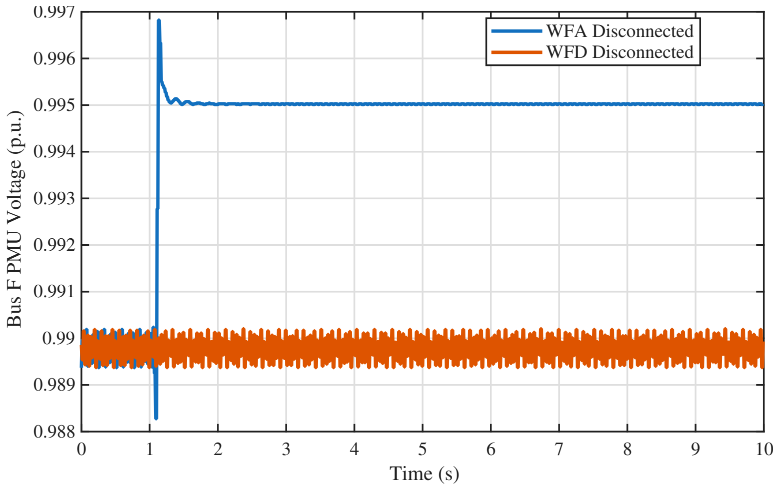

Figure 4.29: Impact of disconnecting potential oscillation sources identified by SWMU and PMU bsed OSL

4.5 Practical Considerations for Real-time Deployment

4.5.1 Computational Complexity

The computational cost of the SWT utilised in the WSCTF is proportional to the window size $\mathcal{O}((N \cdot 2^J)$ [158], while the main computational burden, due to the I-EDFT, is dependent on the number of frequency points (ω_M) evaluated, O(M^2) [148]. A three-phase signal with 50 +/- 30Hz sideband oscillations is input to the algorithm and simulations are performed using the Simulink Desktop Real Time kernel [159] on a computer with 32GB ram and an Intel Core i7, 3.10GHz CPU. Table 4.9 shows the execution times of the G-SWMU algorithm for a sampling rate of 6.4kHz, a 64 point I-EDFT over a 2-cycle window, Ω = 200 Hz, and different resolutions. The WSCTF settings are as described in Section 4.3.

Table 4.9 illustrates the trade-off between computational cost and ability to separate closely spaced oscillations. A target frequency range and/or lower resolution, achieved by specifying Ω or M respectively, improves the execution time. Alternatively, an approximate I-EDFT using the FFT algorithm (O($N \log N$)) [148] can be investigated in future research.

Table 4.9: Computational performance for different settings

Case	**Resolution**	**Execution time**	**All SSO components detected**
1	$f_s/M = 2.67\text{Hz}$	56.77ms	Y
2	$f_s/M = 4\text{Hz}$	24.77ms	Y
3	$f_s/M = 5.33\text{Hz}$	19.48ms	N

4.5.2 Reporting Latency

The IEEE/IEC 60255-118 PMU performance standard defines latency requirements as described in Section 2.1.3. This latency is the delay between the time when an event occurs on the power system to the time that it is reported in data. This is usually estimated as the difference in the UTC time stamp of the measurement and timestamp at which the output communication packet is sent. It can be impacted by estimation method, windowing, processing time, filtering, performance class and reporting rate.

Figure 4.30 illustrates the group delay (no execution delay) of the G-SWMU algorithm for Event 6. Examining the distortion in the waveform at approximately 0.04 seconds shown in Figure 4.30 (a) and comparing the first transient detection output of Figure 4.30 (b) associated with this distortion validates the 1.5 cycle delay of the WSCTF module within the G-SWMU design described in Section 4.3.5. It should be noted that there is a startup portion for the phasor estimation in Figure 4.30 (c). However, examining the beginning of the step change in the phasor estimate with the input waveform shows approximately 4.5 cycles of delay for the G-SWMU phasor output.

Although real-time deployment via a dedicated hardware platform is beyond the scope of this thesis, the sum of the group delay (4.5 cycles) and the real-time Simulink desktop simulation execution is used to estimate the latency of the algorithm. For Case 2 in Table 4.9, the latency is estimated as 0.09s (group delay)+0.0245s (execution delay) = 0.1145s which is within the ($7/50\text{Hz} = 0.14s$) standard limit defined for conventional M-class PMU performance. It should be noted that this value is achieved with minimal optimisation for real-time deployment and without dedicated processing hardware, and it can be significantly improved if algorithmic optimisation and specialised hardware acceleration are employed. The results therefore demonstrate the feasibility of the G-SWMU algorithm for real time deployment. Further refinement and optimisation of the algorithm for hardware deployment will enable practical deployment.

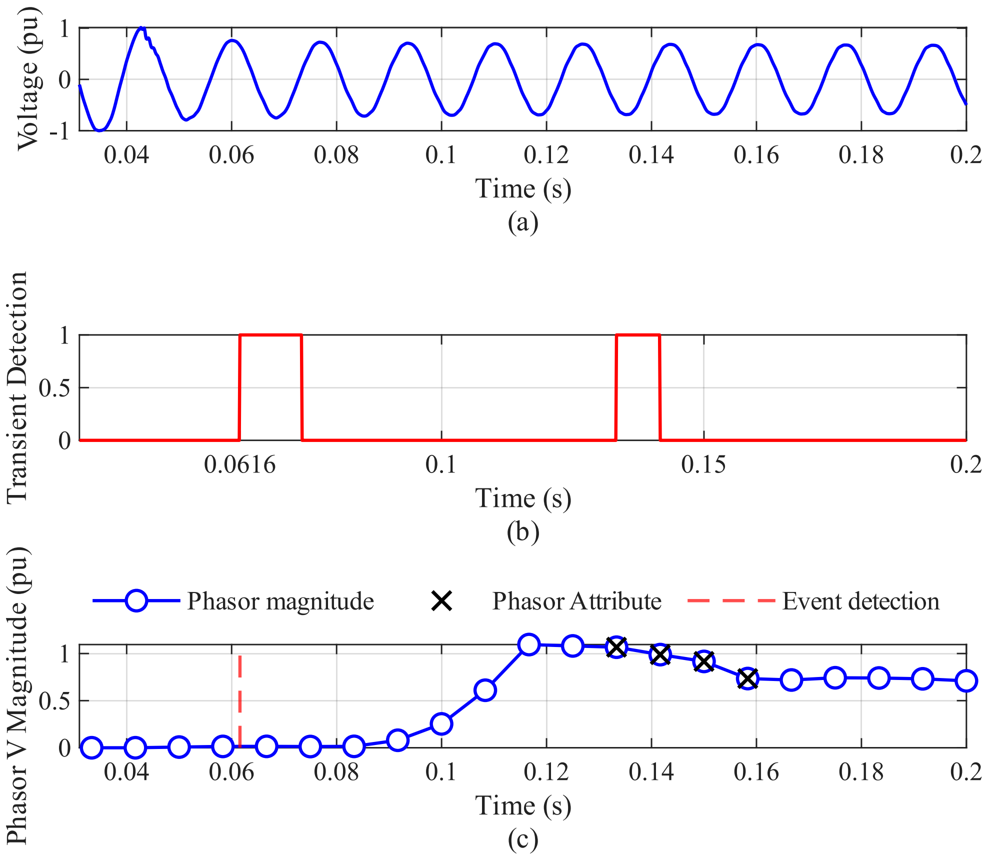

Figure 4.30: Group delay of the G-SWMU algorithm: (a) input, (b) transient detection, (c) phasor output with data attribute: step detected flag status shown.

4.5.3 Communications Protocols

Presently, there is no specific or standard protocol for the proposed G-SWMU algorithm, but it is possible to utilise an existing protocol for the real time publishing of its output. A potential mapping to the IEEEC37.118.2-2024 protocol is presented in Table 4.10 to demonstrate how the G-SWMU algorithm can operate in tandem with both existing and emerging protocol functionalities to support synchro-waveform adoption.

The transient detection output can be used for event detection via the discrete event data frame. It can also be used to set the phasor data attribute: step detected bit of the periodic data frame, thus informing users or applications that the measurement window contains a transient and the phasor estimate may be unreliable. Examining Figure 4.30, the transient detection flag is activated in between phasor reporting instants. The asynchronous event data frame of the IEEE C37.118.2-2024 standard can be utilised here if fast detection is desirable. Additionally, this status can also be retained and communicated with the highlighted phasor reporting instants as a phasor data attribute flag.

The sparse matrix of wavelet coefficients W_{tr}, associated with the transient distortions in the waveform, can be encoded and communicated via the analogue field in the periodic data frame. Established encoding techniques include the compressed sparse row [160], which retains non-zero elements and their positions can be utilised. Alternatively, combining the proposed method with emerging synchro-waveform compression techniques like the embedded zero-trees of wavelet transforms used in [69] or the variable length delta encoding compression algorithm of [86] can also be considered. Further derived transient features for a target application, e.g. wavelet energy for protection, can also be sent as an analogue signal within the standard protocol.

Table 4.10: Mapping G-SWMU algorithm outputs to IEEEC37.118.2-2024 protocol

G-SWMU Output	**Frame type**	**Field**	**Comments**
Transient Detect Flag	Discrete event data frame	Digital	Event detection
	Periodic data frame	Data Attribute Phasor (Step detected)	Transient in measurement window
W_{tr}	Periodic data frame	Analogue	Sparse matrix encoding
Multi-frequency Phasors	Periodic data frame	Phasor	Increased number of phasors

Multi-phasor outputs can be communicated via the periodic data frame. The number of communicated phasors depends on the number of oscillatory components detected above a certain noise threshold, as discussed in 4.3.3. A limit on the number of phasors can also be considered, as during an event the majority of the input waveform signal energy is composed of the oscillatory components of interest. For example, returning phasors for the 5 highest energy components was found to be adequate for analysing the real-world SSO case studies in this thesis.

The existing and widely adopted IEEE C37.118.2-2024 protocol discussed in this Section is a frame based protocol with a fixed message structure. It is not the most efficient solution for the G-SWMU or other synchro-waveform applications as the data to be transmitted may be different depending on the dynamics present at the input. There are also overheads associated with the message structure itself, thus limiting its scalability. More recently, alternative communication architectures including peer to peer and publish-subscribe architectures have been investigated for their scalability and flexibility in publishing streams of data [161, 162]. Peer-to-peer communication allows devices to exchange measurements directly. Publish-subscribe communication allows different data streams, for example phasors or event-triggered data, to be published as separate streams. These protocols therefore do not rely on a rigid frame based structure. Such architectures including the STTP protocol as discussed in Chapter 2 or the Message Queuing Telemetry Transport (MQTT) protocol may therefore be more suitable for both continuous streaming of synchro-waveforms or the processed and variable outputs (e.g. the transient coefficients) of the G-SWMU algorithm. The application of these protocols can be investigated in future research.

4.5.4 Estimated Streaming Requirements

The proposed G-SWMU algorithm may process the waveforms locally at the measurement points or within substations, allowing for both local and wide-area applications via the communication of only relevant event data when appropriate. During steady states, conventional synchrophasor data is output, while during events (e.g. faults, system oscillation, etc.), processed outputs (as opposed to raw waveforms) can be derived and communicated. Increased bandwidth is reserved, but only utilised when events occur.

This increase in communication and archiving infrastructure associated with wide area G-SWMU processed outputs will however be significantly less than those associated with continuously streaming of full synchro-waveform data.

Based on the mapping described in Section 4.5.3 a theoretical estimation of data frame sizes and streaming requirements can be found using a guidance provided in Annex D of the IEEE C37.118.2-2024 [26]. The bandwidth requirements (BR) are a function of the data frame size, data rate, and communication overheads and can be estimated via:

$$BR = f_r \times (TCP/UDP\_OH + 118\_OH + 118\_PL) \tag{4.27}$$

where f_r is the reporting rate; TCP/UDP_OH is a fixed number (54B and 43B respectively) of bytes added to each data frame by IP protocols; 118_OH is the fixed number of bytes (16B) in each data frame apart from measured values and 118_PL is the variable payload depending on the measurement data that is transmitted. The payload will change depending on the SWMU output and is dependent on the number of phasors, number of digital and analogue quantities and a bytes-per-quantity value, which is specified in the standard depending on data format. For example, assuming a fixed point 16-bit integer format then 4 bytes per phasor (plus 2 bytes per phasor data attribute), and 2 bytes per frequency, RoCoF and analogue measurement are required. In steady-state, three-phase, fundamental phasors are sent. During SSOs such as those highlighted in the case studies of Section 4.4.5, three phasor frequencies (corresponding to the fundamental, sub and super synchronous components) and nine (three-phase for each oscillation component) phasors are sent.

The estimated payload during transient conditions depends on the number of non-zero elements (NNZ) of the sparse wavelet transient matrix that are encoded. As explained in Section 4.2.1, the output of the transient wavelet matrix W_{tr} consists of $(J - l + 1) \times N$ total elements, where J is the decomposition level, l is the correlation level, and N is the number of samples in the observation window. For the analysis of the real-world event 6 in Section 4.4.4, W_{tr} consisted of $[4 \times 256]$ entries and 61 non-zero elements for transmission. If the synchro-waveform was used and continuously streamed, this would require streaming 256 samples.

In this research, the widely adopted compressed sparse row format [160], is investigated to encode the sparse transient feature matrix via three arrays. The first two arrays consist of the 61 non-zero values and 61 column indices sorted by their respective rows, resulting in 61 NNZ indices. The third array contains row pointers, at which the entries in the previous two arrays change rows in the original sparse matrix. For example, the first element of the row pointer array will be the starting NNZ index and the next value will be the NNZ index between 1 and 61, at which the encoded non-zero value and corresponding column index belong to another row. Row pointers therefore give an indication of the number of non-zero values in each row. This means that the row indices do not need to be explicitly sent. In this way, the number of elements in the third array will be the number of rows + 1. Based on this, the variable payload of the W_{tr} output is estimated as

$$\begin{aligned} W_{tr}\,118\_PL = {} & (\text{NNZ values} \times \text{bytes per measurement}) \\ & + (\text{NNZ columns} \times \text{bytes per measurement}) \\ & + ((\text{number of rows} + 1) \times \text{bytes per measurement}). \end{aligned} \tag{4.28}$$

For the event 6 case study, this result in $(61 \times 2) + ((61 \times 2) + (4 + 1) \times 2) = 254$ B.

Finally, regardless of the G-SWMU output, some overhead to the estimated payload is added for status and time quality indicators. The bandwidth requirements are estimated using (4.27), assuming a UDP overhead, a reporting rate of 50fps (for comparison with existing monitoring solutions [44]) and the variable payload estimates. More details of the calculations are shown in Appendix (B.4). Table 4.11 summarises the estimated payloads of the G-SWMU algorithm for different conditions. Table 4.12 compares the estimated bandwidth requirements (for a single measurement point) for the proposed G-SWMU algorithm, the PMU/WMU solutions described in [44] (VISOR) and continuous streaming of synchro-waveforms.

Table 4.11: Estimated payloads for G-SWMU outputs for different conditions

Condition	**Output**	**Estimated Payload (Bytes)**
Steady-state	Fundamental Phasor Quantities	32
SSO	Multi-Phasor Quantities	88
Transient	W_{tr} Fundamental Phasors Transient Detected	288

Table 4.12: Comparison of bandwidth requirements

Solution	**Estimated Bandwidth (kbps)**
VISOR PMU [44]	34-50 kbps
VISOR WMU (200fps, +'ve Seq.) [44]	125 kbps
Proposed G-SWMU Steady State	32 kpbs
Proposed G-SWMU SSO	50.4 kbps
Proposed G-SWMU Transient (analyses 128 samples per cycle, reported at 50fps only when detected)	134-402 kbps
Three-phase synchro-waveform streamed at 4 kHz [27]	5000 kbps

The above theoretical analysis shows that the proposed G-SWMU algorithm has similar bandwidth requirements as standard PMUs during steady state. In comparison to VISOR's WMU solution, which streams the positive sequence waveform at 200 samples per second, the G-SWMU is able to send multiple oscillation phasors with relatively less ($\sim$ 60% less) bandwidth. VISOR's WMU solution also loses details of the transients in the waveform due to downsampling. The G-SWMU algorithm retains details available at a resolution of several kHz (7.68kHz), addressing the limitations of the PMU and VISOR's WMU, but is able to communicate these features with less bandwidth than continuously streaming the synchro-waveform. The wide estimated bandwidth range of the SWMU transient caters for all three phases being distorted. It should be noted that transient events may not need to be communicated to a central location in real time, with the exception of protection applications, which can have dedicated communications infrastructure. These events can be stored locally, further processed by local applications (e.g. event classification) or buffered and transmitted with a tolerable delay if there are bandwidth restrictions.

It is noted that as of 2018, a 4 Mbps (4000 kbps) bandwidth is utilised by a GB transmission owner for the existing VISOR WAM system [44]. Overall, the G-SWMU algorithm allows for extracting insights from high resolution (several kHZ) synchro-waveform data and enables real-time communications via conventional supporting infrastructure, simultaneously addressing the limitations of PMUs that filter out dynamics and the challenge of continuous synchro-waveform streaming, which has high communication burden.

4.6 Chapter Summary

A generalised synchro-waveform processing algorithm i.e. the G-SWMU algorithm, which utilises correlations across discrete wavelet scales to represent distortions and a novel I-EDFT based EWT for multi-phasor extraction, has been presented in this Chapter. The design of the G-SWMU algorithm is based on extracting the information contained in the input waveform and addresses the reliance on a fundamental sinusoidal reference in the standard synchrophasor definition. The G-SWMU algorithm extracts relevant features from synchro-waveforms, which is capable of more accurately reflecting the underlying dynamics present in the waveforms as compared with standard PMUs and existing synchro-waveform processing algorithms. The I-EDFT-EWT multi-phasor extraction has improved frequency resolution, allowing for improved detection of IBR driven SSO events. The design and performance of the G-SWMU algorithm can be optimised via interpretable settings and design considerations, such as frequency resolutions and noise rejection thresholds.

The performance of the G-SWMU algorithm is benchmarked against conventional PMUs and existing synchro-waveform processing methods. The results demonstrate the versatility of the G-SWMU algorithm to detect and characterise different dynamics present in synchro-waveforms, ranging from non-sinusoidal transients to closely spaced inter-harmonic SSOs. The WSCTF outputs of the G-SWMU were found to detect and accurately represent distortions present in different real-world event waveforms. An SSO monitoring application was demonstrated via case studies with actual measurements, which highlighted sub/super-synchronous oscillation components in the GB system. The G-SWMU algorithm extracts relevant features from different event types (transients, oscillations) without any changes or modifications to the algorithm and with limited prior knowledge of the events.

Practical considerations for the deployment of the proposed algorithm were also discussed. A mapping of G-SWMU algorithm outputs with emerging communications protocols demonstrate its compatibility with such protocols. Theoretical estimates of the bandwidth requirements provide evidence that the G-SWMU outputs greatly reduces the supporting infrastructure requirements compared to continuously streaming synchro-waveforms, while extracting critical information that PMUs and other synchro-waveform processing methods may exclude. The G-SWMU algorithm can therefore be considered a general purpose, adaptable algorithm that can extract insights from synchro-waveforms, while being able to utilise the continuous streaming/storage infrastructure of conventional PMUs. The adaptability and scalability of the G-SWMU can enable improved monitoring of IBR dynamics and, in a broader context, support wider synchro-waveform applications. Datasets curated from increased deployment of G-SWMUs can potentially serve as valuable input to enable AI/ML-based applications (e.g. event classification), thus improving situational awareness. This application will be explored in Chapter 5. Finally, desktop simulations show the feasibility of real-time deployment of the algorithm. Further refinement and optimisation of the G-SWMU algorithm for hardware deployment provides a promising avenue for future deployment.

Chapter 5

G-SWMU based Open-Set Classification of Power System Events

The G-SWMU algorithm, proposed in Chapter 4, accurately represents a wide range of system conditions with reduced requirements on supporting infrastructure. Previously, the G-SWMU algorithm was demonstrated to support improved monitoring of IBR-induced oscillations, however, its wider deployment can be further justified by utilising its adaptability and scalability to enable concurrent applications across different aspects of the power system. Pattern recognition based event classification, utilising the information captured by raw synchro-waveforms and retained by the G-SWMU outputs, is one such application. The identification and mitigation of anomalous events is of particular importance in IBR-dominated power systems that may be more sensitive to such events. However, a key challenge to translating the information contained in synchro-waveforms into accurate event cause identification remains the lack of labelled event waveforms. Limited training data introduces biases in event classification models, leading to inaccurate event identifications that inform incorrect or inefficient mitigation strategies. This Chapter therefore presents a G-SWMU based wavelet scattering open-set nearest neighbours (WS-OSNN) power system event classification model that is compatible with limited training data and capable of detecting unknown class instances to avoid inaccurate results.

The extracted wavelet features of the G-SWMU algorithm are integrated into a deep convolution network (similar to state-of-the-art ML methods) via the wavelet scattering transform (WST). Conventional ML methods learn optimal filter weights as part of their feature extraction process, thus requiring large datasets. In contrast, the feature extraction of the G-SWMU algorithm combined with the WST utilises pre-defined wavelet filters and is therefore more suitable for limited training data. To further enhance the capabilities of the proposed classifier, this research incorporates open set recognition (OSR) which aims to accurately classify known class instances and simultaneously recognise inputs that do not belong to known classes in order to classify them as unknown.

The proposed WS-OSNN, will be trained and evaluated using only real-world data. Noting that historic G-SWMU datasets are not available, the WS-OSNN is firstly developed and demonstrated using an open-sourced database of raw synchro-waveforms. Case studies demonstrating the performance of the WS-OSNN with the processed G-SWMU outputs are then presented. The G-SWMU based WS-OSNN therefore utilises existing limited labelled training datasets while the practicality of OSR addresses the limitations of state-of-the-art power system event classifiers. This allows for informed decision-making to better mitigate known events while aiding in further investigations into unknown events. A framework to identify, group and label anomalous waveforms is also presented. The proposed classification tool will be capable of deriving valuable insights from high resolution synchro-waveform measurements, thus supporting event classification, improving training datasets, and facilitating enhanced situational awareness.

5.1 The Need For Synchro-Waveform Based Power System Event Classification

Synchro-waveforms contain valuable information about the dynamics and transients of the system, which can be used to enable critical situation awareness applications. One such application is event classification, based on learnt patterns present in the voltage and current waveforms. As demonstrated in Chapter 4, synchro-waveforms, as well as the processed outputs of the proposed SWMU algorithm, better capture underlying dynamics (that PMUs filter out) associated with abnormal events. Figure 5.1 compares synchro-waveform and PMU measurements, available from [108], for the faulted phase voltage during two different event categories. The PMU measurements are quite similar, showing a voltage drop. In contrast, the synchro-waveform measurements highlight distortions which can potentially be used as fault signatures for pattern recognition.

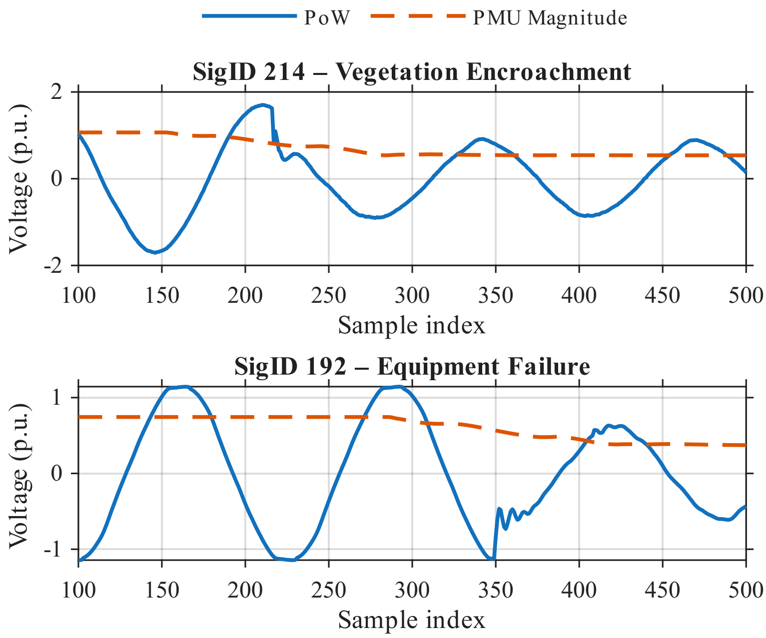

Figure 5.1: Comparison between synchro-waveform and PMU measurements for different event types

Furthermore, ageing infrastructure, severe weather, and complex behaviours of IBRs can increase the occurrence and impact of anomalous events (e.g., faults, equipment failure, etc.). These events can have severe consequences, ranging from increased unplanned outages [163] to widespread damage to life and property, e.g. from wildfires ignited by vegetation encroaching on energised lines [88]. Such occurrences negatively impact consumers, with utilities subject to regulatory penalties. Maintenance interventions are required to perform preventative measures or to isolate faults and restore service in a timely manner. Pairing the event detection and feature extraction capabilities of the proposed G-SWMU algorithm with data analytics can enable accurate identification and classification of anomalous event waveforms. This is critical to informing safe, timely and efficient mitigation strategies, thus improving the system resiliency and meeting operational code requirements.

5.2 Limitations of Existing Synchro-Waveform Based Event Classification Methods

Typically, event waveforms are captured and stored locally by DFRs. Event cause identification relies on domain expertise to manually collate and process the available fault waveforms (along with weather, maintenance records, etc.) to identify signatures, trends and correlations that point to a specific underlying cause. This is a time-consuming and labour-intensive process, requiring the processing of large volumes of data. Automated ML based classifiers have been proposed in the literature, however, a key challenge to deriving actionable insights from synchro-waveform measurements remains the limited availability of labelled datasets containing actual event waveforms. Limited training data can lead to inherent biases in the performance of such classifiers. [132] processes voltage and current waveforms to extract time-frequency spectrograms and inputs these into a convolution neural network (CNN) classifier. The dataset used consisted of real-world event data augmented with simulated motor starts and system faults. Similarly, multi-time-frequency features encompassing short time transients and slower dynamics across the observation window are input to an ML based classifier trained on simulated data and tested on real waveform measurements [106]. However, the events of interest were limited to events that were straightforward to accurately model, such as switching, line faults and generator trips. While high classification accuracies are achieved, physics based modelling cannot realistically simulate certain causes (e.g. vegetation, equipment failure) or fully represent measurement noise and possible variations within the same event cause.

The state-of-the-art GESL open access repository contains approximately 5600 event records (at its inception) with only 50% of PMU and synchro-waveform records labelled. Furthermore, synchro-waveform data accounted for only 8% of its total records [164]. Deep learning methods have provided satisfactory classification performance in domains where large labelled datasets are available [165]. However, their practical deployment towards power system classification can be hindered by limited real-world, labelled data [166]. Although the information retained by synchro-waveforms can potentially improve power system event classification, insufficient labelled PoW datasets can result in training biases, thus methods suitable for limited training datasets are required. A signature matching tool that uses statistical features and support vector machine (SVM) to classify events in the GESL, e.g., transients and lightning strikes, with up to 80% accuracy is presented in [164]. The authors note that improved feature engineering can lead to better results. [105] incorporates a dynamic time warping (DTW) waveform similarity metric and context similarity into a one-nearest neighbour(1-NN) classifier. DTW performs a time-alignment prior to calculating the similarity of two waveforms. This allows for feature extraction and suitable comparison of waveforms with different sampling frequencies, observation windows and event start times. This method utilises waveforms from the GESL and offers enhanced accuracy with limited data.

A key limitation of the aforementioned methods is that the training and testing data are sampled from the same label and feature spaces, therefore, there is an underlying assumption that the ML classifier will only ever encounter known classes. This is referred to as closed-set classification, where the goal is to classify input data as one of the known classes [167]. However, in practice, a power system event classifier can face novel inputs after deployment, which were not seen in training, and thus unknown to the classifier. This can include signatures associated with normal events (e.g. capacitor switching, transformer inrush) that were simply not considered in training, as well as new fault types or behaviours resulting from the increasing penetration of IBRs.

Therefore, it is critical to ensure that events unknown to the trained model are not erroneously classified as known classes. Instead, such events must be explicitly identified as unknown, thereby preventing incorrect decision-making and missed opportunities to identify new phenomena. This can be achieved by open-set classification. Information present in raw-synchro-waveforms or features derived through processing the synchro-waveform using the proposed G-SWMU algorithm presented in Chapter 4, can enable such open-set classification with limited training data, which is discussed in detail in the following sections.

5.3 G-SWMU based Open Set Power System Classification

In this Section, OSR and the WST will first be defined, followed by the design of the proposed WS-OSNN classification model.

5.3.1 Open-Set Recognition (OSR)

OSR Problem Formulation

For various event classes, y, and corresponding d-dimensional feature vectors, x, the goal of ML classification is to obtain a recognition function, $f(x)$, which maps features in x to the corresponding class label in y. The overall feature space, S_o, encompasses all known training examples and corresponding positively labelled feature space labelled by $f(x)$, as well as open space, O. In this context, open space refers to regions of the feature space that is outside the optimal decision support region learnt from known data, where there is no reliable basis for assigning a known class (KC) label. Open space risk is the inherent risk that f will label open space as positive with respect to any of the KCs, resulting in a sample from an unknown class (UC) being misclassified as a KC.

The open space risk, $R_o(f)$ can therefore be defined in terms of the ratio of positively labelled open space to the overall positively labelled feature space as in [168]:

$$R_o(f) = \frac{\int_O f(x)dx}{\int_{S_o} f(x)dx}. \tag{5.1}$$

As can be seen from (5.1), the more open space that is labelled as positive, the greater the open space risk. This is illustrated in Figure 5.2. For closed-set classification (Figure 5.2(a)), S_o is divided by decision boundaries around the known classes. Inputs from an unknown class, represented by '+', are classified as KC 3. In OSR, however, the goal is to balance accurate KC prediction with minimised open space risk, thus enabling the identification of UC instances as illustrated in Figure 5.2(b).

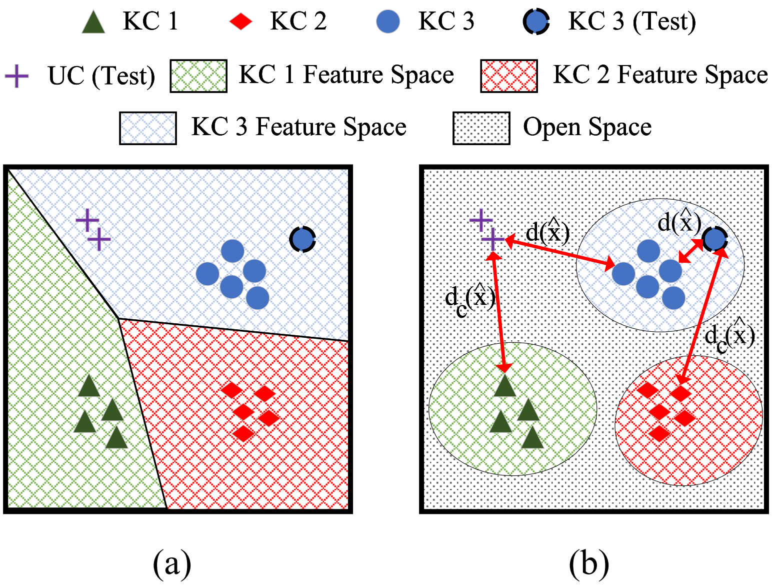

Figure 5.2: Comparison between closed set and open set classification, (a) closed set, (b) open set classification with distance ratios of a known class and an unknown class instance highlighted.

For each known power system event class, let $\hat{X}_{C_I}$ be the training features of the class of interest C_I, and $\hat{X}_K$ be training features of all other KCs denoted by K. The training dataset C_{TR} consists of $C_I \cup K$. Under realistic conditions, new data input to the classifier may contain UCs denoted by U, so the testing dataset, C_{TE}, contains $C_I \cup K \cup U$. OSR is therefore defined as finding f as [168]:

$$f = \arg\min_f \{R_o(f) + \lambda_r R_\epsilon(f(\hat{X}_{C_I} \cup \hat{X}_K))\}, \tag{5.2}$$

where R_ϵ is the risk of closed set misclassification and λ_r is a regularisation constant to prevent overfitting. $\lambda_r R_\epsilon(f(\hat{X}_{C_I} \cup \hat{X}_K)$ is therefore a representation of traditional closed-set classification with λ_r and f dependent on respective ML methods, hyperparameters and training data. It should be noted that (5.2) is a generic OSR objective rather than a closed-form optimisation problem that is solved directly. The nonlinearity, solution procedure, and convergence properties depend on the selected classifier and OSR algorithm. In this research, the implemented classifier approximates this objective through wavelet scattering feature extraction and nearest neighbour decision rules as will be discussed in the following Sections.

As seen in Figure 5.2(b), OSR aims to discriminate between KCs while defining decision boundaries (using only known data) that limit open space risk. This allows UCs that are different from KCs in the learnt feature space to be identified without prior knowledge of the UCs.

OSR Methods

A range of OSR methods have been proposed and reviewed in [167]. A typical OSR approach is based on the fact that UCs will be different from the KC instances. This means that extracted features from UC instances will lie in the tails (i.e., they will be outliers) of the distributions of similarly extracted features from KCs. By definition, the tail of distributions contains a small number of instances, making it difficult to reliably model. To address this challenge, specialised tools that estimate the probabilities of rare events can be applied. In this research, the extreme value theory (EVT) is applied. EVT models exceedances over a high threshold using a Generalised Pareto Distribution, (GPD) (based on Pickands-Balkema-de Haan theorem [169, 170]) to infer statistical properties from a limited number of extreme observations. EVT models the tail region of the known class distribution, which can then be used to assess new input data to determine if it has a low probability of belonging to the known class distribution and should therefore be rejected as an unknown class instance [168].

[171, 172] achieve OSR within SVM classifiers via applying EVT to model the tail of the distribution of distances from decision boundaries learnt from the known classes. Such an open set SVM classifier penalises decision scores of new data that move further away from known data to open space. This allows for an OSR threshold based on known data to be determined. A similar concept is applied in OpenMax to recalibrate the class probabilities of deep neural networks in [173]. [174] builds a dictionary corresponding to known classes, then aims to find a sparse representation of input data using this dictionary. EVT is used to model the tail distribution of reconstruction errors to get an OSR threshold.

The open set nearest neighbour (OSNN) algorithm proposed by [175] applies a threshold on the ratio of distances between new data and its nearest neighbour from its closest class and the distance to its nearest neighbour from its second closest class. If the ratio is small, it implies that the new data belongs to the first class, while a large ratio implies it lies in open space. This method remains efficient as the number of KCs increases, but may be sensitive to outliers due to using only two reference samples [167]. This is addressed by [176], which generalises the OSNN to k-OSNN which uses k reference samples and incorporates EVT for modelling the distribution of distance ratios to perform OSR. OSR has been successfully applied in computer vision systems [177], mechanical bearing fault diagnosis [178] and electrical load classification [179]. The novel application of OSR to power system event classification in this research can improve situational awareness and inform improved decision-making.

It should be noted that there are other frameworks that partially address OSR, but have different formulations and goals (see [167]). Anomaly detection may treat all KCs as a single class and detects when new data are different from all KCs. Ignoring discriminative features between KCs may impact the accuracy of such methods to detect anomalies [167]. Out of distribution detection similarly uses statistical deviation from the training data distribution to detect anomalies. Such methods may be used as part of an OSR framework which aims to accurately classify known classes and label anomalies as unknown.

Open Set Nearest Neighbours (OSNN)

Due to the low complexity and scalability to multi-class classification of the k-OSNN algorithm [176], this method is adapted for power system event classification in this PhD research. For feature vectors x_i, corresponding class labels, $y_i \in \mathcal{Y}$, and a target vector $\hat{x}$, k-NN classification finds the k nearest training points, $\mathcal{N}_k(\hat{x})$, using a distance metric such as Euclidean distance [180]. The predicted label, $\hat{y}$, is the class label with the highest occurrence among these points. To facilitate OSR, a distance ratio, $r(\hat{x})$, is defined as [176]:

$$r(\hat{x}) = \frac{d(\hat{x})}{d_c(\hat{x})}, \tag{5.3}$$

where $d(\hat{x})$ represents the average distance between $\hat{x}$ and the set of points in $\mathcal{N}_k(\hat{x})$ and $d_c(\hat{x})$ represents the average distance between $\hat{x}$ and k nearest points that are not in class $\hat{y}$. As illustrated in Figure 5.2, this ratio is small if $\hat{x}$ is close to a known class and is larger if $\hat{x}$ moves into open space away from known classes. If $r(\hat{x})$ is above a specified threshold, then $\hat{x}$ should be classed as unknown.

During the training phase, no knowledge of the unknown classes is available. Therefore, the rejection threshold is determined based on distribution of the distance ratios, $r(x_i) \in R$, of the training data. It is expected that an unknown class instance will have a large distance ratio, $r(\hat{x})$, compared to the majority of the training distance ratios associated with known classes. This means that the proportion of training distance ratios that are greater than $r(\hat{x})$, estimated by $P(R > r(\hat{x}))$, will be small. $r(\hat{x})$ of an unknown class instance is therefore in the tail of the distribution. Based on EVT, it is shown in [176] that $P(R > r(\hat{x}))$ can be approximated by:

$$P(R > r(\hat{x})) = P(R > t) \times \overline{G}_{\tau,\gamma}(r(\hat{x}) - t), \tag{5.4}$$

where $P(R > t)$ is the proportion of samples above a threshold t, chosen so that values of $R > t$ are considered to be in the tail of the distribution and $\overline{G}_{\tau,\gamma}(r(\hat{x}) - t)$ is the conditional probability that R exceeds $r(\hat{x})$ given that it is already above t. This probability is estimated by fitting the generalised Pareto distribution (GPD) to the tail (i.e. values above t) of R. The OSNN class prediction, y^O, becomes:

$$y^O = \begin{cases} \arg\max\limits_{y \in \mathcal{Y}} \sum\limits_{i \in \mathcal{N}_k(\hat{x})} \mathbf{1}\{y_i = y\}, & \text{if } P\big(R \geq r(\hat{x})\big) \geq \alpha, \\ \text{Unknown}, & \text{otherwise}. \end{cases} \tag{5.5}$$

where α is a user specified parameter that determines the sensitivity to UCs. α can be interpreted as the percentage of known class instances that are at risk of being classed as unknown. The choice of α is a tradeoff between closed-set misclassification and failure to detect unknown classes. (5.5) effectively classifies new inputs as the class associated with its nearest neighbours (i.e., traditional kNN classification) when the input does not lie in the tail of the known class distribution, otherwise, it is rejected as unknown. Another key strength of open-set classification is that the training process will simultaneously optimise the known class classification performance, while fitting the tail distribution. It therefore balances closed set accuracy with the ability to reject unknown classes. It should also be noted that (5.5) cannot differentiate between different unknown classes.

5.3.2 Wavelet Scattering Transform (WST)

Event classification and OSR require discriminative features that reduce within-class variability and maximises variability across different classes. To achieve this, the wavelet features produced by the proposed G-SWMU can be further enhanced using the WST. The WST is a deep convolution network consisting of cascading layers of convolution with complex wavelet filters, non-linear modulus operations and average pooling [181]. Wavelets localise transients in the input waveforms, extracting amplitude and phase information across different frequency scales. The modulus of the wavelet coefficients captures the energy of the signal, and removes the impact of phase information that may be sensitive to translations within the same event class (e.g. similar events with different inception angles) [182]. Low pass filtering produces an average representation over the width of the filter, leading to scattering coefficients with local translation invariance.

Cascading layers capture different information structures. The zero$^{\text{th}}$, $S_0x(t)$, first, $S_1x(t,\lambda_1)$, and second, $S_2x(t,\lambda_1,\lambda_2)$, order WST of a time series signal $x(t)$ are defined as:

$$S_0x(t) = x(t) * \phi_J(t), \tag{5.6}$$

$$S_1x(t,\lambda_1) = |x(t) * \psi_{\lambda_1}| * \phi_J(t), \tag{5.7}$$

$$S_2x(t, \lambda_1, \lambda_2) = ||x * \psi_{\lambda_1}| * \psi_{\lambda_2}| * \phi_J(t), \tag{5.8}$$

where $\phi_J(t)$ is a low pass filter with averaging scale of 2^J, ψ is a wavelet filter bank and λ_1, λ_2 are the centre frequencies of the corresponding wavelet filter banks that are specified via the number of wavelets per octave Q [182]. The zero$^{\text{th}}$order scattering represents a local average of the signal. The first order scattering captures local energy at different frequency scales, thus extracting oscillatory and transient structures within the input. It should be noted that the expression $x(t)*\psi_{\lambda_1}$ in (5.7) produces the wavelet coefficients utilised and retained by the G-SWMU. The second order scattering captures patterns of how that energy changes over time, thus enhancing patterns and structures in the occurrence of transients over the observation window. Figure 5.3 illustrates the first and second order WST coefficients for the faulted voltage waveforms associated with a splice failure and vegetation encroachment, respectively.

It can be seen that features associated with transient distortions are more clearly represented in the second order scattering. The differences between the extracted WST coefficients across both scattering orders can help discriminate between different events. The multi-layer network and predefined wavelet filters make the WST suitable for deep feature extraction from limited labelled event training data. It is also invariant to local translations and stable to time-warping deformations, based on the averaging scale of $\phi_J(t)$ (2^J samples), making it robust to within-class variations present in power system event waveforms.

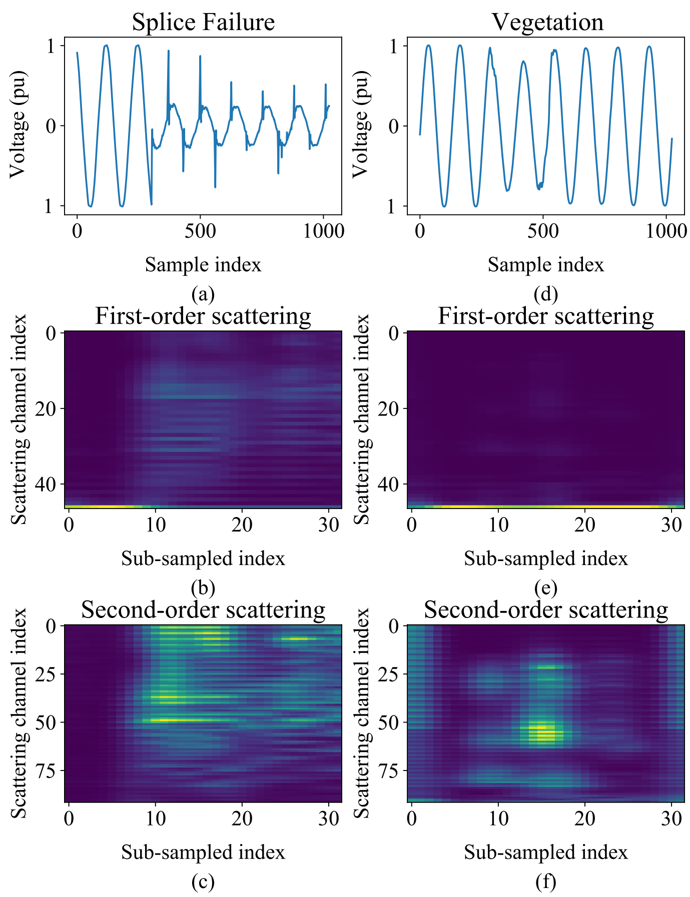

Figure 5.3: Visualisation of Wavelet scattering coefficients for different events: (a)-(c) Splice failure and (d)-(f) Vegetation encroachment

5.3.3 Wavelet Scattering based Open Set Nearest Neighbours (WS-OSNN) Classifier

The proposed WS-OSNN is illustrated in Figure 5.4. The wavelet scattering on its own provides a deep feature extraction (different layers of information correlated to different structures) with limited data. This richer feature extraction allows discriminating between known classes. This research further extends the discriminative ability of the wavelet scattering transform by embedding open set recognition within the distribution of scattering features to determine a threshold to reject unknown class instances, which are likely in real-world conditions especially if the training data is limited .

Three-phase voltage and current waveforms (data from the GESL is used in this study) are scaled to per unit values based on nominal voltage levels and pre-event currents. The Clarke transform is then applied to obtain orthogonal alpha and beta components, $V_{\alpha,\beta}, I_{\alpha,\beta}$ to represent unbalanced conditions. The use of the Clarke transform is beneficial, since conventional WST implementations typically also assume input channel independence. This is then input to the WST as implemented based on [183]. J, which influences the time invariance, is specified in terms of number of samples in the observation window, depending on the application and the data. A minimum of 1 nominal cycle should be specified for different event inception angles. In the case of DFR records, which contain several cycles of measurements before and after an event of interest, a fraction of the observation window can be chosen up to 1/2 of the input window.

The design of the wavelet centre frequencies impacts the feature extraction. A higher Q leads to increased frequency resolution, but will result in lower time resolution, and it is better suited to oscillatory dynamics. A lower Q results in a higher time resolution and is better suited to transients or impulses. A Q factor of 1 is therefore selected for the second scattering order to better characterise transients [182]. It is proven in [181] that for an increasing order of the scattering transform, the energy converges to zero, hence a scattering order of 2 is sufficient for this application. The values of J and the first order Q are considered hyperparameters and will be selected in the training phase.

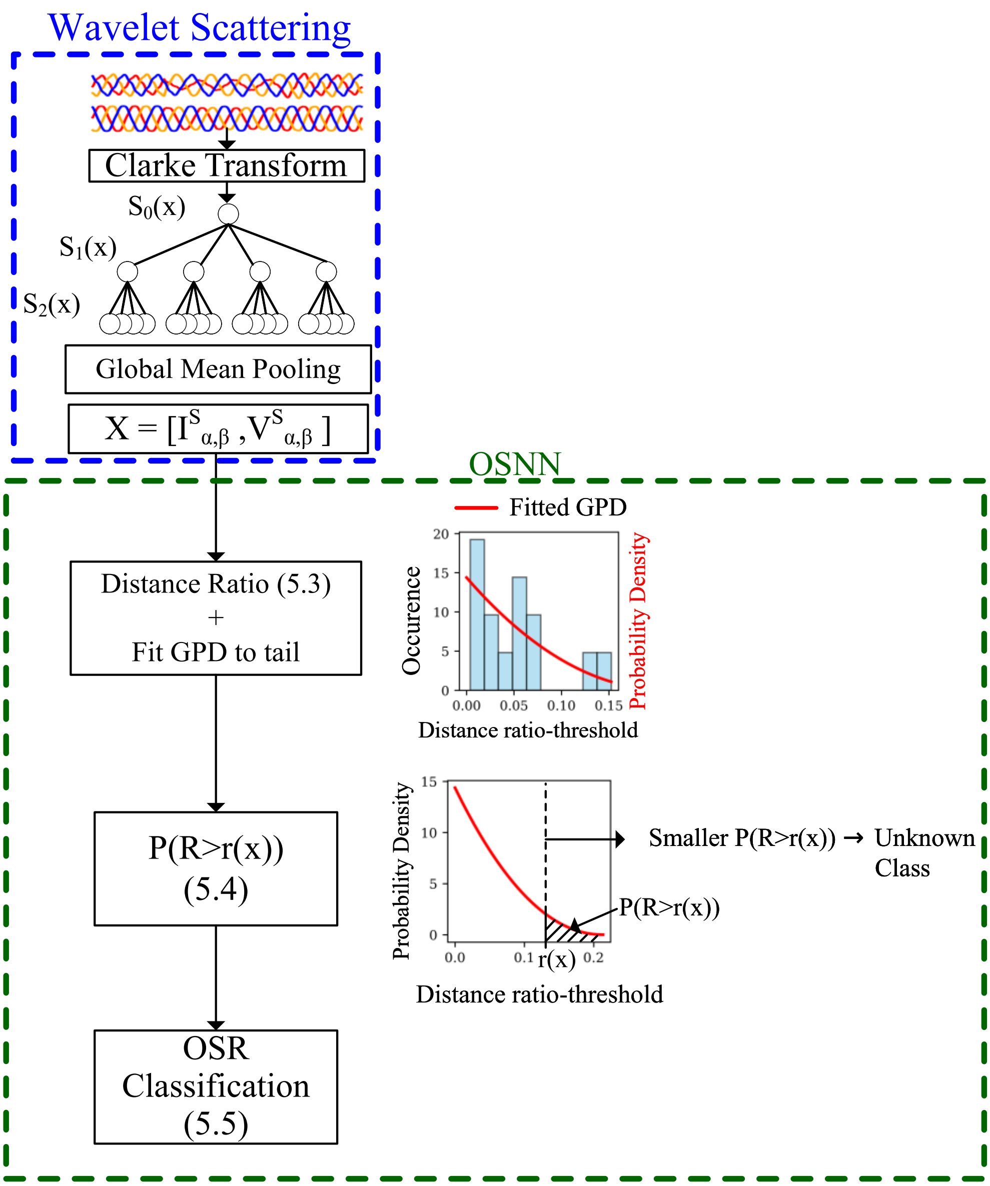

Figure 5.4: Architecture of the proposed WS-OSNN power system event classifier

For each input to the WST, mean pooling is applied to combine the different scattering layers, resulting in scattering vectors $V^S_{\alpha,\beta}, I^S_{\alpha,\beta}$. These are then combined for each event, resulting in feature vector $x_i = \{I^S_{\alpha,\beta}, V^S_{\alpha,\beta}\}$, $x \in X, i = 1...N$, where X is the feature matrix for N events. The training features are then input to the OSNN. For each feature vector, distance ratios are calculated using (5.3) and the tail of this distribution is modelled by fitting a GPD to the values above a threshold t, using an iterative maximum likelihood procedure. The optimal k and t are found so that they give good known class classification accuracy and a good GPD fit for the training data. More details of this procedure can be found in [176].

The resultant classification model therefore has an OSR mechanism via (5.4) to evaluate the probability that a new input produces a distance ratio in the WST feature space that is extreme in comparison to the training data. (5.5) is then used to perform the open set classification. Since unknown class instances are unavailable during training, an initial value for α is set as an acceptable risk factor of classifying known classes as unknown and can be adjusted in open-set validation testing and/or updated after deployment. An initial α of 0.2 is adopted in this research based on a sensitvity analysis that will be subsequently discussed. The proposed WS-OSNN can therefore extract relevant features from limited labelled power system event waveforms and classify known classes while remaining robust to unknown classes that may be encountered in deployment.

5.3.4 Open-set Power System Event Classification Framework

Figure 5.5 illustrates an open set power system event classification framework consisting of three main phases. In the open set model training phase, historical labelled event waveforms (e.g. from the GESL in this work) are processed and input to a supervised classification model such as the proposed WS-OSNN. Only known class training data are utilised to minimise the training/validation closed set error and incorporate OSR.

The trained model is then deployed in the open set classification phase. New event waveforms to be classified, that may belong to unknown classes, are input, processed and classified. If the new event waveform is determined to belong to the known classes, then the class prediction is output, otherwise the waveform is classified as unknown. The incremental learning framework builds on OSR, which does not differentiate between different unknown classes. Unsupervised clustering techniques or waveform similarity metrics can be used to find initial clusters of waveforms that may be attributed to similar unknown event causes. This can then be combined with domain knowledge including domain expertise, root cause failure analysis findings, or further investigations to determine suitable event labels. Finally, these event labels and corresponding waveforms can be added to the existing database and the classification models updated, thus facilitating manual incremental learning.

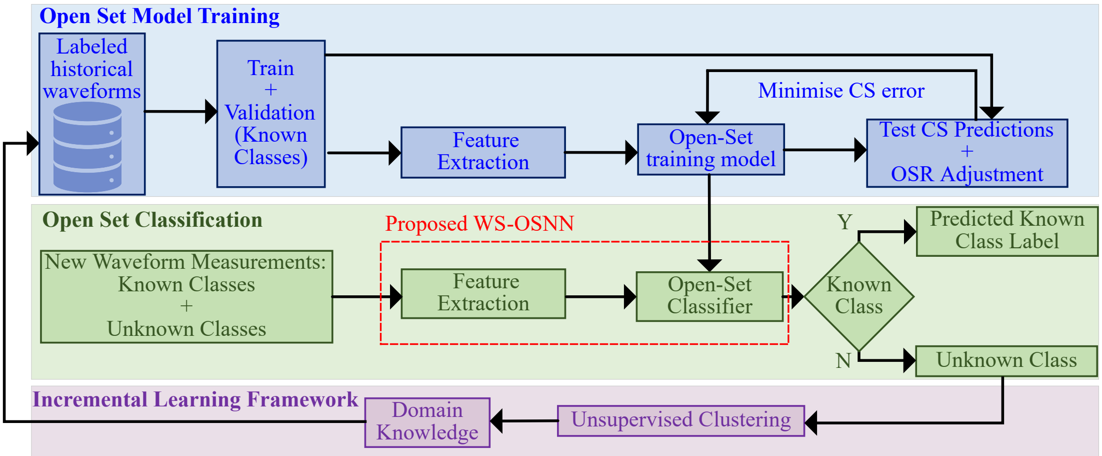

Figure 5.5: Open set power system event classification framework

5.4 Classification Performance and Benchmarking

5.4.1 Class Definition

For ML-based applications, it is critical to have realistic training data. As mentioned previously, the open source data available in the GESL has been used in this work. It contains labelled three-phase voltage and current waveforms sampled at 15,360 Hz and 7,680 Hz with a nominal frequency of 60 Hz. Downsampling is used to create a consistent dataset sampled at 7680 Hz and a window of 1024 samples (8 cycles) is input to the WS-OSNN. Vegetation encroaching on power lines and equipment failures can manifest as intermittent self clearing faults that may not immediately trigger protection relays or lead to a major incident. Identification of these early signs can inform critical interventions. The event classes {and the associated class sizes} used to evaluate the proposed classification model are:

- Vegetation Encroachment, VE, {30}
- Equipment Failure, EF, {25}

- Transformer Inrush, TI, {11}
- Hot Transfer, HTF, {9}
- Splice failure, SF, {2}

VE and EF represent the main closed set targets requiring maintenance intervention. TI and HTF represent transient but normal operations that may be encountered by a classification model but not necessarily accounted for in training. SF may be considered as a sub-class of the EF class (but not in the EF training data). SF is representative of rare unknown class instances that can be encountered in deployment. Case studies are performed with different combinations of classes assigned as KCs and UCs. The degree of openness O^* of the classification task is defined as [167]:

$$O^* = 1 - \sqrt{2C_{TR}/(C_{TR} + C_{TE})}, \tag{5.9}$$

where C_{TR} is the number of KCs in training and C_{TE} is the number of classes in testing including KCs and UCs. For a closed-set dataset, O^* is zero and increases as the number of UCs increases.

5.4.2 Determining Optimal Settings for J and Q

To determine suitable values for J and the first scattering order Q, a grid search is performed for different combinations during the training phase. Each observation window contains 1,024 samples or 8 cycles. J is varied from 6 to 9, where the value of 6 corresponds to $2^6 = 64$ samples, i.e. half a cycle, while the value of 9 corresponds to $2^9 = 512$, i.e. 4 cycles or half the observation window. Q is varied from 1, which is best suited to short time transients, to larger values (up to 16), which provide finer frequency resolution and are therefore better suited to oscillatory components. Closed-set accuracy and unknown detection rates are used to analyse the impacts of J and Q on the performance of the WS-OSNN.

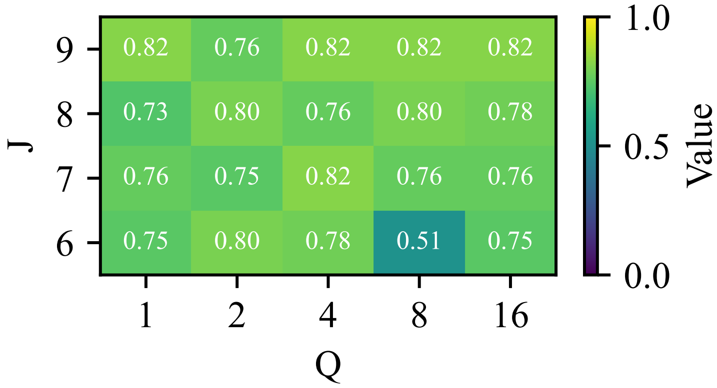

Figure 5.6: Impact of J and Q on closed-set accuracy

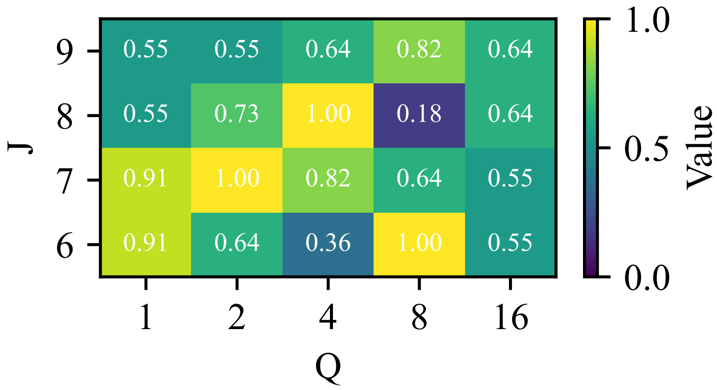

Figure 5.7: Impact of J and Q on unknown detection

Figures 5.6 and 5.7 illustrate heatmaps for closed-set accuracy and unknown detection rate, respectively, for different combinations of J and Q. The analysis indicates that a J of 9 and a Q of 8 gives a relatively balanced performance in terms of maintaining closed-set accuracy and rejecting unknown instances for the dataset used in this research.

5.4.3 Performance Metrics

A true positive (TP) classification of UCs is not strictly defined since it is not represented in the training set [167]. F-measures, as described Section 3.3.2 of Chapter 3, are therefore calculated taking into account the TP rate of KCs only as defined in [167].

These metrics penalise misclassified UCs (via false negatives) and misclassified KCs (via false positives). To assess the WS-OSNN's ability to reject UCs, Youden's index, YI, which captures true negatives (TN), is applied as:

$$R = TP^o/(TP^o + FN^o), \tag{5.10}$$

$$S = TN^o/(TP^o + FN^o), \tag{5.11}$$

$$YI = R + S - 1, \tag{5.12}$$

where R is recall, S is the true negative rate, TP^0 are known samples correctly classified as known, FN^O are known samples incorrectly classified as unknown, TN^O are unknown samples correctly classified as unknown and FP^O are unknown samples incorrectly classified as known. These are highlighted in Figure. 5.8(a). YI ranges from $[-1, 1]$ with a higher value indicating improved OSR. F-measures highlight how incorporating OSR impacts the closed-set performance while YI evaluates OSR performance.

5.4.4 Case Study: Closed-Set Performance in Classifying Known Classes

This case-study evaluates the performance of the trained models when subject to new inputs that belong to the KCs. Accurate classification of KCs and reducing false detection of UCs (by the open-set models) are important performance benchmarks. The closed-set performance of the proposed WS-OSNN model is first demonstrated in its ability to classify Vegetation and Equipment Failure events. The performance of proposed open-set model is compared with its closed-set equivalent WS-NN, the closed set DTW-1NN waveform similarity model of [105] and a kNN classifier with out-of-distribution detection incorporated separately (referred to as OOD+WS-NN). Hyperparameters and settings of these models are listed in Appendix D.

Leave-one-out-cross validation (LOO-CV), which is suitable for small datasets, is used to assess the performance of the models and the performance metrics are summarised in Table 5.1. The high F-scores show that features present in event waveforms can be used for event cause identification. Models that use the WST show an increase in performance compared to the DTW. This highlights the advantage of extracting time-frequency structures from waveforms compared to time-domain similarity based features. Open-set models, e.g. the proposed WS-OSNN, show a slight decrease in closed-set performance compared to the WS-NN, highlighting that incorporating OSR can result in a trade-off with closed set performance as the decision boundaries may change.

Table 5.1: Closed-set Performance

Classifier	**F-score (%)**	
	Vegetation	**Equipment Failure**
WS-OSNN (Proposed)	82.75	80.76
OOD+WS-NN	83.02	79.07
WS-NN	89.23	84.44
DTW-1NN	83.33	80

5.4.5 Case Study: Open-Set Performance in Identifying Unknown Classes

TI is now introduced as an UC into the test set in this case study, which represent a scenario where previously trained models are deployed and encounters an event class not considered during the training phase. LOO-CV is applied on the KCs, the final model is then trained using all the KC training data and the UC is input to the final model. The confusion matrices and open-set performances are presented in Figure 5.8 and Table 5.2 respectively. As expected, UCs are incorrectly classed as a KC by the closed-set models (Figure 5.8(c) and (d)), i.e., a degradation in performance. This translates to false positive detections of the target KCs.

The OOD+WS-kNN had a tendency to class KCs as Unknown, resulting in a lower YI compared to the WS-OSNN, which can lead to missed target event detection. This highlights the advantage of incorporating OSR within the ML training optimisation process as in the WS-OSNN. The WS-OSNN achieves a good balance between detecting UCs (higher YI) and avoiding false negative unknown classifications (higher F-scores).

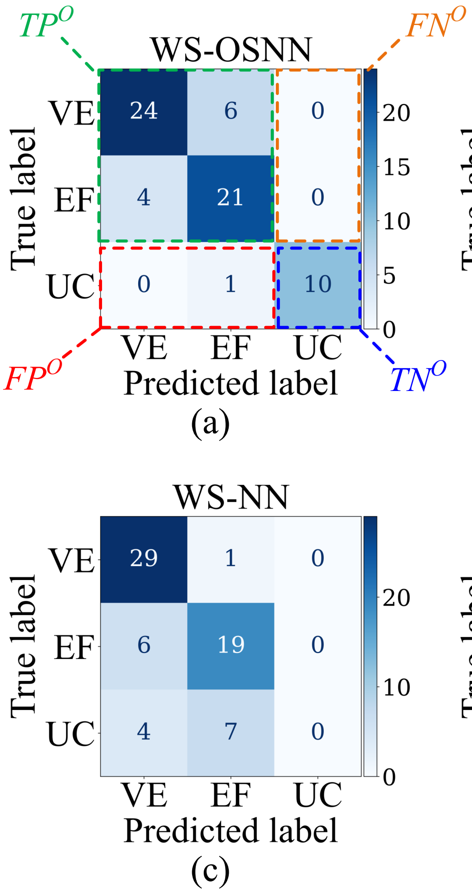

Figure 5.8: Open-Set Performance: (a) WS-OSNN with metrics used to calculate YI highlighted, (b) OOD+WS-NN, (c) WS-NN and (d) DTW-1NN

Table 5.2: Open-set Performance

Classifier	**F-score (%)**		**YI**
	Vegetation	**Equipment Failure**	
WS-OSNN (Proposed)	82.75	79.25	0.9091
OOD+WS-NN	83.02	79.07	0.7454
WS-NN	84.06	73.08	NA
DTW-1NN	78.13	70.18	NA

Deployed classification models are likely to encounter larger proportions of UCs, leading to increasing openness. To evaluate this, different combinations of UCs are added to the test set and the corresponding levels of openness are calculated using (5.9).

Figure 5.9 highlights the performance of the models under different levels of openness. $O^* = 0\%$ corresponds to closed-set with 2 KCs, while the ratios of KC/UC are 3/1, 2/1 and 2/2 for $O^* = 7.4\%, 10.6\%$ and 18.3% respectively. The open-set models are more resilient to UCs with smaller reductions in F-scores compared to the closed-set models as the openness increases. The WS-OSNN also has better OSR performance, as shown by the higher YI, compared to the OOD+WS-NN. However, the OSR performance of the WS-OSNN fluctuates as the class definitions and openness changes, highlighting its reliance on the statistical distribution of the known training data and the selection of the OSR threshold.

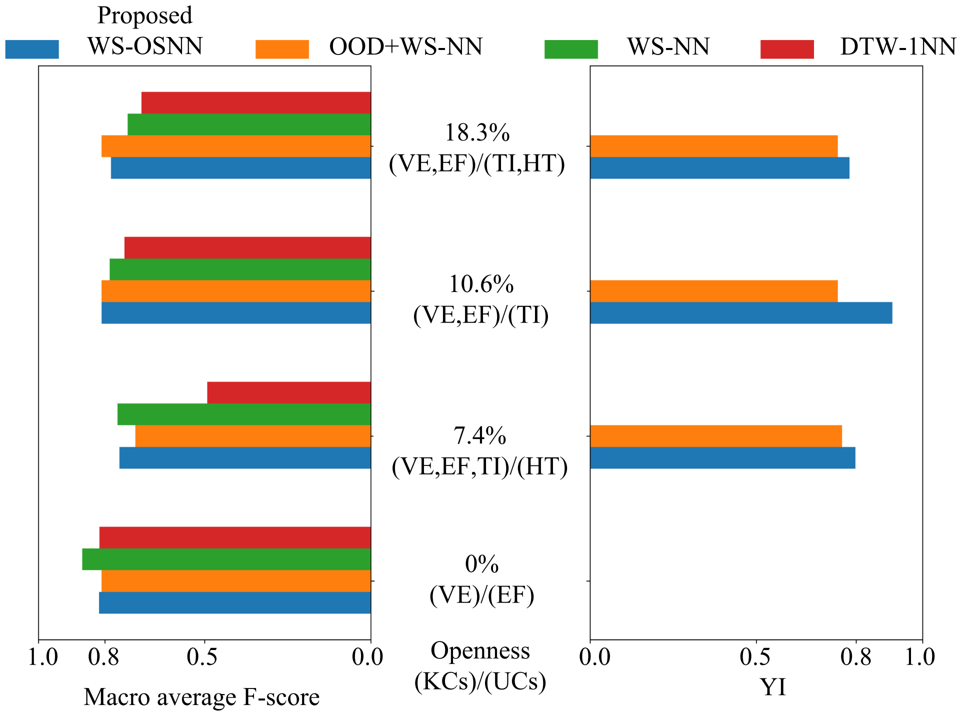

Figure 5.9: Impact of openness on classification performance

5.4.6 Case Study: Sensitivity of the WS-OSNN to Unknown Classes

Table 5.3 highlights the F-scores and YI for different values of α for the $O^* = 7.4\%$ (VE, EF, TI)/(HT) case. A small α decreases the sensitivity to UCs (lower YI) with some UCs being classed as known, lowering the F-scores. Increasing α improves the OSR performance, but this can impact the closed-set performance reflected by lower

F-scores. To set α, the approach adopted in this thesis of assigning some of the KCs as unknown can be used to get an initial setting. α can then be updated after deployment to balance spurious alarms with missed events (with respect to the target known classes). However, there is no prior knowledge of true unknowns, so a choice of α that places greater importance on closed-set performance is a more conservative approach. Based on Table 5.3, $\alpha = 0.2$ appears the best value for this dataset.

Table 5.3: Impact of α on Open-set Performance

α	**Macro-average F-score (%)**	**YI**
0.05	79	0.55
0.2	77	0.78
0.35	72	0.78

5.4.7 Case Study: Identifying Similar Unknown Event Waveforms

To demonstrate how the proposed WS-OSNN can facilitate event investigations, the SF, HTF and TI records, described in Table 5.4, are input to the model trained on the VE and EF classes. The EF training records do not include representative instances of the SF. The closed-set WS-NN classes one instance of the SF class as EF and one as VE, highlighting inconsistencies caused by inputs that are out of the training data distribution. The proposed WS-OSNN classes both of these as Unknown.

Visualising hierarchical relationships within the WST feature space of the UCs detected by the WS-OSNN can aid investigators in identifying similar waveforms. Figure 5.10 illustrates a hierarchical clustering dendrogram for UC instances identified by the WS-OSNN. The lowest level of the dendrogram represents the individual signals. Signals 195 and 193 are the SFs, 914-916 are associated with TI and 893-895 are associated with HTF. A node signifies where two branches merge, and the branch height shows the distance at which two clusters were joined. Initially, each signal is its own cluster. In this analysis, clusters are merged by calculating the maximum distance between members of clusters and merging the two clusters in which this distance is smallest. This process is repeated until all the unknown signals are in one cluster. A key consideration is therefore how to interpret the hierarchical dendrogram to estimate a meaningful number of clusters (if any exist). Statistical methods are described in [184], however, it is also noted that assumptions made about unknown data limit the suitability of these methods. Their application to limited power system data is beyond the scope of this research. Manual interpretation via the application of domain knowledge and engineering judgment is also suitable approaches [184]. One such approach is partitioning the dendrogram at a particular height. Branches that merge below this decision height are considered to belong to a potential cluster. This partition height is therefore a threshold that limits how dissimilar instances can be, in order to be considered in the same cluster.

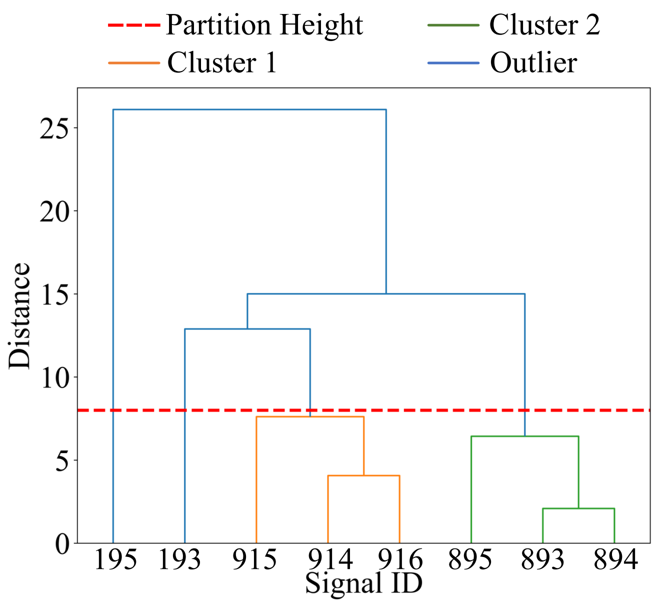

Figure 5.10: Hierarchical clustering dendrogram of Unknown event waveforms

An intuitive way to estimate an initial partition height is to find large changes in the merging heights [184, 185]. An ordered plot of merging heights versus the resulting number of clusters can be examined and inflection (elbow) points corresponding to large changes can be used as the partition height as illustrated in Fig. 5.11. An inflection point in this context is where the rate of decrease changes noticeably, meaning the curve transitions from a steep decline to a gentler decline. This indicates that splitting the data into the corresponding number of clusters captures a significant separation in the data. This is based on the distances between wavelet scattering features of members of the different resulting clusters. An increasing in the number of clusters accompanied by a relatively less steep drop in merging heights means that there could be clustering on noise or over-segmenting the data. The highlighted inflection points correspond to numbers of clusters beyond which further increasing the number of clusters yields only marginal improvements in cluster separation. Applying these thresholds and visualising the dendrogram gives an approximate clustering for further (manual) validation.

The analysis shows that signal 195 is clearly differentiated from other waveforms (corresponding to two clusters in Figure 5.11). The second inflection point in Figure 5.11, corresponding to 4 clusters illustrated in Fig. 5.10 shows that signal 193 is also differentiated from distinct clusters that align with the TI and HTF class labels. This analysis provides a starting point from which investigators can examine and manually verify potential clusters, as illustrated in Figure 5.12. It should be noted that this analysis alone does not provide a basis for attributing signal 193 and signal 195 as being members of the same class. Combining data and learnings from similar events and applying domain expertise may better allow investigators to determine a suitable event clustering and root cause.

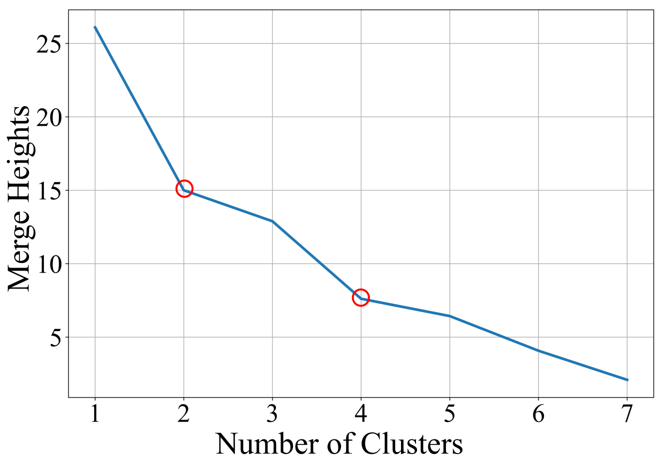

Figure 5.11: Merge heights of the UC instances with large changes highlighted

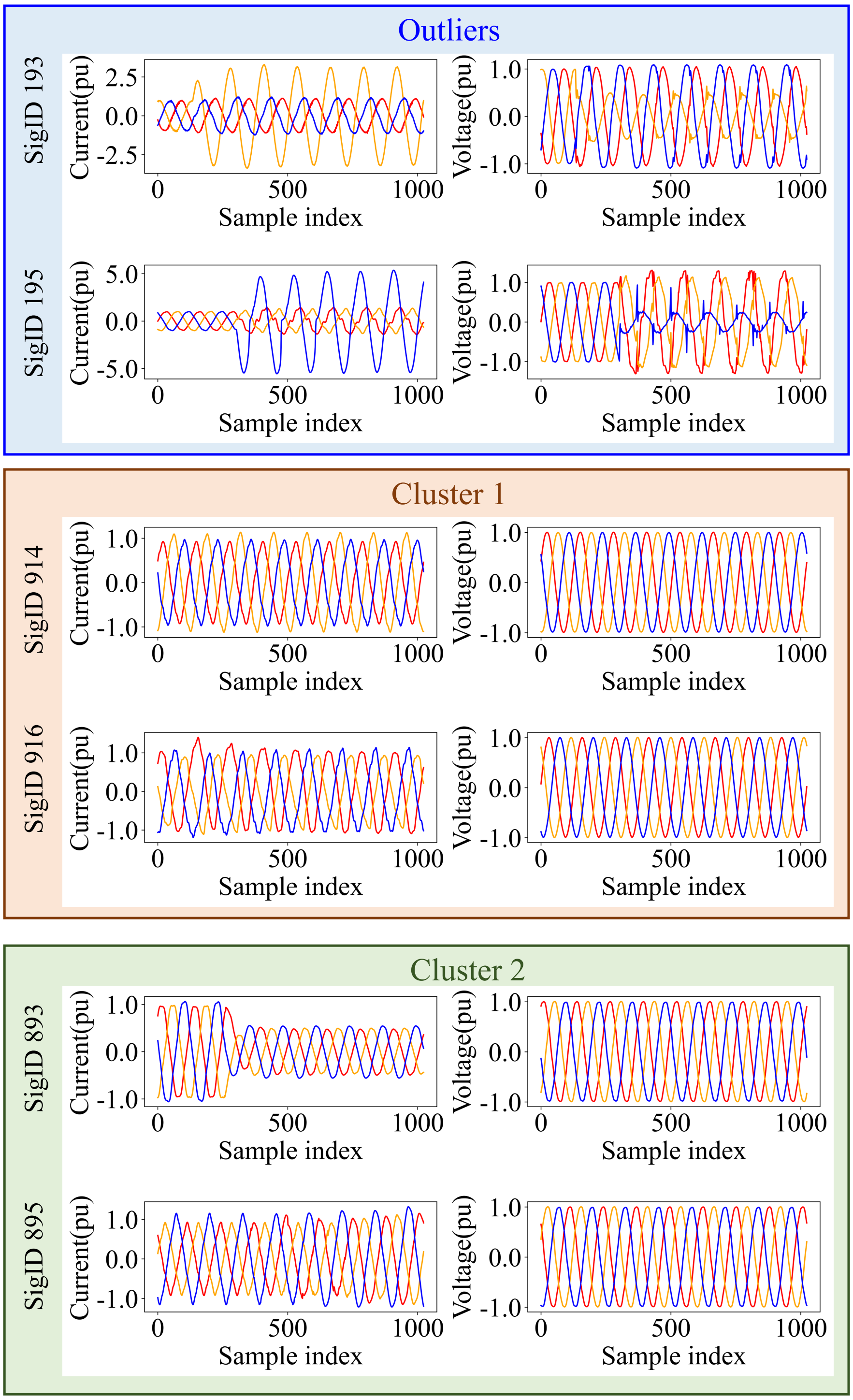

Figure 5.12: Voltage and current waveforms of potential clusters and outliers from clustering analysis

Table 5.4: Event Descriptions from GESL

Signal ID	GESL Description
193	Fault on riser splice
195	Splice failure on aerial cable
914	Small inrush on phase B
916	Small three phase inrush
893	Three phase line switch 50% decrease
895	Three phase line switch 20% increase

5.4.8 Discussion

The proposed classification model is trained entirely on a small (<100 instances) real-world dataset and demonstrates good performance with respect to classes (VE, EF) that are highly variable and difficult to model. This is evidenced by the higher f-scores of 82.57% and 79.25% compared to the scores of the waveform based DTW-1NN (78.13 and 79.25) for the WE and EF classes. This is due to pre-defined wavelet filters, translation invariance and deep time-frequency structures extracted by the WST. The event descriptions in Table 5.4 and the waveforms of Figure 5.12 show different inception angles, durations, magnitudes and affected phases that power system events exhibit. The time-frequency features extracted by the WST resulted in satisfactory classification performance, with little feature engineering required to address or normalise these variations.

Incorporating OSR within power system event classification can improve the performance of traditional closed-set classifiers when unknown inputs (with respect to the known training data) are encountered. It was found that applying out-of-distribution detection separately as a pre-classification step can detect unknown instances. However, it was prone to incorrectly classifying known instances as unknown, resulting in a lower YI score of 0.7454 as shown in Table 5.2. Incorporating OSR within the training framework addressed this issue achieving a higher YI of 0.9091, and a 16% increase in OSR performance. Integrating OSR therefore allows a mechanism, via α, to adjust the tradeoff between sensitivity to unknown classes and closed-set performance.

The case studies highlight the effectiveness of the WS-OSNN to discriminate between different event causes while identifying unknown events. The proposed WS-OSNN is therefore a valuable method for accurately classifying known events and identifying, with the aid of visualisation, clustering analysis and manually applied domain expertise, similar waveforms for further investigation. A key benefit of the proposed WS-OSNN is that it addresses the near-term challenges of adopting state-of-the-art art machine learning methods, which would typically require large labelled datasets, for power system event classification. The proposed method is suitable for training databases with limited labelled event instances, and through the identification of unknown event waveforms, can provide an initial point for further, possibly, manual analysis.

5.5 Integration With the Proposed G-SWMU Algorithm

5.5.1 Classification Using Post-Event G-SWMU Output

The preceding open-set classifier was trained and evaluated using the historical database of raw event waveforms as captured by recording devices. However, curating such datasets may be difficult due to storage requirements and manual data collation. To demonstrate the potential advantages of utilising the informative, yet sparse features produced by the G-SWMU algorithm proposed in Chapter 4, a case study that inputs the reconstructed waveforms via the G-SWMU outputs to the WS-OSNN is presented. The three-phase voltage and current waveforms from event 187, described as an arrester failure, are input to the proposed G-SWMU algorithm, resulting in a wavelet feature matrices and phasor outputs. These outputs are then used to give a partial reconstruction of the event waveforms, as illustrated in Figures 5.13 and 5.14.

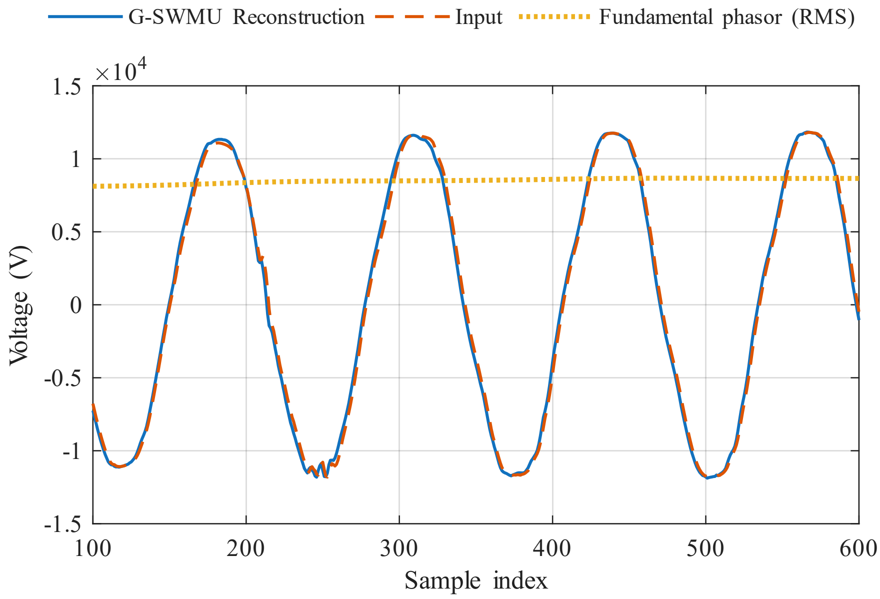

Figure 5.13: Comparison between SWMU algorithm reconstruction and fundamental phasor

Figure 5.13 compares the input phase C voltage waveform from the GESL with the reconstruction created via the processed G-SWMU algorithm outputs. It is observed that the transient distortion, particularly between samples 200 and 300, is preserved. For reference, the fundamental phasor magnitude is also displayed, highlighting the loss of these signatures.

Figure 5.14 demonstrates the reconstructions for all event 187 waveforms. It should be noted that where there are sudden step changes, an error is introduced as the G-SWMU phasor output gradually tracks the step. However, the distortions in the waveforms are retained. Similarly, event 165 (Vegetation) was also processed and reconstructed. The proposed WS-OSNN is trained using all other available, raw waveforms and the reconstructed event waveforms were input to the WS-OSNN. Table 5.5 demonstrates that the WS-OSNN correctly outputs the predicted class labels of the G-SWMU based reconstructed waveforms and the results were also consistent with the predicted label using the raw GESL waveforms.

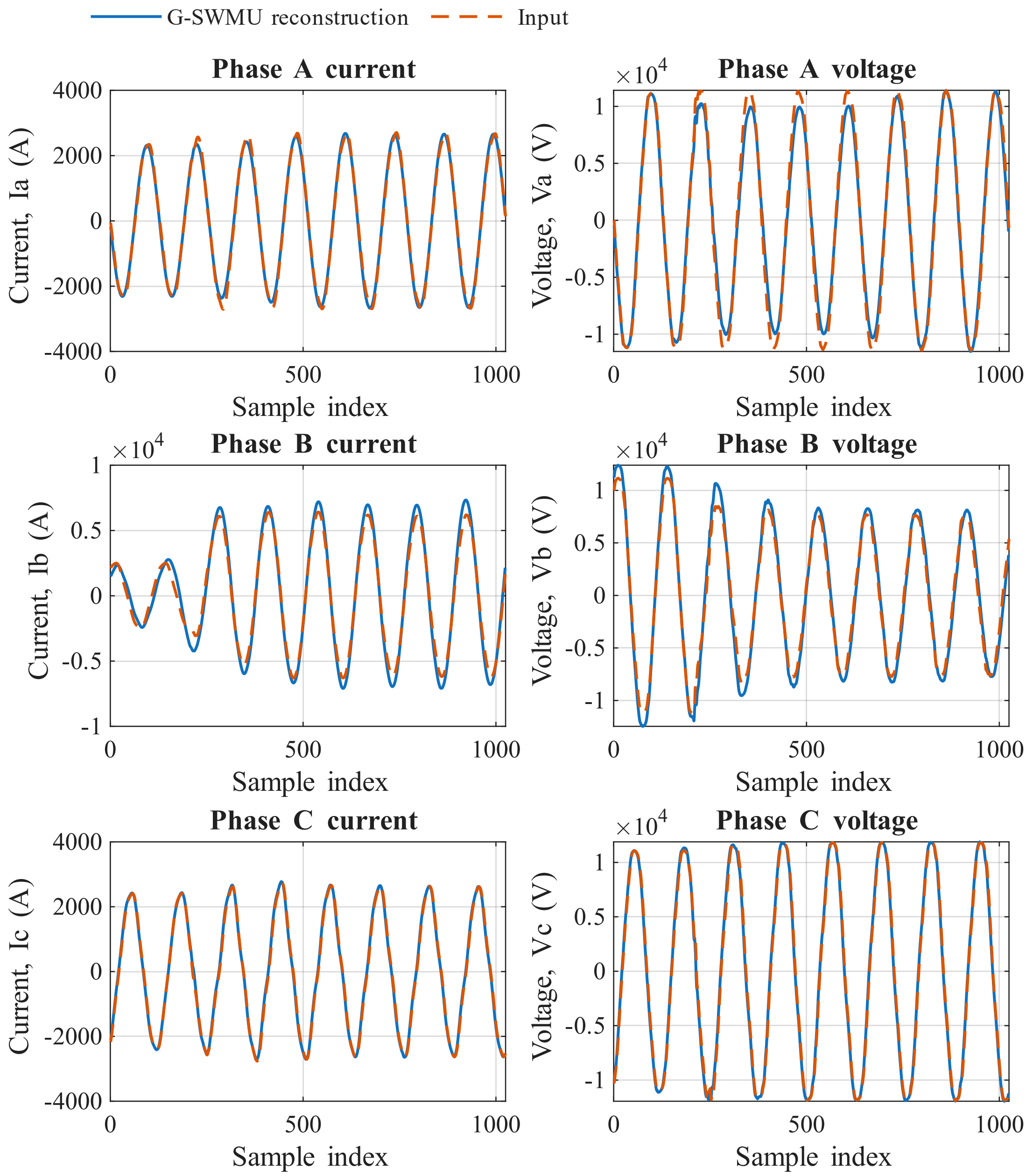

Figure 5.14: Event waveform reconstructed from G-SWMU algorithm outputs

This case study demonstrates that the feature extraction capabilities of the proposed G-SWMU algorithm offers similar classification performances as using raw waveforms. The G-SWMU algorithm therefore better detects and extracts relevant features contained in the input synchro-waveforms compared to PMUs while significantly reducing the burden associated with continuously streaming and archiving synchro-waveforms.

The proposed WS-OSNN classifier can be trained using existing, raw waveform signatures from recording devices and utilise processed G-SWMU outputs in deployment, thus highlighting its practicality and compatibility with existing synchronised measurement technologies.

Event	**Input**	**True Label**	**Predicted Label**
187	GESL Waveform	EF	EF
	SWMU Reconstruction	EF	EF
165	GESL Waveform	VE	VE
	SWMU Reconstruction	VE	VE

Table 5.5: SWMU based WS-OSNN classification results

5.5.2 Design of Online G-SWMU-Based Event Classification

To facilitate online event detection and classification, the trained WS-OSNN classifier can be deployed within the proposed G-SWMU algorithm presented in Chapter 4. Figure 5.15 illustrates a possible configuration for an online, event driven, G-SWMU processing platform capable of event diagnostics. Synchro-waveforms are input to the proposed G-SWMU algorithm. The wavelet based transient filter,WSCTF, is used for event detection as demonstrated in Section 4.2.1. If no transient events are detected, then the appropriate synchrophasors are output.

If an event is detected, the transient detected flag is enabled and communicated within the phasor data attributes, since the estimated phasor may be unreliable. At the same time, input waveforms (consistent with the window size used in offline training) can be input to the trained WS-OSNN classifier. If the event is determined to be from a known class, the event class prediction can be output and communicated to inform situational awareness and mitigation actions. In this case, the transient wavelet matrix that gives an approximate reconstruction of the transients of interest may also be saved or communicated. If the input is determined to be unknown to the pre-trained classifier, the G-SWMU transient output or the raw waveform records, as would typically be done using conventional DFR functionality, may be saved to enable post event investigations.

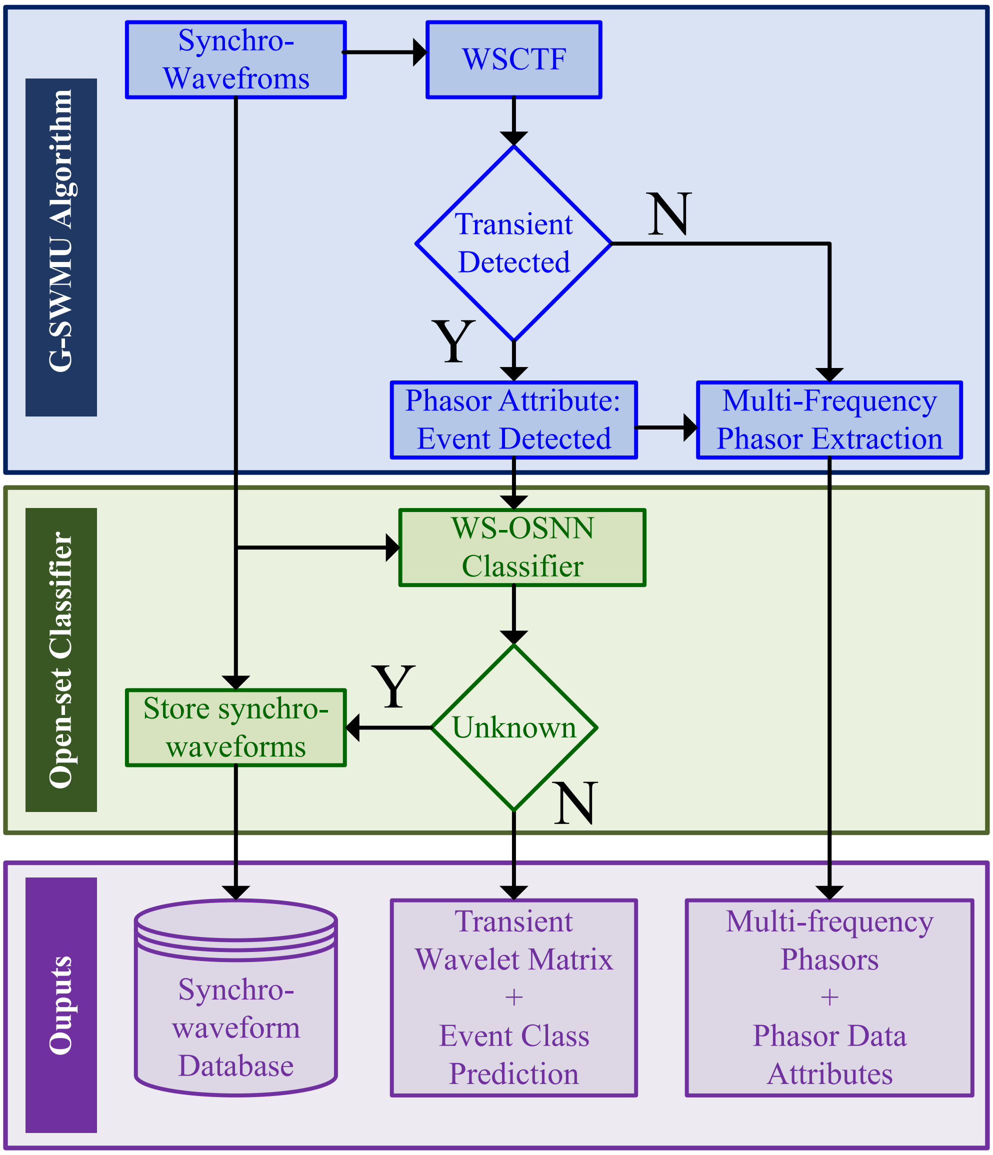

Figure 5.15: G-SWMU algorithm with integrated WS-OSNN functionality

As the deployment of G-SWMU devices increases, the framework illustrated in Figure 5.15 allows actionable information to be communicated while reducing the storage requirements by requiring the storage of only unknown events, either as DFR waveforms or G-SWMU processed outputs.

This design is flexible and extendable depending on the user needs. For example, particular event classes may trigger certain processing or outputs relevant to that event. The recurrence of similar events (or similar unknown event waveforms found by clustering as discussed in Section 5.4.7) may also trigger alarms, as this may be a precursor of a more serious failure, e.g., self-cleaning incipient faults before equipment or insulation failure.

5.6 Chapter Summary

This chapter has presented a G-SWMU based power system event classifier, which is capable of accurately classifying anomalous power system events using limited training data. The wavelet features extracted by the G-SWMU algorithm proposed in Chapter 4 were extended to a deep learning architecture via wavelet scattering networks. The wavelet scattering transform utilises pre-defined wavelets to extract the time-frequency structures of the input waveforms, further expanding the transient features retained by the raw waveforms or processed G-SWMU outputs. This property is useful for waveform based power system event classification where training datasets are limited. To further address potential overfitting and biases associated with limited data, open set recognition, which is a mechanism for classification models to reject unknown instances and avoid misclassifying such instances as known, was also applied.

The proposed WS-OSNN combines wavelet scattering feature extraction and OSR integrated classification. It was trained and evaluated on actual event waveforms available via the open-source GESL. The WS-OSNN was found to accurately classify known classes of interest even when trained with limited labelled examples. Unknown class instances were also successfully rejected, thus reducing false detection of events. To aid in unknown event investigations and potentially improve training datasets, similar instances within the unknown class set can potentially be found by visualising hierarchical clusters among the WST features.

The WS-OSNN was demonstrated using both raw waveforms from the GESL and waveforms reconstructed via the proposed G-SWMU algorithm outputs. The results indicate that the outputs of the G-SWMU algorithm of Chapter 4 can support synchro-waveform based applications, while reducing the requirements of supporting infrastructure associated with continuous streaming of synchro-waveforms. The WS-OSNN may also be integrated with the G-SWMU algorithm to enable online identification of anomalous events of interest. The long term adoption of the G-SWMU and the WS-OSNN can aid utilities in curating event datasets with meaningful diagnostic labels, thus improving situational awareness and enabling more targeted decision support via the accurate identification of critical events.

Chapter 6

Conclusions and Future Research

6.1 Conclusions

The massive integration of IBRs in power systems has fundamentally altered the system behaviour, which introduces significant operational challenges that can severely compromise system security. This thesis has presented research on addressing the challenges associated with real-time monitoring and decision-support, with a specific focus on IBR dominated systems. Current wide-area monitoring systems primarily rely on synchrophasors from PMUs, which assumes a fundamental sinusoidal reference. This limits their suitability in fully capturing emerging system dynamics induced by IBRs, which can frequently contain non-sinusoidal distortions, sub-cycle transients, sub/super synchronous oscillations, etc. High-resolution, synchro-waveforms can accurately capture IBR-induced dynamics, thus addressing the issue with accuracy. However, they typically output large volumes of data, which results in challenges of data transmission (particularly if continuous streaming is required), storage and processing, making them impractical for deployment over wide areas of the power system. Therefore, new synchronised measurement approaches are urgently required that can simultaneously provide accurate representation of diverse system dynamics and maintain compatibility with practical data storage and communication constraints, in order to enable critical real-time monitoring and decision support functions in IBR-dominated power systems.

The first contribution of this thesis addresses the challenge associated with emerging IBR-induced oscillations from the perspective of existing measurements (including synchrophasors and raw synchro-waveforms) and infrastructure. An analysis of a PMU dataset uncovered precursory signs of SSO events in the GB system that persisted within operational timescales. A framework for identifying oscillatory signatures, including precursors, in historic synchronised measurement datasets via statistical change-point analysis was proposed. Based on these signatures, an ML-based SSO early warning system was developed to detect and inform the risk of emerging IBR-driven system oscillations. The SSO early warning system was validated using real-world data and highlights the ability of PMU measurements to detect oscillatory instability. From the study, it was also demonstrated that the fundamental sinusoidal reference and standard filtering of conventional PMUs limit their ability to detect and characterise multiple IBR driven oscillation modes (e.g. sub/super-synchronous oscillations) and their properties. Raw synchro-waveforms can enhance oscillation analysis, however communication and storage infrastructure constraints mean that such measurements are available via threshold-triggered waveform recorders that can miss emerging oscillation events. Improved processing of raw synchro-waveforms to support their real-time and scalable deployment can benefit the analysis of IBR-driven SSO's and other emerging dynamics.

The second contribution of this thesis addresses the measurement challenge of balancing accuracy and data volume by developing a novel, generalised synchro-waveform measurement unit processing algorithm i.e. G-SWMU, which is capable of extracting and translating key meaningful features of raw synchro-waveforms while reducing the volume of data to be communicated. The G-SWMU utilises a two-stage, time-frequency feature extraction method. In the first stage, non-sinusoidal distortions are detected and sparsely represented by a wavelet scale correlation transient filter (WSCTF). In the second stage, multi-frequency phasor estimation is achieved via the iterative extended DFT based empirical wavelet transform (I-EDFT-EWT). The G-SWMU therefore produces fundamental phasors during steady state conditions and adapts to different possible dynamics contained in the input synchro-waveforms. The proposed G-SWMU algorithm was validated using actual waveforms and can detect and characterise a wide variety of conditions, including transient events and oscillations. Accurate and prompt (within conventional PMU processing windows) measurements of closely spaced inter-harmonics associated with IBR-driven oscillations are demonstrated via case studies using waveforms captured during actual SSO events. The suitability of the proposed SWMU algorithm output to more effectively support oscillation source location techniques was demonstrated, providing improved performance relative to a conventional PMU based method.

The G-SWMU algorithm requires little to no prior knowledge of the underlying dynamics, is configurable, (e.g. frequency resolution is a design specification), and provides a balance between noise rejection and sensitivity. Synchro-waveforms are processed locally to extract features that capture information up to several kHz, with the features reported at standard PMU reporting rates (<200 frames per second). A mapping of processed outputs of the proposed G-SWMU algorithm to the IEEE C37-118-2-2024 format has also been presented. Theoretical estimations demonstrated slightly increased but manageable bandwidth requirements compared to traditional PMU outputs and considerably less bandwidth requirements compared to streaming raw synchro-waveform samples at several kHz. The G-SWMU algorithm therefore addresses the measurement limitations of conventional PMUs as well as the challenges of continuously streaming large volumes of raw synchro-waveforms, thus enabling a wide range of monitoring and control applications urgently needed in IBR-dominated power grid.

While motivated by IBR-driven dynamics, the adaptability and scalability of the G-SWMU can enable wider applications that extend beyond IBR-specific use cases, thus supporting broader investment in synchro-waveform platforms. The third contribution of this thesis therefore developed a novel G-SWMU based event classifier, i.e, the WS-OSNN. The outputs of the G-SWMU algorithm were integrated into a feature extraction process suitable for state-of-the-art ML methods via the wavelet scattering transform WST. The improved transient features retained by the G-SWMU along with the predefined wavelet filters of the WST were found to be suitable for event classes with limited labelled instances that are also difficult to accurately model, e.g. vegetation encroachment and equipment failure. To further enhance the capabilities of the proposed G-SWMU based WS-OSNN classifier, this research incorporated open set recognition

(OSR) which aims to accurately classify known class instances and simultaneously recognise inputs that do not belong to known classes in order to classify them as unknown. The WS-OSNN was trained and evaluated using real-world data and achieved accurate classification performance for known classes while successfully rejecting unknown class instances. The G-SWMU enabled WS-OSNN classifier therefore translates high-resolution synchro-waveform features into reliable event classifications, thus enabling improved situational awareness and informing more appropriate, effective mitigation strategies.

The findings of this research demonstrate the critical need for high-resolution yet scalable monitoring techniques for secure IBR integration. The contributions presented in this thesis provide feasible solutions to this challenge, setting the foundation for the adoption of a new generation of synchronised measurement technologies. The adoption of the contributions of this research will enable accurate monitoring and mitigation of critical events in order to ensure the secure and reliable operations of IBR dominated power systems.

6.2 Future Research

6.2.1 Hardware Deployment of the Proposed G-SWMU Algorithm

The development and testing of the G-SWMU algorithm conducted in this thesis was limited to desktop simulations. Practical deployment of the G-SWMU algorithm will require further refinement and optimisation of the algorithm to run on a dedicated hardware platform. The equations describing the transient detection filter and the I-EDFT-EWT phasor extraction module highlight that matrix operations are required to execute the algorithm. The size of these matrices are proportional to the window size, wavelet decomposition levels and required frequency resolutions. Investigations into suitable hardware platforms are needed.

A field programmable gated array (FPGA) processor which is designed for matrix operations and typically used in industrial settings can be utilised. Alternatively, advances in processing hardware to support AI applications, such as graphical processing units (GPUs), can also be adapted to local signal processing and edge ML applications such as the proposed event classification frameworks proposed in Chapters 3 and 5. This is considered to be a promising avenue, as it is shown in this research that AI driven event characterisation can improve the insights derived from synchronised measurements.

A potential mapping of SWMU outputs to IEEE Std C37.118.2-2024 communication messaging format was proposed in this thesis. To future proof the algorithm design, investigations with the emerging IEEE 2664-2024 Standard for Streaming Telemetry Transport Protocol (STTP) can also be conducted. A communication module that actually encodes the SWMU outputs for real-time streaming needs to be developed. Experimental testing with the hardware prototype can then be conducted to validate the estimated bandwidth requirements.

6.2.2 Improved Data Analytics for Situational Awareness

SWMU deployment will be gradual and will operate complimentary to conventional PMUs and SCADA systems. In addition to power system voltage and current measurements available from the aforementioned measurement technologies, system operating data is also available. This can include system topology, system loading, generation profiles and weather etc. Research focused on combining different resolutions of measurements as well as correlating operational conditions with synchronised voltage and current measurements will also play a vital role in understanding system-wide dynamics.

The proposed G-SWMU can capture emerging IBR dynamics, including their responses to different operating conditions. G-SWMU based event classification via supervised ML has been investigated in this thesis, however, these measurements can also be utilised for unsupervised data driven dynamics discovery. Emerging physics-informed ML, symbolic regression, grey-box modelling techniques and digital twins etc, can be utilised to discover mathematical representations of these IBR dynamics. These hybrid physics-based, data-driven approaches can address the complexities of IBR modelling, particularly when IBR control designs and parameters are unknown, but require SWMU measurements that accurately capture the underlying IBR behaviours. G-SWMU informed IBR and power system models can enable or improve a wide variety of applications including, stability assessments, grid code compliance verifications, oscillation source localisation and mitigation, and WAMPAC schemes. The efficient and scalable deployment of SWMUs will therefore be vital to managing IBR dominated power systems.

Appendix A

A Review of Signal Processing Techniques used in Power Systems

This Appendix provides a brief review of selected underlying signal processing techniques that are utilised in the power system monitoring algorithms reviewed in Chapter 2.

A.1 Discrete Fourier Transform

The DFT of an N sampled signal is given by:

$$X(\omega) = \sum_{n=0}^{N-1} x(n)e^{-j2\pi kn/N}, \tag{A.1}$$

and is evaluated over N equally spaced frequencies, $\omega_k = 2\pi k/N$ along the ω axis, such that $0 \leq \omega \leq 2\pi$ and $0 \leq N-1$ [186]. For power system phasor estimation, the window sizes and sampling rates are chosen for computational efficiency (based on the fast Fourier Transform implementation) and to ensure that the nominal frequency coincides with one of the frequency points being evaluated. This is done as the intention is to measure power system fundamental waveform quantities. It also ensures that the nominal and integer harmonics are measured as accurately as possible with minimal spectral leakage. DFT based measurement algorithms are therefore suitable for near steady-state conditions as well as for conditions that result in integer harmonics, e.g. transformer inrush, arc furnaces, switching etc.

The effectiveness of DFT based methods is negatively impacted if there is spectral leakage in the resulting frequency spectrum. This can lead to inaccurate amplitude, phase and frequency measurement. This can occur due to the true frequency of interest not being close to a point evaluated by the DFT, resulting in the associated energy being distributed among several adjacent evaluated frequency points, referred to as bins. To address this, the interpolated-DFT (Ip-DFT) fits an analytical model to the peak frequency and the surrounding bins in which the leakage occurs. It then determines a fractional correction term to reassign the spectral energy across multiple bins to give an interpolated estimate of the true frequency in between evaluated points of the DFT [187]. This method has been widely adopted in the literature for improving fundamental synchrophasor estimates in the presence of noise and more recently for inter-harmonic phasor estimation. [149, 188]

A.2 Modal Decomposition Methods

Power system signals can be modelled as the sum of N damped sinusoids (referred to as modes):

$$x(n) = \sum_{i=1}^{N} A_i e^{\sigma_i n} \cos(\omega_i n + \phi_i), \tag{A.2}$$

where $\lambda_i = \sigma \pm j\omega$ are the eigenvalues and $\omega_i = 2\pi f_i$, σ_i, A_i, ϕ_i are the angular frequency, damping, amplitude and phase of the i-th mode respectively. Using Euler's identity, this can be expressed as:

$$x(n) = \sum_{i=1}^{N} A_i z_i^n, \tag{A.3}$$

where $z_i = e^{(\sigma_i + j(\omega_i + \phi_i))}$. The goal of modal decomposition methods is to estimate the number of sinusoidal modes and their respective modal parameters from measurements. Two popular approaches for this in the literature are the Prony method [189] and the Matrix Pencil (MP) method [120]. Both method seek to find the solutions for z_i first and then estimate the amplitudes via optimisation, typically, using the least squares approach to minimise the error between the reconstruction and the observed data. The Prony method estimates P sinusoidal modes by solving the characteristic equation, $z^P + a_1 z^P - 1 + ... + a_P = 0$, where the coefficients are estimated from a difference equation constructed from lagged samples of the input measurements.

The MP method constructs matrices based on one-sample time-shifted versions of the input. Noting (A.3), the lagged version of X_1 becomes X_2 such that $x(n+1) = \sum_i (A_i z_i) z_i^n$. Projecting onto a subspace, described by the vectors, V, the relation between X_1 and X_2 becomes $X_2 V - z_i X_1 V = 0$. This implies that $(X_2 - z_i X_1)V = 0$. Solving this is equivalent to finding the eigenvalues (z_i) and eigenvectors (V) of $(X_1^{-1} X_2)$ which are obtained from the measurements. This can be done using singular value decomposition and expressions detailed in [190]. These methods have been used in oscillation analysis in power systems, typically for electromechanical oscillations and more recently for IBR driven oscillations [191, 192].

A.3 Time-Frequency Methods

Traditional DFT and modal estimation methods assume the sinal being measured is sinusoidal. These methods are frequency domain methods which assume that modal properties are constant across the observation window, i.e. there is a loss of temporal information. An extension of these methods are time-frequency methods that seek to jointly extract temporal and frequency information. The short time Fourier transform windows a signal into overlapping segments and computes the traditional DFT for each segment. The output is a combination of the spectrums across the time windows, resulting in a spectrogram. This method however still relies on sinusoidal bases.

The wavelet transform applies a set of bases referred to as wavelets that are dilated and translated before comparison with the input signal. The dilation changes the frequency resolution of the wavelet. For each dilated wavelet corresponding to a certain frequency range, a translation retains temporal information, for example the time instants in which a transient occurs within the input window. In contrast to Fourier bases which are sinusoidal, wavelet bases have a variety of shapes and properties arranged in families. This flexibility allows for bases that are more suited for non-sinusoidal distortions [193]. Wavelets have also been used for phasor estimation, however a key challenges arises due to the uncertainty principle that results in a trade-off between temporal and frequency resolution, resulting in energy from a particular frequency spreading into adjacent bins. Phasor extraction requires accurate frequency estimation. To address this, synchro-squeezing is applied. Synchro-squeezing process the wavelet spectrum to identify spectral bands and determines the distribution of energy across adjacent frequency bins. It determines the instantaneous frequency from the phase information in the wavelet transform output and uses this to reassign the energy to the proper frequency, allowing for accurate phasor magnitude estimation and improving separation of multiple oscillatory components [194].

A.4 Matching Pursuit Algorithms

Matching pursuit algorithms (MPA) seeks to find the optimal linear combination of basis functions (referred to as atoms) from a redundant dictionary of such basis functions. By finding the minimum number of atoms, MPA finds sparse representations of signals. User defined dictionary atoms also offer a level of interpretability. MPA initially calculates the inner product of the input signal with the dictionary of atoms to find the most similar atom, for example a sinusoidal wave. An optimal fit between the atom and the input data is found to estimate the parameters of the atoms that best describe the input, for example amplitude, frequency and phase of a sinusoidal atom. A residual is then found by subtracting the parameterised atom from the input waveform. The overall process is repeated to discover the different atoms and parameters (for example a wavelet atom for a transient left over in the residual from the previous iteration) that give a sufficient approximation of the signal, i.e., until the residual reduces beyond an acceptable threshold. The dictionary can include the previously described Fourier and wavelet transforms as well as domain specific, user specified entries. MPA is therefore adaptive to different possible dynamics that may be present in power system waveforms

A.5 Comparison of Methods

A comparison of the above methods and the signal processing methods used in the proposed G-SWMU algorithm of Chapter 4 is presented in Table A.1. In terms of phasor extraction, multiple, closely spaced interharmonic frequencies remain a challenge for the DFT, IpDFT, wavelet and synchro-squeezing methods especially in an online context as PMU processing windows tend to be a few cycles of nominal power system waveforms. Even with interpolation and synchro-squeezing, the spectral leakage from one mode of interest into another mode of interest is difficult to separate, in contrast to simply improving phasor estimates of one mode due to spectral leakage. These methods therefore require further information, i.e. longer observation windows leading to increase detection time. The I-EDFT and MP can address this but can be computationally complex, sensitive to noise and cannot represent non-sinusoidal information. The dictionary based MPA and the proposed G-SWMU approach addresses this limitation and are both adaptive to possible dynamics in input waveforms. The proposed approach presents several advantages of the MPA approach. It does not require complex dictionary design and, through the combined WSCTF and I-EDFT-EWT, is generalised to different input dynamics. This means it can represent information in situations that are not pre-defined in the MPA dictionary. The potential trade-off is a loss of interpretability that the MPA can provide, for example, if angle jumps, RoCoF and other known conditions are defined. Overall, the proposed method is adaptable and generalised to different conditions, with critical design features (such as frequency resolution) configurable, thus making it suitable for emerging IBR driven dynamics.

Table A.1: Comparison of Signal Processing Techniques

Method	**Advantage**	**Limitation**
DFT, Ip-DFT	Computationally efficient	Frequency resolution limited
	Accurate for nominal/harmonic components	Unsuitable for non-sinusoidal distortions
	Interpolation reduces impact of spectral leakage and interhamonics	
Modal de-composition, (Prony/MP)	Suitable for inter-harmonics	Unsuitable for non-sinusoidal distortions
	Provides damping	Online processing design complex
STFT, Wavelet Transform	Suitable for non-sinusoidal distortions	Limited frequency resolution
	Synchro-squeezing reduces impact of spectral leakage and interhamonics	
MPA Dictionary	Suitable for sinusoidal and non-sinusoidal distortions	Complex dictionary design
	Interpretable	Pre-defined dictionary not suitable for all dynamics
G-SWMU WSCTF, I-EDFT-EWT	Suitable for sinusoidal and non-sinusoidal distortions	Some loss of interpretability
	Generalised (not limited to dictionary)	Simplistic noise rejection

Appendix B

Additional Considerations of the Proposed G-SWMU Algorithm

This Appendix provides supplemental information regarding the proposed G-SWMU algorithm of Chapter 4. A more detailed explanation of the theory of the I-EDFT [150, 195] component utilised in the algorithm is provided. Additional G-SWMU algorithm settings are also discussed. Finally, an additional case study illustrating the performance of the algorithm under severe distortions is also presented and discussed.

B.1 Theory of the Iterative-Extended DFT

The continuous time Fourier transform (FT) of a signal and its inverse is given by:

$$F(\omega) = \int_{-\infty}^{\infty} x(t)e^{-i\omega t}\, dt, \tag{B.1}$$

$$x(t) = \frac{1}{2\pi}\int_{-\infty}^{\infty} F(\omega)e^{i\omega t}\, d\omega, \tag{B.2}$$

respectively. For a sampling period, T, and a finite, uniformly sampled observation window consisting of a sequence $x(nT)$, $n = 0, 1...N$, the discrete time Fourier transform

(DTFT) and its inverse become:

$$F_N(\omega) = \sum_{n=0}^{N-1} x(nT)e^{-i\omega NT}, \tag{B.3}$$

$$x(nt) = \frac{1}{2\pi}\int_{-\Omega}^{\Omega} F_N(\omega)e^{i\omega t}\,d\omega, \tag{B.4}$$

respectively. Note that the inverse DTFT is obtained across a band-limited frequency range with $\Omega \leq$ the Nyquist frequency. Recall also that the signal amplitude spectrum $S(\omega)$ is the FT divided by the length of the observation window:

$$S(\omega) = \frac{1}{N}F_N(\omega). \tag{B.5}$$

The extended Fourier transform seeks to calculate the FT in terms of a generalised, extended basis, $\alpha(w, nT)$, such that the extended DFT and its inverse becomes:

$$F_\alpha(\omega) = \sum_{n=0}^{N-1} x(nT)\alpha(w, nT), \tag{B.6}$$

$$x_\alpha(nt) = \frac{1}{2\pi}\int_{-\Omega}^{\Omega} F_\alpha(\omega)e^{i\omega t}\,d\omega. \tag{B.7}$$

and $\alpha(\omega, nT)$ can be evaluated at additional frequencies of interest. To develop a solution for this, the extended DFT formulates the problem as solving the least square minimisation between the (ideal) continuous time FT and the extended DFT, as defined below:

$$\min |F(w) - F_\alpha(\omega)|^2. \tag{B.8}$$

However, the continuous time FT cannot be directly computed for a windowed signal. Recall that a complex exponent signal at a periodic frequency, ω_0, and complex amplitude, $S(\omega_0)$, (like a sinusoidal power system waveform at 50Hz and 1 p.u. amplitude) can be expressed as:

$$x(w_0, t) = S(\omega_0)e^{i\omega_0 t}. \tag{B.9}$$

The FT of such a signal can be expressed by the Dirac delta function, at the point of the frequency axis corresponding to the frequency of the sinusoidal component:

$$\int_{-\infty}^{\infty} x(\omega_0, t)e^{-i\omega t}dt = 2\pi S(\omega_0)\delta(w - \omega_0). \tag{B.10}$$

For example, a steady state power system signal will have its spectral energy concentrated at 50Hz in the frequency domain. Note also that the amplitude spectrum at the frequency ω can be estimated as the ratio of the signal extended FT to the transform of an exponent with unit amplitude in the same extended basis:

$$S_\alpha(\omega) = \frac{\sum_{n=0}^{N-1} x(nT)\alpha(\omega, nT)}{\sum_{n=0}^{N-1} e^{i\omega nT}\alpha(\omega, nT)}. \tag{B.11}$$

$F(\omega)$ in (B.8) can be represented by (B.10) and substituting (B.9) into (B.6) gives the expression for $F_\alpha(\omega)$. Equation (B.8) therefore becomes:

$$\left| \int_{-\Omega}^{\Omega} 2\pi S(\omega_0)\delta(w - \omega_0) - \sum_{n=0}^{N-1} S(\omega_0)e^{i\omega_0 nT}\alpha(w, nT) \right|^2, \tag{B.12}$$

for an N sampled discrete signal, evaluated across a frequency range, $\pm\Omega$. This equation can be solved for $\alpha(\omega, kT)$ via setting the partial derivative of this equation, with respect to $\alpha(\omega, kT)$, equal to zero [150, 195]. The solution to this in matrix form is [148]:

$$A_\omega = |S(\omega)|^2 R^{-1} E_\omega, \tag{B.13}$$

where R becomes an autocorrelation matrix dependent upon the estimated signal power spectrum and E_ω is the matrix form of e^{-iwnT}. Converting to matrix format and substituting (B.13) into (B.6), (B.7) and (B.11) gives:

$$F_\alpha(w) = \mathrm{x}A_\omega = x|S(\omega)|^2 R^{-1} E_\omega, -\Omega \leq \omega \leq \Omega \tag{B.14}$$

$$x_\alpha(t) = xR^{-1}E_\omega, \tag{B.15}$$

$$S_\alpha(\omega) = \frac{x|S(w)|^2 R^{-1} E_w}{E_w^H |S(w)|^2 R^{-1} E_w} = \frac{x R^{-1} E_w}{E_w^H R^{-1} E_w} \tag{B.16}$$

The above equations express the FT and power spectrum in terms of an autocorrelation matrix. Recall the relationship that a signal's autocorrelation and power spectrum are Fourier transform pairs, i.e. a signal's power spectral density is the FT of its autocorrelation function (Wiener-Khinchin theorem [196]). Returning to equations (4.13)-(4.17) listed in Chapter 4 The I-EDFT solves the least square minimisation problem of (B.8) by first making a guess of the signal spectrum via a set of weightings, W, that describe the contributions of each frequency in the extended basis. An autocorrelation, R is then estimated from the assumed spectral properties. Note that no signal information is used at first. Next, the input data is projected unto the extended basis using the initial R and an updated amplitude spectrum is then estimated based on this input data by (4.15). Together, these steps determine how well the measured signal x sampled at nT increments can be represented by the basis, E_w, consisting of the user defined frequencies of interest and the estimated spectrum. Finally, the new estimated spectrum is used to initialise the weightings for the next iteration. This procedure is repeated until there is minimal change in the estimated spectrum relative to the previous iterations.

This method presents a data-driven approach to project the input signal onto a frequency basis that is not strictly limited by the observation window. The method therefore iteratively solves (B.16) using equations (4.13)-(4.17) listed in Chapter 4 and finally calculates the I-EDFT used in the I-EDFT-EWT multi-phasor extraction module of the G-SWMU algorithm of Chapter 4.

B.2 Additional Design Parameters of the Proposed G-SWMU Algorithm

There are several minor design choices involving the I-EDFT-EWT multi-phasor extraction module that will be elaborated in this section.

B.2.1 Spectrum Segmentation and Transition Widths

After the I-EDFT is applied to obtain a spectrum with increased resolution, the spectrum must be processed to determine spectral peaks and determine suitable boundaries in order to isolate these peaks via the EWT filters. This is done via spectrum segmentation. First peak detection is utilised using Matlab's inbuilt 'findpeaks' algorithm [197] which searches for local maxima in the I-EDFT spectrum. A minimum peak size is empirically chosen to disregard any noise. The peaks may also be sorted by amplitude and a max number of peaks may also be specified depending on the amount of components of interest. For example, selecting the top 5 peaks in terms of signal energy may give a good representation of the signal while limiting the amount of phasor outputs to reduce communication requirements.

After determining the peaks, a simplistic method of determining the mid-point between peaks is adopted in this thesis to determine the boundaries. For the first and last peaks, the mid-point between the respective peaks and $\pm\Omega$ (i.e. the end-points of the frequency range being evaluated) are utilised. This method assumes that the I-EDFT spectrum has sufficient resolution to separate the components by at least the transition width, τ_n, to avoid mode-mixing. A small transition width is therefore preferable. It is shown in [145] that the maximum transition width depends on the separation of the detected boundaries. For boundaries ω_{n+1} and ω_n along the frequency axis, the transition width must be less than $\frac{\omega_{n+1}-\omega_n}{\omega_{n+1}+\omega_n}$. The transition width is therefore set as the resolution of the I-EDFT as this represents the minimum it can be.

B.2.2 Initial Spectrum Weighting

The I-EDFT requires an initial spectrum estimate in the form of a set of weightings that are incrementally updated. The weighting matrix must have all non-zero entries and contain a weighting for each frequency point specified in the extended DFT basis. Domain knowledge is applied in this research to specify an initial weighting that emphasises the nominal frequency. Figure B.1 illustrates the initial (two-sided) spectrum weighting for the frequency range ± 200 (i.e. $\Omega = 200$) that serves as an input to the algorithm.

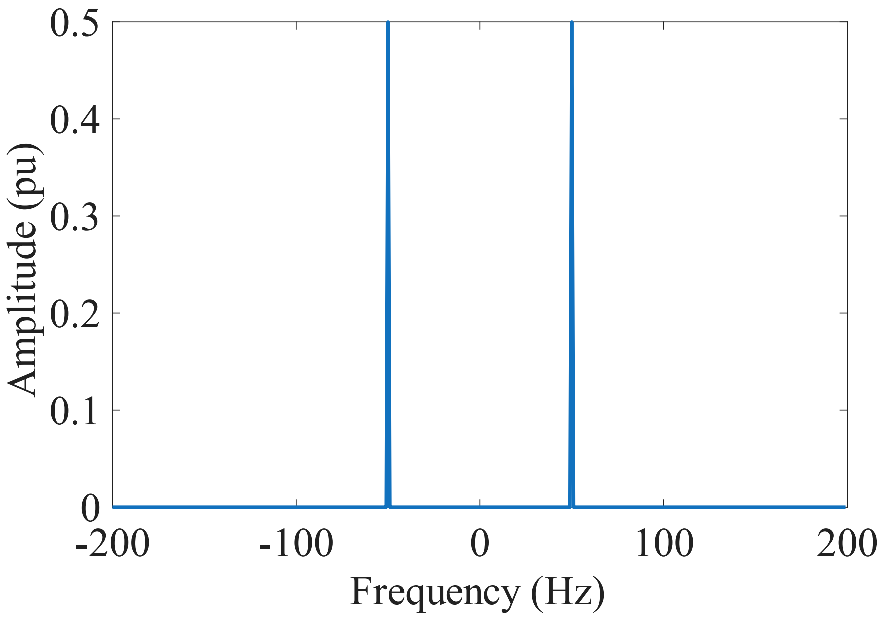

Figure B.1: Initial spectrum weighting

B.2.3 List of G-SWMU Algorithm Settings

A list of settings, with descriptions and examples of typical values and where appropriate dependencies on other settings, are highlighted in Table B.1.

Table B.1: Settings of the proposed G-SWMU algorithm

Setting	**Description**	**Typical Value**
W_name	WSCTF Wavelet Family	db4
J	Wavelet decomposition level	5
l	WSCTF correlation level	3
λ_{tr}	WSCTF transient threshold	$3 \times \sigma^2 \text{of} \, W(j,n)$
λ_{sm}	WSCTF Smoothing threshold	1% of Normalised wavelet energy per level
F_o	Fundamental frequency	50 Hz
f_{sample}	Sampling frequency	12.8 kHz
N	Number of samples per I-EDFT processing window	512
Ω	I-EDFT Frequency range	$\pm$200Hz
T	$[1 \times N]$ Matrix of time instants for I-EDFT basis kernel	$(0 : N-1) \times (1/f_{sample})$
M	Number of frequency points of the I-EDFT	f_{sample}
F	$[1 \times M]$ Matrix of frequency points of the I-EDFT	$-\Omega : f_{sample}/M : \Omega$
E	$[N \times M]$ Kernel matrix of I-EDFT basis	$e^{-i2\pi FT}$
W_init	$[1 \times M]$ matrix of initial spectral weightings	Nominal frequency has greatest weighting
$\lambda_{I\text{-}EDFT}$	Threshold to stop I-EDFT	0.001
pk_{min}	Minimum peak height for I-EDFT-EWT spectrum segmentation	1%
npk_{max}	Maximum number of peaks for I-EDFT-EWT spectrum segmentation	5
τ_n	EWT transition width	f_{sample}/M

B.3 Performance of the G-SWMU Algorithm Under Severe Distortions

Under severe distortions, the I-EDFT will fail to converge to a solution because the sinusoidal basis cannot represent the signal, even after filtering by the WSCTF. Under such conditions, the phasor output cannot give an appropriate representation of the input synchro-waveform, and hence the SWMU algorithm output will consist of the wavelet coefficient matrix of the extracted transients. Figure B.2 illustrates the faulted phase current for event 51 (60Hz signal sampled at 256 samples per cycle) of the GESL [164] that was caused by animal contact. This lead to a sharp increase in current over a short duration, leading to severe non-sinusoidal distortions. For comparison, the distortions associated with event 6 illustrated in Figure 4.18 of Chapter 4 are much less severe. For event 51, the G-SWMU algorithm therefore contains several phasor measurement windows with severe transients and discontinuities, even after the filtering operations. Figure B.2 compares the data-driven I-EDFT solution for a pre-fault window and during fault window, highlighting that if the input cannot be represented by the sinusoidal basis, the SWMU algorithm's phasor extraction can fail to converge to a solution.

However, in this scenario the phasor estimate does not have a clear physical meaning since the waveform is non-sinusoidal. Under severe distortions, analysis or applications utilising phasor outputs are not suitable, however, the wavelet based transient features extracted by the G-SWMU algorithm, illustrated in Figure B.2, can be directly input into ML applications as demonstrated in Chapter 5. The transient detection flag and the unknown class label of the proposed wavelet scattering, open-set (WS-OSNN) classifier can be used as a trigger to capture the waveform for later manual analysis by domain experts. The proposed G-SWMU algorithm can therefore give a useful representation of synchro-waveforms, adapting to various conditions including oscillations, harmonics and severe distortions, thus enabling improved monitoring for IBR dominated power systems.

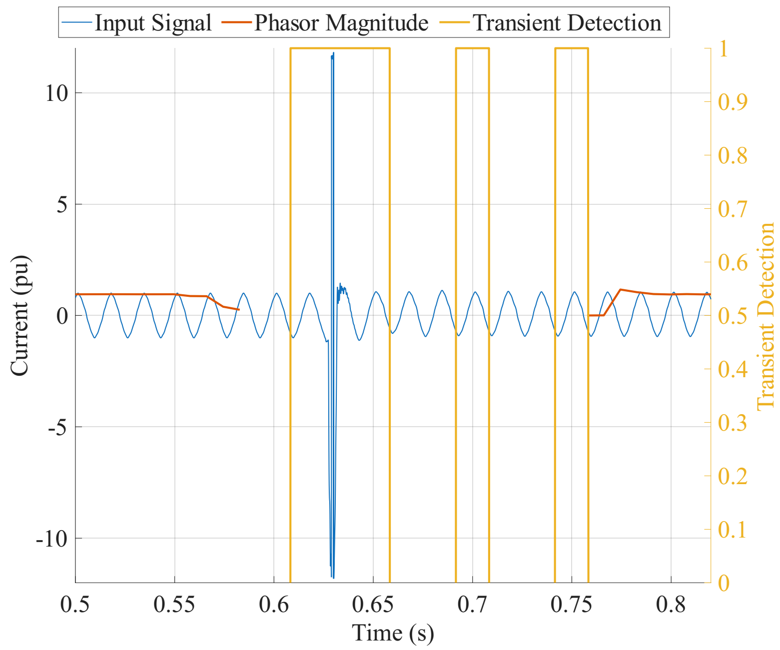

Figure B.2: G-SWMU phasor and transient detection output under severe distortions

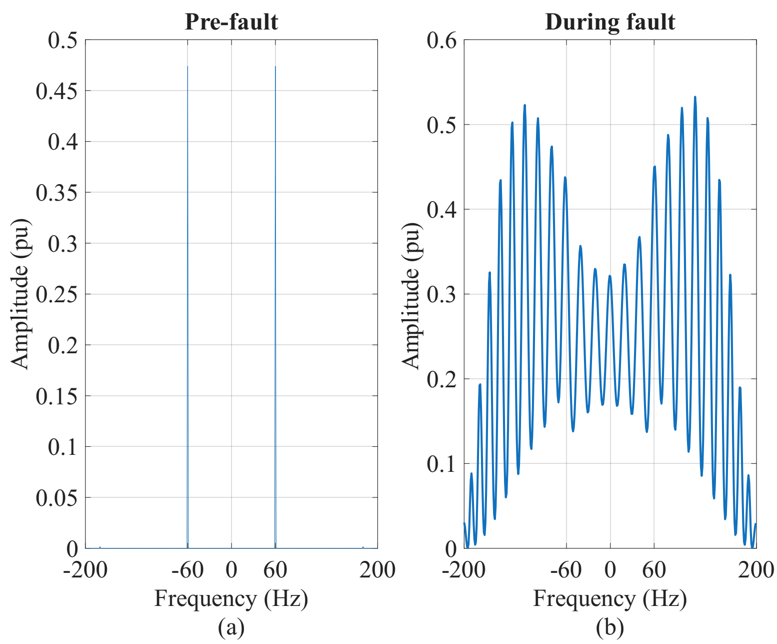

Figure B.3: I-EDFT solution convergence: (a) Pre-fault, (b) During fault

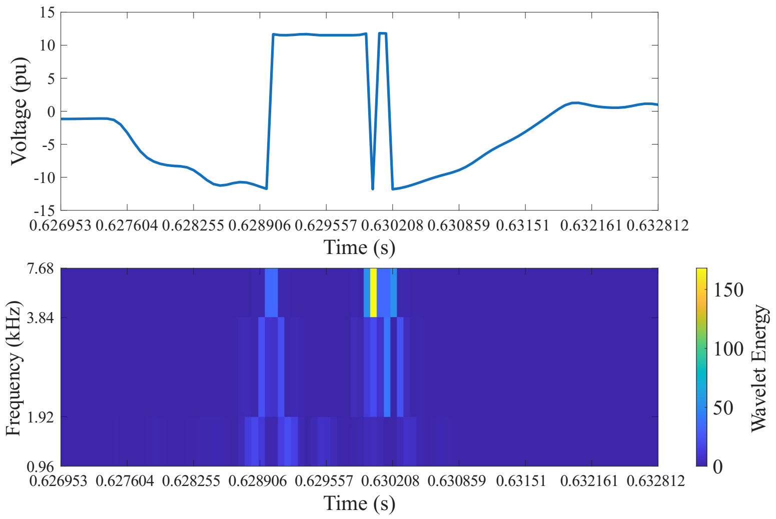

Figure B.4: SWMU algorithm WSCTF output for severe distortion event

B.4 Estimated Bandwidth Requirements of the G-SWMU Algorithm

The theoretical estimations of the bandwidth requirements of the G-SWMU algorithm is based on Table D.1 of IEEE C37-118-2-2024 standard [26]. The estimated payload of Table 4.11 in Chapter 4 is calculated using the following expression:

$$\begin{aligned}\text{118\_PAYLOAD} &= (\text{STAT\_FLAG WORD} = 2B) + (\text{TIME\_QUALITY} = 2B) + \\ &(\text{PHNMR} \times \text{bytes/phasor}) + (\text{ANNMR} \times \text{bytes/analog}) + \\ &(\text{FRNMR} \times \text{bytes/freq}) + (\text{DFDTNMR} \times \text{bytes/dfdt}) + (\text{DGNMR} \times 2). \quad \text{(B.17)}\end{aligned}$$

Table B.2 displays the field name descriptions and bytes per quantity as stated in the IEEE C37-118-2-2024 standard. Assuming a steady state payload of three-phase voltage and currents, frequency and RoCoF measurement, the calculated payload becomes:

$$\text{118\_SS} = 4 + (6 \times 4) + (0 \times 2) + (1 \times 2) + (1 \times 2) + (0 \times 2) = 32 \text{ bytes}$$

In a similar way, an SSO condition resulting in fundamental and sideband components can be estimated as:

$$118\_SSO = 4 + (18 \times 4) + (0 \times 2) + (3 \times 2) + (3 \times 2) + (0 \times 2) = 88 \text{ bytes}$$

For a transient condition, there is variability depending on the size of W_{tr}. Using the result described in Section 4.5.4 the estimated payload for a transient condition assuming the transient detection flag, phasor data attribute (digital signals) and a fundamental phasor estimate, the payload becomes:

$$118\_tr = 4 + (6 \times 4) + (126 \times 2) + (1 \times 2) + (1 \times 2) + (2 \times 2) = 288 \text{ bytes}$$

Table B.2: Field name and typical sizes of standard PMU message format

Field	**Size per quantity (bytes)**	**Description**
PHNMR	4	Number of phasors
ANNMR	2	Number of analogue values
FRNMR	2	Number of frequency signals
DFTNMR	2	Number of df/dt signals
DGNMR	2	Number of digital signals

Appendix C

Supplementary Information for the OSL Test Network of Chapter 4

This Appendix contains details of the IBR control structure, settings and network parameters used in the test network for the OSL study case of Section 4.4.5 and are based on the report and findings of [155].

C.1 IBR Control Structure and Settings

The simplified schematic of the grid side converter control diagram is illustrated in Figure C.1. This represents a generic model in which the control strategy is fully transparent, allowing for investigation of the sensitivity of the oscillation mechanism to different control parameters. The grid side controller consists of inner current dq frame control and outer control loops, which provide references for the inner current controllers, consisting of AC voltage (or reactive power) and DC link voltage (or active power) control. The Phase-Locked Loop (PLL) control of the default model is modified to conform with the design described in [97] in order to have more flexibility in analysing and simulating the oscillation mechanism of interest. Table C.1 lists the control settings and IBR parameters including power ratings and filter elements which are the same across all IBRs unless otherwise stated.

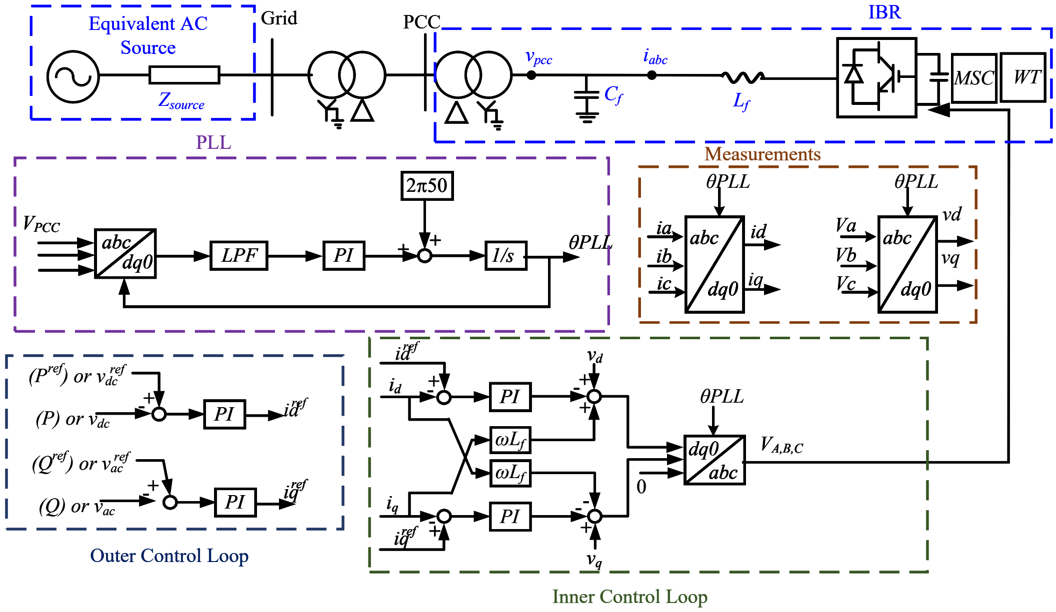

Figure C.1: IBR grid side converter control structure of the OSL test network

Table C.1: Controller parameters and IBR ratings

Parameter	Description	Values
K_p^{PLL}	PLL proportional gain [97]	WFA: 150 WFC,WFD: 60
T_i^{PLL}	PLL integral gain [97]	WFA: 2000 WFC,WFD: 1400
LPF (f_{cutoff})	Cut-off frequency of the PLL 2nd order low pass filter [97]	25 Hz
K_p^{GC}	Inner current control proportional gain [198]	0.51
T_i^{GC}	Inner current control integral gain [198]	0.001
K_p^{PC}	Outer control proportional gain [198]	1.0
T_i^{PC}	Outer control integral gain [198]	0.1678
V_{CONV}	Rated converter voltage [198]	35 kV LL rms
L_f	Filter inductance [198]	0.584 mH
C_f	Filter capacitance [198]	650 μF
S_R	Rated IBR power output	500 MW

C.2 Stability analysis of PLL induced oscillations

PLL induced oscillation mechanisms have been reported as a cause in several real-world events [98], especially when areas of a high penetration of IBRs are connected to a weak grid [97]. It is assumed that the outer loop controls and inner current loop controls are properly tuned and the stable operating point is a constant active power output, with a reactive current reference i_q^{ref} set close to zero, and the voltages at the point of common coupling is maintained at 1 p.u. It is shown in [2] that for such an operating point, the stability is impacted by the PLL controller. The open loop gain of the system is therefore proportional to the term G_{PLL}, which is represented by:

$$G_{PLL} = \frac{G_{PLL\_OL}}{1 + G_{PLL\_OL}} \tag{C.1}$$

where, G_{PLL_OL} is defined as:

$$G_{PLL\_OL} = \frac{V_{PCC}\left(K_p^{PLL} + \frac{T_i^{PLL}}{s}\right)}{s\,LPF(s)} \tag{C.2}$$

Stability analysis of the system under the assumed operating point is performed via Bode plots of, G_{PLL_OL}, with values of K_p^{PLL}, and T_i^{PLL}, specified in Table C.1. The analysis shows an instability for the settings used in windfarm A, as the peak in the magnitude response of the open-loop gain of the PLL loop is above 0 dB when the phase angle crosses 180° (at around 20Hz), while for the settings of windfarm C and D the amplitude is below 0 dB at the same point, and thus, the closed-loop system is expected to be stable.

C.3 Calculation of the DEF using PMU measurements

The conventional DEF method utilises PMU measurements and is derived based on the electro-mechanical swing equation [56]. This method has been successful in detecting traditional electromechanical oscillations and low frequency oscillations in both experimental and real-world applications. The DEF, W, from bus i to bus j, is calculated as:

$$W_{ij,n+1} = W_{ij,n} + 2\pi \Delta P_{ij,n} \Delta f_{ij,n} t_s + \Delta Q_{ij,n} \frac{\Delta V_{i,n+1} - \Delta V_{i,n-1}}{2V^*_{i,n}} \tag{C.3}$$

where

$$V^*_i = \tilde{V} + \Delta V_i \tag{C.4}$$

where, $\tilde{V}$ is the average voltage in the observation window with oscillations of a significant magnitude above noise; quantities with Δ are the filtered phasor voltages, powers, P, and frequency, f, components of an oscillation mode in phasor measurements; ts is the time interval between PMU samples and n is the sample index. Assuming a current measurement flowing from bus j to bus i, a negative DEF is indicative of a source while a positive DEF is indicative of a sink.

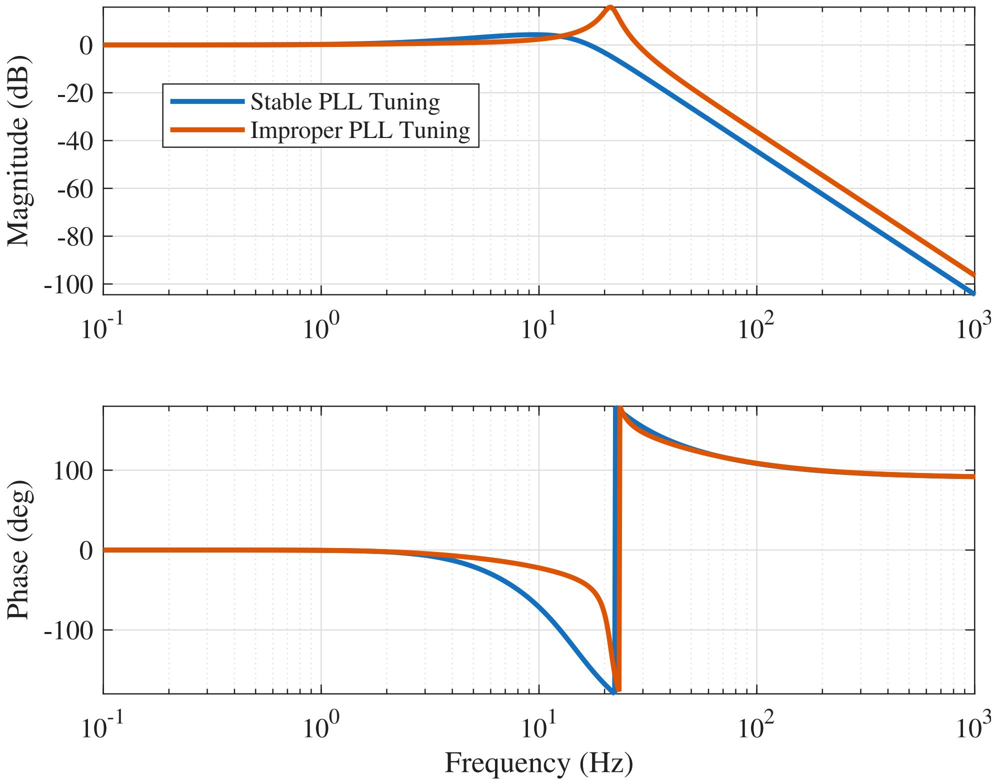

Figure C.2: Stability analysis of PLL tuning

Appendix D

Settings of the Classification Models in Chapter 5

This Appendix lists hyperparameters of the ML classifier models used in Chapter 5.

Table D.1: WS-OSNN / WS-NN Settings

Parameter	Description	Value
k	Neighbours	5
α (WS-OSNN)	OSR threshold	0.2
t (WS-OSNN)	Threshold to define distribution tail	75%
(γ, τ) (WS-OSNN)	Fitted GPD shape parameters	$(-0.74, 0.096)$
Distance metric	-	Euclidean
Standardization	Scale input features	Max-absolute

Table D.2: OOD+WS-NN Settings

Parameter	Description	Value
k	Neighbours	5
Distance metric	-	Euclidean
OOD method	Anomaly detection method	Local outlier factor
Standardization	Scale input features	Max-absolute

Bibliography

[1] United Nations, "Net zero coalition," https://www.un.org/en/climatechange/net-zero-coalition, United Nations, accessed: 2025-09-01. [Online]. Available: https://www.un.org/en/climatechange/net-zero-coalition

[2] International Energy Agency, "World energy outlook 2022," Paris, 2022, licence: CC BY 4.0 (report); CC BY NC SA 4.0 (Annex A). [Online]. Available: https://www.iea.org/reports/world-energy-outlook-2022

[3] J. Kim, "Energy security and the green transition," *IMF Work. Pap.*, vol. 2024, no. 006, p. 1, Jan. 2024.

[4] V. Anatolitis, H. Bahar, P. Bojek, F. Briens, T. Criswell, J. Moorhouse, K. Veerakumar, and L. M. Martinez, "Renewables 2024: Analysis and forecast to 2030," International Energy Agency, Tech. Rep., 2024.

[5] Department for Energy Security and Net Zero, "Energy trends UK, October to December 2024 and 2024, Section 5: Electricity," Tech. Rep., 2025.

[6] National Energy System Operator, "Clean power 2030: Advice on achieving clean power for Great Britain by 2030," Tech. Rep., 2025.

[7] Department for Energy Security and Net Zero, "Net zero government initiative: UK roadmap to net zero government emissions," December 2023.

[8] S. Chakraborty, P. H. Pinheiro, R. G. Bainy, H. Lei, B. K. Johnson, S. Manson, J. Wang, R. Mahmud, A. Hoke, and C. J. Kruse, "Evaluating the impact of fault current limiter schemes of IBRs on transmission line protection elements," in *2025*

IEEE Energy Conversion Conference Congress and Exposition (ECCE), 2025, pp. 1–8.

[9] D. Liu, Q. Hong, A. Dyśko, D. Tzelepis, G. Yang, C. Booth, I. Cowan, and B. Ponnalagan, "Evaluation of HVDC system's impact and quantification of synchronous compensation for distance protection," *IET Renewable Power Generation*, vol. 16, no. 9, pp. 1925–1940, 2022. [Online]. Available: https://ietresearch.onlinelibrary.wiley.com/doi/abs/10.1049/rpg2.12460

[10] Department for Business, Energy and Industrial Stratergy, "GB power system disruption - 9 August 2019 Energy Emergencies Executive Committee: Interim Report," Tech. Rep., 2019.

[11] N. Hatziargyriou, J. Milanovic, C. Rahmann, V. Ajjarapu, C. Canizares, I. Erlich, D. Hill, I. Hiskens, I. Kamwa, B. Pal, P. Pourbeik, J. Sanchez-Gasca, A. Stankovic, T. Van Cutsem, V. Vittal, and C. Vournas, "Definition and classification of power system stability – revisited & extended," *IEEE Transactions on Power Systems*, vol. 36, no. 4, pp. 3271–3281, 2021.

[12] P. Denholm, T. Mai, R. Kenyon, B. Kroposki, and M. O'Malley, "Inertia and the power grid: A guide without the spin," 2020.

[13] B. Badrzadeh, Z. Emin, S. Goyal, S. Grogan, A. Haddadi, A. Halley, A. Louis, T. Lund, J. Matevosyan, T. Morton, D. Premm, and S. Sproul, "System strength," *CIGRE Science & Engineering*, vol. 20, pp. 5–26, Feb. 2021.

[14] North American Electric Reliability Corporation, "Inverter-based resource performance issues report: Findings from the Level 2 alert," https://www.nerc.com/comm/RSTC_Reliability_Guidelines/NERC_Inverter-Based_Resource_Performance_Issues_Public_Report_2023, Tech. Rep., Nov. 2023.

[15] Australian Energy Market Operator, "Power system oscillations in south Australia on 23 June 2022: Reviewable operating incident report under

the national electricity rules," https://aemo.com.au/-/media/files/electricity/nem/market_notices_and_events/power_system_incident_reports/2022/south-australia-power-system-oscillations, Tech. Rep., Feb. 2023.

[16] National Energy System Operator, "Sub-synchronous oscillations in GB: current state and plans for future management," Tech. Rep., 2024.

[17] Department for Energy Security and Net Zero, "Energy Trends: UK electricity - Fuel used in electricity generation and electricity supplied (ET 5.1 - quarterly)," https://www.gov.uk/government/statistics/electricity-section-5-energy-trends.

[18] National Energy System Operator, "Future energy scenarios (FES) 2024: NESO pathways to Net Zero," Tech. Rep., 2024.

[19] National Energy System Operator , "System Operator Transmission Owner Code STCP27-01 System Performance Monitoring Requirements Issue 003," Tech. Rep., 2023.

[20] P. Wall, P. Dattaray, Z. Jin, P. Mohapatra, J. Yu, D. Wilson, K. Hay, S. Clark, M. Osborne, P. M. Ashton, and V. Terzija, "Deployment and demonstration of wide area monitoring system in power system of Great Britain," *Journal of Modern Power Systems and Clean Energy*, vol. 4, no. 3, pp. 506–518, 2016.

[21] W. Xu, Z. Huang, X. Xie, and C. Li, "Synchronized waveforms; a frontier of data-based power system and apparatus monitoring, protection, and control," *IEEE Transactions on Power Delivery*, vol. 37, no. 1, pp. 3–17, 2022.

[22] P. Orr, G. Fusiek, P. Niewczas, C. D. Booth, A. Dysko, F. Kawano, T. Nishida, and P. Beaumont, "Distributed photonic instrumentation for power system protection and control," *IEEE Trans. Instrum. Meas.*, vol. 64, no. 1, pp. 19–26, Jan. 2015.

[23] H. Mohsenian-Rad, J.-Y. Joo, M. Balestrieri, L. Piyasinghe, S. Biswas, K. Chatterjee, H. Valizadeh-Haghi, K. Chang, J. Grappe, T. Laughner, S. Blair, C. Mullins, Y. Liu, Y. Wu, B. Sun, V. Choinière, H. Mohsenzadeh-Yazdi, F. Ahmadi-Gorjayi, L. Chen, J. Follum, Y. S. Hubbell, A. Karpilow, M. Paolone,

M. J. Mousavi, S. R. Samantaray, J. Dagle, A. Wilson, C. Li, A. Shahsavari, M. M. Bonab, A. Ragusa, M. R. Younis, B. Moussa, H. Ghoudjehbaklou, D. Deka, M. Farrokhabadi, F. Aminifar, C. Lackner, F. Rahmatian, and R. Brown, "Synchro-waveform measurements and data analytics in power systems (TR 127)," 2024. [Online]. Available: https://resourcecenter.ieee-pes.org/publications/technical-reports/pes_tr_127_amps_1218724

[24] J. Follum, L. Miller, P. Etingov, H. Kirkham, A. Riepnieks, X. Fan, and E. Ellwein, "Phasors or waveforms: Considerations for choosing measurements to match your application," Pacific Northwest National Laboratory, Tech. Rep. PNNL-31215, Apr. 2021.

[25] NESO, "Data sharing infrastructure: Industry webinar," Webinar, Dec. 2025, available: https://www.neso.energy/about/our-projects/virtual-energy-system/data-sharing-infrastructure-dsi.

[26] "IEEE Standard for Synchrophasor Data Transfer for Power Systems," in *IEEE Std C37.118.2-2024 (Revision of IEEE Std C37.118.2-2011)*, 2024, pp. 1–79.

[27] S. Blair, K. Kawal, P. Papadopoulos, and Q. Hong, "Review of Applications and Practicalities of Synchronized Waveform Monitoring," in *2024 International Conference on Smart Grid Synchronized Measurements and Analytics (SGSMA)*, May 2024, pp. 1–6.

[28] K. Kawal, S. Blair, Q. Hong, and P. N. Papadopoulos, "Selective Auto-Reclosing of Mixed Circuits Based on Multi-Zone Differential Protection Principle and Distributed Sensing," vol. 16, no. 6, p. 2558. [Online]. Available: https://www.mdpi.com/1996-1073/16/6/2558

[29] J. D. Follum, H. Kirkham, A. Riepnieks, P. V. Etingov, L. E. Miller, X. Fan, and E. J. Ellwein, "Roadmap for advanced power system measurements," Pacific Northwest National Lab. (PNNL), Richland, WA (United States), Tech. Rep., 04 2021. [Online]. Available: https://www.osti.gov/biblio/1871292

[30] North American Electric Reliability Corporation, "Real-time application of synchrophasors for improving reliability," NERC, Tech. Rep., October 2010.

[31] U.S. Department of Energy, "Measurements, communications, and controls," U.S. Department of Energy, Tech. Rep., Sep. 2015. [Online]. Available: https://www.energy.gov/quadrennial-technology-review-2015

[32] G. Cheng, Y. Lin, A. Abur, A. Gómez-Expósito, and W. Wu, "A Survey of Power System State Estimation Using Multiple Data Sources: PMUs, SCADA, AMI, and Beyond," *IEEE Transactions on Smart Grid*, vol. 15, no. 1, pp. 1129–1151, 2024.

[33] P. Overholt, K. Uhlen, B. Marchionini, and O. Valentine, "Synchrophasor Applications for Wide Area Monitoring and Control: ISGAN Discussion Paper," IEA–ISGAN / ISGAN Annex 6, Tech. Rep., 2016.

[34] A. Phadke, "Synchronized phasor measurements: A historical overview," in *IEEE/PES Transmission and Distribution Conference and Exhibition*, vol. 1, 2002, pp. 476–479 vol.1.

[35] A. Shrestha, M. Silveira, J. Yellajosula, and S. K. Mutha, "Understanding the impacts of time synchronization and network issues on protection in digital secondary systems," in *Proceedings of the PAC World Global Conference 2021.* Schweitzer Engineering Laboratories, Inc., Aug. 2021, presented at the PAC World Global Conference 2021, Virtual Format, August 31–September 1, 2021.

[36] A. Silverstein, S. Achanta, M. Danielson, P. Evans, T. Jones, H. Kirkham, Y.-S. Li-Baboud, R. Ondrof, K. Thomas, G. Trevino, F. Tuffner, and M. Weiss, "Time synchronization in the electric power system," North American SynchroPhasor Initiative, NASPI Technical Report NASPI-2017-TR-001, Mar. 2017, pNNL-26331.

[37] Q. Hong, K. Kawal, S. Paladhi, G. Zhang, C. Booth, and V. Terzija, "Wide area monitoring, protection and control (WAMPAC)," in *Encyclopedia of Electrical and Electronic Power Engineering.* Elsevier, 2023, pp. 278–293.

[38] "IEEE/IEC International Standard - Measuring relays and protection equipment - Part 118-1: Synchrophasor for power systems - Measurements," *IEC/IEEE 60255-118-1:2018*, pp. 1–78, 2018.

[39] P. Vorobev, D. M. Greenwood, J. H. Bell, J. W. Bialek, P. C. Taylor, and K. Turitsyn, "Deadbands, droop, and inertia impact on power system frequency distribution," *IEEE Transactions on Power Systems*, vol. 34, no. 4, pp. 3098–3108, 2019.

[40] P. Castello, P. Ferrari, P. A. Pegoraro, and S. Rinaldi, "Hardware for PMU and PMU integration," in *Phasor Measurement Units and Wide Area Monitoring Systems*. Elsevier, 2016, pp. 63–86.

[41] C. Muscas and P. A. Pegoraro, "Algorithms for synchrophasors, frequency, and ROCOF," in *Phasor Measurement Units and Wide Area Monitoring Systems*. Elsevier, 2016, pp. 21–51.

[42] A. J. Roscoe, I. F. Abdulhadi, and G. M. Burt, "P and M Class Phasor Measurement Unit Algorithms Using Adaptive Cascaded Filters," *IEEE Transactions on Power Delivery*, vol. 28, no. 3, pp. 1447–1459, 2013.

[43] V. Gharpure, "The North American Synchrophasor Initiatice webinar series: IEEE C37.118.2-2024: Revised Standard for Synchrophasor Data Transfer for Power Systems - Vasudev Gharpure," May 2025, available: https://naspi.org/webinars.

[44] SP Energy Networks, "Visualisation of Real Time System Dynamics using Enhanced Monitoring (VISOR): Close Down Report," Tech. Rep., March 2018.

[45] S. Clark, D. Wilson, N. Al-Ashwal, F. Macleod, P. Mohapatra, J. Yu, P. Wall, P. Dattaray, V. Terzija, P. Ashton, and M. Osborne, "Addressing emerging network management needs with enhanced WAMS in the GB VISOR project," in *2016 Power Systems Computation Conference (PSCC)*, 2016, pp. 1–7.

[46] J. Cepeda, D. Echeverra, and G. Argüello, "Cenace's experiences on implementing a wide area monitoring system (wams) in the ecuadorian power system," in *2014 IEEE Central America and Panama Convention (CONCAPAN XXXIV)*, 2014, pp. 1–7.

[47] K. Chatterjee, S. Biswas, J. D. Follum, and S. Kincic, "Online monitoring applications enabled by phasor measurement units: Technical assistance to the power sectors of southeast asia," Pacific Northwest National Laboratory (PNNL), Richland, WA (United States), Tech. Rep., 12 2023. [Online]. Available: https://www.osti.gov/biblio/2242496

[48] F. Galvan, A. Abur, K. Sun, M. Thomas, V. Venkatasubramanian, and K. C. Rubal, "Implementation of synchrophasor monitoring at entergy: Tools, training and tribulations," in *2012 IEEE Power and Energy Society General Meeting*, 2012, pp. 1–4.

[49] S. Maslennikov and E. Litvinov, "Iso new england experience in locating the source of oscillations online," *IEEE Transactions on Power Systems*, vol. 36, no. 1, pp. 495–503, 2021.

[50] P. Kundu and A. K. Pradhan, "Power network protection using wide-area measurements considering uncertainty in data availability," *IEEE Systems Journal*, vol. 12, no. 4, pp. 3358–3368, 2018.

[51] D. J. Trudnowski, J. Follum, R. T. Elliott, D. A. Schoenwald, and J. W. Pierre, "Characterizing the oscillatory properties of bulk electric systems," *IEEE Access*, vol. 13, pp. 32 883–32 900, 2025.

[52] R. Farmer, A. Schwalb, and E. Katz, "Navajo project report on subsynchronous resonance analysis and solutions," *IEEE Transactions on Power Apparatus and Systems*, vol. 96, no. 4, pp. 1226–1232, 1977.

[53] D. Walker, C. Bowler, R. Jackson, and D. Hodges, "Results of subsynchronous resonance test at mohave," *IEEE Transactions on Power Apparatus and Systems*, vol. 94, no. 5, pp. 1878–1889, 1975.

[54] R. T. Elliott and D. A. Schoenwald, "Visualizing the inter-area modes of the western interconnection," in *2022 IEEE Power & Energy Society General Meeting (PESGM)*, 2022, pp. 1–5.

[55] R. Huang, U. Agrawal, N. Zhou, J. Follum, S. Wang, P. Etingov, Y. Chen, Z. Huang, A. Ghassemian, B. Barazesh, and K. Davis, "WECC Wide-Area Oscillation Assessment and Trending Study Report," Pacific Northwest National Laboratory, Tech. Rep. PNNL-33651, October 2022.

[56] S. Maslennikov, B. Wang, and E. Litvinov, "Dissipating energy flow method for locating the source of sustained oscillations," *International Journal of Electrical Power & Energy Systems*, vol. 88, pp. 55–62, Jun. 2017. [Online]. Available: https://linkinghub.elsevier.com/retrieve/pii/S0142061516323365

[57] Q. Hong, M. Karimi, M. Sun, S. Norris, O. Bagleybter, D. Wilson, I. F. Abdulhadi, V. Terzija, B. Marshall, and C. D. Booth, "Design and validation of a wide area monitoring and control system for fast frequency response," *IEEE Transactions on Smart Grid*, vol. 11, no. 4, pp. 3394–3404, 2020.

[58] J. D. Follum, E. J. Ellwein, P. V. Etingov, X. Fan, H. Kirkham, L. E. Miller, and A. Riepnieks, "Advanced power systems measurements: A literature review," Pacific Northwest National Lab. (PNNL), Richland, WA (United States), Tech. Rep., 12 2020. [Online]. Available: https://www.osti.gov/biblio/1871291

[59] B. Berry, "Inertia estimation methodologies vs measurement methodology: Impact on system operations," in *CIGRE Symposium, Aalborg, Denmark*, June 2019.

[60] H. Yin, W. Qiu, Y. Wu, W. Yu, J. Tan, A. Hoke, C. J. Kruse, B. W. Rockwell, and Y. Liu, "Anomaly identification of synchronized voltage waveform for situational awareness of low inertia systems," *IEEE Transactions on Smart Grid*, vol. 16, no. 3, pp. 2416–2428, 2025.

[61] "Distributed Electrical Sensing (DES)." [Online]. Available: https://synapt.ec/technology/des/

[62] P. Orr and P. Niewczas, "High-speed, solid state, interferometric interrogator and multiplexer for fiber Bragg grating sensors," *Journal of Lightwave Technology*, vol. 29, no. 22, pp. 3387–3392, 2011.

[63] P. Orr, G. Fusiek, P. Niewczas, A. Dyśko, C. Booth, F. Kawano, and G. Baber, "Distributed optical distance protection using fbg-based voltage and current transducers," in *2011 IEEE Power and Energy Society General Meeting*, 2011, pp. 1–5.

[64] D. Tzelepis, A. Dyśko, G. Fusiek, J. Nelson, P. Niewczas, D. Vozikis, P. Orr, N. Gordon, and C. D. Booth, "Single-ended differential protection in MTDC networks using optical sensors," *IEEE Transactions on Power Delivery*, vol. 32, no. 3, pp. 1605–1615, 2017.

[65] J. D. Follum, Y. Agalgaonkar, R. Hovsapian, K. H. Lacommare, J. MacDonald, A. McEachern, N. M. Stenvig, O. Alaca, N. Bhusal, K. Chatterjee *et al.*, "Advanced measurements for resilient integration of inverter-based resources: Progress matrix final report," Pacific Northwest National Laboratory (PNNL), Richland, WA (United States), Tech. Rep., 06 2024. [Online]. Available: https://www.osti.gov/biblio/2462809

[66] J. D. Follum, R. Hovsapian, N. M. Stenvig, Y. Agalgaonkar, K. Chatterjee, K. Mahapatra, A. Riepnieks, A. J. Wilson, S. Chanda, and S. Granda, "Advanced measurements for resilient integration of inverter-based resources: Progress matrix year-1 report," Pacific Northwest National Laboratory (PNNL), Richland, WA (United States), Tech. Rep., 03 2023. [Online]. Available: https://www.osti.gov/biblio/1985697

[67] International Electrotechnical Commission and International Electrotechnical Commission. Technical Committee, *IEC 61850-9-2:2011 Communication Networks and Systems for Power Utility Automation: Réseaux Et Systèmes de Communication Pour L'automatisation Des Systèmes Électriques. Specific communication service mapping (SCSM)–sampled values over ISO/IEC 8802-3. Mise en*

correspondance des services de communication spécifiques (SCSM)–valeurs échantillonnées sur ISO/CEI 8802-3, 2011.

[68] D. Nakafuji, L. Rogers, J. Bestebreur, M. Rourke, and G. Zweigle, "Integrating synchrophasors and oscillography for wide-area power system analysis," in *2017 70th Annual Conference for Protective Relay Engineers (CPRE)*, 2017, pp. 1–10.

[69] D. Sun, H. Liu, S. Liu, and T. Bi, "Development of synchronized waveform measurement and its application on fault detection," *IEEE Trans. Instrum. Meas.*, vol. 72, pp. 1–11, 2023.

[70] "IEEE Standard for Streaming Telemetry Transport Protocol (STTP)," *IEEE Std 2664-2024*, pp. 1–98, 2024.

[71] J. R. Carroll, C. Lackner, F. R. Robertson, and S. Murphy, "Using streaming telemetry transport protocol to send time synchronized real time data at scale," in *2024 International Conference on Smart Grid Synchronized Measurements and Analytics (SGSMA)*, 2024, pp. 1–6.

[72] J. R. Carroll and F. R. Robertson, "A comparison of phasor communication protocols," Pacific Northwest National Laboratory (PNNL), Richland, WA (United States), Tech. Rep., 02 2019. [Online]. Available: https://www.osti.gov/biblio/1504742

[73] Dominion Energy, "Continuous oscillography waveforms from the substation to the cloud," 2024.

[74] North American SynchroPhasor Initiative (NASPI) Data & Network Management Task Team, "Naspi 2020 survey of industry best practices for archiving synchronized measurements (dnmtt)," North American SynchroPhasor Initiative (NASPI), Technical Report NASPI-2020-TR-024, Nov. 2020, accessed: 2025-11-09. [Online]. Available: https://www.naspi.org/documents/naspi-2020-survey-industry-best-practices-archiving-synchronized-measurements-dnmtt

[75] R. Arghandeh, D. Bienstock, P. Etingov, S. Murphy, F. Omitaomu, M. Rhodes, T. Rizy, A. K. Srivastava, K. Sun, and X. Zhou, "Data mining techniques and tools for synchrophasor data," North American Synchrophasor Initiative, Tech. Rep. PNNL-28218, January 2019.

[76] A. Silverstein and J. Follum, "High-resolution, time-synchronized grid monitoring devices," North American SynchroPhasor Initiative, Richland, WA, Technical Report NASPI-2020-TR-004, March 2020.

[77] A. Riepnieks and H. Kirkham, "An introduction to goodness of fit for pmu parameter estimation," *IEEE Transactions on Power Delivery*, vol. 32, no. 5, pp. 2238–2245, 2017.

[78] M. Izadi and H. Mohsenian-Rad, "A synchronized lissajous-based method to detect and classify events in synchro-waveform measurements in power distribution networks," *IEEE Transactions on Smart Grid*, vol. 13, no. 3, pp. 2170–2184, 2022.

[79] H. Mohsenzadeh-Yazdi, F. Ahmadi-Gorjayi, and H. Mohsenian-Rad, "Sub-cycle dynamics modeling of IBRs using LSTM methods and synchro-waveform measurements," in *2024 IEEE Power & Energy Society General Meeting (PESGM)*, 2024, pp. 1–5.

[80] A. Karpilow, A. Derviškadić, G. Frigo, and M. Paolone, "Characterization of non-stationary signals in electric grids: A functional dictionary approach," *IEEE Transactions on Power Systems*, vol. 37, no. 2, pp. 1126–1138, 2022.

[81] C. Presvôts, M. Kieffer, T. Prevost, P. Panciatici, Z. Li, and P. Piantanida, "Multiple-model coding scheme for electrical signal compression," *Signal Processing*, vol. 236, no. 110037, p. 110037, Nov. 2025.

[82] F. A. d. O. Nascimento, R. G. Saraiva, and J. Cormane, "Improved transient data compression algorithm based on wavelet spectral quantization models," *IEEE Transactions on Power Delivery*, vol. 35, no. 5, pp. 2222–2232, 2020.

[83] K. Chauhan, M. V. Reddy, and R. Sodhi, "A novel distribution-level phasor estimation algorithm using empirical wavelet transform," *IEEE Transactions on Industrial Electronics*, vol. 65, no. 10, pp. 7984–7995, 2018.

[84] B. Gao, R. Torquato, W. Xu, and W. Freitas, "Waveform-based method for fast and accurate identification of subsynchronous resonance events," *IEEE Transactions on Power Systems*, vol. 34, no. 5, pp. 3626–3636, 2019.

[85] F. Zhang, J. Li, J. Liu, W. Gao, and J. He, "An improved interpolated DFT-based parameter identification for sub-/super-synchronous oscillations with synchrophasors," *IEEE Transactions on Power Systems*, vol. 38, no. 2, pp. 1714–1727, 2023.

[86] S. Blair and J. Costello, "Slipstream: High-performance lossless compression for streaming synchronized waveform monitoring data," in *2022 International Conference on Smart Grid Synchronized Measurements and Analytics (SGSMA)*, 2022, pp. 1–6.

[87] M. Izadi and H. Mohsenian-Rad, "Synchronous waveform measurements to locate transient events and incipient faults in power distribution networks," *IEEE Transactions on Smart Grid*, vol. 12, no. 5, pp. 4295–4307, 2021.

[88] Envista Forensics, Inc. and Witt O'Briens, "2017-18 Root cause analyses of the 2017-18 wildfires found to have been ignited by PG&E and corrective action report," California Public Utilities Commission, Tech. Rep., 2022.

[89] California Department of Forestry and Fire Protection, "Statistics," https://www.fire.ca.gov/our-impact/statistics, 2025, accessed: 2026-04-21.

[90] Southern California Edison , "SCE Fire Incident Data: 2024," https://www.cpuc.ca.gov/industries-and-topics/wildfires, Apr. 2025.

[91] Southern California Edison, "SCE Fire Incident Data: 2014," https://www.cpuc.ca.gov/industries-and-topics/wildfires, Apr. 2015.

[92] B. D. Russell, J. A. Wischkaemper, C. L. Benner, and K. Manivannan, “Preventing certain powerline caused wildfires by early detection and repair of failing devices,” in *2022 IEEE/PES Transmission and Distribution Conference and Exposition (T&D)*, 2022, pp. 1–5.

[93] J. A. Wischkaemper, C. L. Benner, B. Don Russell, and K. Muthu Manivannan, “Application of advanced electrical waveform monitoring and analytics for reduction of wildfire risk,” in *ISGT 2014*, 2014, pp. 1–5.

[94] A. Saeed, M. Jensen, M. J. Reno, A. Bidram, and A. Zamani, “Utilities perspective on protection challenges with high IBR penetration,” Pacific Gas and Electric Company, San Francisco, CA (United States), Tech. Rep., 09 2024. [Online]. Available: https://www.osti.gov/biblio/2458239

[95] North American Electric Reliability Corporation (NERC), “1,200 mw fault induced solar photovoltaic resource interruption disturbance report: Southern california 8/16/2016 event,” North American Electric Reliability Corporation, Disturbance Report, Jun. 2017, accessed: 2026-01-04. [Online]. Available: https://www.nerc.com/globalassets/our-work/reports/event-reports/1200_mw_fault_induced_solar_photovoltaic_resource_interruption_final.pdf

[96] Energy Systems Integration Group, “Diagnosis and mitigation of observed oscillations in IBR-dominant power systems: A practical guide,” Energy Systems Integration Group, Reston, VA, Tech. Rep., 2024. [Online]. Available: https://www.esig.energy/oscillations-guide/

[97] L. Fan, Z. Miao, S. Shah, Y. Cheng, J. Rose, S.-H. Huang, B. Pal, X. Xie, N. Modi, S. Wang, and S. Zhu, “Real-World 20-Hz IBR Subsynchronous Oscillations: Signatures and Mechanism Analysis,” *IEEE Transactions on Energy Conversion*, vol. 37, no. 4, pp. 2863–2873, Dec. 2022.

[98] Y. Cheng, L. Fan, J. Rose, S.-H. Huang, J. Schmall, X. Wang, X. Xie, J. Shair, J. R. Ramamurthy, N. Modi, C. Li, C. Wang, S. Shah, B. Pal, Z. Miao, A. Isaacs, J. Mahseredjian, and J. Zhou, “Real-World Subsynchronous Oscillation Events in

Power Grids With High Penetrations of Inverter-Based Resources," *IEEE Transactions on Power Systems*, vol. 38, no. 1, pp. 316–330, Jan. 2023.

[99] L. Fan, Z. Miao, and Z. Wang, "A new type of weak grid IBR oscillations," *IEEE Transactions on Power Systems*, vol. 38, no. 1, pp. 988–991, 2023.

[100] Y. Xu, Y. Chen, W. Wu, S. Liao, Z. Wang, A. Luo, S. Aziz, and J. M. Guerrero, "Complex circuit modeling methodology and its application to depict multifrequency coupling effect of asymmetric grid-following converter," *IEEE Journal of Emerging and Selected Topics in Power Electronics*, vol. 11, no. 1, pp. 1203–1218, 2023.

[101] H. Liu, T. Bi, X. Chang, X. Guo, L. Wang, C. Cao, Q. Yan, and J. Li, "Impacts of subsynchronous and supersynchronous frequency components on synchrophasor measurements," *Journal of Modern Power Systems and Clean Energy*, vol. 4, no. 3, pp. 362–369, 2016.

[102] F. Zhang, "Simulated Synchrophasors in SSOs and Phasor Measurement Data Recorded During a Subsynchronous Oscillation Incident in an Actual Power System," 2021. [Online]. Available: https://dx.doi.org/10.21227/dvrr-t131

[103] C. Wang, C. Mishra, K. D. Jones, R. M. Gardner, and L. Vanfretti, "Identifying oscillations injected by inverter-based solar energy sources," in *2022 IEEE Power & Energy Society General Meeting (PESGM)*, 2022, pp. 1–5.

[104] Australian Energy Market Operator, "West Murray Zone Power System Oscillations 2020-2021 ," Tech. Rep., 2023.

[105] X. Jiang, B. Stephen, and S. McArthur, "Automated distribution network fault cause identification with advanced similarity metrics," *IEEE Transactions on Power Delivery*, vol. 36, no. 2, pp. 785–793, 2021.

[106] W. Qiu, H. Yin, Y. Dong, X. Wei, Y. Liu, and W. Yao, "Synchro-waveform-based event identification using multi-task time-frequency transform networks," *IEEE Transactions on Smart Grid*, vol. 16, no. 3, pp. 2647–2658, 2025.

[107] M. Zhang, Q. Xu, and X. Wang, “Physics-informed neural network based on-line impedance identification of voltage source converters,” *IEEE Transactions on Industrial Electronics*, vol. 70, no. 4, pp. 3717–3728, 2023.

[108] Oak Ridge National Laboratory and Lawrence Livermore National Laboratory, “Grid Event Signature Library,” Available: https://gesl.ornl.gov/.

[109] S. Biswas, J. Follum, E. Andersen, and J. S. Banning, “Big data analysis of synchrophasor data: Outcomes of research activities by DOE FOA 1861,” Pacific Northwest National Laboratory, Tech. Rep., 2022.

[110] National Energy System Operator, “National Electricity Transmission System Security and Quality of Supply Standard,” National Energy System Operator, Tech. Rep. Version 2.11, Mar. 2026, published 13 March 2026. Accessed: 25 April 2026. [Online]. Available: https://www.neso.energy/industry-information/codes/security-and-quality-supply-standard-sqss/sqss-code-documents

[111] GSR018 Workgroup, “GSR018: Sub-Synchronous Oscillations (SSO) Workgroup Report,” National Grid Electricity Transmission, Tech. Rep. Version 1.0, Nov. 2015, published 24 November 2015. [Online]. Available: https://www.nationalgrideso.com/document/39791/download

[112] Scottish Government: Energy and Climate Change Directorate, “Scottish Energy Statistics Hub,” Available: https://scotland.shinyapps.io/Energy/.

[113] S. Chen, G. Zhang, S. S. Yu, Z. Li, A. E. Aroudi, and Y. Zhang, “Sub-synchronous oscillations in power systems with high renewable integration: Analytical models, mitigation strategies, and emerging challenges,” *Renew. Sustain. Energy Rev.*, vol. 226, no. 116322, p. 116322, Jan. 2026.

[114] Q. Hong, S. Blair, R. Williams, C. Booth, M. McFarlane, R. Eynon, and N. Matheson, “Design of an open platform for real-time power grid monitoring,” in *2019 IEEE 8th International Conference on Advanced Power System Automation and Protection (APAP)*, 2019, pp. 735–739.

[115] Elexon, "Elexon BSC Insights Solution," available: https://bmrs.elexon.co.uk/.

[116] National Energy System Operator, "NESO Data Portal," https://www.neso.energy/data-portal, 2026.

[117] Schweitzer Engineering Laboratories, "SEL-451 Protection, Automation, and Bay Control System," Product flyer, 2018, accessed: 2026-04-25. [Online]. Available: https://selinc.com/products/451/docs/

[118] Grid Protection Alliance, "openHistorian 2 High-performance Measurement Archive," available:https://github.com/GridProtectionAlliance/openHistorian.

[119] National Energy System Operator, "ESO operational transparency forum 08 November 2023," available: https://www.neso.energy/what-we-do/systems-operations/operational-transparency-forum.

[120] Y. Hua and T. Sarkar, "Matrix pencil method for estimating parameters of exponentially damped/undamped sinusoids in noise," *IEEE Transactions on Acoustics, Speech, and Signal Processing*, vol. 38, no. 5, pp. 814–824, 1990.

[121] S. W. Smith, "Applications of the DFT," in *The scientist and engineer's guide to digital signal processing.* USA: California Technical Publishing, 1997, pp. 169–184.

[122] B. Boashash, Ed., "Chapter I: The time-frequency approach: Essence and Terminology," in *Time-Frequency Signal Analysis and Processing (Second Edition).* Oxford: Academic Press, 2016, pp. 3–29.

[123] S. Aminikhanghahi and D. J. Cook, "A survey of methods for time series change point detection," *Knowledge and Information Systems*, vol. 51, no. 2, pp. 339–367, May 2017.

[124] J. Chen and A. K. Gupta, "Preliminaries," in *Parametric Statistical Change Point Analysis: With Applications to Genetics, Medicine, and Finance.* Boston: Birkhäuser Boston, 2012, pp. 1–5.

[125] M. MansourLakouraj, C. Mishra, L. Vanfretti, J. De La Ree, K. D. Jones, and H. Livani, "Automated step change detection in real-world pmu data addressing practical implications," *IEEE Transactions on Power Delivery*, vol. 40, no. 4, pp. 2194–2205, 2025.

[126] R. Killick, F. , P., and I. A. and Eckley, "Optimal Detection of Changepoints With a Linear Computational Cost," *Journal of the American Statistical Association*, vol. 107, no. 500, pp. 1590–1598, Dec. 2012.

[127] The MathWorks Inc., "findchangepts in signal processing toolbox version: 24.2 (r2024b)," Natick, Massachusetts, United States, 2024. [Online]. Available: https://www.mathworks.com

[128] A. O. Ige and M. Sibiya, "State-of-the-art in 1d convolutional neural networks: A survey," *IEEE Access*, vol. 12, pp. 144 082–144 105, 2024.

[129] Y. Tian, D. Su, S. Lauria, and X. Liu, "Recent advances on loss functions in deep learning for computer vision," *Neurocomputing*, vol. 497, pp. 129–158, Aug. 2022.

[130] M. Krichen, "Convolutional neural networks: A survey," *Computers*, vol. 12, no. 8, p. 151, Jul. 2023.

[131] S. R. Dubey, S. K. Singh, and B. B. Chaudhuri, "Activation functions in deep learning: A comprehensive survey and benchmark," *Neurocomputing*, vol. 503, pp. 92–108, Sep. 2022.

[132] C. Sticht, "Power system waveform classification using time-frequency and CNN," Oak Ridge National Laboratory (ORNL), Oak Ridge, TN (United States), Tech. Rep., 01 2022. [Online]. Available: https://www.osti.gov/biblio/1841478

[133] A. A. Wani, "Comprehensive review of dimensionality reduction algorithms: challenges, limitations, and innovative solutions," *PeerJ Comput. Sci.*, vol. 11, no. e3025, p. e3025, Jul. 2025.

[134] W. Xu, J. Yong, H. J. Marquez, and C. Li, "Interharmonic power – a new concept for power system oscillation source location," *IEEE Transactions on Power Systems*, pp. 1–13, 2025.

[135] I. Daubechies, "1. the what, why, and how of wavelets," in *Ten Lectures on Wavelets*. Society for Industrial and Applied Mathematics, Jan. 1992, pp. 1–16.

[136] M. Stéphane, "CHAPTER 3 - discrete revolution," in *A Wavelet Tour of Signal Processing (Third Edition)*, third edition ed., M. Stéphane, Ed. Boston: Academic Press, 2009, pp. 59–88.

[137] S. Avdaković and N. Čišija, "Wavelets as a tool for power system dynamic events analysis – state-of-the-art and future applications," *J. Electr. Syst. Inf. Technol.*, vol. 2, no. 1, pp. 47–57, May 2015.

[138] D. Liu, A. Dyśko, Q. Hong, D. Tzelepis, and C. D. Booth, "Transient wavelet energy-based protection scheme for inverter-dominated microgrid," *IEEE Transactions on Smart Grid*, vol. 13, no. 4, pp. 2533–2546, 2022.

[139] G. P. Nason and B. W. Silverman, "The stationary wavelet transform and some statistical applications," in *Lecture Notes in Statistics*, ser. Lecture notes in statistics. New York, NY: Springer New York, 1995, pp. 281–299.

[140] The MathWorks Inc., "Continuous and discrete wavelet transforms," in *Wavelet Toolbox Documentation*. Natick, Massachusetts, United States: The MathWorks Inc., 2025, available:https://uk.mathworks.com/help/wavelet/gs/continuous-and-discrete-wavelet-transforms.html.

[141] S. Mallat and W. Hwang, "Singularity detection and processing with wavelets," *IEEE Transactions on Information Theory*, vol. 38, no. 2, pp. 617–643, Mar. 1992.

[142] J. Ren and M. Kezunovic, "An Adaptive Phasor Estimator for Power System Waveforms Containing Transients," *IEEE Transactions on Power Delivery*, vol. 27, no. 2, pp. 735–745, Apr. 2012, conference Name: IEEE Transactions

on Power Delivery. [Online]. Available: https://ieeexplore.ieee.org/document/6156804/?arnumber=6156804

[143] Yansun Xu, J. Weaver, D. Healy, and Jian Lu, "Wavelet transform domain filters: a spatially selective noise filtration technique," *IEEE Transactions on Image Processing*, vol. 3, no. 6, pp. 747–758, Nov. 1994. [Online]. Available: http://ieeexplore.ieee.org/document/336245/

[144] L. Chen, X. Xie, X. Li, L. Yang, and X. Cao, "Online SSO stability analysis-based oscillation parameter estimation in converter-tied grids," *Appl. Energy*, vol. 351, no. 121827, p. 121827, Dec. 2023.

[145] J. Gilles, "Empirical Wavelet Transform," *IEEE Transactions on Signal Processing*, vol. 61, no. 16, pp. 3999–4010, Aug. 2013. [Online]. Available: https://ieeexplore.ieee.org/document/6522142/

[146] I. Daubechies, "9. Characterization of Functional Spaces by Means of Wavelets," in *Ten Lectures on Wavelets*, ser. CBMS-NSF Regional Conference Series in Applied Mathematics. Society for Industrial and Applied Mathematics, Jan. 1992, pp. 289–311. [Online]. Available: https://epubs.siam.org/doi/10.1137/1.9781611970104.ch9

[147] K. Kawal, Q. Hong, Panagiotis, N. Papadopoulos, S. M. Blair, and C. D. Booth, "A Wavelet Based Synchronized Waveform Measurement Unit Algorithm," in *2023 IEEE PES Innovative Smart Grid Technologies Europe (ISGT EUROPE)*, Oct. 2023, pp. 1–5. [Online]. Available: https://ieeexplore.ieee.org/document/10408556

[148] V. Liepins, "Extended fourier analysis of signals," Ph.D. dissertation, University of Latvia, Riga, Latvia, 1998, Ph.D. dissertation. Available on arXiv as CoRR abs/1303.2033. [Online]. Available: https://arxiv.org/abs/1303.2033

[149] Q. Zhang, H. Liu, H. Chen, Q. Li, and Z. Zhang, "A precise and adaptive algorithm for interharmonics measurement based on iterative DFT," *IEEE Transactions on Power Delivery*, vol. 23, no. 4, pp. 1728–1735, 2008.

[150] V. Liepins, "A method of spectrum evaluation applicable to analysis of periodically and nonregularly digitized signals," *Automatic Control and Computer Sciences*, vol. 27, no. 6, pp. 46–52, 1993.

[151] Y. Liu, H. An, and S. Bian, "Hilbert-huang transform and the application," in *2020 IEEE International Conference on Artificial Intelligence and Information Systems (ICAIIS)*, 2020, pp. 534–539.

[152] S. Affijulla and P. Tripathy, "Development of phasor estimation algorithm for p-class pmu suitable in protection applications," *IEEE Transactions on Smart Grid*, vol. 9, no. 2, pp. 1250–1260, 2018.

[153] L. Marple, "Computing the discrete-time "analytic" signal via fft," *IEEE Transactions on Signal Processing*, vol. 47, no. 9, pp. 2600–2603, 1999.

[154] D. M. Laverty, H. Kirkham, D. J. Morrow, and X. Liu, "Estimation of goodness of fit of synchrophasors during transient faults," in *2017 IEEE Power & Energy Society General Meeting*, 2017, pp. 1–5.

[155] Scottish and Southern Electricity Networks - Transmission (SSEN-T), "Innovative Network Status Intelligence Gathered by Holistic use of Telemetry (INSIGHT)-Alpha Phase, End-of-phase meeting," April 2024, available online: https://smarter.energynetworks.org/projects/ukri10079053/.

[156] X. Xie, Y. Zhan, J. Shair, Z. Ka, and X. Chang, "Identifying the Source of Subsynchronous Control Interaction via Wide-Area Monitoring of Sub/Super-Synchronous Power Flows," *IEEE Transactions on Power Delivery*, vol. 35, no. 5, pp. 2177–2185, Oct. 2020. [Online]. Available: https://ieeexplore.ieee.org/document/8946593/

[157] L. Fan, Z. Wang, Z. Miao, and S. Maslennikov, "Oscillation source detection for inverter-based resources via dissipative energy flow," 03 2023.

[158] M. Stéphane, "Wavelet bases," in *A Wavelet Tour of Signal Processing*. Elsevier, 2009, pp. 263–376.

[159] T. M. Inc., "Simulink Desktop Real Time (R2023b)," 2023.

[160] J. Scott and M. Tůma, "An introduction to sparse matrices," in *Nečas Center Series*. Cham: Springer International Publishing, 2023, pp. 1–18.

[161] M. Hoefling, F. Heimgaertner, D. Fuchs, M. Menth, P. Romano, T. Tesfay, M. Paolone, J. Adolph, and V. Gronas, "Integration of ieee c37.118 and publish/subscribe communication," in *2015 IEEE International Conference on Communications (ICC)*, 2015, pp. 764–769.

[162] N. Gurung, C. B. Kliros, L. C. Zhang, M. D. Lelic, M. Sheikholeslami, Z. Li, A. Momeni, O. Alizadeh, and F. Rahmatian, "Sensors with intelligent measurement platform for monitoring and control in distribution circuits," in *2020 IEEE Power & Energy Society General Meeting (PESGM)*, 2020, pp. 1–5.

[163] S. Ericson, J. Cox, M. Abdelmalak, H. Rabinowitz, and E. Hotchkiss, "Exceedance probabilities and recurrence intervals for extended power outages in the United States," National Renewable Energy Laboratory, Golden,CO, USA, Tech. Rep. NREL/TP-5R00-83092, 2022.

[164] A. J. Wilson, A. Riza Ekti, J. Follum, S. Biswas, C. Annalicia, J.-Y. Joo, O. Aziz, and J. Lian, "The grid event signature library: An open-access repository of power system measurement signatures," *IEEE Access*, vol. 12, pp. 76 207–76 218, 2024.

[165] P. Ren, Y. Xiao, X. Chang, P.-Y. Huang, Z. Li, B. B. Gupta, X. Chen, and X. Wang, "A survey of deep active learning," *ACM Comput. Surv.*, vol. 54, no. 9, Oct. 2021. [Online]. Available: https://doi.org/10.1145/3472291

[166] J. Xie, I. Alvarez-Fernandez, and W. Sun, "A review of machine learning applications in power system resilience," in *2020 IEEE Power & Energy Society General Meeting (PESGM)*, 2020, pp. 1–5.

[167] C. Geng, S.-J. Huang, and S. Chen, "Recent advances in open set recognition: A survey," *IEEE Transactions on Pattern Analysis and Machine Intelligence*, vol. 43, no. 10, pp. 3614–3631, 2021.

[168] W. J. Scheirer, A. de Rezende Rocha, A. Sapkota, and T. E. Boult, "Toward open set recognition," *IEEE Transactions on Pattern Analysis and Machine Intelligence*, vol. 35, no. 7, pp. 1757–1772, 2013.

[169] J. P. Iii, "Statistical inference using extreme order statistics," *Ann. Stat.*, vol. 3, no. 1, pp. 119–131, Jan. 1975.

[170] A. A. Balkema and L. de Haan, "Residual life time at great age," *Ann. Probab.*, vol. 2, no. 5, pp. 792–804, Oct. 1974.

[171] W. J. Scheirer, L. P. Jain, and T. E. Boult, "Probability models for open set recognition," *IEEE Transactions on Pattern Analysis and Machine Intelligence*, vol. 36, no. 11, pp. 2317–2324, 2014.

[172] L. P. Jain, W. J. Scheirer, and T. E. Boult, "Multi-class open set recognition using probability of inclusion," in *Computer Vision – ECCV 2014*, D. Fleet, T. Pajdla, B. Schiele, and T. Tuytelaars, Eds. Cham: Springer International Publishing, 2014, pp. 393–409.

[173] A. Bendale and T. E. Boult, "Towards open set deep networks," in *2016 IEEE Conference on Computer Vision and Pattern Recognition (CVPR)*, 2016, pp. 1563–1572.

[174] H. Zhang and V. M. Patel, "Sparse representation-based open set recognition," *IEEE Transactions on Pattern Analysis and Machine Intelligence*, vol. 39, no. 8, pp. 1690–1696, 2017.

[175] P. R. Mendes Júnior, R. M. de Souza, R. d. O. Werneck, B. V. Stein, D. V. Pazinato, W. R. de Almeida, O. A. B. Penatti, R. d. S. Torres, and A. Rocha, "Nearest neighbors distance ratio open-set classifier," *Mach. Learn.*, vol. 106, no. 3, pp. 359–386, Mar. 2017.

[176] M. L. Steyn, T. de Wet, B. D. Baets, and S. L. and, "A nearest neighbor open-set classifier based on excesses of distance ratios," *Journal of Computational*

and Graphical Statistics, vol. 32, no. 1, pp. 319–328, 2023. [Online]. Available: https://doi.org/10.1080/10618600.2022.2096621

[177] Z. Yang, J. Yue, P. Ghamisi, S. Zhang, J. Ma, and L. Fang, "Open set recognition in real world," *Int. J. Comput. Vis.*, vol. 132, no. 8, pp. 3208–3231, Aug. 2024.

[178] Y. Chen, L. Tao, X. Liu, J. Ma, C. Lu, and H. Liu, "Open-set fault recognition and inference for rolling bearing based on open fault semantic subspace," *IEEE Transactions on Instrumentation and Measurement*, vol. 73, pp. 1–11, 2024.

[179] D. I. Németh and K. Tornai, "Detecting unknown electrical loads using open set recognition," in *2022 IEEE 10th International Conference on Smart Energy Grid Engineering (SEGE)*, 2022, pp. 7–11.

[180] G. Guo, H. Wang, D. Bell, Y. Bi, and K. Greer, "KNN model-based approach in classification," in *On The Move to Meaningful Internet Systems 2003: CoopIS, DOA, and ODBASE*, ser. Lecture notes in computer science. Berlin, Heidelberg: Springer Berlin Heidelberg, 2003, pp. 986–996.

[181] J. Bruna and S. Mallat, "Invariant scattering convolution networks," *IEEE Transactions on Pattern Analysis and Machine Intelligence*, vol. 35, no. 8, pp. 1872–1886, 2013.

[182] J. Andén and S. Mallat, "Deep scattering spectrum," *IEEE Transactions on Signal Processing*, vol. 62, no. 16, pp. 4114–4128, 2014.

[183] M. Andreux, T. Angles, G. Exarchakis, R. Leonarduzzi, G. Rochette, L. Thiry, J. Zarka, S. Mallat, J. Andén, E. Belilovsky, J. Bruna, V. Lostanlen, M. Chaudhary, M. J. Hirn, E. Oyallon, S. Zhang, C. Cella, and M. Eickenberg, "Kymatio: Scattering transforms in python," *Journal of Machine Learning Research*, vol. 21, no. 60, pp. 1–6, 2020. [Online]. Available: http://jmlr.org/papers/v21/19-047.html

[184] B. S. Everitt, S. Landau, M. Leese, and D. Stahl, "Hierarchical clustering," in *Cluster Analysis*, 5th ed. "Hoboken, NJ": Wiley-Blackwell, 2011, pp. 71–110.

[185] G. W. Milligan and M. C. Cooper, "An examination of procedures for determining the number of clusters in a data set," *Psychometrika*, vol. 50, no. 2, pp. 159–179, Jun. 1985.

[186] "Discrete transforms," in *Power Systems Signal Processing For Smart Grids*. Chichester, United Kingdom: John Wiley and Sons Ltd, Sep. 2013, pp. 87–133.

[187] B. Quinn, "Estimating frequency by interpolation using fourier coefficients," *IEEE Transactions on Signal Processing*, vol. 42, no. 5, pp. 1264–1268, 1994.

[188] C. García-Veloso, M. Paolone, and J. M. Maza-Ortega, "Computationally efficient synchrophasor estimation: Delayed in-quadrature interpolated DFT," *IEEE Transactions on Instrumentation and Measurement*, vol. 73, pp. 1–16, 2024.

[189] R. Kumaresan, D. Tufts, and L. Scharf, "A prony method for noisy data: Choosing the signal components and selecting the order in exponential signal models," *Proceedings of the IEEE*, vol. 72, no. 2, pp. 230–233, 1984.

[190] A. Almunif, L. Fan, and Z. Miao, "A tutorial on data-driven eigenvalue identification: Prony analysis, matrix pencil, and eigensystem realization algorithm," *Int. Trans. Electr. Energy Syst.*, vol. 30, no. 4, Apr. 2020.

[191] P. N. Papadopoulos, T. A. Papadopoulos, A. I. Chrysochos, and J. V. Milanovic, "Measurement based method for online characterization of generator dynamic behaviour in systems with renewable generation," *IEEE Trans. Power Syst.*, vol. 33, no. 6, pp. 6466–6475, Nov. 2018.

[192] P. Jamanchipalle, K. V. Katariya, D. R. Pullaguram, and A. K. Pradhan, "Mitigation of sustained oscillations caused by IBR controller in weak grid interconnection," in *2025 7th International Conference on Energy, Power and Environment (ICEPE)*, 2025, pp. 1–6.

[193] S. Avdaković and N. Čišija, "Wavelets as a tool for power system dynamic events analysis – State-of-the-art and future applications," *Journal of Electrical Systems*

and Information Technology, vol. 2, no. 1, pp. 47–57, May 2015. [Online]. Available: https://linkinghub.elsevier.com/retrieve/pii/S2314717215000173

[194] L. Li, H. Cai, H. Han, Q. Jiang, and H. Ji, "Adaptive short-time Fourier transform and synchrosqueezing transform for non-stationary signal separation," *Signal Processing*, vol. 166, no. 107231, p. 107231, Jan. 2020.

[195] V. Liepins, "A method for spectral analysis of band-limited signals," *Automatic Control and Computer Sciences*, vol. 27, no. 5, pp. 51–56, 1993.

[196] L. Cohen, "Generalization of the Wiener-Khinchin theorem," *IEEE Signal Processing Letters*, vol. 5, no. 11, pp. 292–294, 1998.

[197] The MathWorks Inc., "findpeaks (Signal Processing Toolbox)," Natick, Massachusetts, United States, 2023. [Online]. Available: https://www.mathworks.com

[198] RTDS Technologies, "Standardization of renewable energy system modelling - example cases," RTDS Technologies, Tech. Rep., 2023.